

## ABSTRACT

Title of dissertation: MEASUREMENT OF THE ELECTRON RECOIL  
BAND OF THE LUX DARK MATTER DETECTOR  
WITH A TRITIUM CALIBRATION SOURCE

Attila Dobi, Doctor of Philosophy, 2014

Dissertation directed by: Professor Carter Hall  
Department of Physics

The Large Underground Xenon (LUX) experiment has recently placed the most stringent limit for the spin-independent WIMP-nucleon scattering cross-section. The WIMP search limit was aided by an internal tritium source resulting in an unprecedented calibration and understanding of the electronic recoil background. Here we discuss corrections to the signals in LUX, the energy scale calibration and present the methodology for extracting fundamental properties of electron recoils in liquid xenon. The tritium calibration is used to measure the ionization and scintillation yield of xenon down to 1 keV, the results is compared to other experiments. Recombination probability and its fluctuation is measured from 1 to 1000 keV, using betas from tritium and Compton scatters from an external  $^{137}\text{Cs}$  source. Finally, the tritium source is described and the most recent results for ER discrimination in LUX is presented.

Measurement of the Electron Recoil Band of the LUX  
Dark Matter Detector With a Tritium Calibration Source

by

Attila Dobi

Dissertation submitted to the Faculty of the Graduate School of the  
University of Maryland, College Park in partial fulfillment  
of the requirements for the degree of  
Doctor of Philosophy  
2014

Advisory Committee:

Professor Carter Hall, Chair/Adviser  
Professor Elizabeth Beise  
Professor Massimo Ricotti  
Professor Thomas Cohen  
Professor Zackaria Chacko

## Acknowledgments

First and foremost, I'd like to thank my adviser Professor Carter Hall, for giving me the opportunity to have worked with him over the past years. I would have ended up in a boring nuclear engineering job had it not been for his intervention. He has always made time for me and has provided me with invaluable insight. I appreciate all your help over the years, I have learned a great deal from you.

I've been fortunate to have been surrounded by talented coworkers all who have helped me to become. Simon, Ruey, Clayton, Tom, Richard, Jon, Doug, I will cherish my graduate experience having worked in the lab with you all.

I would also like to thank Professor Richard Gaitskell and the entire group at Brown University, to whom I owe my familiarity with LUX data analysis and data processing. Jeremy, Dave, James, Monica, Carlos, Alastair, Simon. None of the analysis presented here would have been possible without your guidance. I would especially like to thank Carlos and his wife Fatma for their generosity.

I owe gratitude to all members of the LUX collaboration for contributing towards the development, construction and commissioning of the LUX detector. It was an enormous effort by all. Special thanks to Patrick, Markus, Jeremy, Carmen, Scott, Ethan, Mongkol, Mia, Rachel, Nicole. I had a great time working and living in South Dakota with all of you.

To Matthew, Patrick, Tom Shutt, I am grateful for all the discussions we've had on topic of fluctuations in liquid xenon. Which, several months ago, was utterly incomprehensible to me

All of the personnel at the Sanford Underground laboratory in lead South Dakota deserve special mention. They keep our experiment running smoothing one mile underground, no easy task.

I'd like to acknowledge all my friends who have helped take my mind off physics over the years. Henry, Kyle, Vibhu and Norvik. Special thanks to Kristy and Moose. Also, my friends in Hungary who always make sure I'm well fed and have a drink in my hand. Adam, Petya, Nandi, Enik and my cousin Zoli.

My family members have always been there for me, including our dog Rocco. I could not have made it with the love and support from my step father, grandparents, my sister and mother. Szeretlek!

It is impossible to remember all so many people have helped me along the way, and I apologize to those I've inadvertently left out.

## Table of Contents

List of Figures	vii
1 Introduction	1
1.1 Astrophysical Evidence For Dark Matter	2
1.1.1 Galactic Rotation Curves	2
1.1.2 Big Bang Nucleosynthesis	4
1.1.3 Cosmic Microwave Background	5
1.1.4 Baryonic Acoustic Oscillations	6
1.1.5 Gravitational Lensing	9
1.2 Dark Matter Particles	10
1.2.1 Weakly Interacting Massive Particles	12
1.3 WIMP Dark Matter Searches	13
1.3.1 Direct Detection of WIMPs	14
1.3.2 WIMP Detection Experiments	19
1.4 Outline of the Thesis	20
List of Abbreviations	1
2 The LUX Detector	22
2.1 Introduction	22
2.2 The LUX TPC	23
2.2.1 Target Xenon	25
2.2.2 Background Rejection	26
2.2.3 The Drift Field inside the LUX TPC	28
2.3 Light and Charge Signals in Liquid Xenon	30
2.3.1 Electronic Recoils (ER)	32
2.3.2 Nuclear Recoils (NR)	34
2.3.3 Energy and Position Reconstruction	35
2.4 Identifying S1, S2	36
2.5 LUX Science Result (WIMP limit)	40

3	Corrections to the S1 and S2 signals	47
3.1	$^{83m}\text{Kr}$ Calibration . . . . .	48
3.2	$^{83m}\text{Kr}$ Mixing in Liquid Xenon . . . . .	53
3.3	S2 Electron Lifetime and x,y Correction . . . . .	54
3.4	S1 x,y,z Correction . . . . .	57
3.5	Application of x,y,z Corrections to the Data . . . . .	63
4	The Combined Energy Scale	67
4.1	Introduction . . . . .	67
4.2	Charge vs. Light . . . . .	71
4.3	Refitting in Combined Energy Space . . . . .	75
4.4	Error Determination of $g_1$ and $g_2$ with a Markov Chain Monte Carlo .	79
4.5	Combined Energy Space . . . . .	81
4.6	Light Collection and Electron extraction . . . . .	81
4.7	Tritium Beta Spectrum . . . . .	84
4.8	Summery . . . . .	89
5	Fluctuations in the S1 and S2 Signals	90
5.1	An Introduction to Fluctuations . . . . .	90
5.2	Modeling Intrinsic Detector Resolution . . . . .	96
5.3	Measuring Recombination Fluctuations with Mono-Energetic Sources	103
5.4	Measuring Recombination Fluctuations in Discrete Energy Bins . . .	109
5.4.1	Application to $^{83}\text{Kr}$ . . . . .	119
5.4.2	Application to Simulated Tritium Data . . . . .	122
5.5	Extracting Recombination Fluctuations from Tritium Calibration Data	128
5.5.1	Extracting Recombination fraction From Tritium Data . . . . .	132
5.5.2	Modeling the ER Band . . . . .	133
5.6	Measuring Alpha From the Tritium Data . . . . .	135
5.7	Extracting Recombination Fluctuations from $^{137}\text{Cs}$ Calibration . . . .	137
5.8	Recombination Fluctuations, The Bigger Picture . . . . .	139
5.9	Conclusion . . . . .	143
6	Ionization and Scintillation Yields of Liquid Xenon at Low Energy	145
6.1	Correcting for the Spectral Shape for Finite Resolution . . . . .	146
6.1.1	Calculating the Observed Energy . . . . .	147
6.1.2	Smearing a Toy Spectrum . . . . .	149
6.2	Light Yield, Charge Yield and Comparison to NEST Modeling . . . .	151
6.2.1	Tritium S1 and S2 vs. NEST . . . . .	152
6.2.2	Tritium Energy Spectrum . . . . .	155
6.2.3	Results for Light Yield, Charge Yield and Recombination . . .	159
6.3	Measuring Light Yield, Charge Yield and Recombination, Corrected for Spectral Shape . . . . .	162
6.3.1	Tritium S1 and S2 Correction . . . . .	162
6.4	Ionization and Scintillation Yield After Correction . . . . .	166

6.5	Comparison of Light Yield Measured With Tritium to Other Measurements With Compton Scatters . . . . .	171
6.5.1	The Standard Candle: Light Yield from $^{83m}\text{Kr}$ . . . . .	171
6.5.2	Comparing Tritium Scintillation Yield with Compton Scatters	173
6.6	Summary . . . . .	176
7	The Electron Recoil Band of LUX	178
7.1	The need for an Internal Calibration Source . . . . .	178
7.2	Tritiated-Methane as a Calibration Source . . . . .	180
7.3	Removal of $\text{CH}_4$ from LUX . . . . .	182
7.4	Light Yield Quenching from $\text{CH}_4$ in LUX . . . . .	184
7.4.1	Tritiated Methane injection into the LUX detector . . . . .	186
7.4.2	Mixing of Tritiated Methane in Liquid Xenon . . . . .	187
7.4.3	Definition of the Electronic Recoil Band and the ER Discrimination Factor . . . . .	189
7.5	ER Band Gaussianity . . . . .	193
7.6	S1 Threshold For Golden Events, Using Tritium . . . . .	195
7.7	Conclusion . . . . .	195
8	LUX and Beyond	198
8.1	LUX 2013 Science Run Reanalysis . . . . .	198
8.2	Fundamental Properties of Liquid Xenon . . . . .	199
8.3	Internal Calibration Sources . . . . .	199
	Bibliography	201

## List of Figures

1.1	Measured rotational velocities vs. radius in the Milky Way galaxy. The velocity distribution is expected to fall off as $\sim \frac{1}{r}$ beyond the radius of the luminous disk, shown as the dashed magenta line. The Navarro-Frenk-White model in solid black, along with other models listed in the legend. The velocity distribution appears consistent with that expected due to a halo of mass surrounding the galaxy, well beyond the observed luminous disk [1]. . . . .	3
1.2	Maru the cat explains the cosmic microwave background. Consider that Maru is a photon and the box size represents local energy densities of the universe. The scale of the the box size is inversely proportional to the local energy density and temperature. At the time of last scatter all boxes containing Marus cease to exist. The Marus are now left to propagate freely through the universe, with their configurations unchanged. Figures a-d show Maru the cat contained within increasing box sizes corresponding to decreasing energy densities. . . . .	7
1.3	Improvement of resolution from COBE, first to discover anisotropies in the CMB, to WMAP and Planck which have set stringent limits on cosmological parameters by mapping variations in temperature of 1 part in 100,000. Image credit: NASA/JPL-Caltech/ESA. . . . .	8
1.4	BAO peak obtained from BOSS [2]. The correlation function has a peak at of $100h^{-1}$ Mpc, expected with a dark matter density of $\Omega_{bh}^2 \sim 0.2$ . . . . .	9
1.5	The concentration of mass in the bullet-cluster as observed from X-rays, emitted by baryonic matter, in pink, and the concentration of mass from gravitational lensing in blue. [Composite image credit: X-ray: NASA/CXC/CfA/M.Markevitch et al.; Optical: NASA/STScI; Magellan/U.Arizona/D.Clowe et al.; Lensing Map: NASA/STScI; ESO WFI; Magellan/U.Arizona/D.Clowe et al.] . . . . .	11
1.6	Dark matter density vs. distance from the galactic center, calculated from galactic rotation curves of the Milky Way galaxy. The Earth is located at 8.3 kpc. Figure from [1]. . . . .	15

1.7	Plot of WIMP event rate per kg/day/keV vs. Nuclear recoil energy (keV) for several target nuclei, using parameters from [3]. Figure taken from [4]. At low detection threshold xenon is the most attractive target nuclei. The fall in the xenon curve is due to decoherence described by the Helm factor [5]. . . . .	18
2.1	Photo of the outer vessel of the LUX detector from inside the water tank. . . . .	23
2.2	Illustration of the LUX detector's internals. The detector contains two arrays of PMTs on the top and bottom housing 61 PMTs each. Teflon panels on the edges of the active region are used to reflect scintillation signals. The vertical distance between the two PMT arrays is 60 cm, and the diameter to the inner edge of the Teflon panels is 50 cm. . . . .	24
2.3	Simulation of expected gamma background events inside the LUX detector, using the single scatter cut requirement[6]. There is a factor of 1000 background rejection within the fiducial volume where the WIMP search is conducted (inside the black dashed lines) . . . . .	28
2.4	Plot of the log of the charge-to-light ratio vs. S1 (energy). The variable $\log_{10}(S2_b/S1)$ is used to distinguish ER type events from NR type events. The ER and NR bands are defined from calibrations, a) Betas from a tritium calibration (Blue), and b) Neutrons from AmBe and $^{252}\text{Cf}$ (Red). The band means are solid lines and the 10-90% CL are shown as dashed lines. The ER to NR discrimination by using the charge to light ratio was measured to $99.6 \pm 0.1$ % at 50% NR acceptance [7]. . . . .	29
2.5	Field grids in the LUX detector during the 2013 science run. T,A,G,C,B are biased to -1,+3.5,-1.5,-10,-2 (all in kV), respectively. The PMTs are biased to -1.2 kV on average. The figure on the right shows the electric field model in the drift region between the cathode and gate for drift distance z vs. detector radius r. On average the drift field is 170 V/cm with variation from 140 V/cm to 200 V/cm from cathode to gate. Electric field model from [8]. . . . .	30
2.6	An electronic recoil (ER) event in xenon. The energy deposited is converted primarily to ionization and roughly one tenth for excitation. Only several percent is lost to heat. Xenon excitons and recombining electron ion pairs from xenon dimers which de-excite producing vacuum ultra-violet (VUV) scintillation light at 175 nm producing the primary scintillation signal (S1). Electrons that do not recombine are drifted by an electric field into the gas phase where they are accelerated producing the secondary scintillation (S2) signal. Figure from [9]. . . . .	33

2.7	A nuclear recoil (NR) event in xenon. The energy deposited goes mainly towards heat (phonons), the remaining energy is split evenly between ionization and excitation. Xenon excitons and recombining electron ion pairs form xenon dimers which de-excite producing vacuum ultra-violet (VUV) scintillation light at 175 nm producing the primary scintillation signal (S1). Electrons that do not recombine are drifted in an electric field into the gas phase where they are accelerated producing the secondary scintillation (S2) signal. Figure from [9]. . . . .	34
2.8	Event diagram. . . . .	36
2.9	2 keV ER event as seen by each PMT channel of the LUX detector. The S1 signal summed across all channels is overlaid on the top left, and the S2 signal summed across all channels is overlaid on the top right. . . . .	37
2.10	Density plot of prompt fraction vs. Pulse Area. Top: $^{83m}\text{Kr}$ data set. Bottom: Tritium data set. Populations of single electrons, single photons and the S1 S2 pairs associated with $\gamma$ , $\beta$ and $\alpha$ are highlighted as rectangles. . . . .	39
2.11	All single scatter events seen in the active region of the LUX detector over the course of the first science run passing all cuts listed in table 2.3 excluding the fiducial cut. The dashed cyan box indicates the fiducial volume. . . . .	41
2.12	The remaining events passing the quality cuts listed in table 2.3. The charge to light ratio (S2/S1) is plotted vs. S1 (proportional to energy) to show the separation of ER and NR type events. The 10-90% CF limits of the ER and NR band are plotted as the dashed blue and red curves, respectively. The band means are solid. S2 <sub>b</sub> stands for the S2 signal on the bottom PMT array. . . . .	43
2.13	LUX detector is consistent with a P value of 0.35 of the background only hypothesis. The 90% upper C.L. cross section for various spin independent masses are shown in figure 2.13 in blue. Also shows are limits from Xenon100 (red), CDMS II (green), ZEPLIN III (magenta), and one sigma signal claimed for DAMA/LIBRA (shaded grey), CDMS II Silicon (shaded green), CRESST II (shaded yellow). . .	45
3.1	A simplified decay diagram of $^{83}\text{Rb}$ and $^{83m}\text{Kr}$ , from [10]. . . . .	49
3.2	The S1 and S2 of two $^{83m}\text{Kr}$ events. (a): A $^{83m}\text{Kr}$ event in which the two decays have overlapped within 60 ns. The S2 arrives about 93 $\mu\text{s}$ later. Bottom Figures (b): A $^{83m}\text{Kr}$ event in which the two decays have overlapped within 220 ns. The S2 arrives about 205 $\mu\text{s}$ later. The LUX pulse finder classifies events within a 1 $\mu\text{s}$ window as a single S1. The S2 pulses are insensitive to the timing separation of the dual decay as electron diffusion smears the pulses two together as the electrons drift. The PMT hit map for these events are shown below in figure 3.3. . . . .	51

3.3	The S1 and S2 of two $^{83m}\text{Kr}$ events. Top Figures (a): A $^{83m}\text{Kr}$ event in which the two decays have overlapped within 60 ns. Bottom Figures (b): A $^{83m}\text{Kr}$ event in which the two decays have overlapped within 220 ns. The black, open circle represents the location of the event. The S1 hit pattern is diffuse with more light collected on the bottom arrays due to total internal reflection at the liquid surface. The S2 is localized in the top PMT arrays in x,y at the location where the electrons are extracted, and diffuse on the bottom due to scattering. The summed waveforms for these events are shown in figure 3.2. . . . .	52
3.4	Distribution of $^{83m}\text{Kr}$ events 10 minutes after the injection. The source mixes uniformly throughout the liquid xenon illuminating all regions of the active volume. The solid black lines represent the fiducial volume used for the WIMP search. . . . .	54
3.5	Left: Fits to the mean of $S_{2b}$ of the $^{83m}\text{Kr}$ data in several z slices. Right, the exponential fit to the means of $S_{2b}$ vs. drift time used to extract electron lifetime $\tau$ . The electron lifetime is found to be $\tau = 753.1 \pm 3.2 \mu\text{s}$ . The exponential fit to the means deviates near the top and bottom of the active region since the charge yield from the $^{83m}\text{Kr}$ decay is sensitive to the varying electric field. The data shown was taken on May 10, 2013 (lux10_20130510_T1250) and contains 700,000 $^{83m}\text{Kr}$ events. . . . .	55
3.6	Left: Response of $S_{2b}$ vs. x,y normalized to the response at the center ( $x=y=0$ ). The region of larger response around $x=0, y=-25$ is likely from an enhanced extraction field between the anode and gate wires. Right: Response of $S_{2b}$ vs. x,y after correcting the data using $\mathcal{N}\mathcal{F}_{S_{2b}}$ . . . . .	56
3.7	Improvement of resolution in $S_{2b}$ after applying the z and x,y,z correction. Black: The uncorrected data. Red: The data with only z dependent correction, the electron lifetime correction. Blue: The data with full x,y,z dependent correction. The data shown was taken on May 10, 2013 (lux10_20130510_T1250) and contains 700,000 $^{83m}\text{Kr}$ events. . . . .	57
3.8	S1 x,y,z response normalized to the center of the detector. The interpolated map represents the inverse of the normalization factor $\mathcal{N}\mathcal{F}$ . . . . .	59
3.9	S1 x,y,z response normalized to the center of each z slice. There are greater variations near the very top and bottom 4 z slices as the solid angle for light hitting the PMT arrays increases. For the central slices the x,y response is uniform due to increased scattering off the Teflon panels. . . . .	60
3.10	S1 x,y,z response normalized to the center of the detector after the data has been corrected and normalized to the detector center. The remaining variations in the fiducial volume ( $r < 18\text{cm}$ ) is less than 1%. Near the top and bottom edges the deviation increases to as much as 3% due to the interpolation of the correction becoming poorly constrained. . . . .	62

3.11 Improvement of resolution in S1 after applying the z and x,y,z correction. Black: The uncorrected data. Red: The data with only z dependent correction. Blue: The data with full x,y,z dependent correction. The data shown was taken data on May 10, 2013 (lux10_20130510_T1250) and contains 700,000 $^{83m}\text{Kr}$ events.	63
3.12 Electron lifetime measured using $^{83m}\text{Kr}$ calibrations during the LUX science run in 2013. The blue dashed lines show the boundaries of the WIMP search from April 21 to Aug 8, 2013. The red dashed lines indicate circulation loss events.	64
3.13 Measured response of to light from $^{83m}\text{Kr}$ calibrations at the center of the LUX detector during of the LUX science run in 2013. The blue dashed lines show the boundaries of the WIMP search from April 21 to Aug 8, 2013. The red dashed lines indicate circulation loss events.	65
4.1 LUX calibration data in charge vs. light space (S1 vs. S2). Top figure, shows the xenon activation lines from early in the science run, the black lines indicating the initial cuts by eye used to isolate populations of constant energy. The bottom figure shows all of the data used to calibrate the energy scale, including the $^{83m}\text{Kr}$ and $^{137}\text{Cs}$ calibrations. The centroids found by an un-binned maximum likelihood analysis are shows as a black X, for the sources listed in table 4.1.	72
4.2 The Doke plot showing the mean values of S1/E vs S2/E for each calibration source. The data was cut by plotting the S2 vs the S1 and selecting the populations by eye, shown in figure 4.1. Using equation 4.6, the slope and intercept of the data constrain the parameters $g_1$ and $g_2$ . The black solid line represent the best fit to the data and the red dashed lines represent $\pm 1\sigma$ of $g_1$ and $g_2$ . The open circle is data from the K-shell xenon X-ray and was not used for the fit as its absolute energy and origin from the skin of the detector is uncertain.	73
4.3 Doke plot with all events from the calibration sources, with their S1 and S2 signal normalized to its corresponding energy. The populations of the Xe activation lines and $^{214}\text{Bi}$ were isolated by the cuts shown in figure 4.1. The solid black line represent the best fit to $g_1$ and $g_2$ and the dashed lines represents the $1\sigma$ bounds.	74
4.4 The Doke plot showing the mean values of S1/E vs S2/E for each calibration source. The data has been further cut upon the combined energy reconstructed from an initial best fit to the data. Using equation 4.6, the slope and intercept of the data constrain the parameters $g_1$ and $g_2$ . The black solid line represent the best fit to the data and the red dashed lines represent $\pm 1\sigma$ of $g_1$ and $g_2$ . The open circle is data from the K-shell xenon X-ray and was not used for the fit as its absolute energy and origin from the skin of the detector is uncertain.	76

4.5	S1 fits to sources at nominal field of 170 V/cm unless otherwise noted. Source and energy in keV from top left to bottom right: a) $^{131}\text{Xe}$ : 163, b) $^{127}\text{Xe}$ : 207, c) $^{127}\text{Xe}$ & $^{129\text{m}}\text{Xe}$ : 236.8, d) $^{127}\text{Xe}$ : 410, e) $^{214}\text{Bi}$ : 609, f) $^{137}\text{Cs}$ : 661.6, g) $^{83\text{m}}\text{Kr}$ : 41.5 - at 50 V/cm, h) $^{83\text{m}}\text{Kr}$ 41.5 - at 100 V/cm, i) $^{83\text{m}}\text{Kr}$ 41.5 . . . . .	77
4.6	S2 fits to sources at nominal field of 170 V/cm unless otherwise noted. Source and energy in keV from top left to bottom right: a) $^{131}\text{Xe}$ : 163, b) $^{127}\text{Xe}$ : 207, c) $^{127}\text{Xe}$ & $^{129\text{m}}\text{Xe}$ : 236.8, d) $^{127}\text{Xe}$ : 410, e) $^{214}\text{Bi}$ : 609, f) $^{137}\text{Cs}$ : 661.6, g) $^{83\text{m}}\text{Kr}$ : 41.5 - at 50 V/cm, h) $^{83\text{m}}\text{Kr}$ 41.5 - at 100 V/cm, i) $^{83\text{m}}\text{Kr}$ 41.5 . . . . .	78
4.7	Doke plot of the data showing the light yield vs. charge yield. In this version of the plot, S2/E has been scaled by W/g <sub>2</sub> so that the x-axis corresponds to the ratio of n <sub>e</sub> to total quanta. Similarly S1/E has been scaled by W/g <sub>1</sub> so that the y axis corresponds to the ratio of n <sub><math>\gamma</math></sub> to total quanta. The black horizontal line represents moving along the line of constant quanta, for each additional photon an electron is lost as visa-vera. . . . .	79
4.8	MCMC for the linear fit to the Doke plot. There is a strong negative correlation between the slope m and intercept b which results from the degeneracy between gains g <sub>1</sub> and g <sub>2</sub> . . . . .	80
4.9	Combined energy scale. a) The xenon activation lines from early in Run03 of 2013. b) $^{137}\text{Cs}$ calibration data. c) All calibration data including the $^{83\text{m}}\text{Kr}$ calibration. d) Xenon X-ray. . . . .	82
4.10	Single electron distribution as seen by the bottom PMT array fitted with a skew Gaussian model to account for the underlying Poisson statistics The $\mu$ of the fit represents the true mean of the skew Gaus- sian distribution. . . . .	84
4.11	The tritium energy spectrum reconstructed from the data (black). Along with LUX SIM (blue), and the true tritium beta spectrum (blue) and a tritium spectrum smeared with detector resolution (green). .	86
4.12	Detector threshold calculated by comparing the data to the true tri- tium energy spectrum having applied detector resolution effects. Top: data with a drift field of 170 V/cm. Bottom: data with a drift field of 170 V/cm. . . . .	88
4.13	Tritium calibration data, plotting S2 vs. S1. The horizontal black lines represent contours of constant energy, labeled in keV. . . . .	88

5.1	Fluctuations of the 164 keV line from $^{131}\text{Xe}$ in the LUX detector, with the number of electrons plotted vs. the number of photons. The blue and magenta arrows labeled as $\sigma_{n_{\gamma\text{Det}}}$ and $\sigma_{n_{e\text{Det}}}$ are the size of fluctuations in the light and charge channels due to the resolution of the LUX detector. The black arrow represents the size of recombination fluctuations $\sigma_R$ . The value of $\langle r \rangle$ is the average observed recombination fraction or the average recombination probability $r_p$ . The red lines represent constant $\langle r \rangle \pm \sigma_r$ assuming the expected binomial variance of equation 5.1. The black lines represent constant $\langle r \rangle \pm \sigma_r$ measured from the data. The black dashed line is represent constant energy or constant number of quanta. . . . .	92
5.2	The projection of the population in figure 5.1 onto the combined quanta axis $(n_\gamma + n_e) = E/W$ . Along this projection the dominant recombination fluctuations cancel out, leaving on the components from detector resolution $\sigma_{n_{\gamma\text{Det}}}$ and $\sigma_{n_{e\text{Det}}}$ . . . . .	93
5.3	The fluctuations in the S1-x,y,z corrected signal for the 9.4 keV from $^{83\text{m}}\text{Kr}$ . At 9.4 keV the statistical variance is dominant over recombination fluctuations, $\sigma_{S1} = 8.15$ . The resolution is consistent with that expected from statistical fluctuations of $8.3 \pm 0.1$ PE, from equation 5.8. . . . .	99
5.4	Populations of calibration sources in discrimination space $\log\left(\frac{n_e}{n_\gamma}\right)$ vs. combined energy keV <sub>ee</sub> . The ovals represent the combination of $\sigma_R$ , $\sigma_{n_{\gamma\text{Det}}}$ , $\sigma_{n_{e\text{Det}}}$ in black, white, red respectively. . . . .	107
5.5	Measured values of $\sigma_R$ , $\sigma_{n_{\gamma\text{Det}}}$ , $\sigma_{n_{e\text{Det}}}$ vs. Energy on the left and vs. quanta in photons, electrons and ions, respectively, on the right. Measured using sources listed in Table 5.3. . . . .	108
5.6	A simulated $^{83\text{m}}\text{Kr}$ source with infinite detector resolution and recombination fluctuations set to 90 quanta. The recombination fluctuation move along the line of constant energy about the center, shown in black with bin width of $\Delta_E = 1$ keV. The events between the black lines and projected onto the $n_\gamma$ and $n_e$ axes. The variance in $n_\gamma$ and $n_e$ are $\sigma_{n_\gamma}^2 = \chi_{n_\gamma}^2 = \sigma_R^2$ and $\sigma_{n_e}^2 = \chi_{n_e}^2 = \sigma_R^2$ . . . . .	111
5.7	A simulated $^{83\text{m}}\text{Kr}$ source with no recombination fluctuations and with detector resolution, $\sigma_{n_{\gamma\text{Det}}} = 171$ and $\sigma_{n_{e\text{Det}}} = 51$ . The solid black lines represents constant energy about the center having width of $\Delta_E = 1$ . The events that fall between the black dashed lines are projected onto the $n_\gamma$ and $n_e$ axes. The square root of the observed variance in light and charge are show on the labels with and without the energy cut, as $\chi$ and $\sigma$ respectively. The energy cut has swept out a component of variance $\chi_{\text{Det}}$ that is shared between the light and charge channels. . . . .	113

- 5.8 A simulated  $^{83m}\text{Kr}$  source with no recombination fluctuations and with detector resolution,  $\sigma_{n_e\text{Det}} = \sigma_{n_\gamma\text{Det}} = 100$ . The solid black line represents constant energy about the center having a width of  $\Delta_E = 1$ . The events that fall between the black dashed lines are projected onto the  $n_\gamma$  and  $n_e$  axes. The square root of the observed variance in light and charge are shown on the labels with and without the energy cut, as  $\chi$  and sigma respectively. . . . . 117
- 5.9 Data from a  $^{83m}\text{Kr}$  data set, plotting the number of photons against the number of electrons. The red-dashed oval represents where the population would lie if recombination fluctuations were the dominant fluctuation. The solid black line represents constant energy about the center, and the region between the black dashed lines represents the cut in energy with bin width  $\Delta_E = 1$ . The events that fall between the black dashed lines are projected onto the  $n_\gamma$  and  $n_e$  axes. The observed standard deviation in  $n_\gamma$  and  $n_e$  is shown on the plot labels as  $\chi$  and  $\sigma$ . . . . . 120
- 5.10 Number of photons plotted against the number of electrons from a simulated tritium data set having only recombination fluctuations. Top: Tritium events propagated from 1 keV bins from 1-18 keV. Bottom, the tritium events propagated from 0.1 keV bins from 1-18 keV. The recombination fluctuations move events along the lines of constant energy. . . . . 123
- 5.11 The number of photons plotted against the number of electrons from a simulated tritium data set having recombination fluctuations and detector resolution. The tritium events propagated from 0.1 keV bins from 1-18.6 keV. Events move along the lines of constant energy due to recombination fluctuations and  $\chi_{\text{Det}}$ . . . . . 124
- 5.12 Light yield (left) and Charge yield (right) of a simulated tritium spectrum, with the fit to the centroid show in black. The variance in number of photon and electrons per energy bin is used to extract recombination fluctuations. Recombination fluctuations and detector resolution  $\chi_{\text{Det}}$  move events up and down along lines of constant energy. 125
- 5.13 Simulated tritium spectrum with the detector resolution of the LUX detector and an initial guess of recombination fluctuations. The detector resolution, labeled as  $\sigma_{S1\text{Det}}$  and  $\sigma_{S2\text{Det}}$  is shown in red and green, respectively. The value of recombination fluctuation  $\sigma_R$  input into the simulation is shown in magenta. The methodology described in this previous section is applied to extract  $\sigma_R$  from the electron and photon spectrum, black and blue respectively. The statistical component of the standard deviation in each bin is  $\chi_{\text{Det}}$  is shown in green, equation 5.47. The plots show cases for various bin widths in keV: a)  $\Delta E = 0.1$  b)  $\Delta E = 0.25$  c)  $\Delta E = 0.5$  d)  $\Delta E = 1$ . . . . . 127

- 5.14 a: Density plot of number of photons vs. energy in keV using the tritium calibration data at 170 V/cm. b: Number of electrons vs. energy in keV using the tritium calibration data at 170 V/cm. c: Number of photons vs. energy in keV using the tritium calibration data at 100 V/cm. d: Number of electrons vs. energy in keV using the tritium calibration data at 100 V/cm. The data has been corrected for spectral shape. The black line indicates the quadratic fit to the centroid of the population. . . . . 129
- 5.15 The figures on the left in 5.15 (a: 170 V/cm, c: 100 V/cm) show the extracted recombination fluctuation  $\sigma_R$  from the light (black) and charge (red) channel denoted with subscript  $\gamma$  and  $e$  respectively, note they are identical. Also shown are the fluctuations in light collection  $\sigma_{\gamma_{\text{Det}}}$  (blue), charge collection  $\sigma_{e_{\text{Det}}}$  (cyan), and their manifestation in a combined energy bin,  $\chi_{\text{Det}}$  (magenta). The figures on the right in 5.15 (b: 170 V/cm, d: 100 V/cm) show the mean and one sigma standard deviation of the measured number of photons (blue) and electrons (red). Also shown is the total quanta (in black) which is the sum of photons and electrons and the expected number of ions (magenta) and excitons (cyan) using  $\alpha = 0.20$ . . . . . 130
- 5.16 Recombination Fraction at 170 V/cm (black) and 100 V/cm (blue). The shaded regions represent the one sigma of the observed fluctuations in recombination fractions  $\sigma_r$ . The dashed line at 1.0 keV<sub>ee</sub> represents the 50% detection threshold. . . . . 133
- 5.17 The result of the ER band's mean population and its corresponding 1 sigma fluctuation for the case of 100 V/cm (blue) and 170 V/cm (black). We find an overlap below 4 keV<sub>ee</sub> where the additional strength of the drift field is higher improving threshold of discrimination. Above 4 keV<sub>ee</sub> the band separate as the higher drift field increased the charge extraction leading to better discrimination. . . . 135

- 5.18 Determining the best  $\alpha$  using the tritium calibration data, with  $\alpha = 0.3$ (blue), 0.2(black), 0.15(magenta) and 0.06(red). Left: The y axis is the ratio of the measured standard deviation of recombination to that of a binomial processes and is plotted vs. the expected binomial standard deviation on the x axis. The best  $\alpha$  is one for which the observed standard deviation converges with that of a binomial process as the binomial variance tends to 1. Right, the same y axis as on the left but plotted vs. the number of ions available for recombination. As the number of ions approaches one the standard deviation of recombination should become that of a binomial process. A single ion will either recombine or not with probability  $r$ . The best intercept converging to a purely binomial process (black star) is with  $\alpha = 0.20$ . Falling below the value of one on the y axis implies that recombining electron-ion pairs have a variance better than binomial, which is nonphysical if it is a random process. Note, the fits use only data above 90% threshold at 1.3 keV, starting from the third data point from the left. The higher end cut off at 3 keV corresponds to the end of the fitted lines. . . . . 137
- 5.19 Left: The mean and one sigma standard deviation of the measured number of photons (blue) and electrons (red). Also shown is the total quanta (in black) which is the sum of photons and electrons and the expected number of ions (magenta) and excitons (cyan) using  $\alpha = 0.20$ . Right: The recombination probability  $r$  (solid black) and the one sigma fluctuation  $\sigma_r$  (shaded). . . . . 138
- 5.20 Recombination fluctuations (in quanta) vs. number of ions. The measurements include data from tritium at 170 V/cm, tritium at 100 V/cm,  $^{137}\text{Cs}$  calibration, the line sources used for the energy scale calibration listed in table 4.1 and a  $^{57}\text{Co}$  calibration at several electric fields ranging from 60 to 5000 V/cm from [11]. Top: Black dashed lines represent the values expected from a binomial process and the green line is a fit to the data with a constant amplification given in equation 5.53. Bottom: a linear fit to the data from equation 5.54. Note,  $^{83\text{m}}\text{Kr}$  is shows here is the combination of two decays and is expected to fall below the curve by 40%. . . . . 140
- 6.1 Smearing of a linear spectrum using equation 6.1 for an arbitrary energy scale  $E$ . The counts in each shaded bin are redistributed into normalized Gaussians (blue) with the resolution  $\sigma_E$  growing like  $\sqrt{E}$ . The spectrum smeared with detector resolution is the sum of Gaussians shown in red. . . . . 147

6.2	Top Left: A linearly decaying spectrum, in blue. The black curve represents the sum of the Gaussians assuming a constant resolution. Top Right: A linearly decaying spectrum, in blue. The black curve represents the sum of the Gaussians with a $\sigma = \sqrt{E}$ dependent resolution. Bottom: The observed mean, with finite resolution, compared to the real mean with infinite resolution. The black points are for the case with linear resolution and the red points represent the case with $\sigma = \sqrt{E}$ dependent resolution. . . . .	151
6.3	a): In Black S1 tritium S1 spectrum extracted from the data. In blue, The NEST light yield curve. In red, the NEST light yield curve with recombination fluctuations. Dashed magenta is NEST light yield with smearing from equations 6.7. b): The ratio of the real S1 mean to the S1 observed mean vs. the observed mean after smearing. Note, the S1 threshold at about 3 PE in S1. c): In Black S2 tritium spectrum extracted from the data. In blue, The NEST light yield curve. In red, the NEST light yield curve with recombination fluctuations. Dashed magenta is NEST light yield with smearing from equations 6.8. d): The ratio of the real S2 mean to the S2 observed mean vs. the observed mean after smearing. . . . .	155
6.4	The tritium energy spectrum reconstructed from the data (black). Along with LUX SIM (red), the true tritium beta spectrum (dashed blue) and a tritium spectrum smeared with detector resolution of equation 6.11 (green). . . . .	157
6.5	Left, mapping from real Monte Carlo energy to observed energy plotted vs the observed energy after applying a finite resolution using LUXSIM. Right, comparing the correction determined from the Monte Carlo (Red) to the detector smearing model (black) given in equation 6.11. The dashed lines represent the uncertainty in the measured values. The agreement is within errors from 1 to 18 keV <sub>ee</sub> . The Energy threshold is 50% at 1.0 keV <sub>ee</sub> . . . . .	158
6.6	Top: Extracted recombination fluctuation from the tritium data from fluctuations in photons and electrons (Black and Red respectively). Bottom right: mean number of quanta in photons, electrons, ions, excitons vs. energy keV for the tritium calibrations. Bottom left: Recombination fraction and the one sigma (shaded) vs. energy keV. . . . .	160
6.7	Light yield and charge yield from tritium data without spectral shape correction at 170 V/cm in black. The shaded region represents the one sigma systematic uncertainty on g1 and g2. The NEST yield prediction and its corresponding 1 sigma is shaded in blue. NEST interpolation is shown in magenta to energies where the model is not vetted. Note that the statistical errors are about the size of the data points and the dominant uncertainty illustrated by the shaded region is 100% correlated bin-to-bin. A one sigma shift up in light yield corresponds to a one sigma shift down in charge yield and visa versa. . . . .	161

6.8 a): In Black S1 tritium S1 spectrum extracted from the data. In red, the S1 spectrum based upon the LY and QY measured from the tritium data after applying recombination fluctuations. In dashed blue, the expected S1 spectrum after applying finite detector resolutions of equation 6.7. b): The ratio of the real mean to the observed mean vs. the observed mean after smearing the tritium photon spectrum with detector resolution. Note the S1 threshold at about 3 PE in S1. c): In black, tritium S2 spectrum from the data. In red, the S2 spectrum based upon the LY and QY measured from the tritium data after applying recombination fluctuations. In dashed blue, the expected S2 spectrum after applying finite detector resolutions of equation 6.8. d): The ratio of the real mean to the observed mean vs. the observed mean after smearing the tritium electron spectrum from NEST with detector resolution. Note the S2 threshold at about 400 PE in S2. . . . .	164
6.9 Means of the light yield and charge yield from tritium data corrected for spectral shape along with the 1 sigma statistical errors. . . . .	166
6.10 Light yield and charge yield from tritium data corrected for spectral shape along with the 1 sigma systematic constraint on g1 and g2. The blue and magenta curve are NEST extrapolation and interpolation, respectively. . . . .	168
6.11 In black, the light yield and charge yield from tritium data corrected for spectral shape. In red, the light yield and charge yield from tritium data uncorrected for spectral. The shaded region represent the one sigma systematic error from the constraint on g1 and g2 shaded. . . . .	170
6.12 Left: The light yields of the 9.4 and 32.1 keV decay of $^{83m}\text{Kr}$ plotted vs. timing separation, for events separated by more than 1200 ns. The point at 600 ns is calculated assuming the 32.1 keV yield remains flat to 200 ns as observed in [12] and [13]. Right: the histogram of $^{83m}\text{Kr}$ events vs timing separation finding a best fit to the half life of $159.7 \pm 7.5$ consistent with the measured value of 154 ns [14] [15]. . . . .	172
6.13 Left: S1 $^{83m}\text{Kr}$ peaks at zero field. Right: shows the histogram of the separated 32.1 and 9.4 keV decays plotted above vs. time. The half life fit to the population is in good agreement with the measured half-life of 154 ns [14] [15]. . . . .	173
6.14 LY relative to the light yield of the 32.1 keV decay of $^{83m}\text{Kr}$ at zero field. The black and blue bands represent the results from tritium at 170 and 100 V/cm respectively. The shaded region represents the systematic error due to the one sigma constraints on g1 and g2. Magenta points are Compton scattering measurements from [16]. The gray and red represent zero field and 450 V/cm Compton Scattering measurements from [13]. . . . .	175
7.1 True tritium beta spectrum from [17]. . . . .	181

7.2	Removal of natural methane observed by the integrated xenon sampling system prior to the tritiated-methane injections. The red points indicate measurements at the getter outlet. We find a 97% one-pass removal efficiency at a flow rate of 27 SLPM. The blue curve shows the improved upper limit on the effect of outgassing from the plastics. The black dashed lines shows the exponential fit to the natural methane removal from the xenon with a time constant of $5.9 \pm 0.07$ hours. $5 \times 10^{-3}$ ppb (g/g) is the limit of detection for methane. . . . .	183
7.3	In black, the response to scintillation from $^{83m}\text{Kr}$ at the center of the detector normalized to the first data point before the natural methane ( $\text{CH}_4$ ) injection. The dashed magenta lines represent the time window from the beginning of the natural methane injection to the time the background of 5 ppt is reached. The blue points represent that methane concentration in the gas returning from the bulk liquid of the detector. The concentration in the liquid xenon is roughly 1/6 of the concentration measured in the gas phase due to solubility. . . . .	185
7.4	The rate of single scatter events with S1 below 100 PE in the fiducial volume. (100 PE in S1 is about 18.6 keV <sub>ee</sub> , the endpoint to the tritium beta spectrum). The magenta and red curves are fits to the first and second tritium injection's removal rate. The removal rate of tritiated-methane from the liquid is consistent with the natural methane removal rate observed in the gas by the gas analysis system (figure 7.2. . . . .	187
7.5	The distribution of tritium events vs. detector radius squared. The solid black line represents the fiducial volume. Right: The distribution of tritium events vs. XY in the region between the gate and the cathode. The solid black line represents the fiducial volume and the black circles represent the locations of PMTs (photo multiplier tubes).188	
7.6	Charge-to-light ratio ( $\log_{10}(S2_b/S1)$ ) plotted vs. S1. The energy contours are also shown labeled in keV <sub>ee</sub> . Top, the tritium data uncorrected for spectral shape. Bottom, with the spectral shape correction discussed in section 6.1. The calibration consists of over 112,000 tritium beta decays between 1 and 50 PE in S1 (1 – 10 keV <sub>ee</sub> ), in the fiducial volume of the detector. The black circles represent the ER band mean and 10% to 90% bounds, $\pm 1.28\sigma$ . The red solid line is the NR band mean determined using a DD neutron generator calibration. The dashed red lines indicate the 10% to 90% bounds of the NR band. . . . .	190
7.7	ER discrimination factor and leakage vs. S1 using over 112,000 tritium beta decays between 1 and 50 PE in S1 (1 – 10 keV <sub>ee</sub> ), at 170 V/cm. Top, the tritium data uncorrected for spectral shape. Bottom, with the spectral shape correction discussed in chapter 6.1. The dashed horizontal lines indicate the mean leakage fraction from 1 to 50 PE. . . . .	192

7.8	ER band Gaussianity from 0-50 PE with the centroid of the ER band subtracted off, using tritium data at 170 V/cm. Top, the tritium data uncorrected for spectral shape. Bottom, with the spectral shape correction discussed in section 6.1. The dashed vertical red line indicates the mean of the NR band from 1 to 50 PE. . . . .	194
7.9	The S1 detection efficiency measured from tritium data at 170 V/cm (black square) and 100 V/cm (blue circle) is plotted along with the best fit to an error function to the higher statistics 170 V/cm data. The red triangles are detection efficiency determined from LED pulsing. . . . .	196

## Chapter 1: Introduction

Anomalies in astronomical observations hinting at the existence of dark matter were first observed in 1932 by Oort [18] and more precisely in 1937 by Zwicky [19]. Both noted discrepancies in galactic mass measurements when comparing the luminous mass to that required to support galactic rotational velocities measured by red shifts. Oort had noted up to a factor of ten more mass than luminous mass in the Sombrero Galaxy and Zwicky found a factor of 500 for the Coma cluster. Both observations were far to large to be accounted for by light absorption, indicating the existence of dark matter to account for the missing mass.

Since then more evidence for the existence of dark matter has been compiled, including big bang nucleosynthesis (BBN), anisotropies in the cosmic microwave background (CMB), baryonic acoustic oscillations (BAO), formation of large structures, galactic rotation curves, and gravitational lensing. All independent techniques lead to a unified conclusion for the existence of non-baryonic and non-luminous matter. Individually some pieces of evidence, such as galactic rotation curves, can be explained by modifications to general relativity (GR), but not all simultaneously. The existence of non-relativistic dark matter particles is required in order to unify the current observations. This dark matter does not couple to the electromagnetic

force and is thus able to avoid our standard optical detection techniques, making its presence felt on large scales via gravity.

## 1.1 Astrophysical Evidence For Dark Matter

### 1.1.1 Galactic Rotation Curves

There are two common methods for measuring the mass of a galaxy or cluster of galaxies. First, one can use the total luminosity and the known distance to the galaxy to determine the luminous mass (the mass corresponding to the visible light). Second, the rotational velocities of stars orbiting the galactic center can be mapped to determine the mass distribution as a function of galactic radius. Rotational velocities of stars around galactic centers at large distances can be measured with Doppler shift, with more recent measurement relying on the 21 cm H1 line from hydrogen as the standard candle. The rotational velocities of objects orbiting galaxies are highly non-relativistic, moving at speeds on the order 100 km/s. At the outer edges of the luminous galactic centers, typically past 5 kpc, the velocity distribution is expected to fall off as predicted by Newtonian mechanics ( $\sim \frac{1}{r}$ ). Yet observations from as early as 1932 indicate that velocity distributions tend to remain constant with radius suggesting that the objects are rotating inside a uniform body of dark matter [18] [19] [20] [1]. The velocity distributions measured for the Milky Way galaxy are shown in figure1.1.

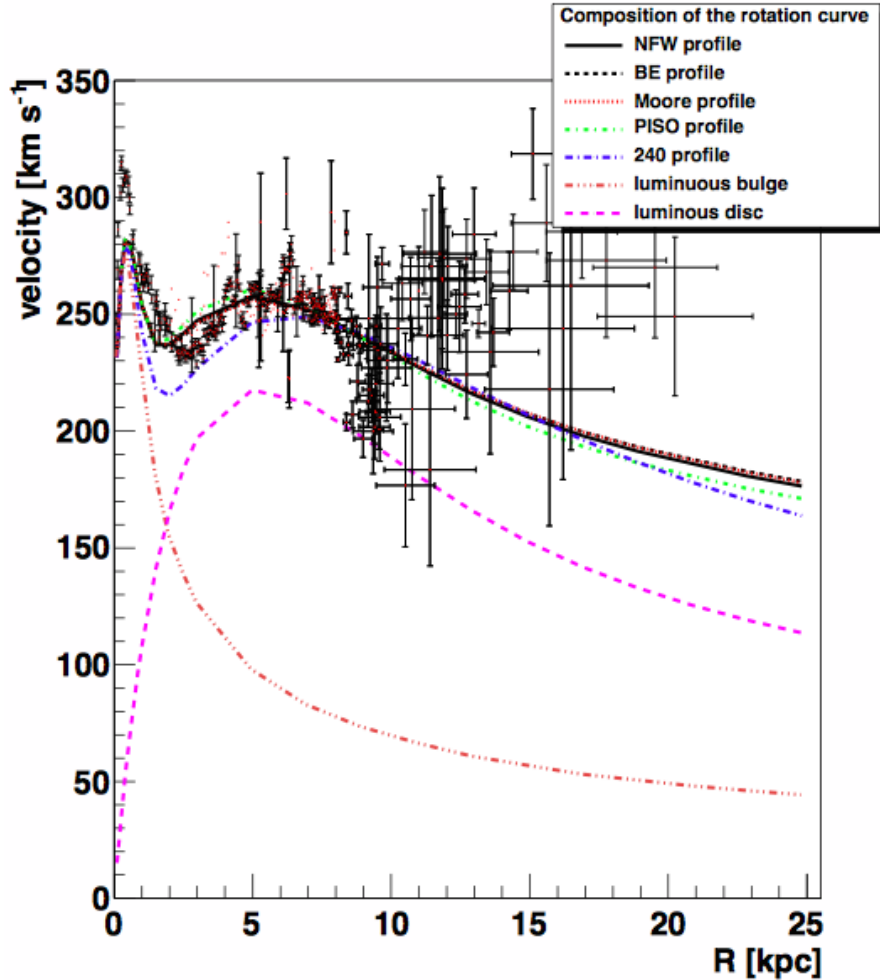


Figure 1.1: Measured rotational velocities vs. radius in the Milky Way galaxy.

The velocity distribution is expected to fall off as  $\sim \frac{1}{r}$  beyond the radius of the luminous disk, shown as the dashed magenta line. The Navarro-Frenk-White model in solid black, along with other models listed in the legend. The velocity distribution appears consistent with that expected due to a halo of mass surrounding the galaxy, well beyond the observed luminous disk [1].

### 1.1.2 Big Bang Nucleosynthesis

Big bang nucleosynthesis (BBN) accounts for the relative abundances of light elements in the universe today, including H, D, He<sup>3</sup>, He<sup>4</sup> and Li<sup>7</sup> [21]. BBN took place in a relatively short time window beginning several seconds after the big bang when the universe cooled below 10<sup>11</sup>K (10 MeV) and ceased as the temperature cooled below 10<sup>9</sup>K (100 keV). Under the temperature conditions of BBN it was energetically favorable for free protons and neutrons to undergo nuclear fusion. This is the only mechanism to produce the light elements we see today. The heavier elements were later fused together in stars and ejected upon the star's death into the cosmos. Nuclear cross sections of protons, neutrons and light elements have been measured to high precision and can be combined with the expansion rate of the universe to precisely predict the relic abundances of baryonic matter. Observations constrain the abundances of the light elements to be H~ 75%, D~ 25%, He<sup>4</sup> ~ 0.01%, Li<sup>7</sup> ~ 10<sup>-10</sup> %. The ratio of D/H has been used to constrain the relic density of baryonic matter to be

$$\Omega_b h^2 = \frac{p_b}{p_c} = 0.02202 \pm 0.00046 \quad [22] \quad (1.1)$$

where h is the Hubble constant (H) dividend by 100 (H<sub>0</sub>/100), p<sub>b</sub> is the baryonic density and p<sub>c</sub> is the critical density required for a flat universe (verified by the CMB). We can write the i<sup>th</sup> density component as:

$$\Omega_i \equiv \frac{p_b}{p_c} = \frac{8\pi G \rho_i}{3H^2} \quad (1.2)$$

where  $G$  is the gravitational constant. The baryon density measured using BBN is constrained to within 1% and is in agreement with the latest constraints from Plank's CMB data,  $\Omega_b h^2 = 0.02205 \pm 0.00028$  [23].

### 1.1.3 Cosmic Microwave Background

The early universe consisted of a plasma opaque to photons as they scattered off free electrons. As the temperature fell below the binding energy of hydrogen (13.6 eV), electrons could bind with free protons forming neutral atoms making the universe transparent to photons. The mean temperature of decoupling was actually at 0.25 eV ( $\sim$ 4000 K) as photons still scatter frequently near the binding energy of hydrogen [21]. After making a final scatter, photons decoupled from electrons effectively attaining a mean free path on the scale of the universe. The photons from the CMB can be observed today at the red shift temperature of  $2.72548 \pm 0.00057$  K [24] from the time of last scatter, 379,000 years after the big bang.

The CMB has encoded within it a wealth of information about the universe as it was at the time of decoupling. The information encoding is illustrated in figure 1.2 using Maru the cat. Consider that Maru is a photon and the box size represents local energy densities of the universe. The smaller boxes represent areas of higher energy density and temperature. At the time of last scatter all boxes containing Marus cease to exist. The cats now propagate freely through the universe with their configuration unchanged. As the universe expands, so will the cats. When the Marus finally reach our telescopes, 13 billion years later, the shape and squeezing

of each Maru informs us of the box size (temperature) from which each Maru has emanated. Using this information from multiple Marus the distribution of box sizes at the time of last scatter can be mapped, revealing areas of slightly larger boxes and areas of slightly smaller boxes. This is roughly the idea behind measuring anisotropies in the cosmic microwave background using microwave telescopes.

Ever more precise measurements from COBE, WMAP and Planck have been able to probe slight temperature variations to 1 part in 100,000 as seen in figure 1.3. Table 1.1 shows the constraints on cosmological parameters set by Planck. The results are in good agreement with baryonic density derived from BBN and predict a dark matter component of 25.8%.

Parameter	Value	Definition
$\Omega_b h^2$	$0.2214 \pm 0.00024$	Baryon energy density
$\Omega_c h^2$	$0.1187 \pm 0.0017$	Cold dark matter energy density
$\Omega_m h^2$	$0.1423 \pm 0.0029$ *	Total matter energy density
$\Omega_\Lambda$	$0.692 \pm 0.010$	Dark energy density
$\Omega_K$	$-0.0005 \pm 0.0065$ (95%)	Curvature
$\Sigma_{m_v}$	$< 0.230$	Sum of neutrino masses [eV]
$H_0$	$67.77 \pm 0.77$	Hubble Constant [ $\text{km s}^{-1} \text{Mpc}^{-1}$ ]

Table 1.1: Cosmological parameters from Planck+WP+highL+BAO [23]. \* Only Planck.

#### 1.1.4 Baryonic Acoustic Oscillations

The universe 379,000 years after the big bang was uniformly distributed, with only small variations observed in the CMB temperature of 1/100,000 [25]. Before decoupling took place, gravity pulled baryons and dark matter into high density regions resulting in an opposing outward force from photon pressure. The outward force

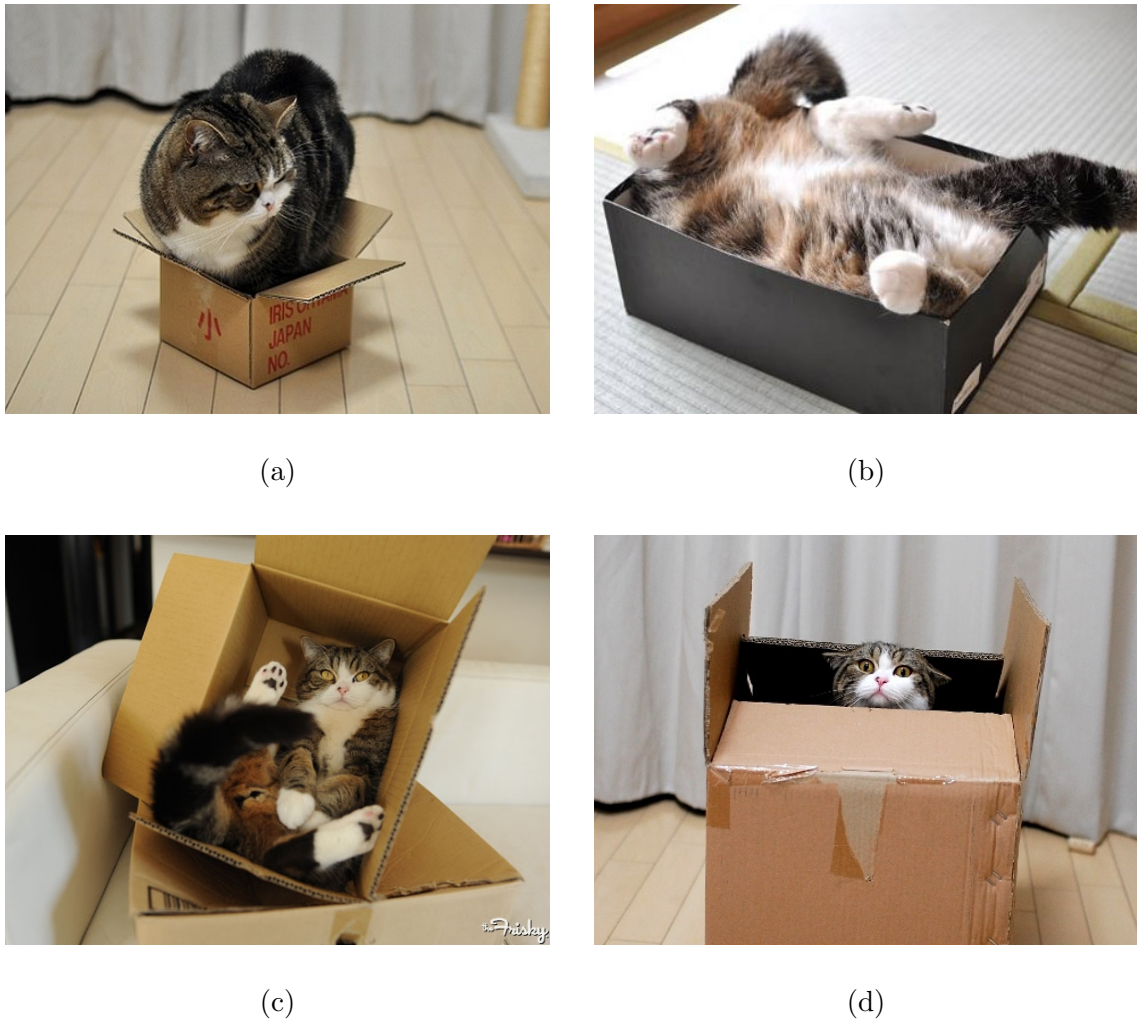


Figure 1.2: Maru the cat explains the cosmic microwave background. Consider that Maru is a photon and the box size represents local energy densities of the universe. The scale of the the box size is inversely proportional to the local energy density and temperature. At the time of last scatter all boxes containing Marus cease to exist. The Marus are now left to propagate freely through the universe, with their configurations unchanged. Figures a-d show Maru the cat contained within increasing box sizes corresponding to decreasing energy densities.

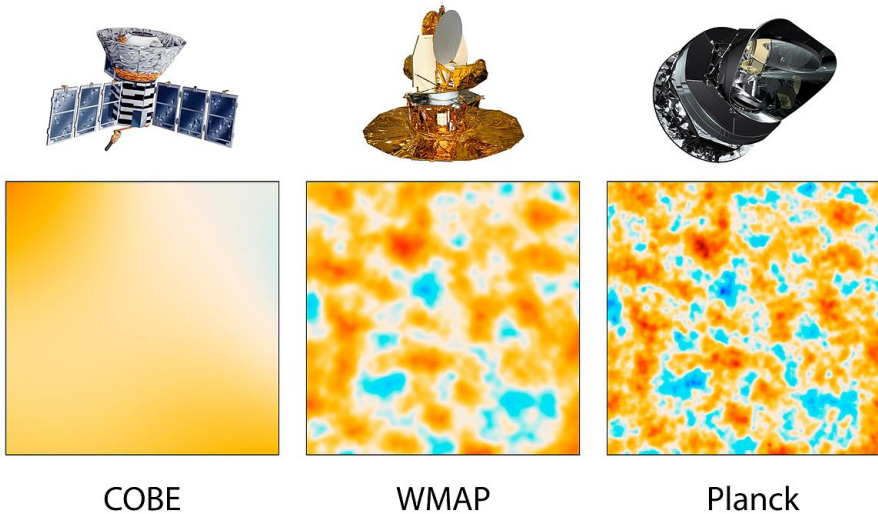


Figure 1.3: Improvement of resolution from COBE, first to discover anisotropies in the CMB, to WMAP and Planck which have set stringent limits on cosmological parameters by mapping variations in temperature of 1 part in 100,000. Image credit: NASA/JPL-Caltech/ESA.

from the photon pressure was only felt by the baryons whereas the dark matter component does not couple to photons. The competing attractive and repulsive forces gave rise to baryonic acoustic oscillations (BAO), with density regions propagating as spherical sound waves. The peaks of the waves are separated by a characteristic radius called the sound horizon ( $r$ ), which is sensitive to the initial dark matter and baryon densities [26]. Anisotropies in the CMB power spectrum probe these oscillations as discussed previously in section 1.1.3. At the time of decoupling the photon pressure ceased providing the opposing force allowing the gravitational restoring force to dampen the oscillations. If this picture is propagated forward in time, we expect that areas of the CMB that were denser would cluster, thus statistically

the universe is expected to have large scale structures on the order of the sound horizon  $r$ . Measurements of galaxy clusters by the Sloan Digital Sky Survey [27] and BOSS [2] are consistent with the sound horizon expected from anisotropies in the CMB, with a preferred scale of  $100h^{-1}$  Mpc ( $\sim 150$  Mpc) between large scale structures. Figure 1.4 shows the result from BOSS using Lyman- $\alpha$  absorption in the quasar emission spectrum due to the presence of neutral hydrogen in the intergalactic medium [2].

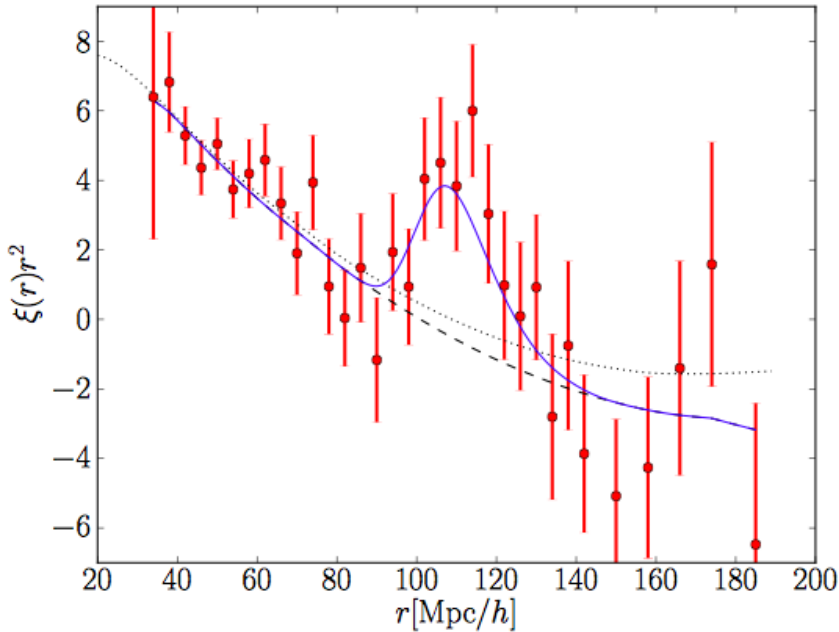


Figure 1.4: BAO peak obtained from BOSS [2]. The correlation function has a peak at of  $100h^{-1}$  Mpc, expected with a dark matter density of  $\Omega_b h^2 \sim 0.2$ .

### 1.1.5 Gravitational Lensing

The Bullet cluster is composed of two galaxy clusters which have recently collided and passed through each other. The collision has caused the ordinary, baryonic

matter to heat and emit X-rays that are observed and used to map the luminous mass distribution [28]. However, the observed concentration of mass is not consistent with the center of mass observed using gravitational lensing via GR [29]. The lensing indicates the presence of a dark-matter shell which, unlike the ordinary matter, has passed through undisturbed due to its lack of interactions. Figure 1.5 shows the concentration of mass in the bullet-cluster as observed from X-rays, emitted by baryonic matter, in pink and the concentration of mass from gravitational lensing in blue. The X-ray mapping from Chandra, when compared with gravitational lensing studies of the Bullet cluster, clearly demonstrate a decoupling of the dark matter center of mass from the baryonic center of mass induced by the cluster's recent collision.

## 1.2 Dark Matter Particles

The evidence for the existence of missing mass outlined in the previous section motivates us to examine solutions to account for those cosmological phenomena. It is natural to first try to solve the anomaly with standard model particles. One such theory is the existence of Massive Compact Halo Objects (MACHOs). A MACHO is a Jupiter size object that could add additional mass at the outer edges of galaxies. However, since MACHOs are baryonic the hypothesis is disfavored by precision measurements (BBN, CMB) that limit baryonic mass to only 2.2% of the total [30] [23] (see table 1.1). A non-baryonic candidate drawn from the standard model is the neutrino, which is known to be massive and only interact

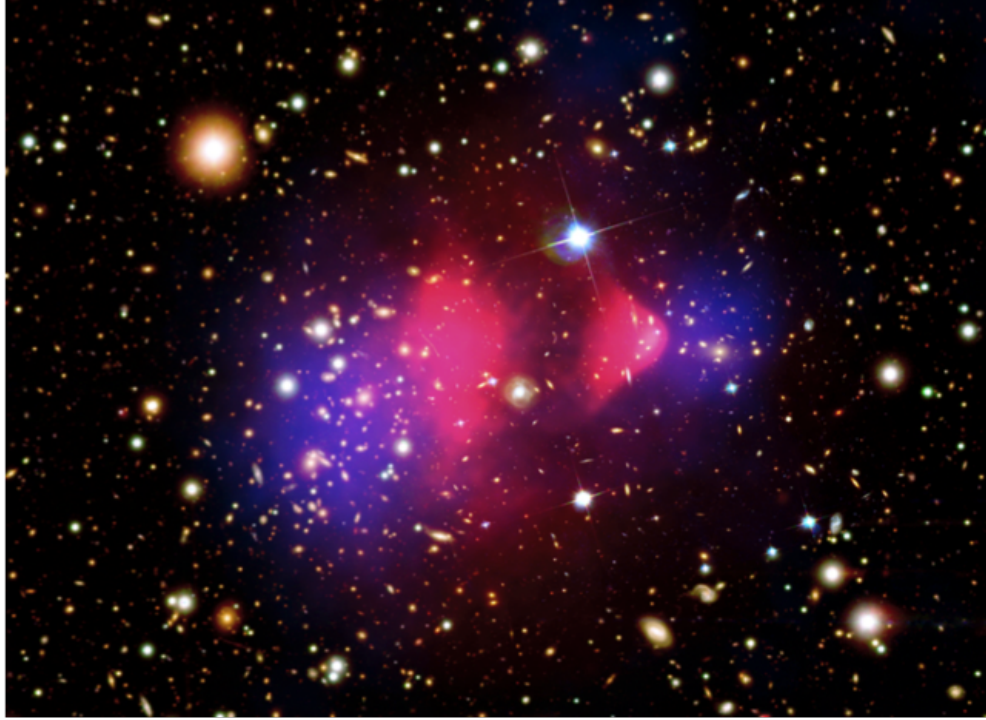


Figure 1.5: The concentration of mass in the bullet-cluster as observed from X-rays, emitted by baryonic matter, in pink, and the concentration of mass from gravitational lensing in blue. [Composite image credit: X-ray: NASA/CXC/CfA/M.Markevitch et al.; Optical: NASA/STScI; Magellan/U.Arizona/D.Clowe et al.; Lensing Map: NASA/STScI; ESO WFI; Magellan/U.Arizona/D.Clowe et al.]

weakly [31]. However, large scale structure formation require that the universe have a ‘cold’ (non-relativistic) dark matter component in order to become gravitationally bound to galaxies. Neutrinos are highly relativistic and would fail to reproduce the structure of the universe observed today [32].

### 1.2.1 Weakly Interacting Massive Particles

A model with Weakly Interacting Massive Particles (WIMP) can account for the dark matter component of the universe. The new particle would be massive, non-baryonic, and couple to ordinary matter via the weak force. The WIMP is theorized to have a mass and cross section on the order of the weak scale.

In the early universe the number density of WIMPs and photons would have been roughly equal as there was sufficient thermal energy keep the creation and annihilation in equilibrium:



where  $\chi$  represents WIMPs and  $q$  are standard model particles. The reaction can go in either direction as long as the thermal temperature of the universe is greater than the WIMP mass, holding the relative abundances constant .

As the universe expanded and cooled, production of WIMPs from standard model particles ceased as the temperature of the universe dropped below the WIMP mass, leaving only WIMP annihilation. The annihilation would continue indefinitely, leaving only a small number density at the tail of an exponentially falling Boltzmann distribution remaining today. However, if the universe's expansion is fast compared to the annihilation rate, then the WIMPs would fail to find each other and their number density could ‘freeze-out’. The freeze-out condition requires that the rate of the Universe’s expansion  $H$  is greater than the number density of WIMPs times the cross section.

$$H > \Gamma_A \equiv n_\chi \langle \sigma_A \nu \rangle \quad (1.4)$$

where  $H$  is the Hubble constant ,  $n_\chi$  is the number density of WIMPs and  $\langle \sigma_A \nu \rangle$  is the thermally averaged annihilation cross-section. The annihilation process can be described by the Boltzmann equation

$$\frac{dn_\chi}{dt} = -3Hn_\chi - \langle \sigma_A \nu \rangle (n_\chi^2 - n_{\chi_{eq}}^2) \quad (1.5)$$

where the first term represents the dilution of WIMP number density with three degrees of freedom,  $n_\chi^2$  is the annihilation process ( $\chi\chi \rightarrow qq$ ) and  $n_{\chi_{eq}}^2$  is from the reverse process ( $qq \rightarrow \chi\chi$ ). Equation 1.5 does not have an analytic solution but has been solved numerically[33]. The relic density is estimated within 10% to be

$$\Omega_\chi h^2 = \frac{3 \times 10^{-27} \text{cm}^3 \text{s}^{-1}}{\langle \sigma_A \nu \rangle} \sim \frac{10^{-10} \text{GeV}^{-2}}{\langle \sigma_A \nu \rangle} \quad (1.6)$$

Using a typical weak scale cross-section in equation 1.6,

$$\langle \sigma_A \nu \rangle \sim \frac{\alpha^2}{m_{weak}^2} \sim 10^{-9} \text{GeV}^{-2} \quad (1.7)$$

we find that the relic WIMP density reduces to  $\Omega_\chi h^2 = 0.1$  for a particle with a weak scale interaction. This is in good agreement with the expected cold dark matter component of the universe  $\Omega_c h^2 = 0.12029$  [23].

### 1.3 WIMP Dark Matter Searches

There are three methods for detecting WIMPs apart from its gravitational effects. First, we can look for the annihilation of dark matter into standard model particles in the universe today. Second, we can try to produce dark matter by colliding standard model particles in accelerators. Third, we can search for the rare collisions

of cosmic dark matter particles with ordinary matter in a laboratory here on earth. The third method is rather attractive as it involves directly observing a collision with a dark matter particle.

### 1.3.1 Direct Detection of WIMPs

WIMPs could have masses in the GeV to TeV range and would comprise a quarter of the total mass of the universe. The local density of dark matter around the earth, at 8 kpc from the galactic center, is about 0.3 GeV/cm<sup>3</sup>, estimated from the galactic rotation curve of the Milky-Way with the assumption of a halo-like distribution (figure 1.6 and [1]). Assuming that the WIMP mass is on the order of the weak scale, 100 GeV, there are roughly three WIMPs per liter of space locally. The velocity of WIMPs near the Earth is similar to the orbital velocity of objects about the galactic center (240km/s at 8.3 kpc), (figure 1.1). WIMPs, being highly non-relativistic, would scatter coherently on nuclei with a cross-section corresponding to  $\sim A^2$ .

WIMP scattering on nuclei can be expressed as a classical inelastic collision.

$$E_{\max} = r \cdot E_0 = \frac{r}{2} M_\chi v^2 \quad (1.8)$$

where  $E_{\max}$  is the most frequent energy deposit,  $E_0$  is the average WIMP energy,  $M_\chi$  is the WIMP mass and  $v$  is the WIMP velocity. The kinematic factor  $r$  for isotropic scattering off a target mass  $M_T$  in the laboratory frame is given by (using  $\frac{1}{2}$  for the average of  $1-\cos\theta$ .):

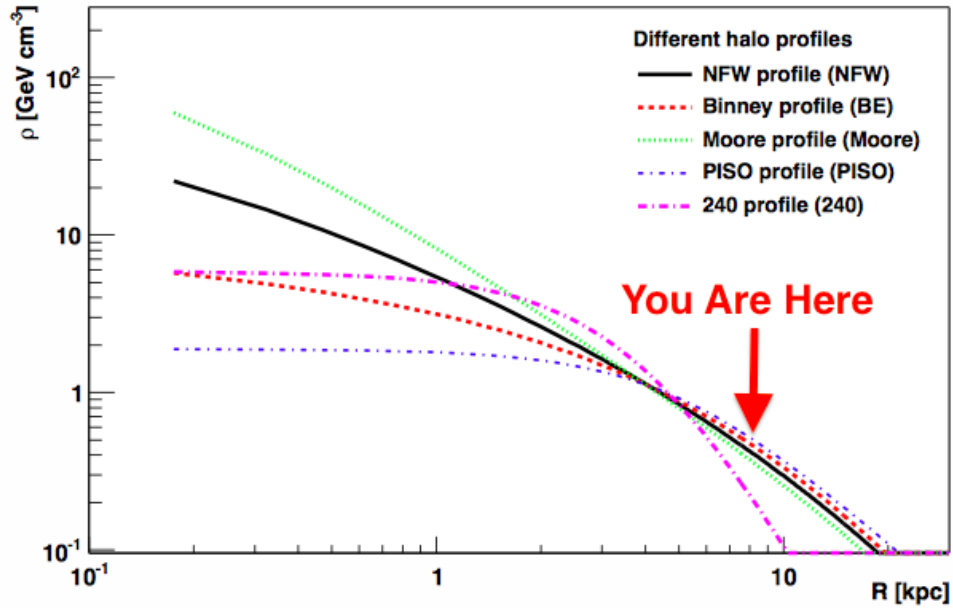


Figure 1.6: Dark matter density vs. distance from the galactic center, calculated from galactic rotation curves of the Milky Way galaxy. The Earth is located at 8.3 kpc. Figure from [1].

$$r = \frac{4M_\chi M_T}{(M_\chi + M_T)^2} \quad (1.9)$$

Assuming classic billiard ball scattering off a xenon nucleus we calculate the expected energy deposits for various WIMP masses ranging from 1 to 1000 GeV/c<sup>2</sup>, the results are listed in table 1.2.

$M_\chi$ [GeV/c <sup>2</sup> ]	r	$E_{\max}$ [keV]
1	0.032	0.01
10	0.28	0.90
100	0.99	31.7
10000	0.40	124

Table 1.2: The kinematic factor r and most common energy deposit  $E_{\max}$  for a WIMP of mass  $M_\chi$  scattering off a xenon nucleus. Calculated using xenon as the target mass ( $M_{Xe} = 122$  GeV/c<sup>2</sup>), and a WIMP velocity of 240 km/s ( $8 \times 10^{-4}$  c).

To calculate the WIMP-target scattering event rate we follow the derivation given by Lewin and Smith [3]. The differential rate of the WIMP nuclear recoils will be an exponentially decaying spectrum.

$$\frac{dR}{dE_R} = \frac{R_0}{E_0 r} e^{-E_R/E_0 r} \quad (1.10)$$

$E_R$  is the recoil energy,  $E_0$  is the most probable WIMP kinetic energy,  $r$  is the kinematic factor,  $R$  is the event rate per unit mass and  $R_0$  is the total rate per unit mass. The event rate  $dR$  scattering off a target size  $A$  can be written as

$$dR = \frac{\mathcal{N}_0}{A} \sigma \nu dn \quad (1.11)$$

where  $\mathcal{N}_0$  is Avagadro's number,  $A$  is the atomic mass,  $\sigma$  is the atomic cross-section,  $\nu$  is the WIMP velocity and  $dn$  is the differential number density of WIMPs given by:

$$dn = \frac{n_o}{k} \mathcal{F}(\nu, \nu_E) d^3\nu \quad (1.12)$$

where  $k = (\pi \nu_0^2)^{3/2}$  as  $\nu_{esc} \rightarrow \infty$ , an approximation good to within 0.5% for the Milky Way.  $n_o$  is the particle number density ( $n_o = p_\chi/m_\chi$ ). The WIMP velocity distribution  $\mathcal{F}(\nu, \nu_E)$  is assumed to be ideal gas described by a Maxwellian distribution:

$$\mathcal{F}(\nu, \nu_E) = e^{-(\nu + \nu_E)^2/\nu_0^2} \quad (1.13)$$

where  $\nu$  is the WIMP velocity,  $\nu_E$  is the earth velocity,  $\nu_0$  is the average velocity (about 230 km/s). We now rewrite equation 1.10 in terms of an integral over all

possible velocities and use in the result for  $dR$  (1.11) and  $dn$  (1.12) leading to :

$$\frac{dR}{dE_R} = \frac{R_0}{E_{0r}} \frac{1}{k} \frac{1}{2\pi\nu_0^2} \int_{\nu_{min}}^{\nu_{max}} \frac{1}{\nu} \mathcal{F}(\nu, \nu_E) d^3\nu \quad (1.14)$$

$$R_0 \text{ absorbs the constants } R_0 = \frac{2}{\pi^{1/2}} \frac{N}{A} \frac{\rho_\chi}{M_\chi} \sigma_T \nu_o.$$

Having solved for the differential rate we now calculate the total spin-independent cross section for WIMP scattering off nucleons of an atom ( $\sigma_T$ ). We write the cross section as a sum off scattering off protons and neutrons in the nucleus. We use the fact that nucleon coupling for protons and neutrons is approximately equal [34].

$$\sigma_T = \frac{4\mu^2 A}{\pi} [Z \cdot f_p + (A - Z)f_n] \approx \frac{4\mu^2 A^2}{\pi} \sigma_n \quad (1.15)$$

where  $\mu$  is the reduced mass of the WIMP nucleon system given by,

$$\mu = \frac{M_\chi M_n}{M_\chi + M_n} \quad (1.16)$$

Finally we must add the particular nuclear form factor for the specific target atom to account for decoherence, as described by the Helm factor [5]  $F(q)$ . The cross section for spin-independent scattering can be written as a product of the idealized cross section and Helm factor:

$$\sigma_T(q) = \sigma_T F^2(q) = \frac{4A^2}{\pi} \left( \frac{M_\chi M_n}{M_\chi + M_n} \right)^2 \sigma_n F^2(q) \quad (1.17)$$

The spin-independent cross section is found to be proportional to the atomic number squared ( $A^2$ ). The event rate per nuclear recoil energy is plotted for several target nuclei in figure 1.7.

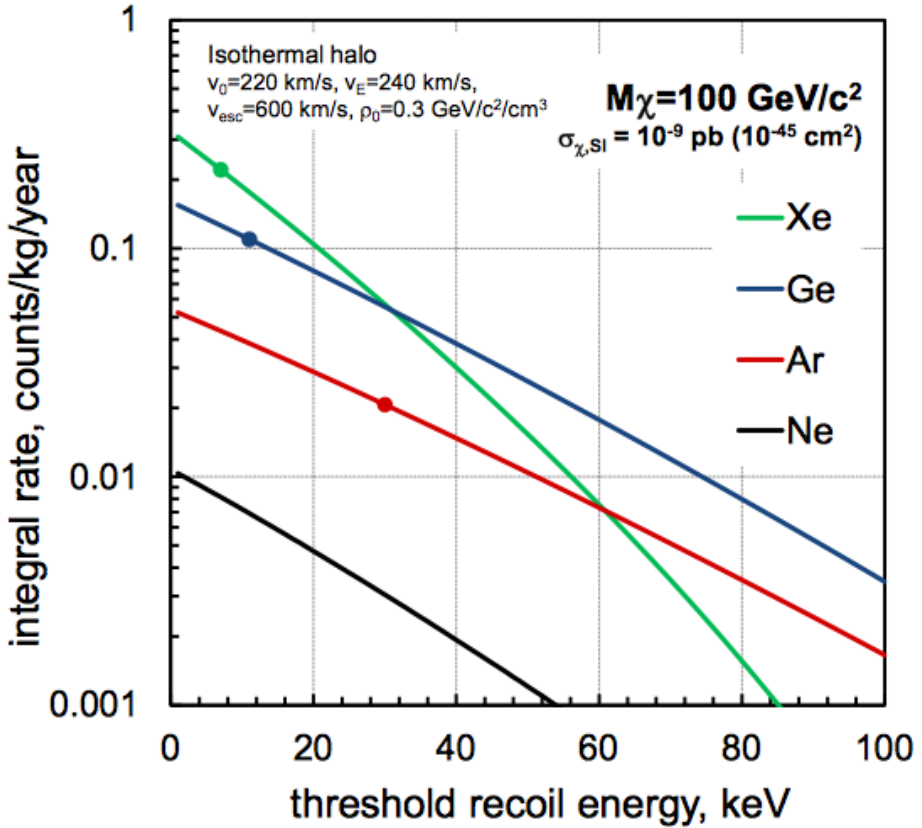


Figure 1.7: Plot of WIMP event rate per kg/day/keV vs. Nuclear recoil energy (keV) for several target nuclei, using parameters from [3]. Figure taken from [4]. At low detection threshold xenon is the most attractive target nuclei. The fall in the xenon curve is due to decoherence described by the Helm factor [5].

Xenon, being a relatively heavy element, ( $A=131$ ), is an ideal candidate for a WIMP dark-matter search at low energy thresholds. Xenon detectors have achieved thresholds as low as 3 keV<sub>nr</sub> [7]. Other common detection mediums are germanium, which is rather expensive on the ton scale, and argon which is inexpensive but contains a troublesome radioactive isotope ( $^{39}\text{Ar}$ ). To probe smaller dark matter cross sections, the next generation of experiments must be larger and contain less

radioactive background contamination. Given current limits on the WIMP cross section, a ton-scale xenon experiment may only detect a handful of events per year.

### 1.3.2 WIMP Detection Experiments

Several experiments are currently conducting WIMP dark matter searches using a variety of targets, including xenon [7, 35, 36, 37], argon [38, 39], germanium [40, 41] and fluorine [42, 43]. In the event that a WIMP strikes a target in the detector, it will primarily interact with the nucleus, deposit energy, and traverse across the detector without a second interaction. Neutrons could also interact with atomic nuclei and fake a WIMP signal, however after the initial energy deposit they are likely to interact again. Thus, neutrons can be rejected by removing multiple scatter events in the detectors.

The most common source of backgrounds are electromagnetic in nature: gammas and betas from the rock surrounding the experiment, detector components, and internal to the xenon. As for the case of neutrons, the likelihood of a single scatter within the detector is small for a  $\beta$  or  $\gamma$  particle. Naked beta decays are the most troublesome, appearing as a single energy deposit in the detector medium. Fortunately, electronic recoil events can be discriminated from WIMP-like nuclear recoil events by more than 1/100 using the ratio of charge-to-light or charge-to-phonons produced in the interaction, as described in thesis, chapter 7. Xenon based experiments currently hold the most stringent limits on WIMP nucleon cross sections [7].

## 1.4 Outline of the Thesis

In this section we have reviewed the cosmological evidence for the existence of dark matter and the WIMP model. The WIMP hypothesis can be tested by searching for scattering off target nuclei.

In Chap. 2, the LUX detector, a liquid xenon time projection chamber (TPC), is described. We discuss how the light (S1) and charge (S2) signals from energy deposits are selected. The S1 and S2 signals are then used to reconstruct the energy, reject backgrounds and define the x,y,z coordinate of each event. We conclude the chapter with the most recent LUX science results which holds the leading limit for spin-independent WIMP nucleon scattering cross section.

In Chap. 3, the spatial dependent correction of the S1 and S2 signals are discussed. A  $^{83\text{m}}\text{Kr}$  line source is injected periodically producing hundreds of thousands of events in the LUX detector. The calibration data are used to create the position dependent corrections which are then applied to the physics data.

In Chap. 4, the energy scale calibration of the LUX detector using line sources is discussed. The energy scale calibration is validated in the WIMP search region of interest (1-5 keV) by a reconstructing the beta spectrum of a tritium calibration source (1-18 keV).

In Chap. 5 recombination fluctuations inherent to liquid xenon are reviewed. We model detector resolution based on the PMT response to single photons and electrons along with light collection and charge extraction efficiency. We then proceed to extract recombination and statistical fluctuations from line source calibrations.

The method is then adapted to the case of continuous energy spectra allowing for the extraction of recombination fluctuations from the tritium data. We end with a discussion of the underlying physical processes that produces the fluctuations.

In Chap. 6 the ionization and scintillation yield of liquid xenon is measured using the tritium calibration source. We discuss the spectral shape corrections to the true tritium spectrum caused by detector resolution. We compare our scintillation yield measurements (from 1-16 keV) with recent results from other experiments.

In Chap. 7 we overview the development and deployment of the tritiated-methane calibration source. The source was successfully injected and removed from the LUX detector producing high purity calibration data in the fiducial volume. The tritium calibration data is used to determine the electronic recoil band in terms of the observables S1 and S2 and define the background rejection for the WIMP search.

In Chap. 8 future work is discussed in terms of detector calibrations, understanding event level fundamental fluctuations, and tighter constraints on the WIMP limit.

## Chapter 2: The LUX Detector

### 2.1 Introduction

The LUX experiment is located 4850 ft underground (4300 m w.e.) at the Sanford Underground Research Facility in Lead, South Dakota. After running for 85.3 live days in 2013, LUX has set the most sensitive limit for a spin-independent WIMP scattering cross section [7] and is expected to achieve five times the sensitivity after a 300 day run ending in 2015.

Noble elements are promising candidates for WIMP detection. They are easy to purify and are transparent to their own scintillation light. Xenon is especially favorable due to its large atomic mass (131.3 amu) and high liquid phase density ( $\sim 2.9$  kg/l) which provides both an excellent target for coherent WIMP scattering while simultaneously providing excellent stopping power from external radioactivity. Xenon is also free of any long lived radioactive isotopes which contribute backgrounds for the WIMP search. There are well established techniques to remove and monitor the residual, troublesome radio isotopes of  $^{39}\text{Ar}$  and  $^{85}\text{Kr}$  found in the atmosphere from which the xenon is distilled [44] [45] [46] [47].

WIMPs, being weakly interacting and non-relativistic, primarily interact with the xenon target nuclei producing nuclear recoil (NR) events, whereas typical back-

grounds in the detector, gammas and betas, interact with the atomic electrons producing electronic recoils (ER). In liquid xenon ER events can be further discriminated from NR events a factor of 100 or more by measuring the charge to light ratio of the interaction, as explained in section 2.2.2.

## 2.2 The LUX TPC



Figure 2.1: Photo of the outer vessel of the LUX detector from inside the water tank.

Figures 2.1 shows the LUX detector held in place by a stainless steel frame and the water tank that surrounds it. The water tank provides shielding from gammas and neutrons emanating from the surrounding rock. The water tank PMTs, may be used as an active muon veto, are also pictured along the sides of the water tank. Figure 2.2 show a cross sector of the LUX detector’s inner and outer vessel. The LUX detector is a two phase xenon time projection chamber (TPC) [7]. The detector

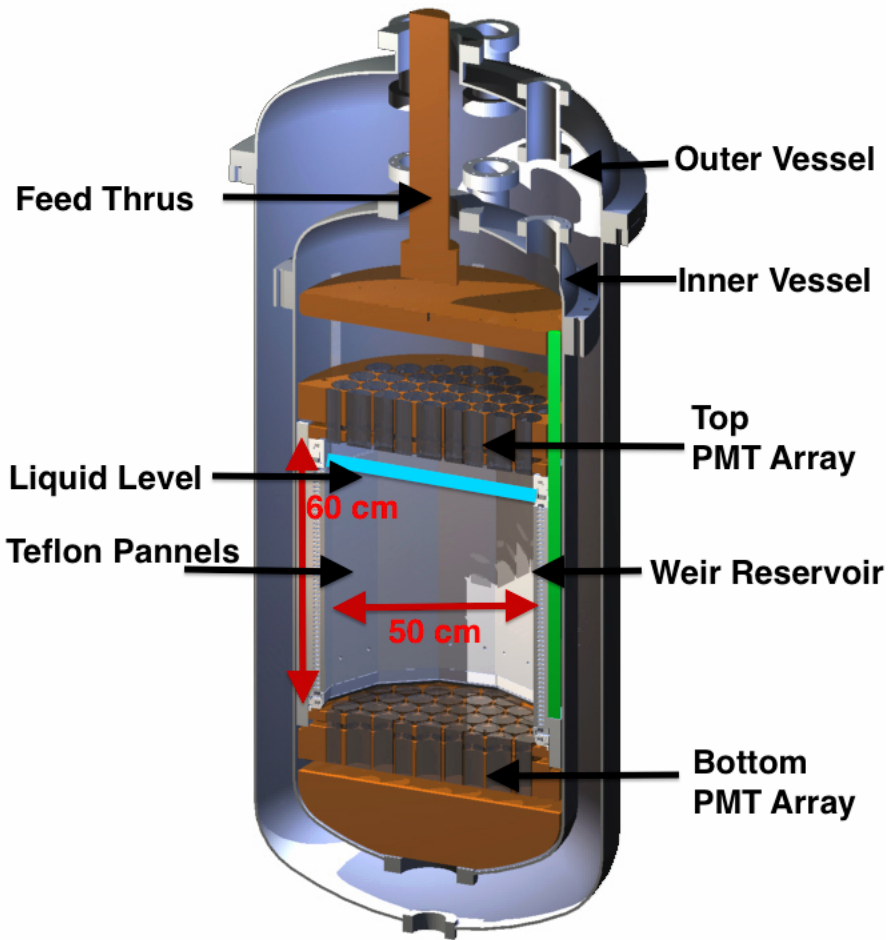


Figure 2.2: Illustration of the LUX detector’s internals. The detector contains two arrays of PMTs on the top and bottom housing 61 PMTs each. Teflon panels on the edges of the active region are used to reflect scintillation signals. The vertical distance between the two PMT arrays is 60 cm, and the diameter to the inner edge of the Teflon panels is 50 cm.

contains two PMT arrays on the top and bottom with 61 PMTs each for a total of 122 PMTs. The quantum efficiencies range from 30 to 40%.

The active region consists of a 49 cm length between the cathode and gate grid with a 47 cm diameter of the dodecagonal geometry. The drift field between the

cathode and gate is 170 V/cm resulting in an electron drift velocity of 1.51 mm/ $\mu$ s. The liquid level terminates 5-6mm above the gate grid. The liquid level is precisely maintained by a weir reservoir into which xenon between the anode and gate spills. The anode grid is 1.0 cm above the gate grid and creates an extraction field of 6 [kV/cm] where electrons are removed from the liquid and accelerated causing electroluminescence in the gas phase. LUX contains a gross mass of 370 kg of xenon of which 250 kg are in the active region.

### 2.2.1 Target Xenon

The target xenon is commercially available natural xenon with standard isotopic abundances (table 2.1), initially distilled to  $\sim$  1 part per million (ppm) residual air contamination (N<sub>2</sub>, O<sub>2</sub>, Ar). The commercially available xenon also contained  $\sim$  100 parts per billion (ppb) of krypton which is far greater than the background allowance of 5 parts per trillion (ppt). Krypton contains trace amounts of a beta emitter <sup>85</sup>Kr and is a troublesome internal background dissolved uniformly directly in the detection medium (xenon). The unwanted krypton was removed from the bulk xenon using a gas chromatography technique [46], with the removal independently verified before the science run with a xenon gas analysis technique developed for EXO-200 and LUX [45]. The xenon purity was monitored daily throughout the 2013 science run by an in situ gas analysis system which will be described in a future LUX publication. Just one standard liter of air contains enough krypton to raise the concentration in the LUX xenon above the background goals. Daily krypton

monitoring ensured that the krypton content in the xenon remained constant at 4 parts per trillion over the 2013 science run[6].

Electronegative impurities such as N<sub>2</sub>, O<sub>2</sub> and H<sub>2</sub>O attenuate electrons drifting through the xenon and must be removed in order to properly reconstruct events originating deep in the detector. These impurities continuously emanate from detector components degrading the free electron attenuation length. The accumulation of electronegative impurities is countered by circulating the xenon at 26.5 SLPM through a heated zirconium getter. The gross mass of 370 kg has a turn-over time of 1.65 days. Throughout the 2013 science the electron attenuation length was measured to be 75 cm to 150 cm, corresponding to 70% to 50% charge loss for events originating from the bottom of the active region.

Isotope	Natural Abundance (%)
<sup>124</sup> Xe	0.09
<sup>126</sup> Xe	0.09
<sup>128</sup> Xe	1.92
<sup>129</sup> Xe	26.44
<sup>130</sup> Xe	4.08
<sup>131</sup> Xe	21.18
<sup>132</sup> Xe	26.86
<sup>134</sup> Xe	10.44
<sup>136</sup> Xe	8.87

Table 2.1: Xenon isotopic abundances, from [48]

### 2.2.2 Background Rejection

Liquid xenon at 178 K has a density of  $\sim 2.88 \text{ g/cm}^3$ , providing excellent stopping power for shielding against external radioactivity. External radioactivity with ener-

gies in the WIMP search region of interest (below 50 keV) only penetrate millimeters in liquid xenon, being completely absorbed in the outer edges of the detector. Gammas in the MeV range have mean free paths on the order of 3 cm and are likely to be rejected by the single scattering requirement. The most troublesome of the gamma backgrounds are from PMT materials containing trace amounts of uranium and thorium located inside the TPC. Figure 2.3 shows a simulation of expected gamma background events inside the LUX detector, using the single scatter cut requirement. By removing the edge events we gain at least an additional factor of 1000 background rejection within the fiducial volume (inside the black dashed lines) [6].

Another means for discriminating background events is through measuring the charge-to-light ratio of each event. WIMPs will produce nuclear recoils whereas gammas and betas interact primarily with atomic electrons, resulting in different charge to light ratios of a given energy deposit. Using AmBe and  $^{252}\text{Cf}$  neutron sources along with a tritium calibration source, the NR to ER discrimination factor was measured to be  $99.6 \pm 1\%$  at 50% NR acceptance (in section 7.4.3). This means that only one in 250 of the residual gamma and beta background events is expected to fake a WIMP signal when cutting out half of the potential nuclear recoil candidates. The ER type and NR type bands are shown in figure 2.4 with the band means as solid lines (Blue and Red, respectively) and the 10-90% CL as dashed lines. The internal tritium calibration source will be discussed in chapter 7.

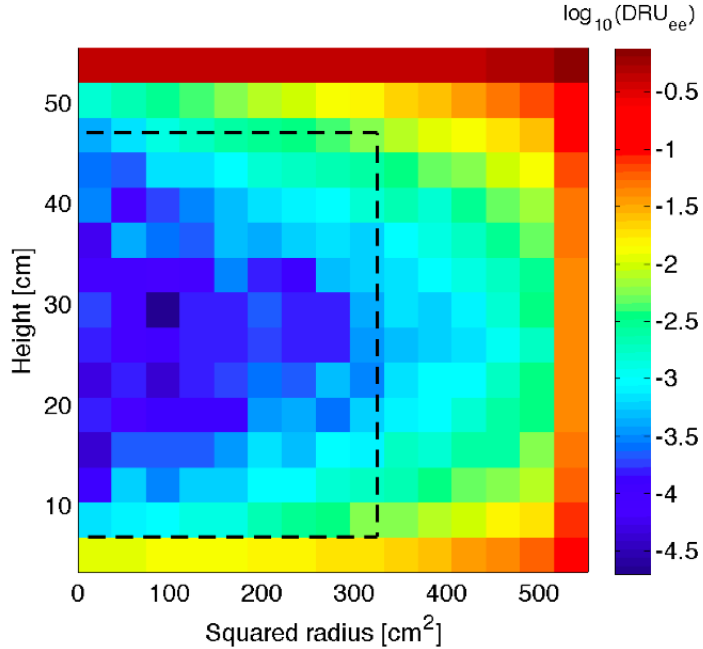


Figure 2.3: Simulation of expected gamma background events inside the LUX detector, using the single scatter cut requirement[6]. There is a factor of 1000 background rejection within the fiducial volume where the WIMP search is conducted (inside the black dashed lines) .

### 2.2.3 The Drift Field inside the LUX TPC

The LUX TPC contains five wire grids used to control the electric fields inside the detector. The grids and their spacing are shown in figure 2.5, labeled from top to bottom as Top (T), Anode (A), Gate (G), Cathode (C), Bottom (B). The grids T,A,G,C,B are biased at -1,+3.5,-1.5,-10,-2 (all in kV), respectively. The PMT photocathodes are biased to -1.2 kV on average. The field created in the active liquid xenon region between the cathode and gate is also shown in figure 2.5. On average the drift field is 170 V/cm with variation from 140 V/cm to 200 V/cm from

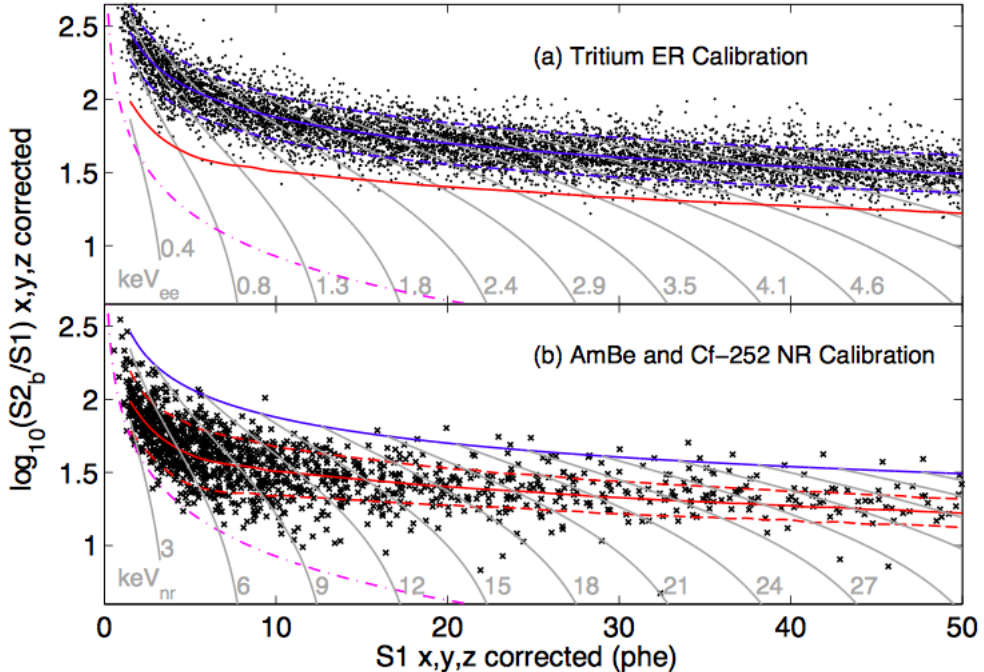


Figure 2.4: Plot of the log of the charge-to-light ratio vs. S1 (energy). The variable  $\log_{10}(S2_b/S1)$  is used to distinguish ER type events from NR type events. The ER and NR bands are defined from calibrations, a) Betas from a tritium calibration (Blue), and b) Neutrons from AmBe and  $^{252}\text{Cf}$  (Red). The band means are solid lines and the 10-90% CL are shown as dashed lines. The ER to NR discrimination by using the charge to light ratio was measured to  $99.6 \pm 0.1\%$  at 50% NR acceptance [7].

cathode to gate. The extraction region between the anode and gate has a 6 kV/cm field. This extraction field is used to create the secondary scintillation (S2) signal via electroluminescence as the electrons are extracted and accelerated. The top and bottom grids serve to shield the PMTs from the anode and cathode voltages.

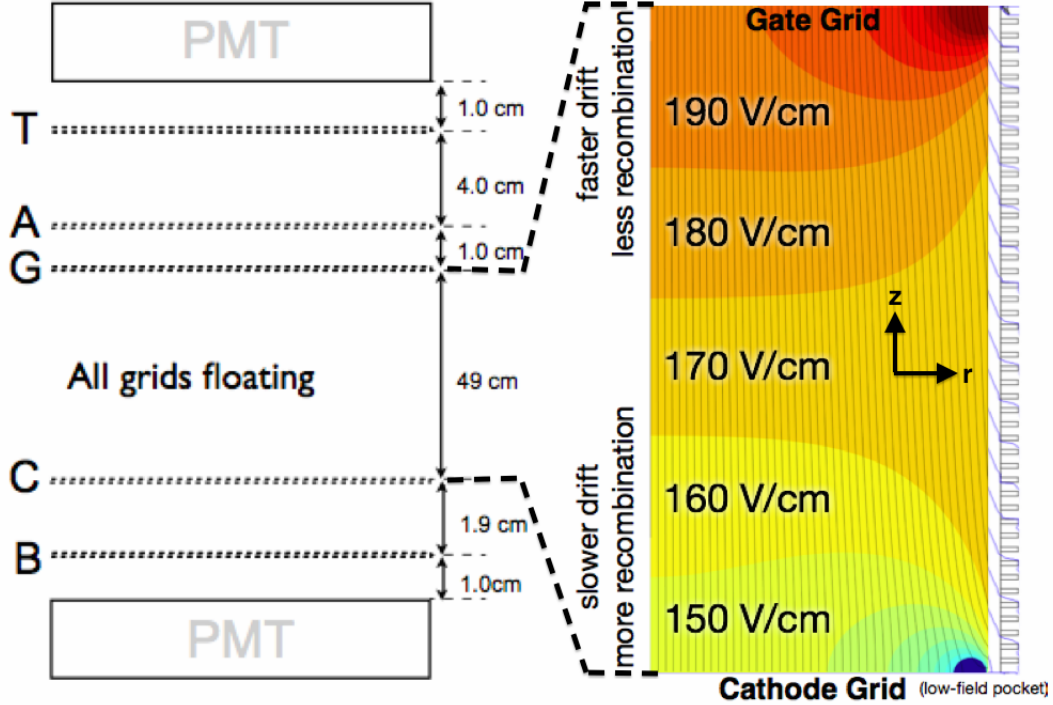


Figure 2.5: Field grids in the LUX detector during the 2013 science run. T,A,G,C,B are biased to -1,+3.5,-1.5,-10,-2 (all in kV), respectively. The PMTs are biased to -1.2 kV on average. The figure on the right shows the electric field model in the drift region between the cathode and gate for drift distance  $z$  vs. detector radius  $r$ . On average the drift field is 170 V/cm with variation from 140 V/cm to 200 V/cm from cathode to gate. Electric field model from [8].

### 2.3 Light and Charge Signals in Liquid Xenon

When energy is deposited in the active region of the xenon TPC it is converted to ionization, atomic excitation and heat.

$$E = W(n_i + n_{ex}) + \text{Heat} \quad (2.1)$$

$$E = W \times n_q + \text{Heat}$$

where  $E$  is the energy of the deposition in keV,  $n_i$ ,  $n_{ex}$  and  $n_q$  are the number of ions, excitons and quanta respectively. An exciton is a bound state of an electron and the xenon ion. The work function ( $W$ ) for xenon has been measured to be  $13.7 \pm 0.2$  eV/quanta [11].

The number of photons produced in an event is equal to number of initial excitons in addition to the excitons resulting from ions which recombine with freed electrons. Each de-excitation of an exciton produces one photon. The number of electrons produced in an event is equal to the number of electron-ion pairs which do not recombine.

$$\begin{aligned} n_\gamma &= n_{ex} + n_i r = n_i(r + \alpha) \\ n_e &= n_i(1 - r) \end{aligned} \tag{2.2}$$

where  $n_\gamma$  and  $n_e$  are the number of photons and electrons and quanta. The value of  $r$  is the electron-ion recombination probability and  $\alpha$  represents the ratio  $n_{ex}/n_{ion}$ . Note,  $n_{ex}$  represents the number of primary excitons. The model given in equation 2.2 states that for each additional photon produced from recombination a corresponding electron is lost, and visa versa. The value of  $\alpha$  for an ER event is approximately 0.2 and is expected to be independent of energy [49] [50]. For nuclear recoils  $\alpha$  is approximately 1 [11]. Equation 2.2 can be written in terms of the number of photons and electrons for each energy deposit [51].

$$E = W(n_\gamma + n_e) + \text{Heat} \tag{2.3}$$

The light and charge production in liquid xenon will be discussed in further detail

below. Some useful properties of xenon are listed in table listed in table 2.2.

Parameter	Value	Ref.
Scintillation wavelength	174-178 nm	[52]
W (work function)	$13.7 \pm 0.2$ [eV/quanta]	[11]
Xe <sub>2</sub> <sup>*</sup> singlet lifetime	$3.1 \pm 0.7$ ns	[53] [54] [55]
Xe <sub>2</sub> <sup>*</sup> triplet lifetime	$24 \pm 1$ ns	[53] [54] [55]
Recombination time	7.5 ns **	[56] [55]
Liquid density at boiling point	2.95 g/l	[57]

Table 2.2: Properties of xenon. \*\* The expected recombination for the LUX drift field of 170 V/cm. Recombination time ranges from 0 to 46 ns depending on electric field, energy deposit, and interaction type [55] [56].

### 2.3.1 Electronic Recoils (ER)

For an electronic recoil event the energy lost to heat is only about 5% [58] thus, equation 2.1 is valid for use with electronic recoils, we simply drop the small loss to heat. A schematic of an ER event is shown in figure 2.6 which we describe here. When an incoming beta or gamma interacts with the electron of the xenon atom, the energy deposited is converted primarily to ionization, with roughly 6% excitation and  $\sim 5\%$  is lost to heat [59] [58]. Excitons arise from ionized xenon atoms that bond together forming diatomic molecules (Xe<sub>2</sub><sup>\*</sup>). Xenon excitons will de-excite with characteristic time constants of 2.2 and 27 ns for the singlet and triplet state, respectively, producing  $\sim 175$  nm scintillation light. Ion-electron pairs produced via ionization can also recombine, with probability  $r$ , producing additional excitons resulting in the production of additional  $\sim 175$  nm scintillation light. The characteristic recombination time constant in LUX is 7.5 ns [54]. Each initial exciton or recombining ion produces one scintillation photon, as written in equation 2.2. The

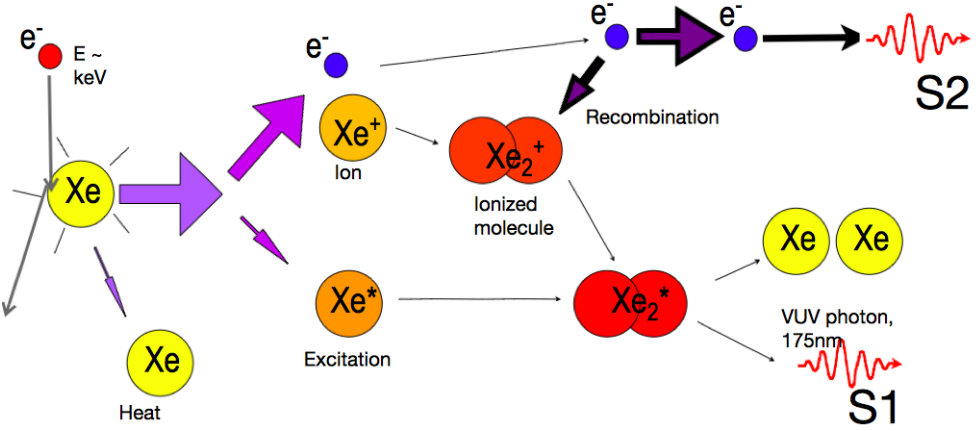


Figure 2.6: An electronic recoil (ER) event in xenon. The energy deposited is converted primarily to ionization and roughly one tenth for excitation. Only several percent is lost to heat. Xenon excitons and recombining electron ion pairs from xenon dimers which de-excite producing vacuum ultra-violet (VUV) scintillation light at 175 nm producing the primary scintillation signal (S1). Electrons that do not recombine are drifted by an electric field into the gas phase where they are accelerated producing the secondary scintillation (S2) signal. Figure from [9].

two paths for photon production overlap in time and sum to produce the primary scintillation signal (S1).

Electrons that escape recombination, with probability  $1-r$ , begin to drift upwards under the influence of the electric field between the cathode and gate (shown in 2.5). The electrons eventually reach the liquid-gas interface where they are extracted into the gas. As they accelerate, the extracted electrons produce a larger secondary scintillation signal (S2) that is proportional the the number of electrons extracted. The drift times for the electrons in the 49 cm, vertical length, active region range from 1 to 324  $\mu$ s with an average drift velocity of 1.51 mm/ $\mu$ s. Thus, the S2 signal is well separated from the S1.

### 2.3.2 Nuclear Recoils (NR)

For nuclear recoils the energy lost to heat is more than half the total energy deposition [58]. This energy is lost through elastic collisions with other xenon atoms that fall below the ionization threshold. The energy lost to heat is characterized by an energy dependent Lindhard factor ( $\mathcal{L}$ ) [60], written as:

$$E = \mathcal{L}^{-1} W(n_\gamma + n_e) \quad (2.4)$$

A schematic of a NR event is shown in figure 2.7. The signal production follows the same process as described above for an ER event but with greater amount of energy going towards heat and exciton production.

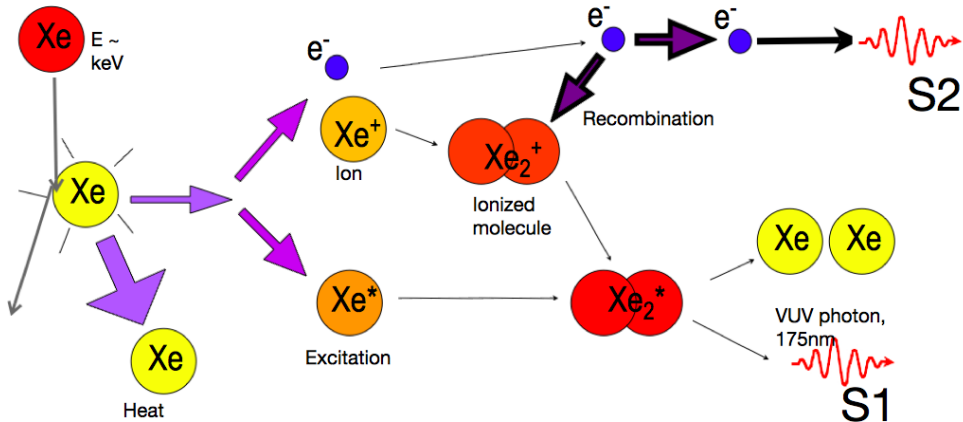


Figure 2.7: A nuclear recoil (NR) event in xenon. The energy deposited goes mainly towards heat (phonons), the remaining energy is split evenly between ionization and excitation. Xenon excitons and recombining electron ion pairs for xenon dimers which de-excite producing vacuum ultra-violet (VUV) scintillation light at 175 nm producing the primary scintillation signal (S1). Electrons that do not recombine are drifted in an electric field into the gas phase where they are accelerated producing the secondary scintillation (S2) signal. Figure from [9].

The additional energy lost to heat leaves less energy available for excitation and

ionization for an NR event. Further, NR events produce roughly equal amounts of ionization and excitation whereas ER events produce mostly ionization [58] [11]. Relative to an ER event, a NR event will have fewer electron ion pairs leading to a reduction of the S2 signal and enhancement the S1. Thus, the ratio of S2 to S1 for a NR event is “quenched”, or smaller, compared to an ER event with an equivalent energy deposition. The quenching of the charge to light ratio is what allows for discrimination between nuclear and electronic recoils as demonstrated in figure 2.4.

### 2.3.3 Energy and Position Reconstruction

In order to reconstruct the true energy of an event we need to know its nature, ER or NR. For ER events we work in units of electronic equivalent energy, ( $\text{keV}_{\text{ee}}$ ), using equation 2.1 and neglecting the small heat loss. ER calibrations will be discussed in greater detail in chapter 4. For NR events the energy is reconstructed in terms of nuclear recoil equivalent energy ( $\text{keV}_{\text{nr}}$ ), using equation 2.4 with the Lindhard factor measured from calibration data given in [61] [62].

An illustration of an energy deposition in the LUX detector is show in figure 2.8. The time difference between the S1 and S2 pulse defines the drift time, the drift time gives the measure of the z coordinate (depth). The hit pattern of the S2 signal on the top PMT array measures the x,y coordinates of the event. From the S1 and S2 signals the full x,y,z position and the energy of the event can be reconstructed.

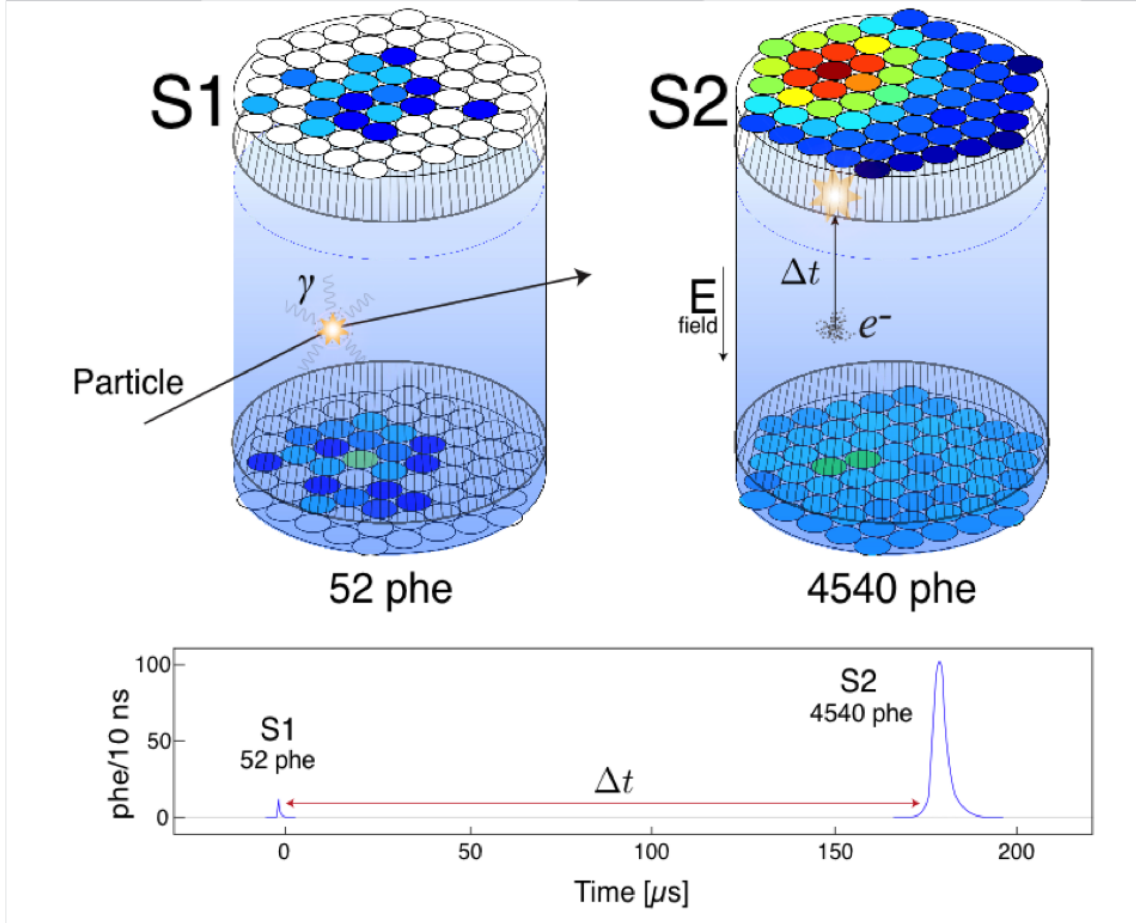


Figure 2.8: Event diagram.

## 2.4 Identifying S1, S2

The primary and secondary scintillation signals can be identified by their unique properties. The S1 signal has a fast rise time and decays on the order of 10's of nano-seconds as the dimers of xenon produced through excitation and recombination de-excite (time constants listed in table 2.2). The S2 signal arrives several  $\mu s$  later with the electron population spread out spatially about its centroid due to diffusion, transverse and radial [63]. The characteristic S2 signal is thus one with a slow rise and corresponding slow fall. It resembles a bell curve, as the diffused electron

population arrives, peaking at the centroid of the distribution. A 2 keV event as seen by all 122 PMT channels is shown in figure 2.9. The S1 pulse is fast and the S2 pulse is much larger with a slower rise-time. The S2 pulse is larger since a single electron creates hundred of photons as it is accelerated in the extraction region.

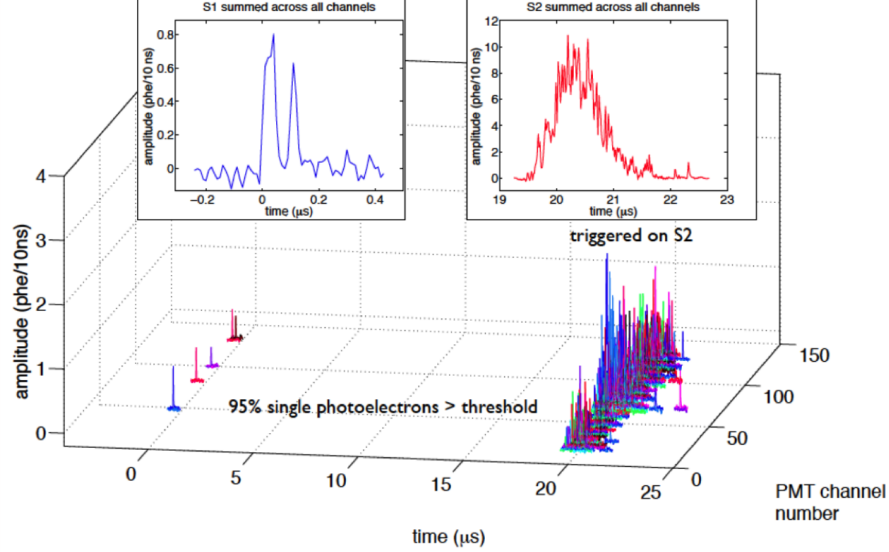


Figure 2.9: 2 keV ER event as seen by each PMT channel of the LUX detector. The S1 signal summed across all channels is overlaid on the top left, and the S2 signal summed across all channels is overlaid on the top right.

To identify S1 and S2 populations we define the variable “Prompt Fraction” as the area covered in the first 10% of the pulse waveform normalized to the total area. The calculation is performed on the summed waveform after a first pass which defines the pulse’s start and end time-stamp. The separation of population density when plotting the total Pulse Area (measured in detected photo electrons [PE]) vs. Prompt Fraction is shown in figure 2.10, for the case of a  $^{83m}\text{Kr}$  data set

(41.5 keV) and a tritium calibration data set (1-18.5 keV). The population of single electrons, single photons and the S1 S2 pairs associated with  $\gamma$ ,  $\beta$  and  $\alpha$  interactions are well separated and are highlighted as rectangles. The upper left corner is the single photon population. The area is approximately 1 PE, this defines the PMTs' response to a detected photon. The single electron population is labeled SE and peaks at roughly 20 PE with a prompt fraction of 0.1. For all S1 pulses the prompt fraction is found to be between 1 and 0.3 ( $\log_{10}$  of 0 and -0.5) for the entire range of Pulse Area. The pulse area is a proxy for energy, spanning from 1 keV tritium events to 7 MeV alphas. The populations of S2 from  $^{83m}\text{Kr}$ , tritium,  $\gamma$ ,  $\beta$  and  $\alpha$  are found to have Prompt Fractions more than an order of magnitude smaller than their corresponding S1.

The S1 and S2 signals corresponding to an event are identified using a prompt fraction selection that has been tuned to calibration data. Valid S1 and S2 signals that spill into the single electron and single photon region at low energies can be identified by requiring the pulses be paired. For the WIMP search we define ‘golden’ events consisting of single scatters with a single S1 paired with a subsequent S2 pulse with a timing separation within the maximum drift time of the TPC. With the golden requirement each event has a well defined x,y coordinate and z making it possible to correct the signals for geometrical effects and electron attenuation.

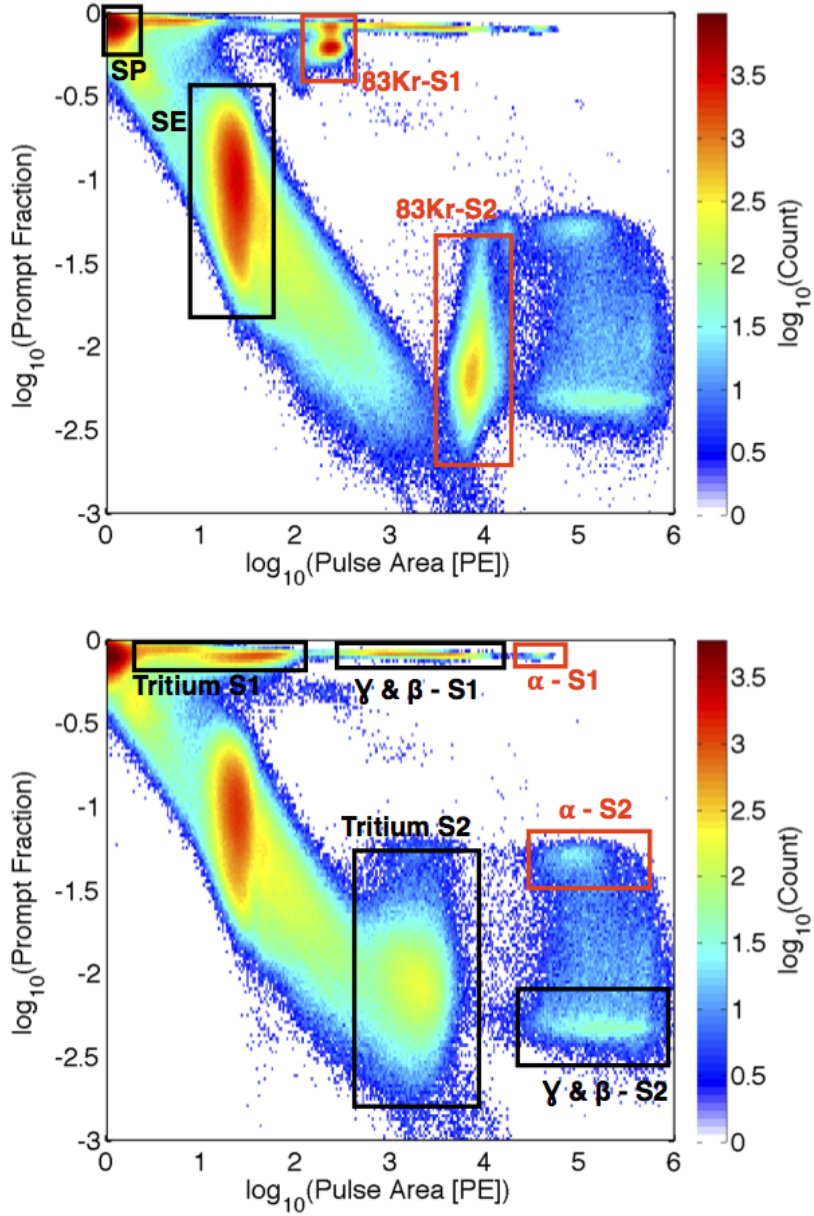


Figure 2.10: Density plot of prompt fraction vs. Pulse Area. Top:  $^{83\text{m}}\text{Kr}$  data set.

Bottom: Tritium data set. Populations of single electrons, single photons and the

S1 S2 pairs associated with  $\gamma$ ,  $\beta$  and  $\alpha$  are highlighted as rectangles.

## 2.5 LUX Science Result (WIMP limit)

The first science run of the LUX detector consisted of 85.3 live days between April 21, 2013 to Aug 8, 2013. A total of 83,673,413 triggers were recorded with 160 remaining as golden after applying quality cuts, listed in table 2.3.

Cut	Events Remaining
all triggers	83, 673, 413
detector stability	82, 918, 902
single scatter	6, 585, 686
S1 energy (2 - 30 phe)	26, 824
S2 energy (200 - 3300 phe)	20, 989
single electron background	19, 796
fiducial volume	160

Table 2.3: Data quality cuts used for the WIMP search results presented in [7].

Detector stability cuts remove the live time in which liquid level, gas pressure or grid voltages were out of normal ranges. The single scatter cut requires a single S1 with a subsequent S2 within a time window of  $324 \mu\text{s}$ , the maximum time required for electrons to traverse the active region. An area cut was also placed on both the S1 and S2 in order to narrow the energy region of interest. The minimum S2 requirement of 200 PE ensures the quality of the x,y position reconstruction, with  $\sim 8$  extracted electrons. An additional cut was placed around time windows with anomalously high single electron rates. All single scatter WIMP search events before applying the fiducial cut are shown in figure 2.11, the vast majority of events occurring at the edges of the detector. The fiducial cut reduces residual radioactivity from the detector surface and PMTs by another two orders of magnitude. The fiducial cut consists of a radial cut at radius less than 18 cm from the detector

center. The z coordinate in drift time is defined to be 0  $\mu\text{s}$  at the liquid surface and 324  $\mu\text{s}$  at the cathode. The fiducial cut in z required that event drift times be between 38 and 305  $\mu\text{s}$ , corresponding to 6 to 46 cm below the liquid surface (drift velocity = 1.51 mm/ $\mu\text{s}$ ). The fiducial cut is shown as the dashed cyan line in figure 2.11.

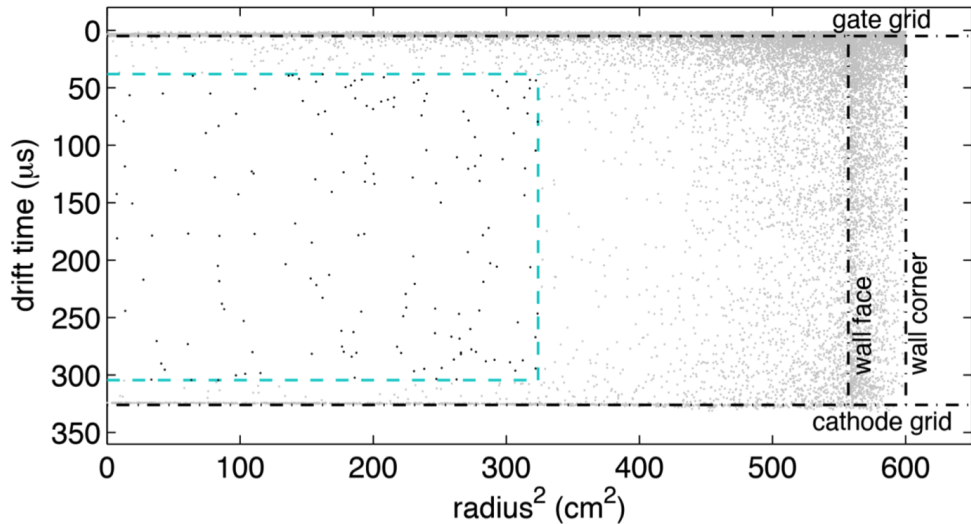


Figure 2.11: All single scatter events seen in the active region of the LUX detector over the course of the first science run passing all cuts listed in table 2.3 excluding the fiducial cut. The dashed cyan box indicates the fiducial volume.

Within the fiducial volume 160 events remain which meet our WIMP search energy requirement. The energy cut is placed in terms of S1 from 2-30 PE. As explained in chapter 4, this corresponds to roughly 1.0 to 6 keV<sub>ee</sub> or 3 to 25 keV<sub>nr</sub>. We choose to select events based on S1 because it is directly observed, whereas true energy depends on the nature of the event (ER or NR) and must be inferred. The ER and NR discrimination band was measured using calibration data as shown

in figure 2.4 is reproduced in 2.12. The blue and red bands represent the 10% to 90% confidence bounds of events being ER and NR type, respectively. The ER band was measured using a tritium calibration source ( $\beta^-$ ) and the NR band was measured with neutrons from AmBe and  $^{252}\text{Cf}$  along with NEST simulations [62]. The ER/NR discrimination at 50% NR acceptance was measured to be  $99.6 \pm 0.1\%$ . This value serves as a measure of background rejection, which is ultimately treated with a profile likelihood method on an event-by-event basis. Both the S1 and S2 signal have been corrected for spatial dependence, as discussed in further detail in Chapter 3.

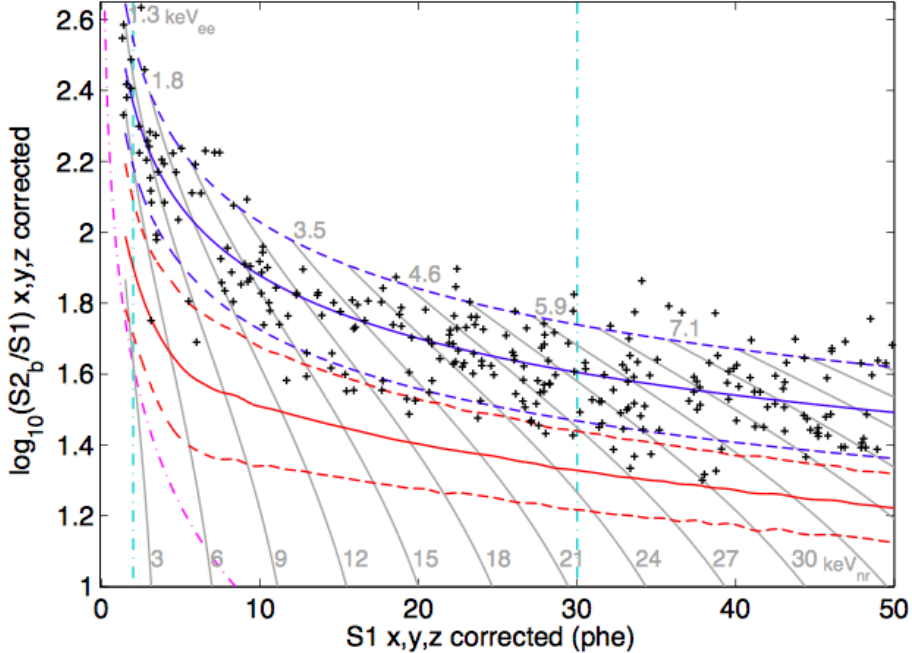


Figure 2.12: The remaining events passing the quality cuts listed in table 2.3. The charge to light ratio ( $S_2/S_1$ ) is plotted vs.  $S_1$  (proportional to energy) to show the separation of ER and NR type events. The 10-90% CF limits of the ER and NR band are plotted as the dashed blue and red curves, respectively. The band means are solid.  $S_{2b}$  stands for the  $S_2$  signal on the bottom PMT array.

All 160 remaining events in the fiducial volume are consistent with being ER type events. The main source of background events include residual  $^{85}\text{Kr}$ , activated  $^{127}\text{Xe}$  and  $^{214}\text{Pb}$  from  $^{222}\text{Rn}$ , described in further detail in [6]. The residual ER background rate in the WIMP region of interest as found to be  $3.6 \pm 0.3$  mDRU ( $10^{-3}$  cnts/keVee/kg/day) with an expectation of  $2.6 \pm 0.2_{\text{stat}} \pm 0.4_{\text{sys}}$  mDRU.

A profile likelihood test is conducted on all WIMP search candidates remaining after the cuts listed in table 2.3. The signal model is derived from AmBe and  $^{252}\text{Cf}$  neutron calibrations. The background rates input into the profile likelihood

were independently measured and modeled with LUXSIM using NEST, described in further detail in [6] [7] [62]. The WIMP signal model was generated using an isothermal halo with a Maxwellian distribution, with a local WIMP density of 0.3 GeV/cm<sup>3</sup> (as discussed in section 1.3). The galactic escape velocity input into the model is 544 km/s (cutting off the high end of WIMP velocity distribution), with an average WIMP velocity of 220 km/s. The earth’s seasonal velocity being 245 km/s with respect to the galactic center. The result from the 2013 science run with the LUX detector is consistent with a P value of 0.35 for the background-only hypothesis. The 90% upper C.L. cross section for various spin independent masses are shown in figure 2.13. The minimum cross section reported occurs at  $7.6 \times 10^{-46}$  cm<sup>2</sup> for a WIMP mass of 33 GeV/c<sup>2</sup> [7]. The LUX result is a factor of two improvement in WIMP cross section sensitivity over the Xenon100 limit reported in 2012 [35] and is in tension with reported WIMP signal claims from CoGent [41], CDMSLite (Silicon) [64], CRESST II [65] and DAMA/LIBRA [66].

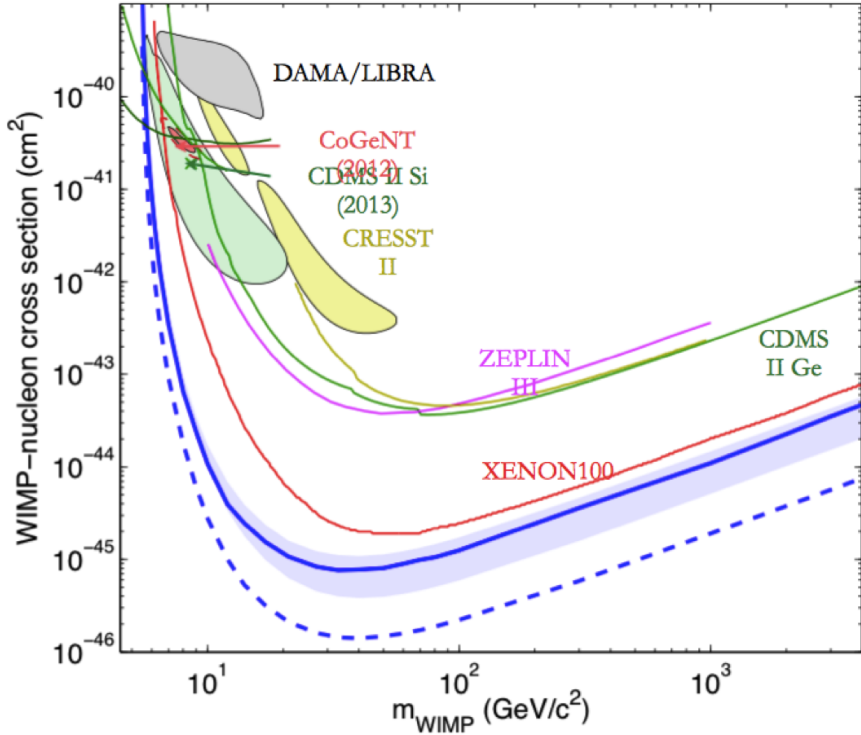


Figure 2.13: LUX detector is consistent with a P value of 0.35 of the background only hypothesis. The 90% upper C.L. cross section for various spin independent masses are shown in figure 2.13 in blue. Also shows are limits from Xenon100 (red), CDMS II (green), ZEPLIN III (magenta), and one sigma signal claimed for DAMA/LIBRA (shaded grey), CDMS II Silicon (shaded green), CRESST II (shaded yellow).

As mentioned above the ER band is measured with a tritium calibration source and will be discussed in further detail in chapter 7. Since the initial science run we have gathered twenty times the tritium statistics to further study the ER band, with over 140,000 tritium events in the fiducial volume. We also spent several months calibrating the LUX detector with a DD neutron generator to further study the NR band mean. The results from the improved ER calibrations will be reported here

and will be used for a reanalysis of the LUX WIMP search data. The result will be submitted for publication in late 2014.

## Chapter 3: Corrections to the S1 and S2 signals

In this chapter we address the spatially-dependent corrections applied to the S1 and S2 signals. During the 2013 science run,  $^{83\text{m}}\text{Kr}$  injections were performed periodically to measure the position-dependent corrections. The better we can correct the S1 and S2 signals for position-dependence, the smaller the signal variations will be, leading to better background rejection for the WIMP search.

The dominant correction is typically made on the S2 signal, considering the free electron lifetime. As charge drifts from the event site to the extraction region (0-47 cm), it may become attached to electronegative impurities in the liquid. S2s of equal sizes are exponentially attenuated with increasing drift distance in the detector by impurities such as O<sub>2</sub>, H<sub>2</sub>O, N<sub>2</sub> (3 ppb O<sub>2</sub> corresponds to roughly 100  $\mu\text{s}$  lifetime [67]). The S2 signal also has x and y variations due to non-uniformities in the extraction field, tilt in the liquid level, and non-uniformities in the anode-gate separation.

Unlike the charge signal, the S1 light propagates isotropically from the interaction site and has about a 30% variation in light collection efficiency between events near the top and bottom of the detector due to geometric effects. For events in the bulk liquid xenon, about 2/3 of the S1 light is collected on the bottom PMT arrays

due to total internal reflection at the liquid gas interface. The closer the event to the bottom PMTs, the larger the solid angle of the bottom PMT array, increasing the probability of the detecting a photon and producing a photo electron (PE). Other position-dependent effects include the photon absorption length, which is negligible at the purities achieved in LUX, and Teflon reflectivity which is  $> 90\%$  in liquid xenon [68] [69]. The S1 position-dependent correction used in the LUX analysis normalizes the photon detection probability of all events to the center of the active region, an arbitrary choice corresponding roughly to the average light response.

It should also be noted that variation in light yield and charge yield due to the non-uniformity of the electric field are also folded into x,y,z correction. The field increases from about 140 to 200 V/cm from the cathode to gate in the LUX detector, the electric field model is shown in Figure 2.5. The effect of light yield and charge yield for  $^{83m}\text{Kr}$  due to dependence of recombination on the local electric field is on the order of 10% [62]. Also, all S1 and S2 signals are measured as photo electrons (PE) that have been calibrated by pulsing LEDs (450 ns) located inside the TPC. Any quantum efficiency (QE) or gain variations in the 122 PMTs which are not properly normalized by the individual gain corrections are also folded into the position-dependent corrections measured from the  $^{83m}\text{Kr}$  calibrations.

### 3.1 $^{83m}\text{Kr}$ Calibration

Throughout the science run, periodic  $^{83m}\text{Kr}$  injections were performed to calculate position-dependent corrections.  $^{83m}\text{Kr}$  is produced from the  $\beta$  decay  $^{83}\text{Rb}$  with a

half life of 86.2 days. The  $^{83}\text{Rb}$  source is housed in charcoal and plumbed directly into the LUX circulation system. The decay scheme of  $^{83}\text{Rb}$  and  $^{83\text{m}}\text{Kr}$  is shown in figure 3.1.

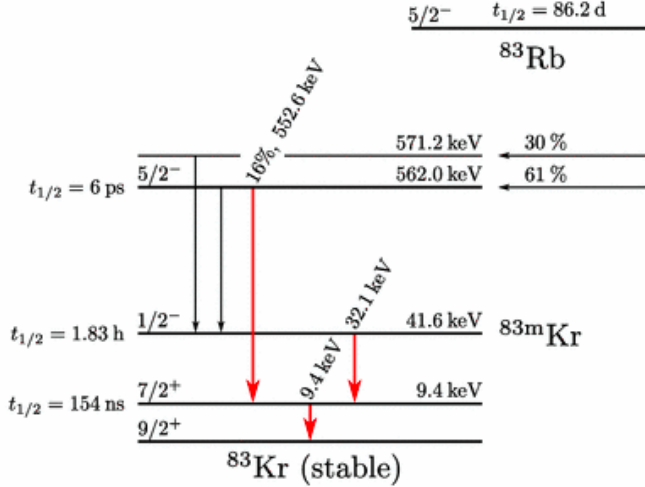


Figure 3.1: A simplified decay diagram of  $^{83}\text{Rb}$  and  $^{83\text{m}}\text{Kr}$ , from [10].

$^{83\text{m}}\text{Kr}$  which is continuously produced in the charcoal housing, is a meta-stable excited state of  $^{83}\text{Kr}$ . It has a half-life 1.8 hours.  $^{83\text{m}}\text{Kr}$  decays via an electron capture first emitting a 32.1 keV  $\beta$  followed by a 9.4 keV  $\beta$  with a half life of 154 ns for the intermediate state [70] [12]. For the vast majority of the decays, LUX observes the combined S1 pulse corresponding to 41.55 keV, since the minimum S1 pulse separation in the LUX reconstruction is 1000 ns. Figure 3.2 (a) and (b) shows two  $^{83\text{m}}\text{Kr}$  events with the decay of the 32.1 and 9.4 keV  $\beta$  separated by 60 and 220 ns, respectively. The two S1s are classified as a single S1 event by LUX in both cases. The timing separation between the S1 and S2 is used to infer the drift distance to be 14.0 and 40.0 cm below the liquid surface, respectively. The attenuation of the S2 signal due to electronegative impurities is apparent by comparing the amplitudes

of the S2 signals, with roughly 50% charge loss. The S2 pulses are insensitive to the timing separation of the dual decay as electron diffusion smears the charge deposits together as the electrons drift through the active region before extraction [63]. The PMT hit map for the events is shown in figure 3.3.

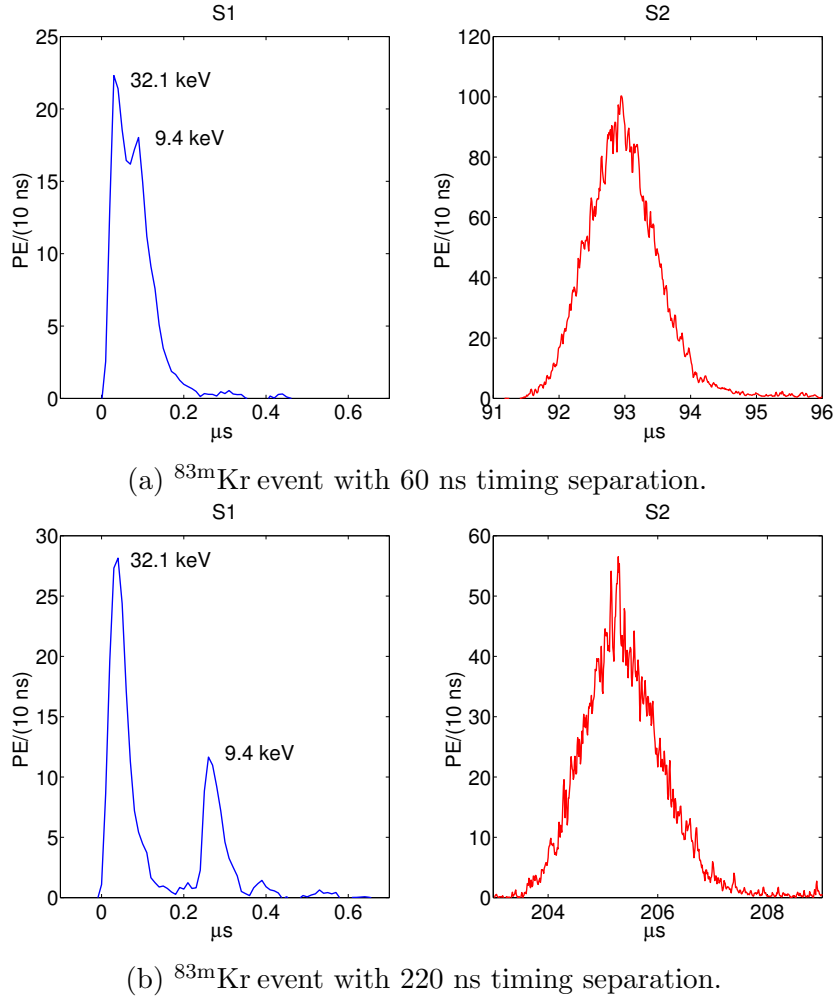
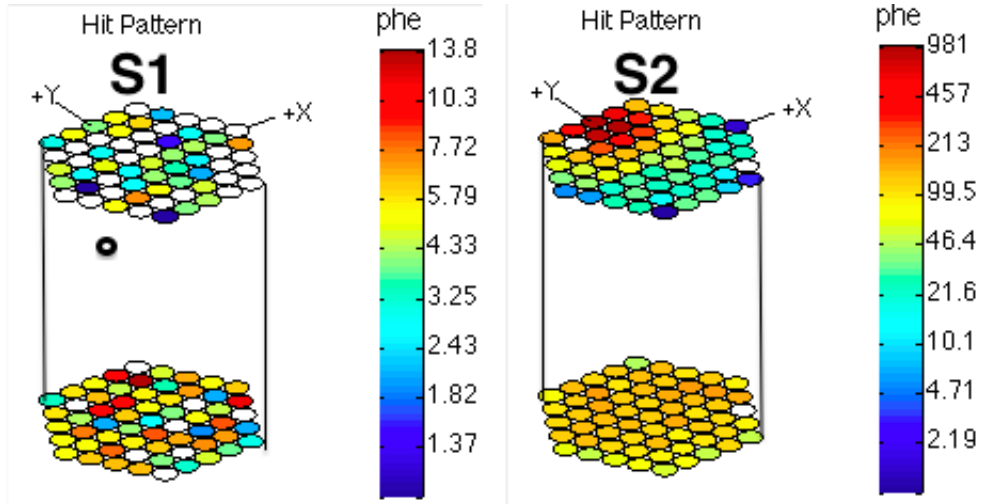
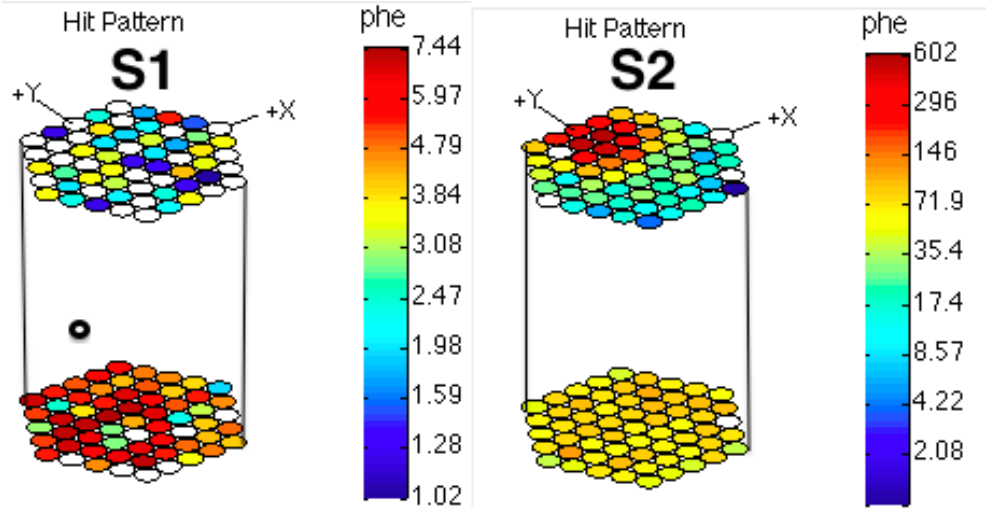


Figure 3.2: The S1 and S2 of two  $^{83\text{m}}\text{Kr}$  events. (a): A  $^{83\text{m}}\text{Kr}$  event in which the two decays have overlapped within 60 ns. The S2 arrives about 93  $\mu\text{s}$  later. Bottom Figures (b): A  $^{83\text{m}}\text{Kr}$  event in which the two decays have overlapped within 220 ns. The S2 arrives about 205  $\mu\text{s}$  later. The LUX pulse finder classifies events within a 1  $\mu\text{s}$  window as a single S1. The S2 pulses are insensitive to the timing separation of the dual decay as electron diffusion smears the pulses two together as the electrons drift. The PMT hit map for these events are shown below in figure 3.3.



(a)  $^{83\text{m}}\text{Kr}$  event with 60 ns timing separation.



(b)  $^{83\text{m}}\text{Kr}$  event with 220 ns timing separation.

Figure 3.3: The S1 and S2 of two  $^{83\text{m}}\text{Kr}$  events. Top Figures (a): A  $^{83\text{m}}\text{Kr}$  event in which the two decays have overlapped within 60 ns. Bottom Figures (b): A  $^{83\text{m}}\text{Kr}$  event in which the two decays have overlapped within 220 ns. The black, open circle represents the location of the event. The S1 hit pattern is diffuse with more light collected on the bottom arrays due to total internal reflection at the liquid surface. The S2 is localized in the top PMT arrays in x,y at the location where the electrons are extracted, and diffuse on the bottom due to scattering. The summed waveforms for these events are shown in figure 3.2.

### 3.2 $^{83m}\text{Kr}$ Mixing in Liquid Xenon

$^{83m}\text{Kr}$  is introduced when needed into the LUX detector by flushing the charcoal housing with xenon gas and diverting the flow inline with the main circulation path. The  $^{83m}\text{Kr}$  source and its delivery into the xenon detector is described in more detail in [12]. The relatively short half-life of 1.8 hours allows for several injections per week, as the source decays to negligible levels within hours. Once injected, the activity is uniformly mixed into the liquid xenon within minutes. Figure 3.4 shows the uniform distribution of  $^{83m}\text{Kr}$  events in the LUX detector thirty minutes after the injection. Once uniformly mixed, the decay of  $^{83m}\text{Kr}$  produces a well defined mono-energetic peak in the detector. The S1, S2, and energy spectra are shown in section 4.5. Measuring the location of the spectral peak vs. event position allows the detector's spatial response to be monitored over the course of the science run.

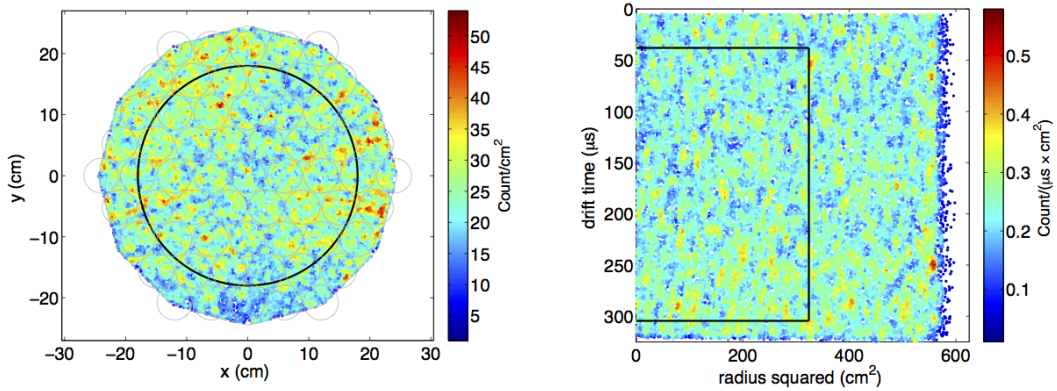


Figure 3.4: Distribution of  $^{83\text{m}}\text{Kr}$  events 10 minutes after the injection. The source mixes uniformly throughout the liquid xenon illuminating all regions of the active volume. The solid black lines represent the fiducial volume used for the WIMP search.

### 3.3 S2 Electron Lifetime and x,y Correction

As mentioned previously, events in LUX have well-defined x,y,z positions computed from the S2 hit pattern (x,y) and the S1-S2 signal separation time (z). The electron lifetime is calculated by binning the detector in drift time into 60 slices. In each slice a Gaussian is fit to the  $^{83\text{m}}\text{Kr}$  S2 signal to determine the mean. An exponential is fit to the mean S2 response as a function of z, shown in figure 3.5. The characteristic attenuation length is  $\lambda = \tau v_{drift}$ , where  $v_{drift}$  is the electron drift velocity and  $\tau$  is the electron lifetime from the exponential fit. For this analysis we use the S2 response of the bottom PMT array ( $S2_b$ ) as it was used for the 2013 WIMP search analysis discussed in Chapter 2.

To remove the effect of the finite electron lifetime, the z-corrected  $S2_b$  from

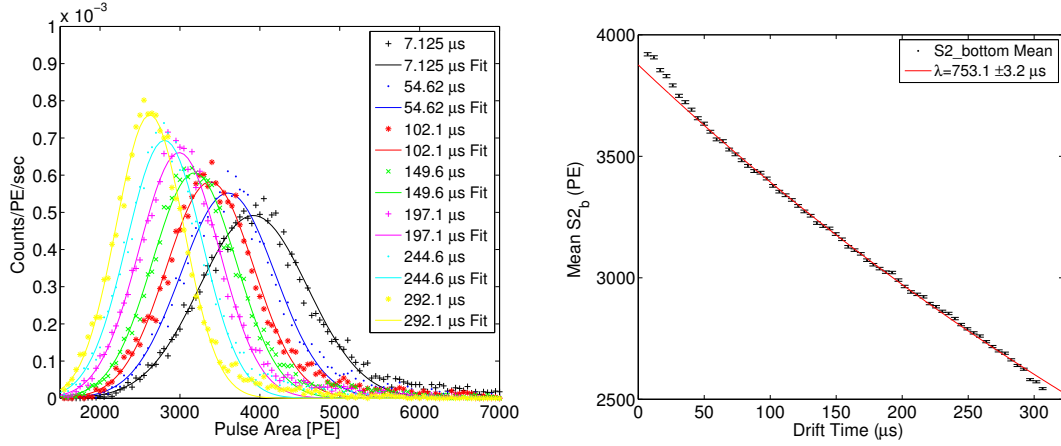


Figure 3.5: Left: Fits to the mean of  $S2_b$  of the  $^{83m}\text{Kr}$  data in several  $z$  slices. Right, the exponential fit to the means of  $S2_b$  vs. drift time used to extract electron lifetime  $\tau$ . The electron lifetime is found to be  $\tau = 753.1 \pm 3.2 \mu\text{s}$ . The exponential fit to the means deviates near the top and bottom of the active region since the charge yield from the  $^{83m}\text{Kr}$  decay is sensitive to the varying electric field. The data shown was taken on May 10, 2013 (lux10\_20130510\_T1250) and contains 700,000  $^{83m}\text{Kr}$  events.

each signal is calculated as follows:

$$S2_{b-z} = S2_b \cdot \exp\left(\frac{\text{drift time}[\mu\text{s}]}{\tau[\mu\text{s}]}\right) \quad (3.1)$$

Where  $S2_{b-z}$  is the  $z$  corrected  $S2_b$  signal and  $\tau$  is the free electron lifetime. After correcting the dominant  $z$  dependent electron attenuation, corrected to 0 drift time, we calculate the normalization factor ( $\mathcal{N}\mathcal{F}$ ) that will be used to correct for the  $x,y$  dependent variations in the  $S2$  signal.

The normalization is calculated by creating a 25 x 25 grid on the  $x-y$  plane, corresponding to 2 cm x 2 cm  $x,y$  bins. For each bin the average  $S2_b$  light response is determined by fitting a Gaussian. Figure 3.6 (left) shows the measured  $S2_b$  response to 700,000  $^{83m}\text{Kr}$  decays normalized to the response at the center,  $x=y=0$ . This map represents the inverse of the normalization factor that we call  $\mathcal{N}\mathcal{F}(x, y)$ .  $\mathcal{N}\mathcal{F}$  is then applied to the  $S2_b$  data by using a spline interpolation of the  $x,y$  coordinate

of each event relative to the bin centers  $\mathcal{N}\mathcal{F}(x, y)$ . Figure 3.6 (right) shows the  $S_{2b}$  response after correcting the data relative to the center  $x=y=0$  using  $\mathcal{N}\mathcal{F}(x, y)$ . After applying the  $x, y$  correction the variation decreases from 10% to 1% in the inner 18 cm radius of the detector (the fiducial volume).

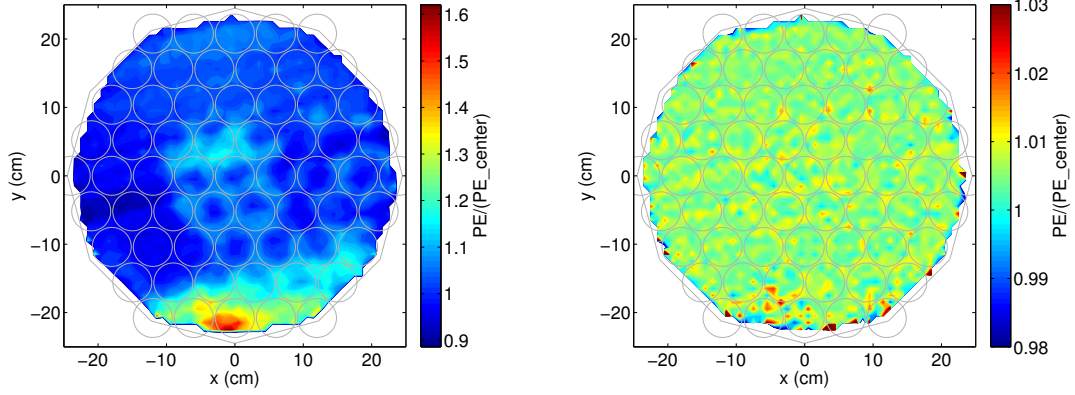


Figure 3.6: Left: Response of  $S_{2b}$  vs.  $x, y$  normalized to the response at the center ( $x=y=0$ ). The region of larger response around  $x=0, y=-25$  is likely from an enhanced extraction field between the anode and gate wires. Right: Response of  $S_{2b}$  vs.  $x, y$  after correcting the data using  $\mathcal{N}\mathcal{F}_{S_{2b}}$ .

After correcting for  $z$  and  $x, y$  we can define the position-dependent  $(x, y, z)$  corrected  $S_{2b}$  signal, which we will call  $S_{2b-c}$  calculated as follows:

$$S_{2b-c} = S_{2b-z} \cdot \mathcal{N}\mathcal{F}_{S_{2b}}(x, y) \quad (3.2)$$

where  $S_{2b-c}$  is the  $x, y, z$  corrected  $S_{2b}$  signal and  $\mathcal{N}\mathcal{F}_{S_{2b}}(x, y)$  is the Normalization Factor of the bottom PMT array for S2s and is a function of  $x, y$ . The interpolation of the inverse of  $\mathcal{N}\mathcal{F}_{S_{2b}}(x, y)$  along the  $x, y$  grid is plotted in figure 3.6.

Figure 3.7 shows the improvement in the  $S_{2b}$  signal after applying the  $z$  and  $x, y$  correction. After applying the  $z$  correction to  $S_{2b}$  there is a fractional improvement

in resolution of 18%, for the case of an  $750 \mu\text{s}$  electron lifetime. The correcting in the x,y plane provides an additional 4.9% improvement in resolution to the  $\text{S2}_b$  signal.

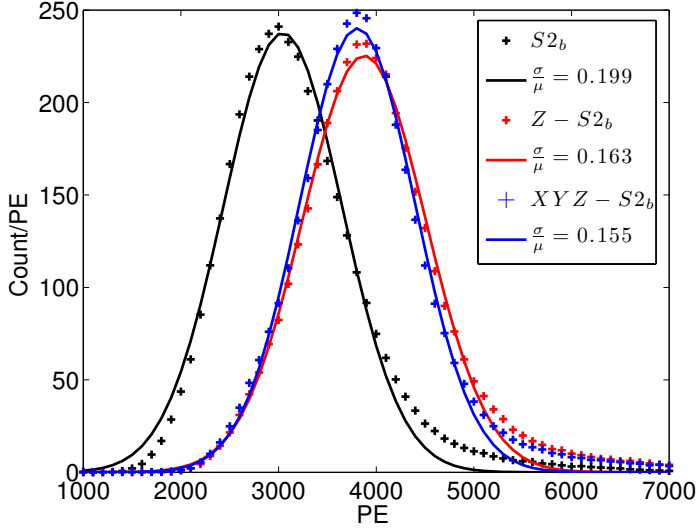


Figure 3.7: Improvement of resolution in  $\text{S2}_b$  after applying the z and x,y,z correction. Black: The uncorrected data. Red: The data with only z dependent correction, the electron lifetime correction. Blue: The data with full x,y,z dependent correction. The data shown was taken data on May 10, 2013 (lux10\_20130510\_T1250) and contains 700,000  $^{83\text{m}}\text{Kr}$  events.

### 3.4 S1 x,y,z Correction

To measure the x,y,z dependent Normalization Factor for S1 ( $\mathcal{N}\mathcal{F}_{\text{S1}}$ ), we divide the detector into a  $25 \times 25 \times 16$  x,y,z mesh with each voxel having dimensions of  $2 \text{ cm} \times 2 \text{ cm} \times 20 \mu\text{s}$ . To achieve sufficient statistics for the correction we require at least 400,000  $^{83\text{m}}\text{Kr}$  events, about 40 events per voxel to define the mean. Monthly high stats calibrations are performed that yield about 1 million counts to providing precise  $\mathcal{N}\mathcal{F}$  correction maps. Unlike the S2 correction, which is highly dependent

on purity, the S1 has been found to be invariant to within a percent over the course of the science run, thus the monthly calibrations with high statistics are sufficient to provide the position-dependent correction.

Figure 3.10 shows the response of the detector to  $^{83m}\text{Kr}$  normalized to the center of the detector in 16 slices of z, each with a 2 cm x 2 cm x,y grid. The plotted maps and normalized to the center of the detector and represent the inverse of the normalization factor ( $\mathcal{N}\mathcal{F}_{S1}$ ). We choose to normalize the the center of the detector as it represents the average light collection efficiency of the detector. Though the dominant correction is the z-dependence, there is also substructure in x,y to each z slice which is illustrated in figure 3.9, where we have normalized each slice to its own center. It is evident that near the top and bottom there are additional geometric effects around the radial edges, whereas in the central z slices the uniformity in x,y is much better due to the diffusion of the light scattering on the Teflon.

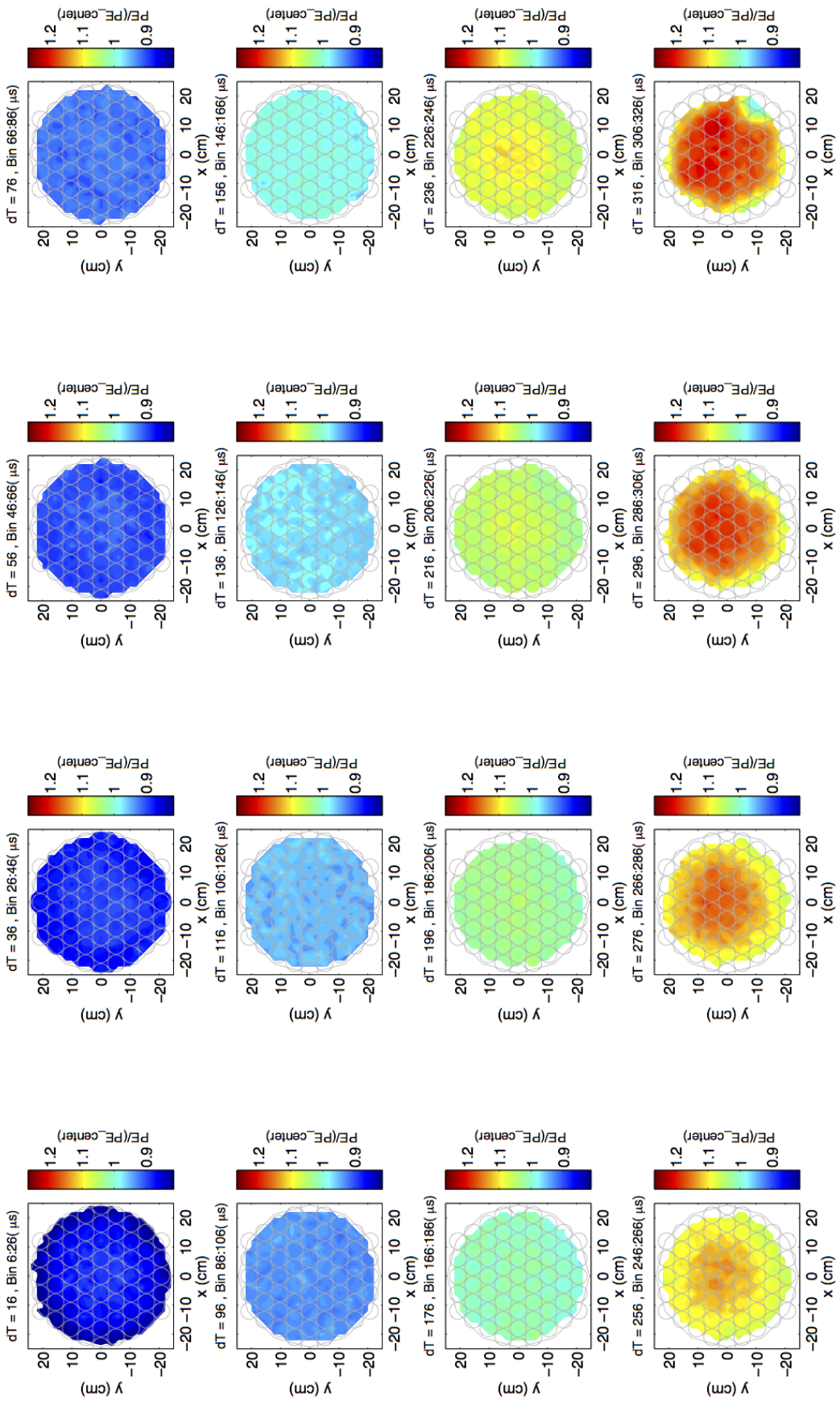


Figure 3.8: S1 x,y,z response normalized to the center of the detector. The interpolated map represents the inverse of the normalization factor  $\mathcal{N}\mathcal{F}$ .

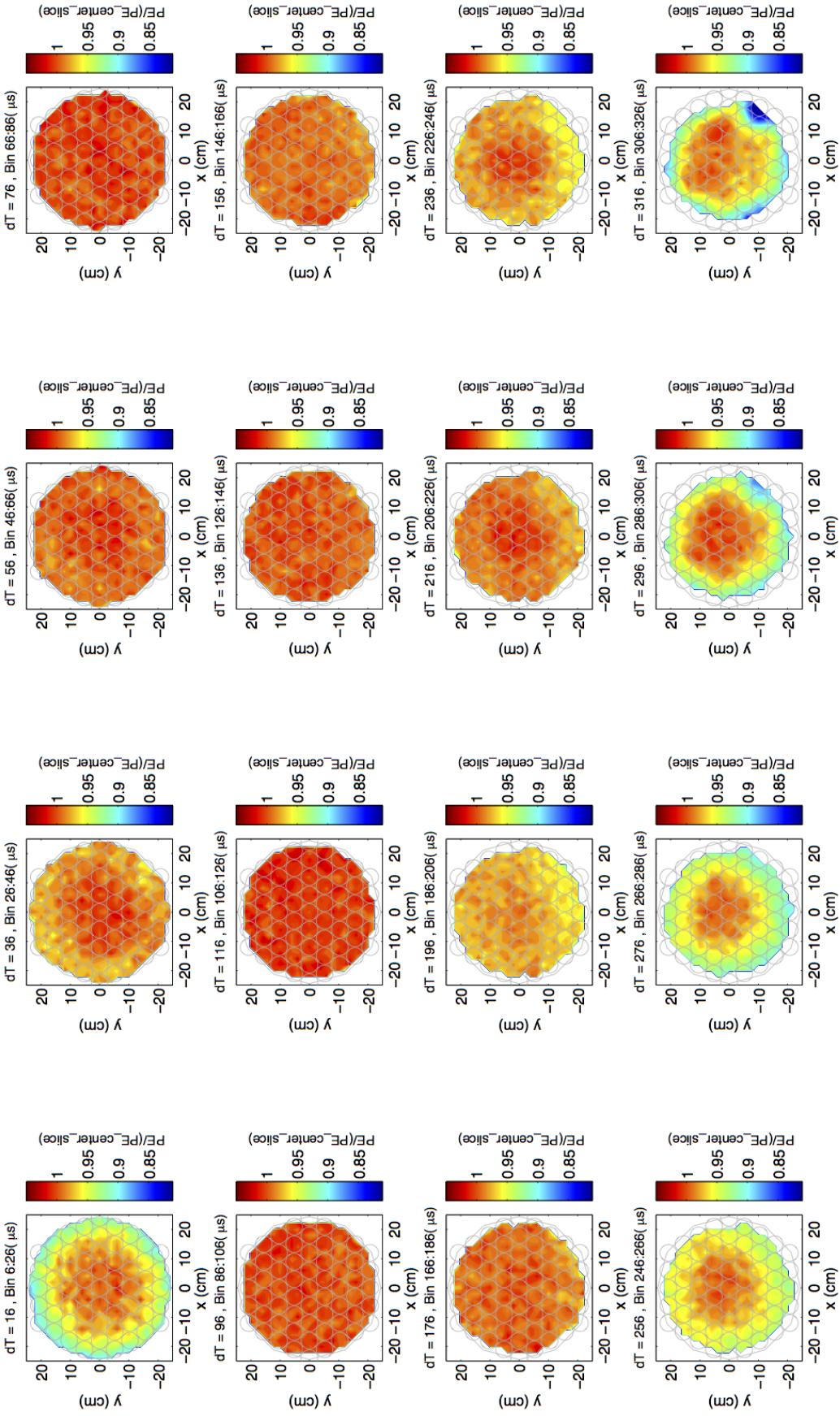


Figure 3.9: S1 x,y,z response normalized to the center of each z slice. There are greater variations near the very top and bottom 4 z slices as the solid angle for light hitting the PMT arrays increases. For the central slices the x,y response is uniform due to increased scattering off the Teflon panels.

We define the position-dependent ( $x,y,z$ ) corrected S1 signal as  $S1_c$ , normalized to the center of the detector ( $x=y=0$  and  $z=160\mu s$ ) calculated as follows:

$$S1_c = S1_{(x,z,y)} = S1 \cdot \mathcal{N}\mathcal{F}_{S1}(x, y, z) \quad (3.3)$$

where  $S1_c$  is the  $x,y,z$  corrected S1 signal and  $\mathcal{N}\mathcal{F}_{S1}(x, y, z)$  is the Normalization Factor of the sum of all PMTs for S1s and is a function of  $x,y,z$ . The interpolation of the inverse of  $\mathcal{N}\mathcal{F}_{S1}(x, y, z)$  along the  $x,y$  grid in  $z$  slices is plotted in figure 3.10. The normalization factor is applied to the S1 data by using a spline interpolation of the  $x,y,z$  coordinate of each event relative to the bin centers  $\mathcal{N}\mathcal{F}_{S1}(x, z, y)$ . Figure 3.10 shows the S1 response after correcting the data relative to the center of the detector. After applying the  $x,y,z$  correction the position-dependent variations decrease to less than 1% in the inner radial 18 cm of the detector (the fiducial volume), with as much as 3% variations near the top and bottom edges where the interpolation fails.

Figure 3.11 shows the improvement in the S1 signal after applying the  $z$  and  $x,y,z$  correction. With  $z$ -only correction to S1 there is a fractional improvement in resolution of 31.5%. The combined correction in  $z$  and the  $x,y$  plane provides an additional 2.0% improvement in resolution over the  $z$  only correction.

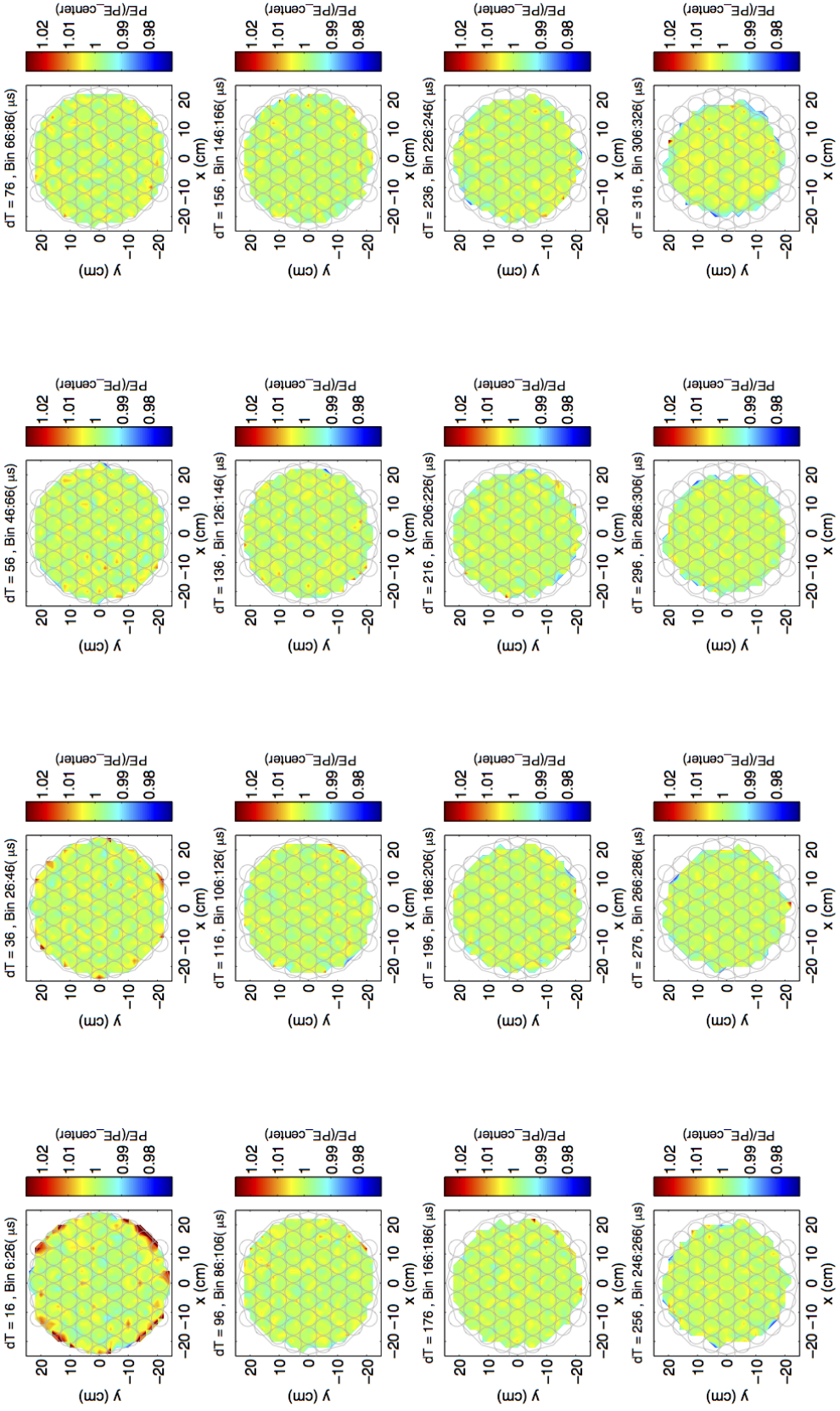


Figure 3.10: S1 x,y,z response normalized to the center of the detector after the data has been corrected and normalized to the detector center. The remaining variations in the fiducial volume ( $r < 18\text{cm}$ ) is less than 1%. Near the top and bottom edges the deviation increases to as much as 3% due to the interpolation of the correction becoming poorly constrained.

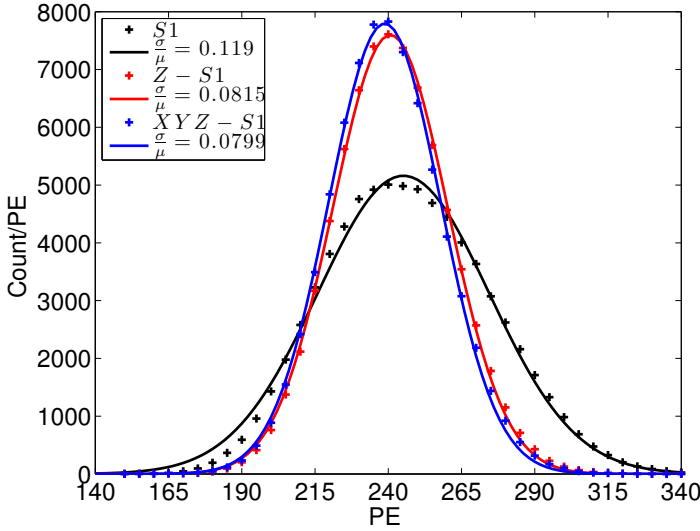


Figure 3.11: Improvement of resolution in S1 after applying the z and x,y,z correction. Black: The uncorrected data. Red: The data with only z dependent correction. Blue: The data with full x,y,z dependent correction. The data shown was taken data on May 10, 2013 (lux10\_20130510\_T1250) and contains 700,000  $^{83m}\text{Kr}$  events.

### 3.5 Application of x,y,z Corrections to the Data

As mentioned earlier, the purpose of the periodic  $^{83m}\text{Kr}$  calibrations is to measure the position-dependent S1 and S2 corrections over the course of the 2013 science run. Before processing the WIMP search data the calibration sets were processed and a MYSQL table of electron lifetimes and corrections maps were populated for each calibration date. The electron lifetime applied to each WIMP search data set was a linear interpolation between calibration dates shown in figure 3.12. The electron lifetimes measured for the science run are between 500 to 1000  $\mu\text{s}$ , or an attenuation length of 75 to 150 cm with a drift velocity of 1.51mm/ $\mu\text{s}$ . For the

S2 x,y correction the nearest  $\mathcal{N}\mathcal{F}_{S2}(x, y)$  entry in time was used. Combined these produced the corrected  $S2_c$  quantity to be used for the WIMP analysis. For the S1 x,y,z corrections, the nearest  $\mathcal{N}\mathcal{F}_{S1}(x, y, z)$  entry is used to produce the corrected  $S1_c$  quantity via a spline interpolation in x,y,z. For both the S2-x,y and S1-x,y,z correction the time dependence is assumed to be negligible as these are geometric effects, whereas the electron lifetime varies with liquid purity each day. The electron lifetime and the stability of the S1 correction over the course of the 2013 science run is shown in figure 3.12 and 3.13. While the electron lifetime needs frequent monitoring, the S1 x,y,z response is fixed over several months of running. For the results discussed in the subsequent sections of the thesis we will only work with the x,y,z corrected S1 and S2<sub>b</sub> pulses (  $S1_c$  and  $S2_{bc}$  respectively) .

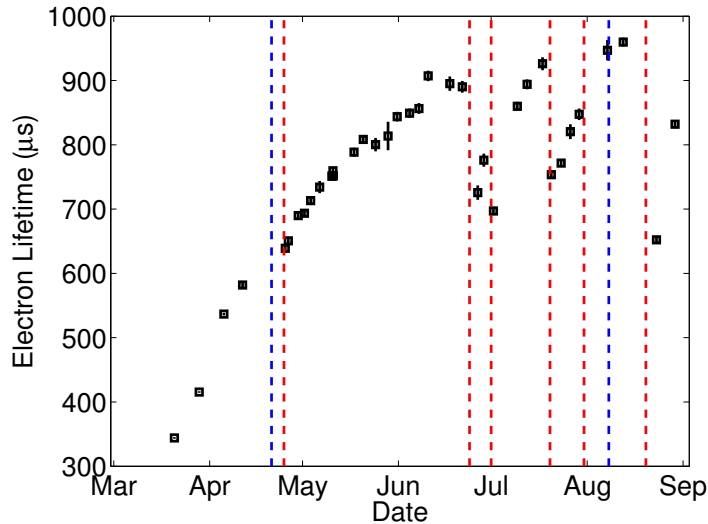


Figure 3.12: Electron lifetime measured using  $^{83m}\text{Kr}$  calibrations during the LUX science run in 2013. The blue dashed lines show the boundaries of the WIMP search from April 21 to Aug 8, 2013. The red dashed lines indicate circulation loss events.

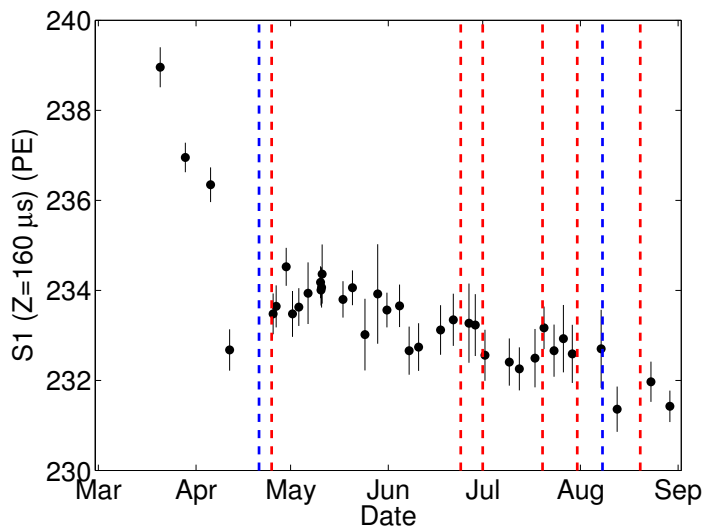


Figure 3.13: Measured response of to light from  $^{83\text{m}}\text{Kr}$  calibrations at the center of the LUX detector during of the LUX science run in 2013. The blue dashed lines show the boundaries of the WIMP search from April 21 to Aug 8, 2013. The red dashed lines indicate circulation loss events.

$^{83m}\text{Kr}$ Calibration Set lux10_YYYYMMDDThhmm	Number of $^{83m}\text{Kr}$ Events
lux10_20130320T1430	136,877
lux10_20130328T1437	444,622
lux10_20130405T1417	187,059
lux10_20130411T1524	99,724
lux10_20130425T1047	104,231
lux10_20130426T1019	92,024
lux10_20130429T1447	133,652
lux10_20130501T1508	91,465
lux10_20130503T1457	108,898
lux10_20130506T1328	45,678
lux10_20130510T1250	670,895
lux10_20130510T1607	499,743
lux10_20130510T2008	113,347
lux10_20130511T0014	44,372
lux10_20130517T1542	138,432
lux10_20130520T1504	216,709
lux10_20130524T1503	28,975
lux10_20130528T1546	11,569
lux10_20130531T1421	125,921
lux10_20130604T1421	110,219
lux10_20130607T1512	106,315
lux10_20130610T1518	116,349
lux10_20130617T1457	61,737
lux10_20130621T1533	78,707
lux10_20130626T1517	25,124
lux10_20130628T1444	44,134
lux10_20130701T1646	71,410
lux10_20130709T1009	106,230
lux10_20130712T1427	104,150
lux10_20130717T1424	66,801
lux10_20130720T1045	88,945
lux10_20130723T1452	88,626
lux10_20130726T1431	35,056
lux10_20130729T1004	59,906
lux10_20130807T1403	27,015
lux10_20130812T1546	113,560
lux10_20130823T0953	107,820
lux10_20130829T1005	479,676

Table 3.1:  $^{83m}\text{Kr}$  sets used to calculating corrections for the 2013 LUX WIMP search [7].

## Chapter 4: The Combined Energy Scale

The ratio of the charge (S2) to light (S1) signals provide the bases for identifying ER and NR events in the LUX detector. Once the recoil type is determined, the next step is to determine the energy deposited by the interaction. The energy from the interaction will go towards the productions of light (S1), charge (S2) and heat (not observed in LUX). The method is to combine the measured scintillation signals (S1 and S2) from multiple calibration sources and electric field values. The optimal combination of S1 and S2 are calibrated with sources with high energy relative to the WIMP search region of interest (1-10 keV<sub>ee</sub>). In order to validate the energy scale calibration down to the keV range we reconstruct the beta spectrum of a tritium calibration source. The energy scale calibration is also need to model background rejection from known backgrounds sources. The energy scale calibration also works in reverse for converting energy spectra into the observables S1 and S2.

### 4.1 Introduction

For a given energy deposit in liquid xenon the amount of quanta released is proportional to a work function  $W$ . For nuclear recoils we must also consider heat loss. For an electronic recoil (ER), the quanta created at the interaction site are the result

of electron-ion pairs and excitons produced by the recoiling electron. These quanta are observed as ionization and scintillation [51].

$$\begin{aligned} E &= W(n_i + n_{ex}) \\ E &= W(n_\gamma + n_e) \end{aligned} \quad (4.1)$$

where  $E$  is the energy of the deposition in keV,  $n_i$ ,  $n_{ex}$ ,  $n_\gamma$  and  $n_e$  are the number of ions, excitons, photons and electrons respectively. The work function ( $W$ ) for xenon has been measured to be  $13.7 \pm 0.2$  eV/quanta [11], as discussed in section 2.3.

Excitons quickly de-excite and contribute to the primary scintillation signal (S1). Ions that recombine with their electron pairs produce scintillation light (S1), while those electrons that do not recombine are collected several microseconds later in the extraction region as the larger secondary scintillation signal (S2).

There are two knobs to turn that change the recombination fraction and probe combined energy space over a variety of S1 and S2: the energy of the source and the drift field. The larger the variation in S1 and S2 that we probe, the more constrained the combined energy scale will be. Measuring both light and charge allows for a vastly improved energy resolution compared with using only S1 or S2 alone, since recombination fluctuations cancel out if energy is reconstructed correctly.

Using equation 4.1 and assuming that the heat loss is negligible for electronic recoils (ER), we can reconstruct energy by knowing the work function and the conversion from measured S1(light) and S2(charge) signals to the number of quanta ( $n_\gamma + n_e$ ) liberated by the interaction. We define gain-1 ( $g_1$ ) and gain-2 ( $g_2$ ) as the conversion from the average number of photons and electrons propagated from the

interaction site to the observed signal by the PMT arrays as photo electrons (PE), given in equation 5.2. Note, that for the value of S2 in this section we only use the signal on the bottom PMT array, S2<sub>b</sub>.

$$\begin{aligned}\langle n_\gamma \rangle &= \frac{\langle S1 \rangle}{g_1} \\ \langle n_e \rangle &= \frac{\langle S2 \rangle}{g_2}\end{aligned}\tag{4.2}$$

the combined energy of equation 4.1 can be written in terms of the observable S1 and S2 as

$$E = W \left( \frac{S1}{g_1} + \frac{S2}{g_2} \right)\tag{4.3}$$

By using multiple line sources with known energies we can extract a best fit for the value of the gains (g<sub>1</sub>, g<sub>2</sub>) by making a “Doke plot” [49] [59]. The line sources used for the purposes of the calibration are listed in table 4.1. For each calibration line we calculate the mean light yield and charge yield and fit a line, S1/E and S2/E respectively, (Equation 4.4).

$$\begin{aligned}S1/E &= \frac{n_\gamma}{(n_\gamma + n_e)} \times \frac{g_1}{W} \\ S2/E &= \frac{n_e}{(n_\gamma + n_e)} \times \frac{g_2}{W}\end{aligned}\tag{4.4}$$

Fitting the two equations in 4.4 to a line yields

$$\begin{aligned}\left( \frac{S1}{E} \right) &= \left( \frac{g_1}{W} \right) - \left( \frac{S2}{E} \right) \left( \frac{g_1}{g_2} \right) \\ y &= \frac{S1}{E}, x = \frac{S2}{E} \\ y &= m \cdot x + b\end{aligned}\tag{4.5}$$

The x and y intercepts from Equation 4.5 can be used to solve for g<sub>1</sub> and g<sub>2</sub>.

$$g_1 = \mathbf{b} \cdot \mathbf{W}$$

$$g_2 = \frac{g_1}{m} = \frac{\mathbf{b} \cdot \mathbf{W}}{m}$$
(4.6)

The values of  $g_1$  and  $g_2$  measured in this way highly correlated such that the ratio of  $g_1:g_2$  is constrained by the calibration data. However, a reduction in  $g_1$  can be compensated by an increase in  $g_2$  and still yield the same number of initial quanta and visa versa. Tightening the constraint requires calibration data over a wide range of S1 and S2 values near the intercept of the Doke plot (the x and y intercepts yield  $g_1$  and  $g_2$ ). Due to the strong correlation in the fit parameters the data is fit by minimizing the likelihood and the errors in intercept and slope are determined using MCMC (Markov Chain Monte Carlo).

Source	Energy [keV]	Decay Type	Data
Xe K shell	29.7, 34	X-ray	Early physics run (2013)
<sup>83m</sup> Kr	41.55**	Internal Conversion	Periodic internal calibration
<sup>131</sup> Xe	163.9	Internal Conversion	Early physics run (2013)
<sup>127</sup> Xe	203 or 375	$\gamma$ -emission	Early physics run (2013)
<sup>127</sup> Xe	33.8	Kb shell X-ray	Early physics run (2013)
<sup>127</sup> Xe	5.3	L shell X-ray	Early physics run (2013)
<sup>129m</sup> Xe	236.1	Internal Conversion	Early physics run (2013)
<sup>214</sup> Bi	609	$\gamma$ -emission	Background from Det. components
<sup>137</sup> Cs	661.6	$\gamma$ -emission	External calibration source

Table 4.1: Mono energetic peaks used for  $g_1$   $g_2$  calibration. \*\* <sup>83m</sup>Kr data was taken at 50 and 100 V/cm along with the standard field of 170 V/cm.

## 4.2 Charge vs. Light

The first step in calibrating the energy scale is to plot the observables S1 vs. S2. By doing this the anti-correlation between light and charge at a given energy becomes apparent, as shown in figure 4.1. Before fitting the data a fiducial cut was placed at a radius of less than 18 cm and drift distance between 6 and 46 cm which greatly reduces the background event rate. To extract  $g_1$  and  $g_2$  we first determine the average values of S1 and S2 at each known energy. Initially loose diagonal cuts are placed by eye on the populations, shown in figure 4.1. Next, using an un-binned maximum likelihood Gaussian fit the mean and sigma are estimated and then refit using  $\pm 1.5\sigma$  of the initial distribution to remove tails from backgrounds. The fit is performed on the S1 and S2 populations separately. Using the mean S1 and S2 of each line source, the gains  $g_1$  and  $g_2$  are determined by fitting the data to a line per equation 4.6. The resulting values of  $g_1$  and  $g_2$  are found to be  $0.096 \pm 0.009$  and  $5.94 \pm 1.68$  respectively. The fit is shown in figure 4.2. The values of  $g_1$  and  $g_2$  represent a best fit to the underlying recombination theory where for each additional photon there is a corresponding reduction of one electron and visa versa. The method for extracting the uncertainties using MCMC will be discussed later in section 4.4.

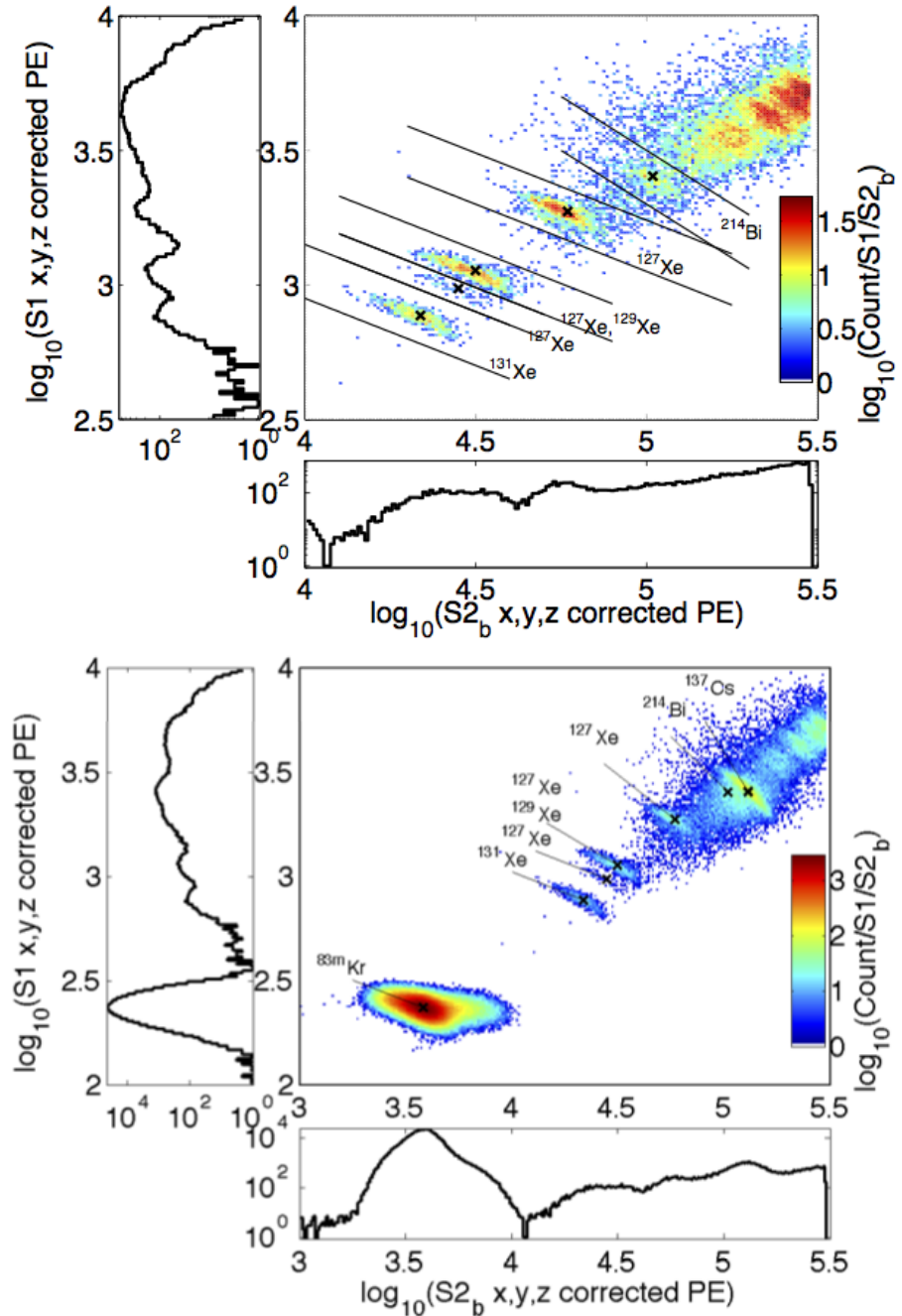


Figure 4.1: LUX calibration data in charge vs. light space (S1 vs. S2). Top figure, shows the xenon activation lines from early in the science run, the black lines indicating the initial cuts by eye used to isolate populations of constant energy. The bottom figure shows all of the data used to calibrate the energy scale, including the  $^{83m}\text{Kr}$  and  $^{137}\text{Cs}$  calibrations. The centroids found by an un-binned maximum likelihood analysis are shown as a black X, for the sources listed in table 4.1.

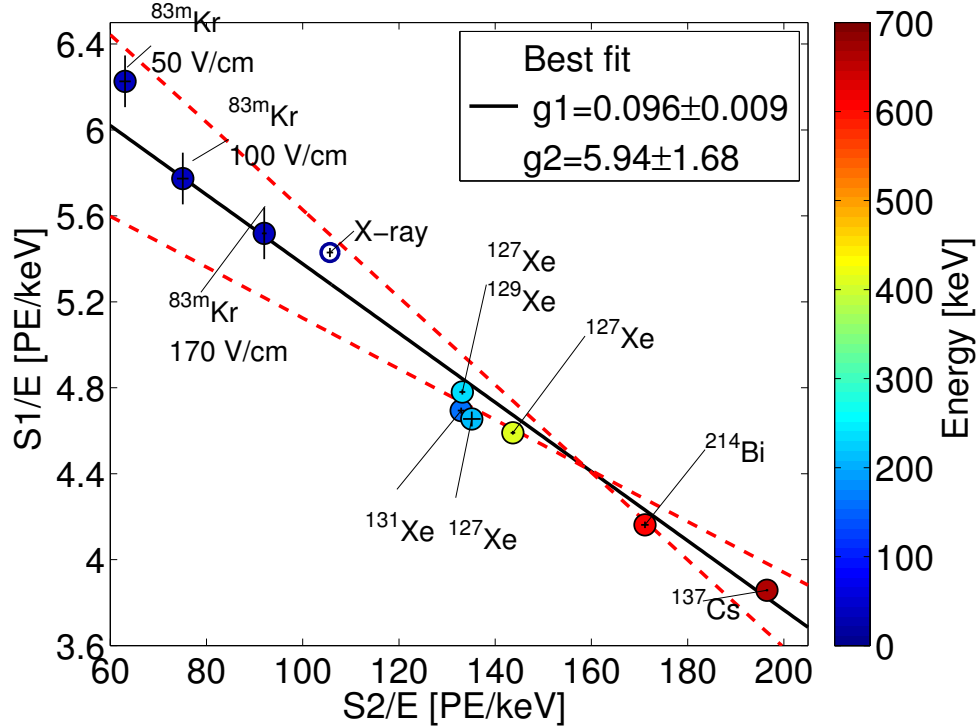


Figure 4.2: The Doke plot showing the mean values of  $S1/E$  vs  $S2/E$  for each calibration source. The data was cut by plotting the  $S2$  vs the  $S1$  and selecting the populations by eye, shown in figure 4.1. Using equation 4.6, the slope and intercept of the data constrain the parameters  $g_1$  and  $g_2$ . The black solid line represent the best fit to the data and the red dashed lines represent  $\pm 1\sigma$  of  $g_1$  and  $g_2$ . The open circle is data from the K-shell xenon X-ray and was not used for the fit as its absolute energy and origin from the skin of the detector is uncertain.

To better visualize the data on the Doke plot in figure 4.2 all events from the calibration sources were added on the Doke plot, shown in figure 4.3. The populations of the Xe activation lines and  $^{214}\text{Bi}$  were isolated by the cuts shown in figure 4.1. By plotting in this way the populations of each source can be seen moving along a line of constant quanta (photons + electrons), which corresponds to the best fit for  $g_1$  and  $g_2$ . The  $^{137}\text{Cs}$  is moved along the line of constant quanta by recombination fluctuations and the  $^{83m}\text{Kr}$  data is shifted as the different electric fields alter recombination probability. Note, recombination fluctuations will be discussed

in section 5.

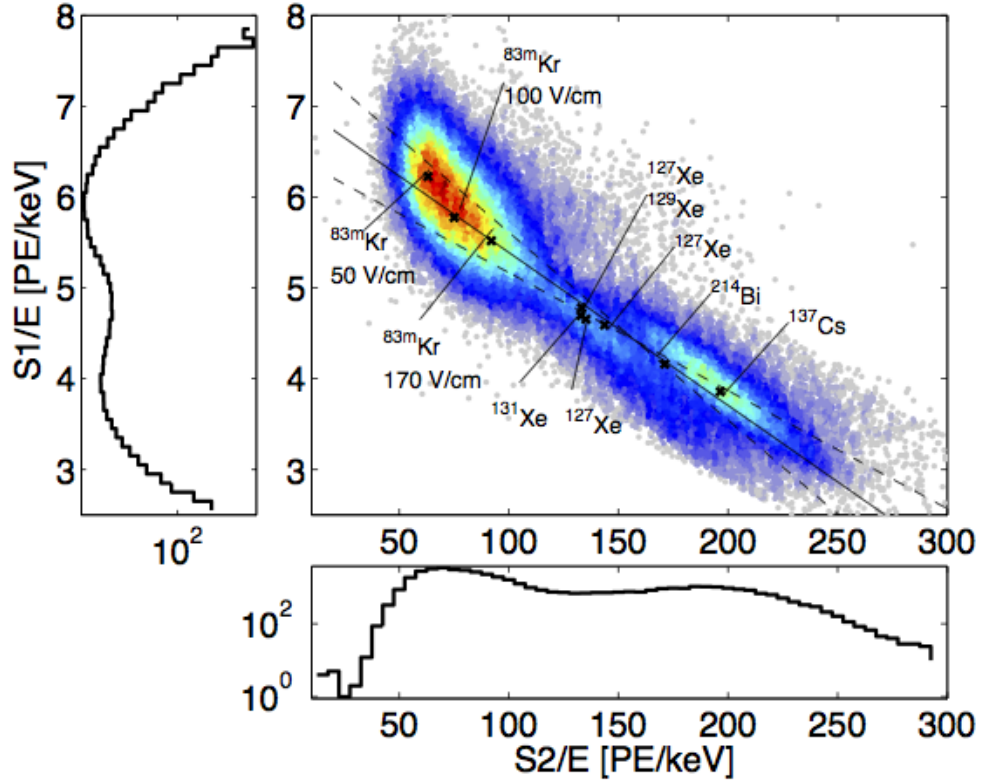


Figure 4.3: Doke plot with all events from the calibration sources, with their S1 and S2 signal normalized to its corresponding energy. The populations of the Xe activation lines and  $^{214}\text{Bi}$  were isolated by the cuts shown in figure 4.1. The solid black line represent the best fit to  $g_1$  and  $g_2$  and the dashed lines represents the  $1\sigma$  bounds.

### 4.3 Refitting in Combined Energy Space

This first result for  $g_1$  and  $g_2$ , shown in figure 4.2, is only a crude estimate derived from isolating the populations in S1 vs. S2 space. Once we have an initial estimate of gains  $g_1$  and  $g_2$ , a combined energy scale can be constructed with significantly improved resolution over the initial guess, due to the fact that recombination fluctuations are canceled. With the improved resolution the data are selected around their combined energy and fit using an un-binned maximum likelihood fit to a normal distribution. Then the data are refit around  $1.5\sigma$  of the mean. The fits used to extract the means and sigmas of the S1 and S2 signals at a given energy are shown in figures 4.5 and 4.6. The energy spectra are shown later in figure 4.9. The steps outlined are iterated twice as the convergence is rapid. In this case the initial value of  $g_1$  and  $g_2$  derived from cutting in S2 vs S1 space is already a close approximation to the true value. The resulting values of  $g_1$  and  $g_2$  are found to be  $0.097 \pm 0.008$  and  $5.75 \pm 1.4$  respectively. The fit is shown in figure 4.4. After refitting there is a significant improvement over figure 4.2, in terms of how well the data are described by the linear model of equation 4.6. This is especially notable for the the xenon activation lines in the center of the plot. Note, the error on  $g_2$  is large relative to  $g_1$  due to the greater separation of the calibration pints from the x intercept.

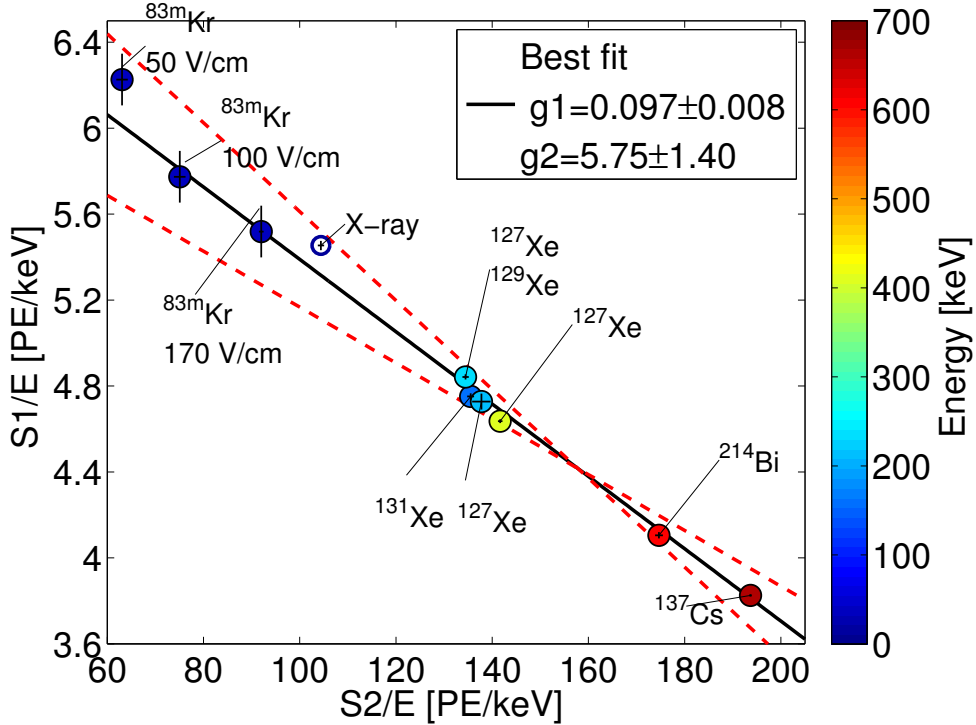


Figure 4.4: The Doke plot showing the mean values of  $S1/E$  vs  $S2/E$  for each calibration source. The data has been further cut upon the combined energy reconstructed from an initial best fit to the data. Using equation 4.6, the slope and intercept of the data constrain the parameters  $g_1$  and  $g_2$ . The black solid line represents the best fit to the data and the red dashed lines represent  $\pm 1\sigma$  of  $g_1$  and  $g_2$ . The open circle is data from the K-shell xenon X-ray and was not used for the fit as its absolute energy and origin from the skin of the detector is uncertain.

Figure 4.7 shows another representation of the idea behind equation 4.6. The combined energy model describes the data well using the optimal fit for  $g_1$  and  $g_2$ . For each increase in number of photons there is a corresponding equal decrease in the number of electrons and visa-versa. As stated before the values of  $g_1$  and  $g_2$  are highly anti-correlated because the data, relatively far from the x and y intercepts, constrains their ratio only. Thus, for future studies it will be important to probe more of the charge vs light parameter space in order to place a tighter constraint on gains  $g_1$  and  $g_2$ . This can be achieved by both modifying the electric field inside

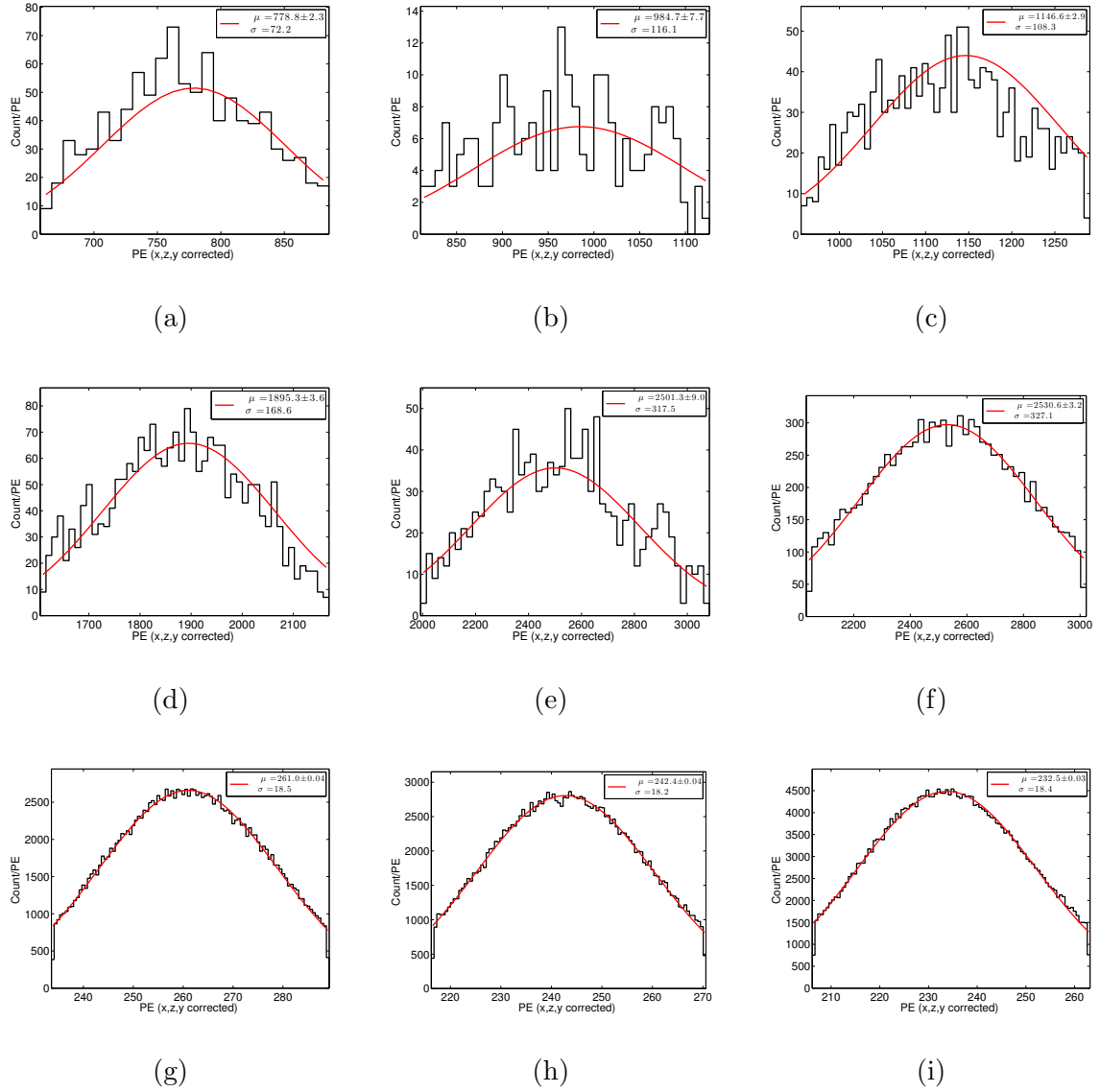


Figure 4.5: S1 fits to sources at nominal field of 170 V/cm unless otherwise noted.

Source and energy in keV from top left to bottom right: a)  $^{131}\text{Xe}$ : 163, b)  $^{127}\text{Xe}$ : 207, c)  $^{127}\text{Xe} \& ^{129\text{m}}\text{Xe}$ : 236.8, d)  $^{127}\text{Xe}$ : 410, e)  $^{214}\text{Bi}$ : 609, f)  $^{137}\text{Cs}$ : 661.6, g)  $^{83\text{m}}\text{Kr}$ : 41.5 - at 50 V/cm, h)  $^{83\text{m}}\text{Kr}$  41.5 - at 100 V/cm, i)  $^{83\text{m}}\text{Kr}$  41.5 .

the detector and by using more calibration sources.

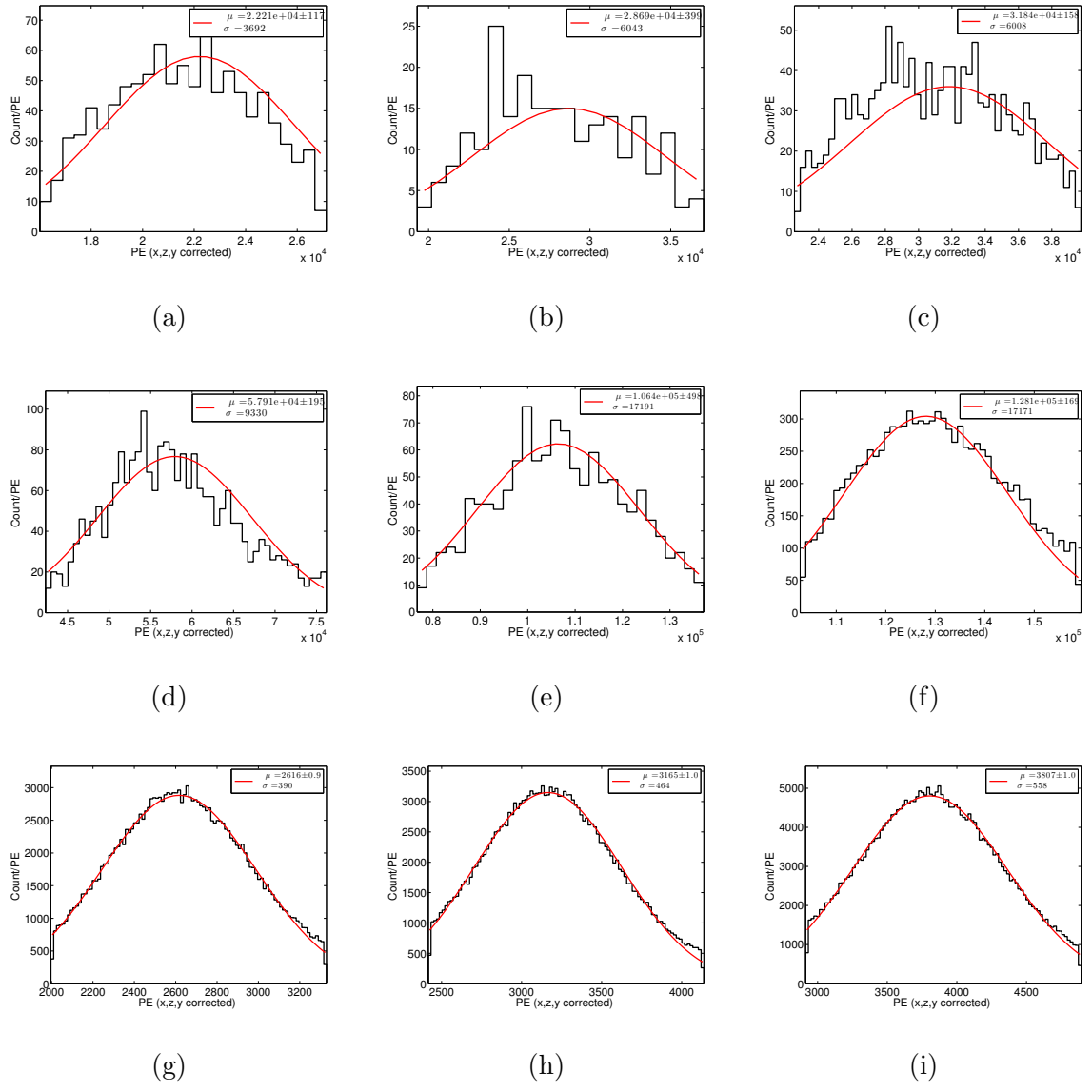


Figure 4.6: S2 fits to sources at nominal field of 170 V/cm unless otherwise noted.

Source and energy in keV from top left to bottom right: a)  $^{131}\text{Xe}$ : 163, b)  $^{127}\text{Xe}$ : 207, c)  $^{127}\text{Xe} \& ^{129\text{m}}\text{Xe}$ : 236.8, d)  $^{127}\text{Xe}$ : 410, e)  $^{214}\text{Bi}$ : 609, f)  $^{137}\text{Cs}$ : 661.6, g)  $^{83\text{m}}\text{Kr}$ : 41.5 - at 50 V/cm, h)  $^{83\text{m}}\text{Kr}$  41.5 - at 100 V/cm, i)  $^{83\text{m}}\text{Kr}$  41.5 .

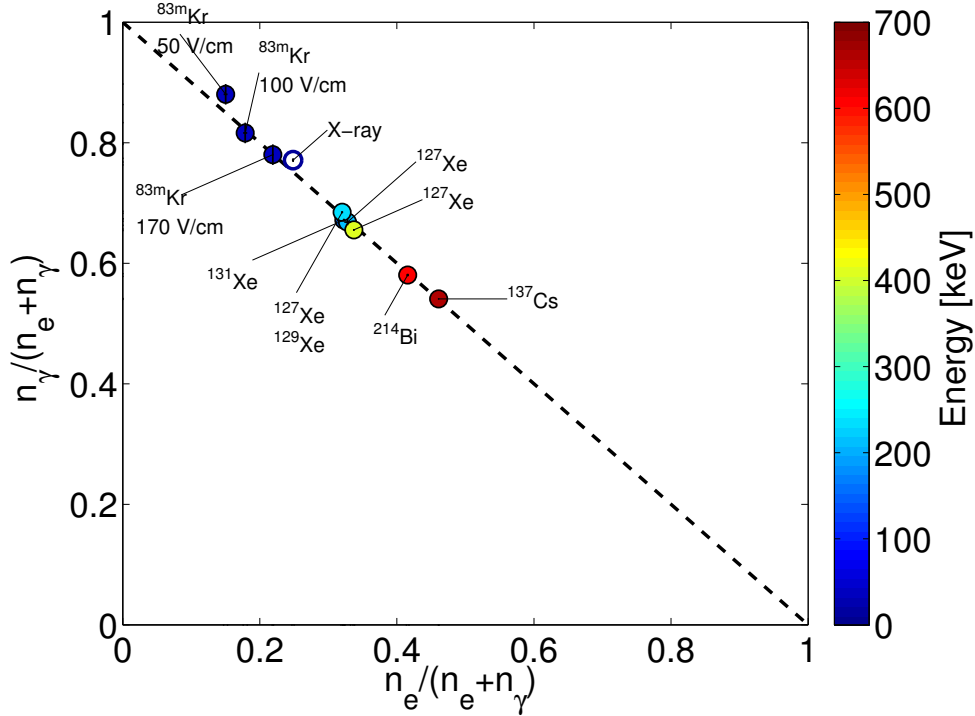


Figure 4.7: Doke plot of the data showing the light yield vs. charge yield. In this version of the plot, S2/E has been scaled by  $W/g_2$  so that the x-axis corresponds to the ratio of  $n_e$  to total quanta. Similarly S1/E has been scaled by  $W/g_1$  so that the y axis corresponds to the ratio of  $n_\gamma$  to total quanta. The black horizontal line represents moving along the line of constant quanta, for each additional photon an electron is lost as visa-vera.

#### 4.4 Error Determination of $g_1$ and $g_2$ with a Markov Chain Monte Carlo

The error bars reported in sections 4.2 and 4.2 on  $g_1$  and  $g_2$  are from the error in the slope and intercept of the linear fit in the Doke plot and are derived using a MCMC (Markov Chain Monte Carlo). For calculating the error in slope and intercept three

random walkers were used at each data point and allowed to take 500 steps. The MCMC takes into account the covariance of the parameters, shown in figure 4.8 as a two dimensional Gaussian. There is a strong negative correlation between the slope  $m$  and intercept  $b$  which is the result of the degeneracy between gains  $g_1$  and  $g_2$ . Thus, the error on  $g_1$  and  $g_2$  is such that for the positive maxima deviation in  $g_1$  we reach the negative maxima of the error on  $g_2$ , and visa-versa.

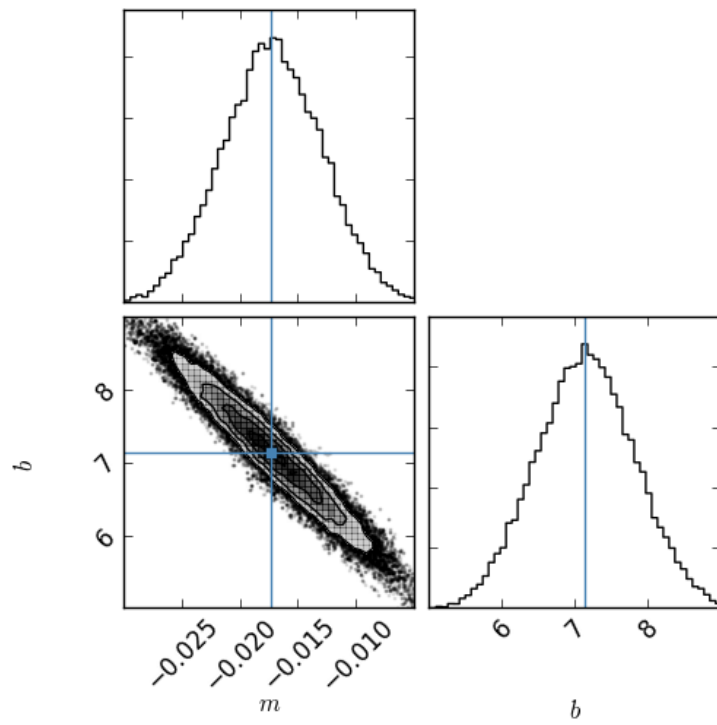


Figure 4.8: MCMC for the linear fit to the Doke plot. There is a strong negative correlation between the slope  $m$  and intercept  $b$  which results from the degeneracy between gains  $g_1$  and  $g_2$ .

## 4.5 Combined Energy Space

With the values of  $g_1$  and  $g_2$  known the combined energy of events can be reconstructed with a significant improvement over using only the light or charge channel. In combined energy space recombination fluctuations are removed by the anti correlation of light and charge production and any residual smearing is due to intrinsic detector resolution (discussed later in section 5) . Figure 4.9 shows the energy histograms of the data used for the fits to gains  $g_1$  and  $g_2$  including the xenon activation lines and the  $^{137}\text{Cs}$  calibration, along with a zoom-in of the xenon K shell Xray around 29-34 keV.

## 4.6 Light Collection and Electron extraction

The value of  $g_1$  represents the mean efficiency for collecting photons at the center of the LUX detector times the average quantum efficiency of the PMTs. The measured value of  $g_1 = 0.097 \pm 0.008$  implies a 9.7% probability of a photon propagated from the center of the detector, striking a PMT, and being converted into a photo electron (PE). The value of  $g_2$  represents the average number of PE collected for each electron that initiated secondary scintillation in the anode region. The value of  $g_2$  can be thought of as the average single electron size in PE times the extraction probability.

$$g_2 = \epsilon \times SE \quad (4.7)$$

where SE is the average S2 pulse area of a single electron and  $\epsilon$  is the extraction efficiency of electrons from the liquid-gas interface. The LUX detector has a low

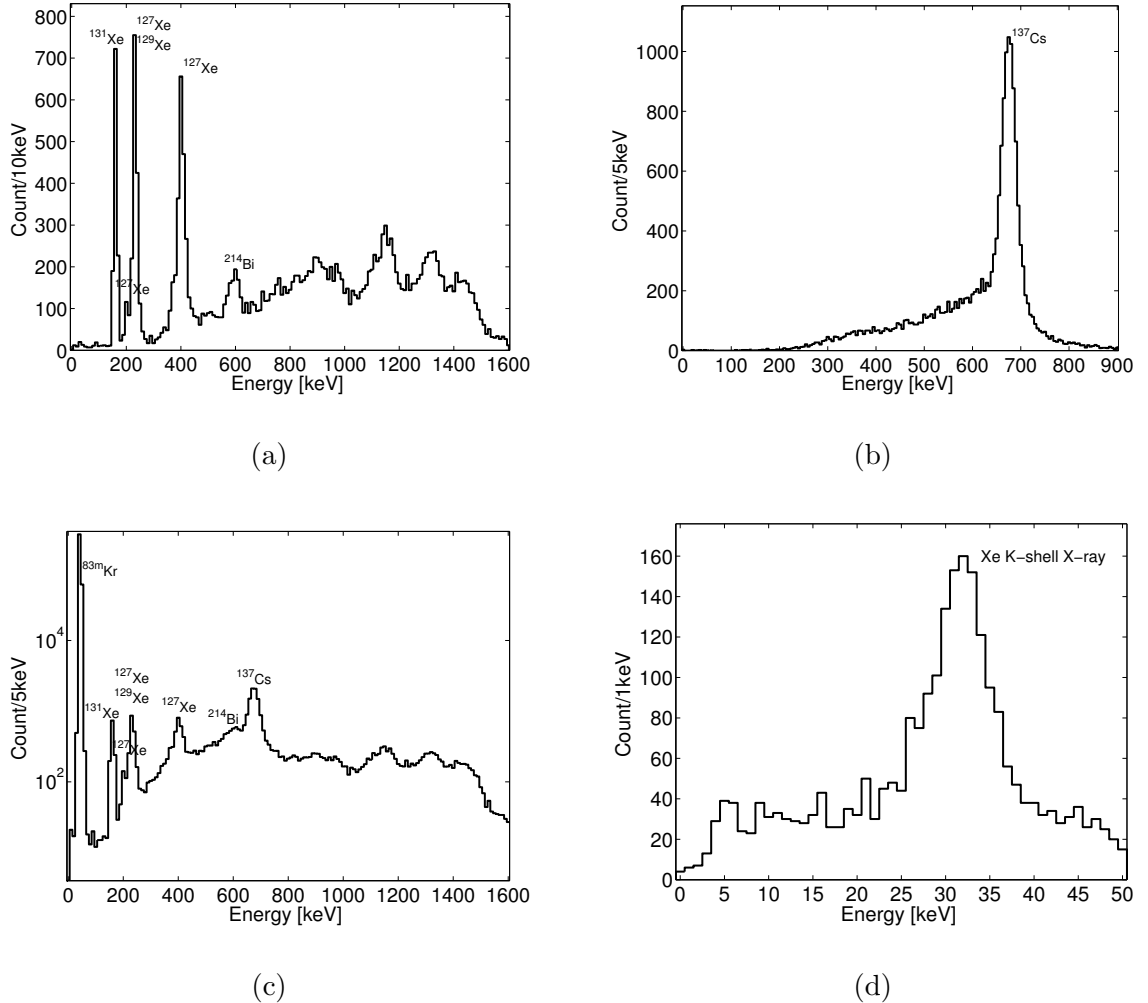


Figure 4.9: Combined energy scale. a) The xenon activation lines from early in Run03 of 2013. b)  $^{137}\text{Cs}$  calibration data. c) All calibration data including the  $^{83\text{m}}\text{Kr}$  calibration. d) Xenon X-ray.

enough threshold to observe single electrons being extracted from the liquid. Comparing the value of  $g_2$  derived from the Doke method with the single electron size is a good cross check on the  $g_2$  calibration.

As the electrons are extracted from the liquid they are accelerated by a larger field between the gate and anode where they initiate electroluminescence. A single

extracted electron creates tens to hundreds of photons which are collected by both PMT arrays [55]. We can identify a the single electron signal (small S2 pulses without an associated S1) and measure the single electron size in PE.

For a given event the extraction of electrons is a binomial processes with a rate approaching unity for fields above 5 kV/cm in the liquid [56] [44]. In LUX the extraction field is 3.5 kV/cm. Figure 4.10, shows the single electron size as measured by the bottom PMT array ( $S2_b$ ). The population is modeled by a skew Gaussian due to the Poisson nature of measuring only a handful of photo electrons (PE) per extracted electron. The mean of the distribution is found to be  $9.7 \text{ PE}/e^-$  with a width of  $\sigma_{\text{SE}} = 3.6 \text{ Phe}/e^-$ . The extraction efficiency is  $g_2$  over the single electron size and is found to be

$$\epsilon = \frac{g_2}{\text{SE}} = \frac{5.7 \pm 1.4(\text{PE}/e^-)}{9.7 \pm 3.6(\text{PE}/e^-)} = 59.3 \pm 14\% \quad (4.8)$$

Given the LUX the extraction field, this value is in good agreement with previous measurements in other xenon detectors [56] [44]. Note, if the extraction field between the gate and the anode can be tuned to a field for which  $\epsilon \simeq 1$  the value of  $g_2$  can be determined from the single electron size thus making  $g_1$  calibration trivial.

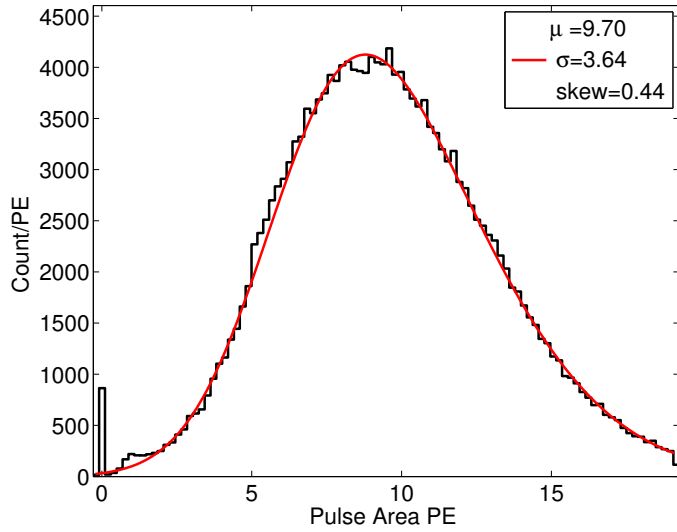


Figure 4.10: Single electron distribution as seen by the bottom PMT array fitted with a skew Gaussian model to account for the underlying Poisson statistics. The  $\mu$  of the fit represents the true mean of the skew Gaussian distribution.

## 4.7 Tritium Beta Spectrum

The energy calibration in the WIMP search region can be tested by using the tritium calibration source described in Chapter 7. Tritium has a Q value of 18.6 keV [71], a mean beta energy of 5.6 keV [72] and a mode of 3.4 keV [17] making it ideal for calibrating the LUX detector at the lowest energies. The tritium beta spectrum produces events at energies well below the detector threshold. Therefore, by comparing the reconstructed energy to the true tritium beta spectrum we can extract the energy threshold of the detector. We account for the detector resolution, smearing, by applying the empirically determined resolution measured in Chapter 5.

Figure 6.4 (a,b) shows the reconstructed energy from a tritium calibration at the default field setting of 170 V/cm. The calibration data set contains 140,000 tritium events with only an expected  $4\pm 2$  background events and is shown in black. A simulated tritium beta spectrum is shown in red, from the LUXSIM package with modeled detector resolution. In blue and green are the theoretical tritium beta spectrum with infinite detector resolution and with the added resolution of the LUX detector, respectively. Figure 6.4 (c,d) shows the same calibration but at a lower drift field setting of 100 V/cm with only 4,500 tritium events and an expected  $1\pm 1$  background events.

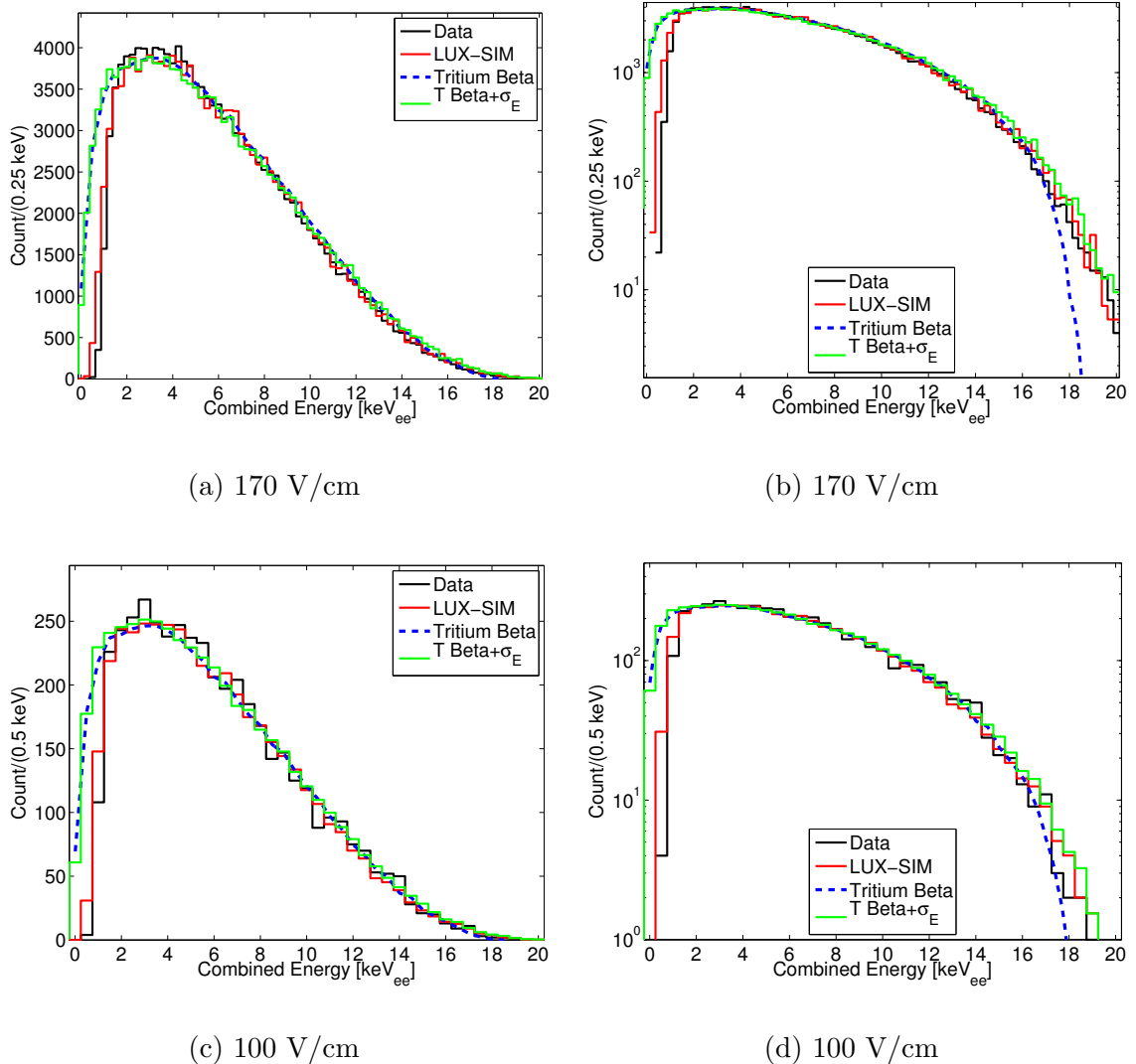


Figure 4.11: The tritium energy spectrum reconstructed from the data (black).

Along with LUX SIM (blue), and the true tritium beta spectrum (blue) and a tritium spectrum smeared with detector resolution (green).

The reconstructed energy spectrum is in good agreement with the expected tritium beta spectrum with detector resolution, using both LUXSIM and the empirically determined resolution. The detector threshold reaches 100% at about 1.5 keV, making the tritium beta peak clearly visible and providing crucial cross check

of the reconstructed energy around the WIMP search region of interest (1-5 keV) and the model for energy given in equation 4.3.

The 18.6 keV endpoint is another good low energy calibration point. We find that the end point of the reconstructed energy spectrum is consistent with that expected when convolving the true tritium beta spectrum with detector resolution. Though the energy scale for ER events was calibrated using mono-energetic sources well above the tritium Q value, the reconstructed tritium beta spectrum agrees with the expectation all the way down to the 1.5 keV threshold. The agreement at low energy is remarkable, considering we have reconstructed the energy scale for ER events by summing photons and electrons and ignoring the term lost to heat. We find that the modeling outlined in section 2.3 holds even at 1 keV<sub>ee</sub>.

Figure 4.12 shows the Energy threshold attained by comparing the data to the expected photon, electron and energy spectrum, at 170 and 100 V/cm. The energy threshold is set by the light collection of the much smaller S1 signal. For the energy threshold we find roughly 50% efficiency at 1 keV<sub>ee</sub> approaching 100% at 1.5 keV<sub>ee</sub> for both drift fields. The S1 and S2 detection threshold threshold will be discussed in Chapter 6.

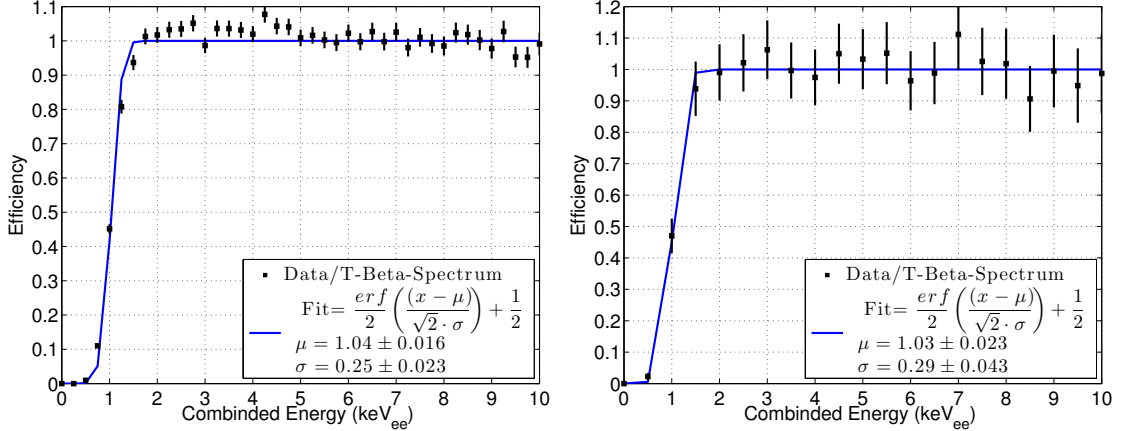


Figure 4.12: Detector threshold calculated by comparing the data to the true tritium energy spectrum having applied detector resolution effects. Top: data with a drift field of 170 V/cm. Bottom: data with a drift field of 1700 V/cm.

Figure 4.13 shown the tritium spectrum in S2 vs. S1 space. Having calibrated the energy scale we can overlay contours of constant energy with respect to the axes.

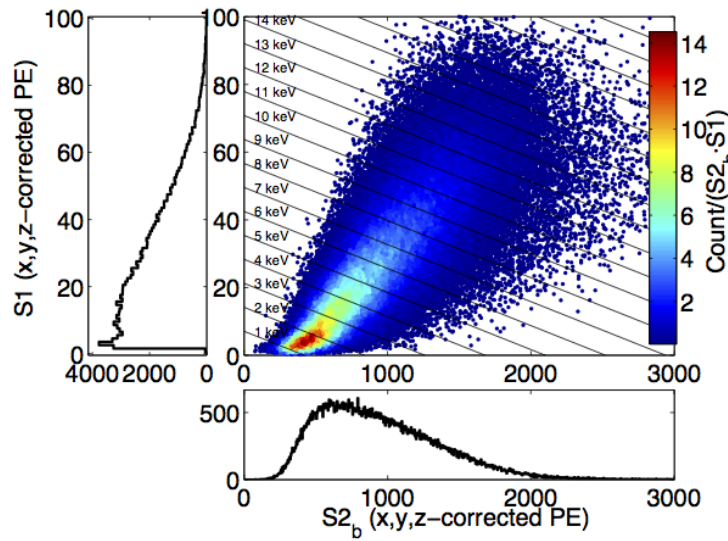


Figure 4.13: Tritium calibration data, plotting S2 vs. S1. The horizontal black lines represent contours of constant energy, labeled in keV.

## 4.8 Summery

We have constrained the value of  $g_1$  and  $g_2$  to be  $0.097 \pm 0.008$  and  $5.75 \pm 1.40$  respectively. The final fit for the values of  $g_1$  and  $g_2$  is shown in figure 4.4. Comparing the value of the single electron size measured the LUX detector to  $g_2$ , we find the electron extraction efficiency  $\epsilon$  to be  $59.3 \pm 14\%$ . The value for  $\epsilon$  is in good agreement with the expectation at the extraction field of 3.5 kV/cm. Having calibrated the combined energy scale using line sources above 40 keV we test the model of equation 4.3 by reconstructing a tritium beta spectrum. We find that the tritium beta shape reconstructed in energy by counting photons and electrons is in good agreement with the true shape. Specifically, both the end point (18.6 keV) and the mode (3-4 keV) of the spectrum line up. By comparing the data to the tritium beta spectrum the detector energy threshold is found to be 50% at 1 keV and approaching 100% above 1.5 keV.

## Chapter 5: Fluctuations in the S1 and S2 Signals

In this chapter we discuss extracting recombination fluctuations from line sources and continuous spectra such as tritium. The method outlined here will be used to measure recombination fluctuations from the tritium calibration data down to 1 keV. We begin by modeling the intrinsic resolution of the LUX detector, based on counting statistics. We then separate the fluctuations in light and charge collection from recombination fluctuations using line source calibrations. Once the variances from light and charge collection are modeled, the recombination fluctuations from continuous spectra can be extracted, specifically for the tritium beta spectrum. We conclude with the results for recombination and recombination fluctuations as measured from tritium beta decay in the LUX detector along with a measure of the exciton-to-ion ratio  $\alpha$  for ER events. Since we use photons and electrons (S1 and S2) to discriminate background events in LUX, understanding recombination fluctuations are of great importance.

### 5.1 An Introduction to Fluctuations

When Xenon TPCs were first developed it was expected that the resolution in the ionization and scintillation channels would be dominated by detector resolution.

The only fluctuations fundamental to liquid xenon is theorized to be from the Fano factor along with an additional binomial variance in electron ion pair recombination. Recombination models from [73] and [74], used in [62], assume that the total observed recombination is the result each electron-ion pairs interacting with itself, known as geminate recombination. The variance for such a process with recombination probability  $r_p$  acting on  $n_i$  number of ions is  $(1 - r_p)r_p n_i$ . Thus, a liquid xenon detector with infinite resolution should observe fluctuations governed by,

$$\begin{aligned}\sigma_{n_\gamma}^2 &= r_p^2 F n_i + (1 - r_p)r_p n_i \\ \sigma_{n_e}^2 &= (1 - r_p)^2 F n_i + (1 - r_p)r_p n_i\end{aligned}\tag{5.1}$$

where  $F$  is the Fano factor,  $F = 0.05$  in liquid xenon [58], and  $r_p$  is the recombination probability. Note, equation 5.1 will be derived later in this chapter (given in equations 5.25 and 5.26). The recombination probability  $r_p$  is equal to the average observed recombination  $\langle r \rangle$  as the number of events becomes large, given in table 5.1.

The variance in equation 5.1 is, in fact, orders of magnitude smaller than the observed variance. This has been an unsolved mystery since the first xenon TPCs was built. Fortunately, these large fluctuations in scintillation and ionization are 100% anti-correlated and cancel when both light and charge is combined to measure energy. We refer to these fluctuations as recombination fluctuations  $\sigma_R$ . The 100% anti-correlation implies that for each additional electron-ion recombination a single photon is produced at the cost of a single electron, and visa versa.

Let us consider the 164 keV line from  $^{131}\text{Xe}$  used to produce the Doke plots in chapter 4. An illustration with all the fluctuations in units of quanta is shown in

figure 5.1, with the number of photons ( $S_1/g_1$ ) plotted vs the number of electrons ( $S_2/g_2$ ). The values of  $g_1$  and  $g_2$  were determined from calibrations in chapter 4.

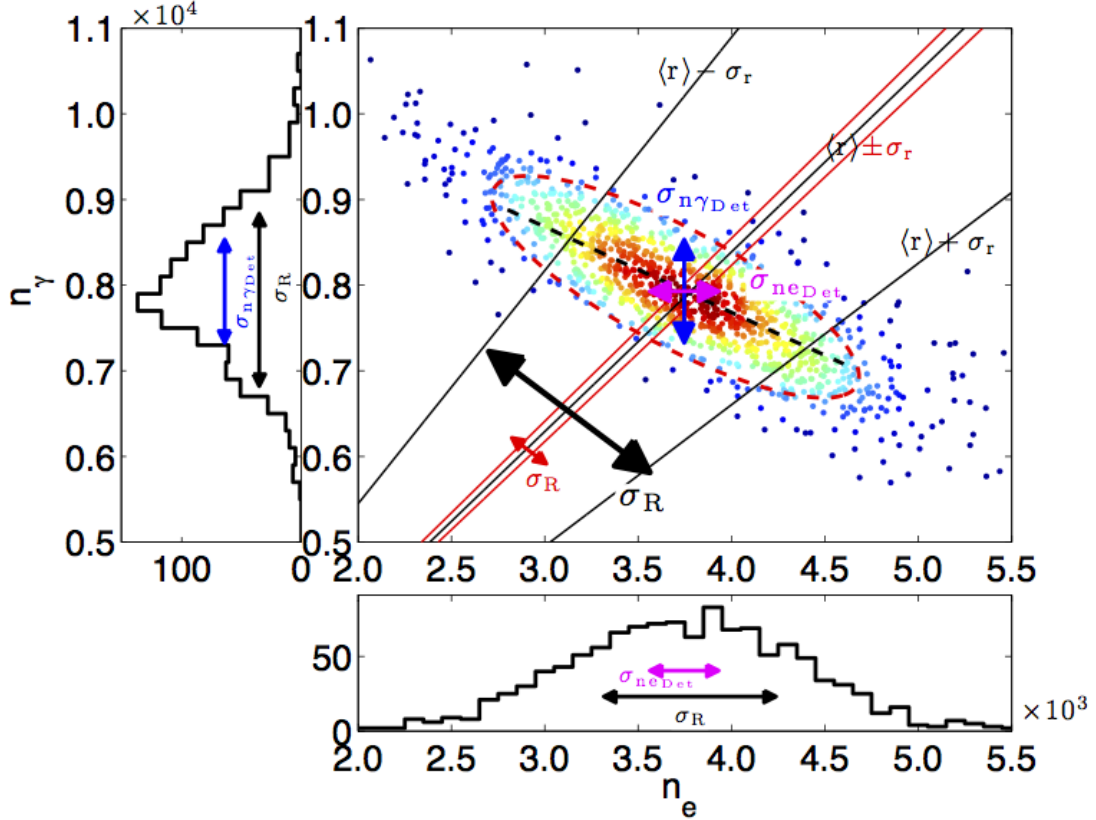


Figure 5.1: Fluctuations of the 164 keV line from  $^{131}\text{Xe}$  in the LUX detector, with the number of photons plotted vs. the number of electrons. The blue and magenta arrows labeled as  $\sigma_{n\gamma\text{Det}}$  and  $\sigma_{n_e\text{Det}}$  are the size of fluctuations in the light and charge channels due to the resolution of the LUX detector. The black arrow represents the size of recombination fluctuations  $\sigma_R$ . The value of  $\langle r \rangle$  is the average observed recombination fraction or the average recombination probability  $r_p$ . The red lines represent constant  $\langle r \rangle \pm \sigma_r$  assuming the expected binomial variance of equation 5.1. The black lines represent constant  $\langle r \rangle \pm \sigma_r$  measured from the data. The black dashed line is represent constant energy or constant number of quanta.

The blue and magenta arrows labeled as  $\sigma_{n\gamma\text{Det}}$  and  $\sigma_{n_e\text{Det}}$  are the size of fluctuations in the light and charge measurement due to the resolution of the LUX detector. The value of  $\langle r \rangle$  is the average observed recombination fraction and can be thought of as the average recombination probability  $r_p$ . The red lines represent constant

$\langle r \rangle \pm \sigma_r$  assuming the expected binomial variance of equation 5.1. The expected recombination (in red) is small compared to fluctuations from detector resolutions and is more than a factor of ten less than that observed. The black lines represent constant  $\langle r \rangle \pm \sigma_r$  measured from the data. The size of recombination fluctuations  $\sigma_R$  are dominant over detector resolution stretching the island size along lines of constant energy (black dashed line). The island is not stretched exactly along the black dashed line as the non negligible component from detector resolution also warp the population. The projection of the population onto the combined quanta axis  $(n_\gamma + n_e)$ , or energy  $E/W$ , is shown in figure 5.2.

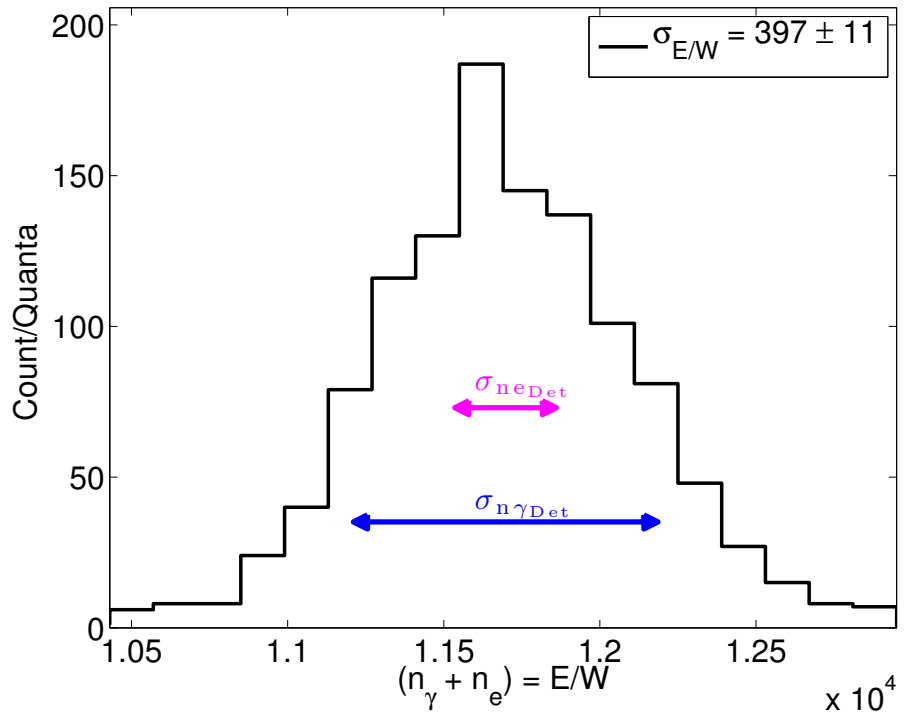


Figure 5.2: The projection of the population in figure 5.1 onto the combined quanta axis  $(n_\gamma + n_e) = E/W$ . Along this projection the dominant recombination fluctuations cancel out, leaving on the components from detector resolution  $\sigma_{n_\gamma \text{Det}}$  and  $\sigma_{n_e \text{Det}}$ .

In the combined light and charge axis we find that the recombination fluctuations

have vanished, leaving only the statistical variance from detector resolution. Some useful definitions of parameters which will be discussed in this section are given in table 5.1.

Parameter	Description	Definition
$n_\gamma$	Number of photons	$\langle S1 \rangle / g_1$
$n_e$	Number of electrons	$\langle S2 \rangle / g_2$
$n_i$	Number of ions	$(n_\gamma + n_e) / (1 + \alpha)$
$n_{ex}$	Number of excitons	$\alpha n_i$
$\alpha$	Exciton to ion ratio	$n_{ex} / n_i$
$\sigma_{n_{\gamma, \text{Det}}}$	$n_\gamma$ detector fluctuations	equation 5.17
$\sigma_{n_{e, \text{Det}}}$	$n_e$ detector fluctuations	equation 5.17
$r$	Recombination fraction	$\left( \frac{n_\gamma}{n_e} - \alpha \right) / \left( \frac{n_\gamma}{n_e} + 1 \right)$
$r_p$	Recombination probability	$\langle r \rangle$
$R$	Recombined ions	$\langle r \rangle n_i$
$\sigma_R$	Recombination fluctuations	$\sigma_{\langle r \rangle} n_i$

Table 5.1: LUX detector parameters, used to measure statistical fluctuations in the light ( $S1$ ) and charge ( $S2$ ) channels. Where the  $S1$  and  $S2$  signals have been corrected for position dependence outlined in section 3. The values of  $g_1$  and  $g_2$  were measured in section 4.

For the rest of this section we will build on the example from figure 5.1 to better understand recombination fluctuations. We will explore recombination fluctuations

with line-source calibrations then expand the picture to deal with continuous sources.

## 5.2 Modeling Intrinsic Detector Resolution

Intrinsic statistical fluctuations in light and charge (S1 and S2) collection in the LUX detector lead to a spread in collected quanta. To measure effects from recombination fluctuations and the Fano factor, we must first decouple the detector component of resolution. We use the model described in [51] [11] in which the measured scintillation and ionization signals (S1 and S2 measured in PE) are related to the number of photons and electrons by gains  $g_1$  and  $g_2$ , equation 5.2 and 5.3. Specifically, the average number of photons and electrons produced for a given energy deposit are proportional to the average S1 and S2 signals.

$$\langle n_\gamma \rangle = \frac{\langle S1 \rangle}{g_1} \quad (5.2)$$

$$\langle n_e \rangle = \frac{\langle S2 \rangle}{g_2} \quad (5.3)$$

where the gain  $g_1$  represents photon detection efficiency, the probability of a photon from an energy deposit striking a PMT and producing a photo electron signal (PE). Gain  $g_2$  represents the average S2 signal of a single electron multiplied by the electron extraction efficiency  $\epsilon$ . Here, we are only using the S2 of the bottom PMT array and is corrected for electron-lifetime. The fluctuations in photons and electrons are related to the observables S1 and S2 by equations 5.2 and 5.3

$$\sigma_{n_{\gamma_{\text{stat}}}}^2 = \frac{\sigma_{S1_{\text{stat}}}^2}{g_1^2} \quad (5.4)$$

$$\sigma_{n_{e_{\text{stat}}}}^2 = \frac{\sigma_{S2_{\text{stat}}}^2}{g_2^2} \quad (5.5)$$

where  $\sigma_{n_{\gamma_{\text{stat}}}}^2$  and  $\sigma_{n_{e_{\text{stat}}}}^2$  represent the variance in the average number of measured photons and electrons as measured through S1 and S2, respectively. The variances in S1 and S2,  $\sigma_{S1_{\text{stat}}}^2$  and  $\sigma_{S2_{\text{stat}}}^2$ , are the observable quantities with the detector. The variance in terms of quanta ( $n_{\gamma}$  and  $n_e$ ) must be considered in terms of the PE being counted by the PMTs. Note, here we are working with the x,y,z corrected signals outlined in chapter 3.

Before proceeding to derive the statistical variance in light and charge, we overview a list of terms and their values in the LUX detector, given in table 5.2.

The statistical variance of the x,y,z corrected S1 signal, in equation 5.4, can be broken into two linearly independent parts. First we consider the binomial variance. For each event there are  $n_{\gamma}$  number of PE to be collected by the PMTs with probability  $g_1$ . Here,  $n_{\gamma}$  should be thought of as the number of trials. The binomial variance is,

$$\sigma_{S1_{\text{Bin}}}^2 = (1 - g_1)g_1 n_{\gamma} \quad (5.6)$$

where  $\sigma_{S1_{\text{Bin}}}^2$  is the binomial variance of the S1 light collection process with probability  $g_1$  and  $n_{\gamma}$  number of trials. Each PE that was collected by a PMT then undergoes a second fluctuation due to the resolution of the PMTs. The variance from PMT resolution can be written as

$$\sigma_{S1_{\text{PMT}}}^2 = g_1 n_{\gamma} \sigma_{\text{PE}}^2 \quad (5.7)$$

Parameter	Definition	Value
$g_1$	photon detection probability	$0.097 \pm 0.008$ [PE/n <sub><math>\gamma</math></sub> ]
$\sigma_{\text{PE}}$	single PE resolution, all PMTs	0.50 [PE/n <sub><math>\gamma</math></sub> ]
$g_2 = \epsilon \text{SE}_b$	average electron signal	$5.75 \pm 1.4$ [PE/n <sub>e</sub> ]
$\text{SE}_b$	single electron size, bottom PMT array	$9.70 \pm 0.1$ [PE/n <sub>e</sub> ]
$\epsilon$	electron extraction probability	$0.593 \pm 0.144$
$\sigma_{\text{SE}_b}$	single electron resolution, bottom PMT array	3.6 [PE/n <sub>e</sub> ]
$\kappa$	fraction of non-attenuated electrons	0.85

Table 5.2: LUX detector parameters, used to measure statistical fluctuations in the light (S1) and charge (S2) channels. Where the S1 and S2 signals have been corrected for position dependence outlined in section 3. The values of  $g_1$  and  $g_2$  were measured in section 4.

where  $\sigma_{\text{S1}_{\text{PMT}}}^2$  is the average variance due to PMT resolution. The average single PE resolution of the PMTs is  $\sigma_{\text{PE}}^2$  and is multiplied by the number of PE collected,  $g_1 n_\gamma$ .

Combining the two linearly independent processes of equation 5.6 and 5.7 leads to the result in equation 5.8.

$$\sigma_{\text{S1}_{\text{stat}}}^2 = (1 - g_1 + \sigma_{\text{PE}}^2)(g_1 n_\gamma) = (1 - g_1 + \sigma_{\text{PE}}^2)\text{S1} \quad (5.8)$$

where  $\sigma_{\text{S1}_{\text{stat}}}^2$  is the statistical variance of the S1 signal. The variance in the measured

number of photons is then equation 5.8 divided by  $g_1^2$ , using equation ??.

$$\sigma_{n_{\gamma}^{stat}}^2 = \frac{(1 - g_1 + \sigma_{PE}^2)}{g_1} n_{\gamma} \quad (5.9)$$

We test equation 5.8 and 5.9 by using the 9.4 keV S1 signal from  $^{83m}\text{Kr}$ . At that energy the dominant fluctuation is due the statistical variance of light collection, we can ignore contributions from recombination fluctuations and instrumental fluctuations (will be discussed later in this section). The S1 signal is shown in figure 5.3.

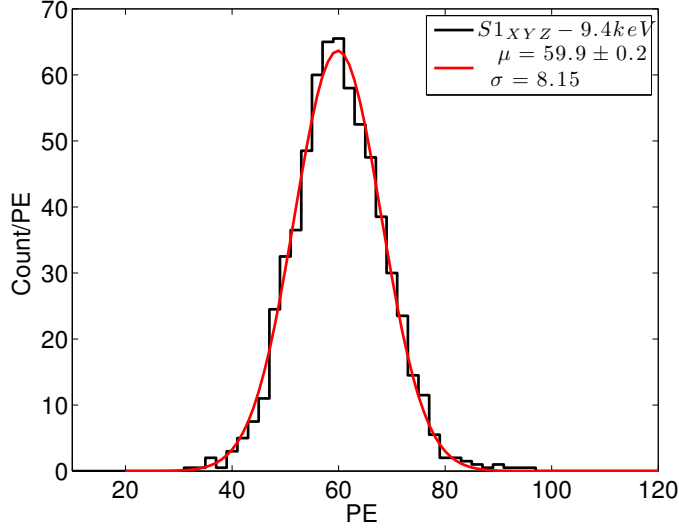


Figure 5.3: The fluctuations in the S1-x,y,z corrected signal for the 9.4 keV from  $^{83m}\text{Kr}$ . At 9.4 keV the statistical variance is dominant over recombination fluctuations,  $\sigma_{S1} = 8.15$ . The resolution is consistent with that expected from statistical fluctuations of  $8.3 \pm 0.1$  PE, from equation 5.8.

We find that the observed  $\sigma_{S1} = 8.15$  PE is in good agreement with the expectation from equation 5.8 of  $8.3 \pm 0.1$  PE. In terms of photons,  $\sigma_{n_{\gamma_{\text{stat}}}} = 84.1$  with the expectation from equation 5.9 of  $85.7 \pm 1$ , (having used the values listed in table 5.2).

The variance of the x,y,z corrected S2 signal, given in ??, is also comprised of several independent processes. Each electron that reaches the liquid-gas interface without being attenuated will either be extracted into the gas producing  $SE_b$  number of PE or not. The binomial variance of such a process is,

$$\sigma_{S2_{\text{bino}}}^2 = (1 - \epsilon)\epsilon(\kappa n_e)SE_b^2 \quad (5.10)$$

where  $\epsilon$  is the electron extraction probability, and  $\kappa n_e$  is the average number of electrons that reach the liquid surface from the interaction site, also the number of trials. Recalling that  $\kappa$  is the average electron probability of an electron to not be captured by an electronegative impurity. For the case of LUX with an electron lifetime of  $\sim 1000 \mu s$  and an average drift time of  $160 \mu s$  the value of  $\kappa = 0.85$  and is listed in table 5.2. Each electron that gets extracted then multiplies producing  $SE_b$  PE in the bottom PMT array, this multiplicative factor must be squared in the variance.

Next, we consider the spread of the single electron size as measured by the bottom PMT array,  $\sigma_{SE_b}$ . The variance from the PMT resolution for the  $\epsilon(\kappa n_e)$  number of electrons extracted is,

$$\sigma_{S2_{\text{PMT}}}^2 = \epsilon(\kappa n_e)\sigma_{SE}^2 \quad (5.11)$$

where  $\epsilon\kappa n_e$  is the number of extracted electrons each with PMT resolution  $\sigma_{SE}^2$ .

For the S2 signal we must also consider the additional variance from electron attenuation as the electrons drift. We model the process with a Poisson probability of electron capture in each Z slice of the detector. The variance from each Z slice depends of the average number of electrons that will be attenuated. The probability of attenuation at each slice in drift-time T is  $P(T) = 1 - e^{-T/\tau}$ , where  $\tau$  for the data sets to be considered is 1000  $\mu s$ . The drift region considered in the fiducial volume is from 38 to 304.5  $\mu s$ . The average variance from events in the fiducial can be given by equation 5.12.

$$\sigma_{n_{e_{att}}}^2 = n_e \frac{\int_{T_{min}}^{T_{max}} (1 - e^{-T/\tau}) dT}{\int_{T_{min}}^{T_{max}} dT} = 0.155 \times n_e \quad (5.12)$$

Combining the variances from equations 5.10 5.11 and 5.12 leads to the the result for the statistical variance in the observed S2 signal,

$$\begin{aligned} \sigma_{S2_{stat}}^2 &= (1 - \epsilon)\epsilon(\kappa n_e)SE_b^2 + \epsilon(\kappa n_e)\sigma_{SE}^2 + g_2^2\sigma_{n_{e_{att}}}^2 \\ \sigma_{S2_{stat}}^2 &= ((1 - \epsilon)SE_b\kappa + \sigma_{SE}^2\kappa/g_2 + 0.155g_2) S2 \end{aligned} \quad (5.13)$$

$$\sigma_{n_{e_{stat}}}^2 = \frac{(1 - \epsilon)\epsilon SE_b^2 + \epsilon\sigma_{SE}^2}{g_2^2} \kappa n_e + \sigma_{n_{e_{att}}}^2 \quad (5.14)$$

Using equations 5.9, 5.14 and table 5.2 we calculate the intrinsic detector resolution for S1 and S2 signals in the LUX detector, given equation 5.15. Note, the

intrinsic resolution in S2 is sub-dominant to that of S1, since on average one extracted electron multiplies to about ten PE detected by the bottom PMT array, while one photon leads to 0.097 PE. Also listed in 5.16, are the instrumental fluctuations with a linear dependence on quanta measured using calibrations discussed in section 5.3. The total variance that the detector observes in the light and charge is the linear combination of the statistical and instrumental variance given in equation 5.17.

$$\begin{aligned}\sigma_{n_{\gamma_{\text{stat}}}} &= 3.45 \pm^{0.17}_{0.15} \sqrt{n_{\gamma}} \\ \sigma_{n_{e_{\text{stat}}}} &= 1.04 \pm^{0.26}_{0.20} \sqrt{n_e}\end{aligned}\quad (5.15)$$

where  $\sigma_{n_{\gamma_{\text{stat}}}}$  and  $\sigma_{n_{e_{\text{stat}}}}$  are the statistical fluctuations outlined in this section.

$$\begin{aligned}\sigma_{n_{\gamma_{\text{inst}}}} &= \frac{6.4 \pm 1.7}{100} \times n_{\gamma} \\ \sigma_{n_{e_{\text{inst}}}} &= \frac{6.6 \pm 0.9}{100} \times n_e\end{aligned}\quad (5.16)$$

where  $\sigma_{n_{\gamma_{\text{inst}}}}$  and  $\sigma_{n_{e_{\text{inst}}}}$  are instrumental fluctuations extracted in section 5.3 that grow like number of quanta n but only appear to turn on above 200 keV.

$$\begin{aligned}\sigma_{n_{\gamma_{\text{Det}}}}^2 &= \sigma_{n_{\gamma_{\text{stat}}}}^2 + \sigma_{n_{\gamma_{\text{inst}}}}^2 \\ \sigma_{n_{e_{\text{Det}}}}^2 &= \sigma_{n_{e_{\text{stat}}}}^2 + \sigma_{n_{e_{\text{inst}}}}^2\end{aligned}\quad (5.17)$$

where  $\sigma_{n_{\gamma_{\text{Det}}}}^2$  and  $\sigma_{n_{e_{\text{Det}}}}^2$  are the fluctuations in counting photons and electrons, respectively, due to detector resolution.

### 5.3 Measuring Recombination Fluctuations with Mono-Energetic Sources

To model recombination we start with the assumption that for a given energy deposit in liquid xenon the number of quanta produced is equal to the number of excitons and the number of ions [51].

$$\begin{aligned}\frac{E}{W} &= n_q = n_i + n_{ex} = n_i(1 + \alpha) \\ \frac{E}{W} &= n_\gamma + n_e = \frac{S_1}{g_1} + \frac{S_2}{g_2}\end{aligned}\tag{5.18}$$

where  $E$  is energy in keV,  $W$  is the work function in keV/quanta,  $n_q$  is the number of quanta,  $n_i$  is the number of ions,  $n_{ex}$  is the number of excitons and  $\alpha$  is the exciton-to-ion ratio. The measured value of the number of excitons produced to ions is  $\frac{n_{ex}}{n_i} = \alpha = 0.20$  [49] and is not expected to change as a function of energy [50] [59] [11]. For the subsequent equations in this section we will simplify equations 5.18:

$$\begin{aligned}\alpha &= 0.20 \\ n_i &= \frac{E}{W} \frac{1}{(1 + \alpha)} = \frac{n_\gamma + n_e}{(1 + \alpha)}\end{aligned}\tag{5.19}$$

Equation 5.19 gives us a simple model for the number of ions produced for a given interaction. We work in number of ions for convenience as the recombination fluctuations act only on ions. The only variation in quanta thus far is due to a Fano

factor governing the variation in initial quanta produced.

$$\sigma_{n_i}^2 = F \times n_i \quad (5.20)$$

where  $F$  is the Fano factor. The value of  $F$  for liquid xenon is small and has a theoretical value of 0.05 [58].

We now describe the observed scintillation and ionization signals that are measured in the LUX detector as a function of  $n_i$ . The number of photons observed for a given energy deposit arise from the excitons that de-excite and from ions which recombine with freed electrons.

$$n_\gamma = n_{ex} + n_i \times r = n_i \times (r + \alpha) \quad (5.21)$$

The number of electrons corresponding to a given energy deposit is equal to the number of ions that did not recombine with a free electron.

$$n_e = n_i \times (1 - r) \quad (5.22)$$

The recombination fraction of each event can be solved for in terms of number of photons and electrons produced,

$$r = \frac{\frac{n_\gamma}{n_e} - \alpha}{\frac{n_\gamma}{n_e} + 1} \quad (5.23)$$

where  $r$  represents the electron-ion recombination probability of each event.

Two key measurable quantities from the scintillation and ionization signals are the average recombination fraction  $\langle r \rangle$  and the spread in recombination probability  $\sigma_{\langle r \rangle}$ . The average recombination fraction  $\langle r \rangle$  can be interpreted as the electron-ion

pair recombination probability  $r_p$ . The recombination fluctuation in units of quanta is

$$\sigma_R = \sigma_{\langle r \rangle} \times n_i \quad (5.24)$$

where  $\sigma_R$  is the recombination fluctuation. As mentioned earlier, the recombination fluctuations in the data are much larger than those expected from the binomial variance of a binomial process with probability  $r_p$  or from the Fano factor, as illustrated in figure 5.1.

We now combine the variance from the Fano factor, recombination and detector resolution (equation 5.17) and solve for the total observed variance in photons and electrons given in 5.25 and 5.26

$$\sigma_{n_\gamma}^2 = \sigma_{n_{ex}}^2 + \sigma_{n_i}^2 r_p^2 + \sigma_{\langle r \rangle}^2 n_i^2 + \sigma_{n_{\gamma_{Det}}}^2 = [\sigma_{n_{ex}}^2 + n_i F r_p^2] + \sigma_{\langle r \rangle}^2 n_i^2 + \sigma_{n_{\gamma_{Det}}}^2 \quad (5.25)$$

$$\sigma_{n_e}^2 = \sigma_{n_i}^2 (1 - r_p)^2 + \sigma_{\langle r \rangle}^2 n_i^2 + \sigma_{n_{e_{Det}}}^2 = [n_i F (1 - r)^2] + \sigma_{\langle r \rangle}^2 n_i^2 + \sigma_{n_{e_{Det}}}^2 \quad (5.26)$$

where  $\sigma_{n_{ex}}^2$  is the variance in exciton production,  $F$  is the Fano factor, the term  $\sigma_{\langle r \rangle}^2 n_i^2$  is the recombination fluctuation  $\sigma_R$ . The remaining variables are described in table 5.1.

Using a line source, we measure combined energy (equation 5.18) and  $\sigma_{n_\gamma}^2$ ,  $\sigma_{n_e}^2$  and  $\sigma_E^2$ . Dropping the contribution form the Fano factor and the the number of excitons in equations 5.25 and 5.26 the variance of  $\sigma_{n_\gamma}^2$  and  $\sigma_{n_e}^2$  is a linear combination of detector resolution and recombination fluctuations.

$$\sigma_{n_\gamma}^2 = \sigma_{n_{\gamma_{\text{Det}}}}^2 + \sigma_R^2 \quad (5.27)$$

$$\sigma_{n_e}^2 = \sigma_{n_{e_{\text{Det}}}}^2 + \sigma_R^2 \quad (5.28)$$

this concept is illustrated in figure 5.1. The value of recombination fluctuation  $\sigma_R$  can be determined by rearranging equations 5.27 and 5.28. As shown in figure 5.2, when the light and charge signals are combined the resulting variance  $\sigma_E^2$  contains no recombination fluctuations, as recombination fluctuations are 100% anti-correlated in light and charge.

$$\sigma_R^2 = \frac{1}{2} \left( \sigma_{n_\gamma}^2 + \sigma_{n_e}^2 - \frac{\sigma_E^2}{W^2} \right) \quad (5.29)$$

where the variance in photons  $\sigma_{n_\gamma}^2$ , electrons  $\sigma_{n_e}^2$  and quanta  $\frac{\sigma_E^2}{W^2}$  are all observable quantities with a line source. The recombination variance can be written in terms of the observable quantities S1 and S2.

$$\sigma_R^2 = \frac{1}{2} \left( \frac{\sigma_{S1}^2}{g_1^2} + \frac{\sigma_{S2}^2}{g_2^2} - \frac{\sigma_E^2}{W^2} \right) \quad (5.30)$$

We now have a method to extract the recombination fluctuation  $\sigma_R$  using a line calibration source. To complete our treatment of line sources, the variance in the light and charge due to detector resolution can also be measured.

$$\sigma_{n_{\gamma_{\text{Det}}}}^2 = \frac{\sigma_{S1}^2}{g_1^2} - \sigma_R^2 \quad (5.31)$$

$$\sigma_{n_{e_{\text{Det}}}}^2 = \frac{\sigma_{S2}^2}{g_2^2} - \sigma_R^2 \quad (5.32)$$

Using equation 5.30, 5.31 and 5.32 along with the measurements of  $g_1$   $g_2$ , we construct a combined energy and deconvolve the recombination fluctuations from variances in the light and charge observed by the detector. The result is shown in figure 5.4, The black white and red lines represent  $\sigma_R$ ,  $\sigma_{n_{\gamma\text{Det}}}$ ,  $\sigma_{n_{e\text{Det}}}$ , respectively. The values and sources are listed in table 5.3.

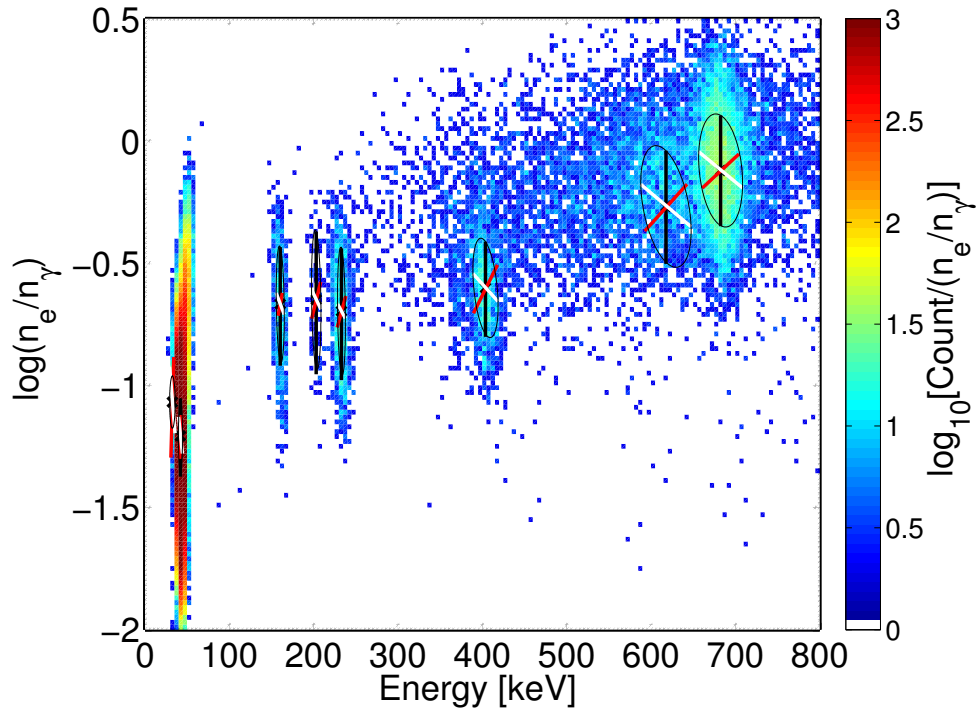


Figure 5.4: Populations of calibration sources in discrimination space  $\log \left( \frac{n_e}{n_\gamma} \right)$  vs. combined energy keV<sub>ee</sub>. The ovals represent the combination of  $\sigma_R$ ,  $\sigma_{n_{\gamma\text{Det}}}$ ,  $\sigma_{n_{e\text{Det}}}$  in black, white, red respectively.

The values of  $\sigma_R$ ,  $\sigma_{n_{\gamma\text{Det}}}$ ,  $\sigma_{n_{e\text{Det}}}$  from table 5.3 are plotted in figure 5.5.

A variance with a linear and root term is fit to the data with the results given in 5.33. The linear term corresponds to instrumental fluctuations and the root term corresponds to statistical fluctuations. Instrumental fluctuations are proportional to the signal size and cause the fluctuations in  $\sigma_{n_{\gamma\text{Det}}}$ ,  $\sigma_{n_{e\text{Det}}}$  at high energies to deviate

Source	Energy [keV]	$\sigma_R$	$\sigma_{n_{\gamma\text{Det}}}$	$\sigma_{n_{e\text{Det}}}$	$\sigma_E/W$
K-shell X-ray	$\sim 32$	$52.6 \pm 23$	$244 \pm 5$	$116 \pm 3$	$269 \pm 5$
$^{83\text{m}}\text{Kr}$	41.55	$89.1 \pm 0.6$	$171 \pm 0.3$	$51.2 \pm 0.3$	$173 \pm 0.2$
$^{131}\text{Xe}$	163.9	$637 \pm 20$	$388 \pm 31$	$83 \pm 77$	$375 \pm 8$
$^{127}\text{Xe}$	208.3	$916 \pm 59$	$506 \pm 96$	$260 \pm 133$	$568 \pm 26$
$^{127}\text{Xe}, ^{129\text{m}}\text{Xe}$	236.8	$1001 \pm 23$	$441 \pm 50$	$253 \pm 71$	$491 \pm 9$
$^{127}\text{Xe}$	408.8	$1294 \pm 44$	$1166 \pm 39$	$949 \pm 40$	$1562 \pm 22$
$^{214}\text{Bi}$	609	$2488 \pm 109$	$2298 \pm 99$	$1627 \pm 107$	$3291 \pm 60$
$^{137}\text{Cs}$	661.6	$2686 \pm 34$	$2059 \pm 38$	$1368 \pm 46$	$2564 \pm 17$

Table 5.3: Extracted fluctuations from the line source calibration data in units of quanta. The method of extracting the quantities is given in 5.30, 5.31 and 5.32 and illustrated for the case of  $^{131}\text{Xe}$  in figures 5.1 and 5.2. Note, the K-shell X-ray may include a fairly large systematic as no radial cut was made in order to observe the signal near the detector edge.

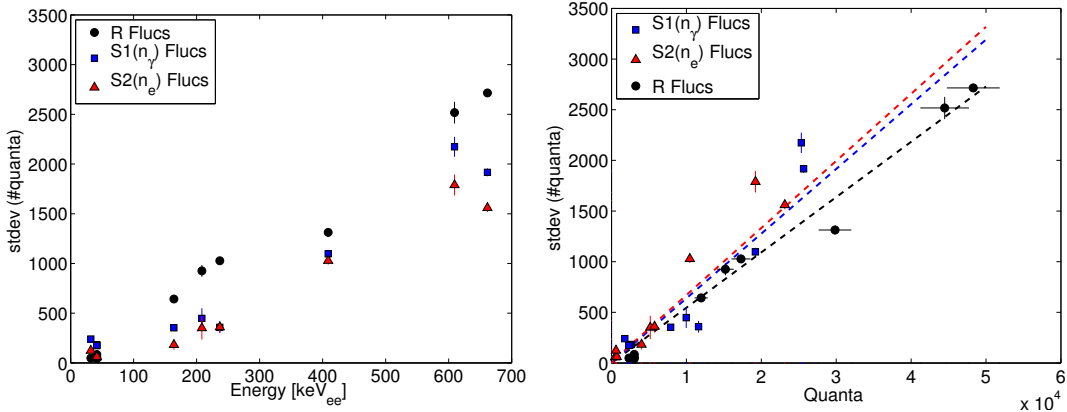


Figure 5.5: Measured values of  $\sigma_R$ ,  $\sigma_{n_{\gamma\text{Det}}}$ ,  $\sigma_{n_{e\text{Det}}}$  vs. Energy on the left and vs. quanta in photons, electrons and ions, respectively, on the right. Measured using sources listed in Table 5.3.

from statistical fluctuations alone.

$$\begin{aligned} \sigma_{n_{\gamma\text{Det}}}^2 &= \sigma_{n_{\gamma\text{Stat}}}^2 + \sigma_{n_{\gamma\text{Inst}}}^2 = (0 \pm 10 \cdot \sqrt{n_{\gamma}})^2 + ((6.4 \pm 1.8)/100 \cdot n_{\gamma})^2 \\ \sigma_{n_{e\text{Det}}}^2 &= \sigma_{n_{e\text{Stat}}}^2 + \sigma_{n_{e\text{Inst}}}^2 = (1 \pm 4 \cdot \sqrt{n_e})^2 + ((6.6 \pm 0.6)/100 \cdot n_e)^2 \\ \sigma_R^2 &= ((5.5 \pm 0.5)/100 \cdot n_q)^2 \end{aligned} \quad (5.33)$$

With the limited data we can not tightly constrain the root-n term. The statistical

fluctuation expected from equation 5.15 is consistent with the observed values without the instrumental component for calibration energies at and below 236.8 keV. The instrumental fluctuations appear to turn on above  $\sim$ 200 keV and may be due to ripples in the liquid surface caused by xenon bubbles or other systematics.

## 5.4 Measuring Recombination Fluctuations in Discrete Energy Bins

The previous section outlined a method to extract recombination fluctuations from line source calibrations, equation 5.30. In this section the formalism to measure recombination fluctuations when considering events binned in energy will be outlined. The consideration of discrete binning is crucial when dealing with a continual energy spectrum. Take the tritium beta spectrum as an example. We lose the ability to independently measure  $\sigma_{n_\gamma}^2$ ,  $\sigma_{n_e}^2$ ,  $\sigma_E^2$  and are only left with a smear of  $n_\gamma$ ,  $n_e$ ,  $E$ . However, there are two key pieces of information still left at our disposal. Knowing  $g_1$ ,  $g_2$  and the intrinsic detector resolution is sufficient to measure recombination fluctuations for a continual energy spectrum.

To simplify the picture we introduce new variables when dealing with events having been cut in energy of bin of width  $\Delta_E$ . After cutting in energy, we define the remaining variance projected onto light and charge as  $\chi_{n_\gamma}^2$  and  $\chi_{n_e}^2$ , which is analogous to  $\sigma_{n_\gamma}^2$  and  $\sigma_{n_e}^2$  of equations 5.27 5.28, respectively. We denote the component of variance from detector resolution contained in the slice of energy as  $\chi_{\text{Det}}$ . These concepts will be clarified in the subsequent examples and are summarized in table 5.4.

Parameter	Definition	Analogy Without Binning
$\chi^2_{n_\gamma}$	Total variance with E cut projected onto $n_\gamma$	$\sigma_{n_\gamma}^2$
$\chi^2_{n_e}$	Total variance with E cut projected onto $n_e$	$\sigma_{n_e}^2$
$\chi^2_{\text{Det}}$	Variance from detector resolution shared between $n_\gamma$ and $n_e$ , with E cut	$\sigma_{n_{\gamma\text{Det}}}^2 \sigma_{n_{e\text{Det}}}^2$

Table 5.4: Useful definitions when considering cutting events in a bin of energy and projecting onto the  $n_\gamma$  and  $n_e$  axis.

We will overview the treatment of binning by considering two cases using a simulated  $^{83m}\text{Kr}$  line-source. For each case, the energy is defined using equation 5.18 and a cut is energy of width  $\Delta_E = 1\text{keV}$  is made about the energy center. First, variance from detector resolution is turned off leaving only recombination fluctuations. The value of recombination fluctuations in terms of quanta is set to  $\sigma_R = 90$  in the simulation, similar to the value extracted from the  $^{83m}\text{Kr}$  data in table 5.3. Figure 5.6 shows the result of such a system.

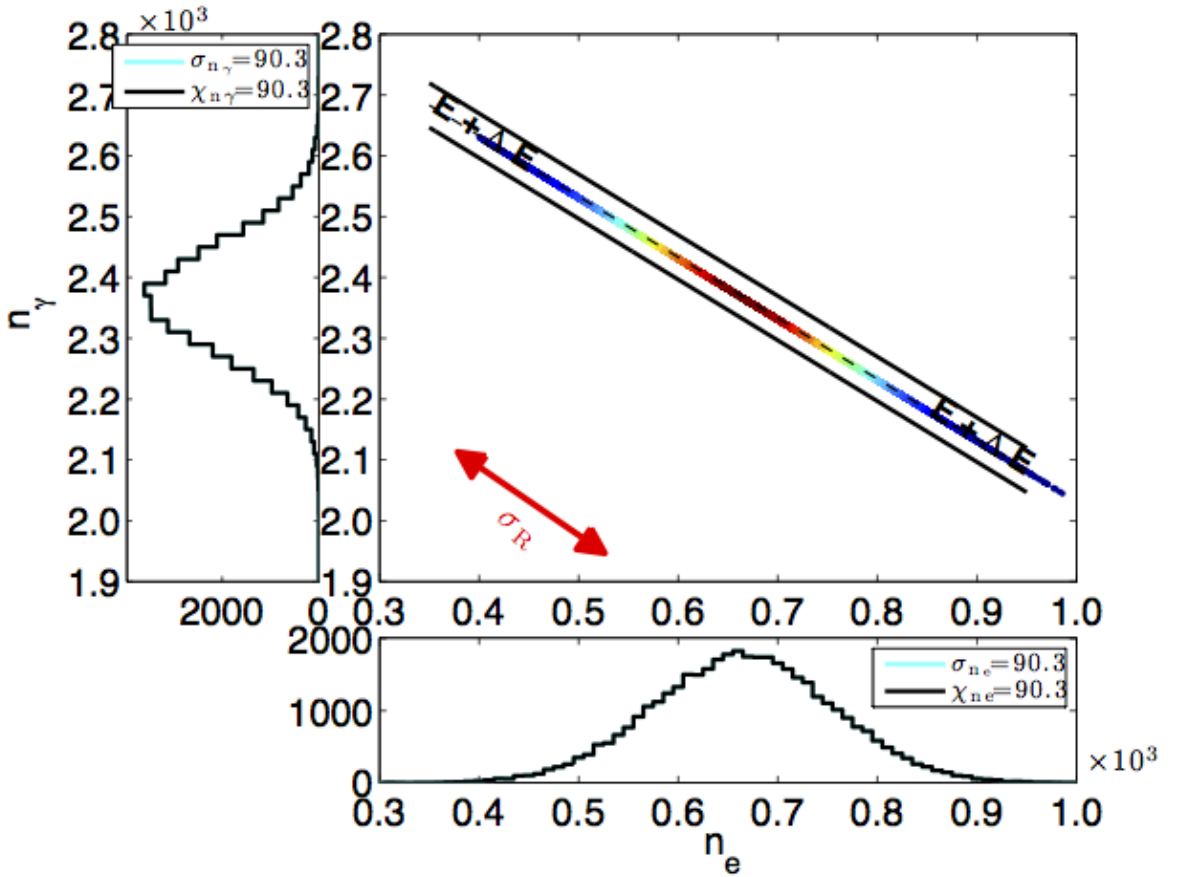


Figure 5.6: A simulated  $^{83\text{m}}\text{Kr}$  source with infinite detector resolution and recombination fluctuations set to 90 quanta. The recombination fluctuation move along the line of constant energy about the center, shown in black with bin width of  $\Delta_E = 1 \text{ keV}$ . The events between the black lines and projected onto the  $n_\gamma$  and  $n_e$  axes. The variance in  $n_\gamma$  and  $n_e$  are  $\sigma_{n_\gamma}^2 = \chi_{n_\gamma}^2 = \sigma_R^2$  and  $\sigma_{n_e}^2 = \chi_{n_e}^2 = \sigma_R^2$ .

In figure 5.6 we see that recombination fluctuations move events along the diagonal of constant energy, as expected. The standard deviation in light and charge is found by the fit to be  $90.3 \pm 0.3$ , consistent to what was input into the simulation, 90. For the case of only recombination fluctuations and perfect detector resolution we find,

$$\begin{aligned} \sigma_{n_\gamma}^2 &= \chi_{n_\gamma}^2 = \sigma_R^2 \\ \sigma_{n_e}^2 &= \chi_{n_e}^2 = \sigma_R^2 \end{aligned} \tag{5.34}$$

The key point demonstrated in figure 5.6 is that all contribution from recombination fluctuations are included when slicing along a contour of energy about the center, no matter how thin we make the cut. Note, with infinite detector resolution the population becomes a delta function in energy about the central value.

Next, we visualize how the intrinsic detector resolution,  $\sigma_{n_{\gamma_{\text{Det}}}}^2$  and  $\sigma_{n_{e_{\text{Det}}}}^2$ , appears along a contour of constant energy for a simulated  $^{83\text{m}}\text{Kr}$  source. The recombination fluctuations are set to zero and the fluctuations from detector resolution are set to  $\sigma_{n_{\gamma_{\text{Det}}}} = 171$  and  $\sigma_{n_{\gamma_{\text{Det}}}} = 51$ , close to the true values of the LUX detector in table 5.3. The slice in combined energy is illustrated in figure 5.6, using a bin width of  $\Delta_E = 1 \text{ keV}$  (73 quanta).

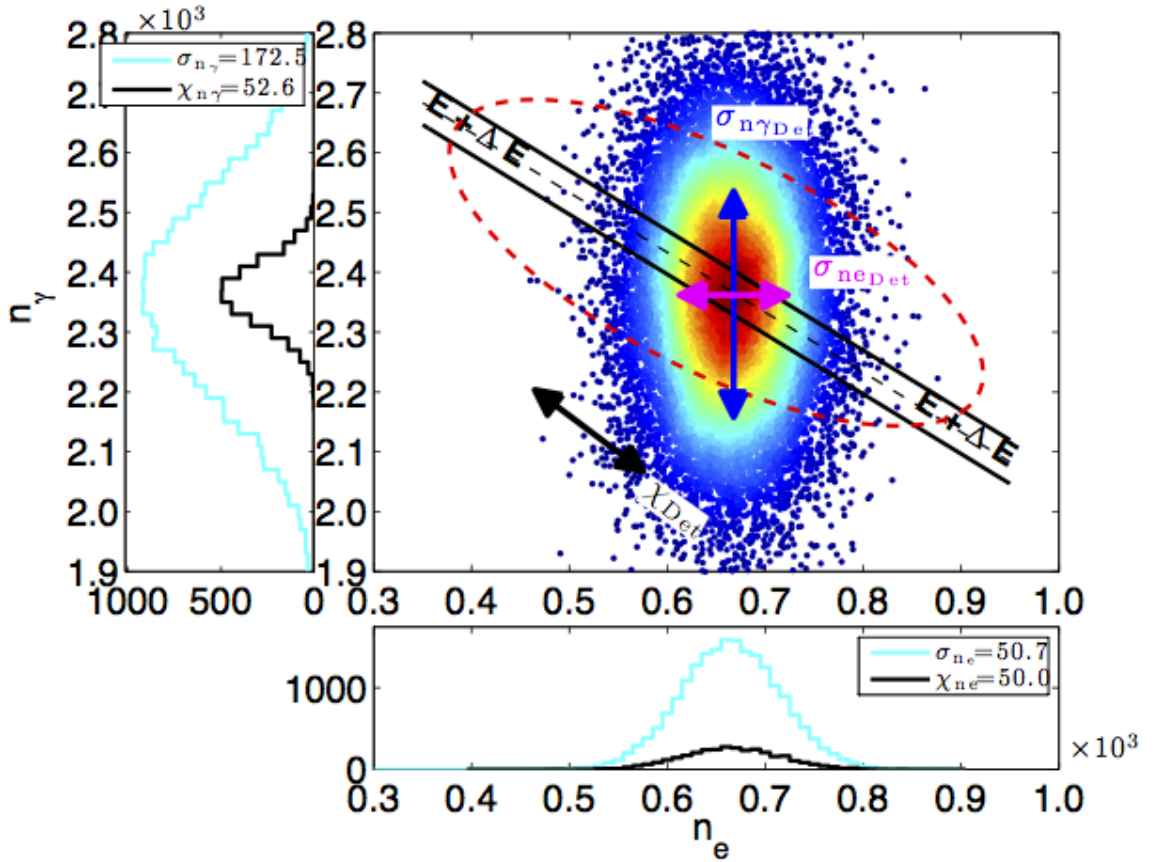


Figure 5.7: A simulated  $^{83\text{m}}\text{Kr}$  source with no recombination fluctuations and with detector resolution,  $\sigma_{n_\gamma \text{Det}} = 171$  and  $\sigma_{n_e \text{Det}} = 51$ . The solid black lines represents constant energy about the center having width of  $\Delta E = 1$ . The events that fall between the black dashed lines are projected onto the  $n_\gamma$  and  $n_e$  axes. The square root of the observed variance in light and charge are show on the labels with and without the energy cut, as  $\chi$  and  $\sigma$  respectively. The energy cut has swept out a component of variance  $\chi_{\text{Det}}$  that is shared between the light and charge channels.

In the example pictured in figure 5.7 we find that the energy cut leaves a reduced statistical component to be projected onto  $n_\gamma$  and  $n_e$ . The reduction in variance projected onto  $n_\gamma$  is an order of magnitude. However, this is expected as only a small portion of  $n_\gamma$  is included with the energy cut shown in figure 5.7.

With the examples shown in figure 5.6 and 5.7 we can now visualize the effect of an energy cut on fluctuations in the light ( $n_\gamma$ ) and charge signals ( $n_e$ ). The

slice, by definition, contains only events which fluctuated about the contour of constant energy thus, automatically including all recombination fluctuations and only a reduced component from detector resolution ( $\chi_{\text{Det}}$ ).

To solve for the value of  $\chi_{\text{Det}}$  we write the detector-resolution fluctuations  $\sigma_{n_{\gamma\text{Det}}}$  and  $\sigma_{n_{e\text{Det}}}$  as a function of combined energy in number quanta.

$$n_q = E/W = n_\gamma + n_e \quad (5.35)$$

where  $n_q$  is the number of quanta (photons + electrons),  $E$  is energy in keV, and  $W=13.7\pm0.001$  keV/quanta. Next, consider the the slope induced by the statistical variance of  $\sigma_{n_{\gamma\text{Det}}}$  and  $\sigma_{n_{e\text{Det}}}$  as a function quanta  $n_q$ . The slope between  $n_\gamma$  with respect to total quanta  $n_q$  (energy) is the variance in  $n_\gamma$  over the variance in  $n_q$ , and the same for  $n_e$ . The result for the slope  $M$  considering a detector with resolution  $\sigma_{n_{\gamma\text{Det}}}$  and  $\sigma_{n_{e\text{Det}}}$  is,

$$\begin{aligned} M &= \tan(\theta_{n_{\gamma\text{Det}}}) = \frac{\sigma_{n_{\gamma\text{Det}}}^2}{\sigma_{n_{\gamma\text{Det}}}^2 + \sigma_{n_{e\text{Det}}}^2} \\ 1 - M &= \tan(\theta_{n_{e\text{Det}}}) = \frac{\sigma_{n_{e\text{Det}}}^2}{\sigma_{n_{\gamma\text{Det}}}^2 + \sigma_{n_{e\text{Det}}}^2} \end{aligned} \quad (5.36)$$

where  $M$  is the slope of  $n_\gamma$  with respect to  $n_q$ . Once  $M$  is defined, the angle between  $n_e$  and  $n_q$  is the complementary slope ( $1-M$ ). The slope  $M$  can also be thought of as  $\tan(\theta)$  where  $\theta$  is the angle between  $n_\gamma$  and  $n_q$ , ranging from 0 to  $\pi/4$ . The slope of the population induced by the statistical variance of  $n_\gamma$  and  $n_e$  with respect to the quanta (or  $E/W$ ) axis can be expressed interns of the slope  $M$ .

$$\begin{aligned} n_\gamma &= Mn_q \\ n_e &= (1 - M)n_q \end{aligned} \tag{5.37}$$

Using equation 5.37 and 5.35 we solve for the for a small variation in  $n_q$  induced by the fluctuations in  $n_\gamma$  and  $n_e$  along a contour of constant  $n_q$ . First holding the number of photons  $n_\gamma$  constant and allowing for small variations in  $n_e$  and then holding the number of electrons  $n_e$  constant and allowing for small variations in  $n_\gamma$ .

$$\begin{aligned} \delta n_q &= \frac{\partial n_\gamma}{\partial n_q} \delta n_q \Big|_{n_\gamma} + \frac{\partial n_e}{\partial n_q} \delta n_q \Big|_{n_e} \\ \delta n_q &= \frac{\partial(n_q - n_e)}{\partial n_q} \delta n_e + \frac{\partial(n_q - n_\gamma)}{\partial n_q} \delta n_\gamma \\ \delta n_q &= \left[ \frac{\partial n_q}{\partial n_q} - \frac{\partial n_e}{\partial n_q} \right]^{(1-M)} \delta n_e + \left[ \frac{\partial n_q}{\partial n_q} - \frac{\partial n_\gamma}{\partial n_q} \right]^M \delta n_\gamma \\ \delta n_q &= (M)\delta n_e + (1 - M)\delta n_\gamma \end{aligned} \tag{5.38}$$

squaring the result from equation 5.38 the variance along an infinitely thin line of constant energy induced by statistical fluctuations is,

$$\chi_{\text{Det}}^2 = \text{Var}(\delta n_q) = M^2 \sigma_{n_{e\text{Det}}}^2 + (1 - M)^2 \sigma_{n_{\gamma\text{Det}}}^2 \tag{5.39}$$

where  $M$  is given in equation 5.36 and the cross term  $\delta n_\gamma \delta n_e$  has been dropped as the statistical variance from detector resolution ( $\sigma_{n_{\gamma\text{Det}}}^2$  and  $\sigma_{n_{e\text{Det}}}^2$ ) are uncorrelated.

Combining equation 5.39 and the equation for slope M in equation 5.36 simplifies the expression for  $\chi_{\text{Det}}^2$  to,

$$\chi_{\text{Det}}^2 = \frac{\sigma_{n_{\gamma_{\text{Det}}}}^2 \sigma_{n_{e_{\text{Det}}}}^2}{\sigma_{n_{\gamma_{\text{Det}}}}^2 + \sigma_{n_{e_{\text{Det}}}}^2} \quad (5.40)$$

the expression for  $\chi_{\text{Det}}^2$  describes the amount of statistical variance that will be included with the recombination fluctuations when events are cut along contours of constant energy. The only information needed to determine are  $\chi_{\text{Det}}^2$  is  $\sigma_{n_{\gamma_{\text{Det}}}}^2$  and  $\sigma_{n_{e_{\text{Det}}}}^2$ , which are given in equation 5.17 as a function of quanta.

The example shown in figure 5.7 can now be understood in terms of  $\chi_{\text{Det}}^2$ . The simulation had used values of  $\sigma_{n_{\gamma_{\text{Det}}}} = 171$  and  $\sigma_{n_{e_{\text{Det}}}} = 51$ . Solving for M using equation 5.36 we find,  $M = 0.92$ , meaning that the angle  $\theta$  of the bulk population between the  $n_\gamma$  axis and the line of constant quanta (E/W) is  $42.6^\circ$ . Plugging the values into equation 5.40 the value of  $\chi_{\text{Det}} = 49$  quanta. This is within 10% of the value of  $\chi_{n_\gamma}$  and  $\chi_{n_e}$  observed in the simulated data set. Later we will expand upon equation 5.38 to account for the finite bin width.

Let us briefly consider the implication of equation 5.39 and 5.40. In the case of equal detector resolution in light and charge,  $\sigma_{n_{e_{\text{Det}}}}^2 = \sigma_{n_{\gamma_{\text{Det}}}}^2$ , the value of M is 0.5 leading to,  $\chi_{\text{Det}}^2 = \frac{1}{2}\sigma_{n_{e_{\text{Det}}}}^2$ . Curiously, regardless of the resolution in light and charge the statistical variance in a cut of energy is always less than the variance of the best channel. Specifically for the LUX detector, the implication of equation 5.39 is that the statistical variance measured in a cut on energy will be less than that of the S2 statistical uncertainty. The illustration for the case of  $\sigma_{n_{e_{\text{Det}}}} = \sigma_{n_{\gamma_{\text{Det}}}}$

$= 100$  is shown in figure 5.8. As expected, the square root of the variance along the line of constant energy is about  $100/\sqrt{2} = 70.7$ .

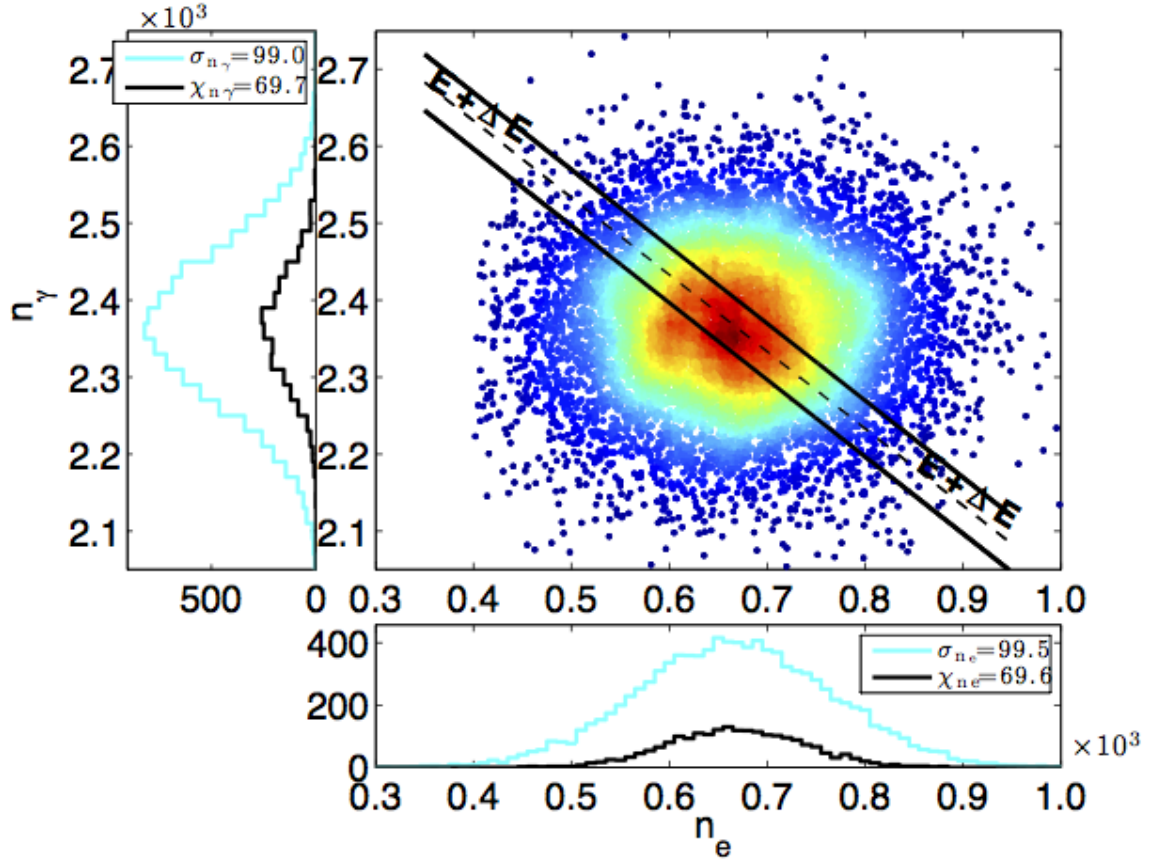


Figure 5.8: A simulated  $^{83\text{m}}\text{Kr}$  source with no recombination fluctuations and with detector resolution,  $\sigma_{n_e\text{Det}} = \sigma_{n_\gamma\text{Det}} = 100$ . The solid black line represents constant energy about the center having a width of  $\Delta_E = 1$ . The events that fall between the black dashed lines are projected onto the  $n_\gamma$  and  $n_e$  axes. The square root of the observed variance in light and charge are shown on the labels with and without the energy cut, as  $\chi$  and sigma respectively.

To complete the treatment of  $\chi_{\text{Det}}^2$  we add the contribution to variance from the finite bin width  $\Delta_E$ . The residual variance arises from projecting the rotated population onto  $n_\gamma$  or  $n_e$ , the rotation having a slope of  $M$  and  $(1-M)$  respectively, given in equation 5.36. Note, the residual variance from the rotation can also be removed by working with the centroid subtracted projections of number of photons and electrons as a function of energy, as discussed later in section 5.4.2. Considering the bin width, the total variance from detector resolution projected in  $n_\gamma$  and  $n_e$  is

$$\begin{aligned}\chi_{n_{\gamma\text{Det}}}^2 &= \chi_{\text{Det}}^2 + \frac{(MW\Delta_E)^2}{12} \\ \chi_{n_{e\text{Det}}}^2 &= \chi_{\text{Det}}^2 + \frac{((1-M)W\Delta_E)^2}{12}\end{aligned}\quad (5.41)$$

where  $\chi_{\text{Det}}^2$  is defined in 5.40,  $M$  is given in equation 5.36,  $W$  is the work function in quanta/keV,  $\Delta_E$  is the bin width in energy keV, the normalization of 1/12 arises from rotating a uniform population about its center. The value of  $\chi_{n_{\gamma\text{Det}}}^2$  is the variance from statistical fluctuations after cutting along a line of constant energy having width  $\Delta_E$  and then projecting onto the  $n_\gamma$  axis. Similarly,  $\chi_{n_{e\text{Det}}}^2$  is the variance from statistical fluctuations after cutting along a line of constant energy and projecting onto the  $n_e$  axis.

The correction given in equation 5.41 is applied to the example in figure 5.7, which used a bin width of 1 keV (73 quanta). The value of  $\chi_{\text{Det}}$  was previously calculated to be 49 quanta. The additional contribution from bin width results in  $\chi_{n_{\gamma\text{Det}}} = 52.5$  quanta and  $\chi_{n_{e\text{Det}}} = 49$  quanta. These values are consistent with those observed in the simulation shown in figure 5.7,  $\chi_{n_\gamma} = 52.6 \pm 0.6$  and  $\chi_e = 50.0 \pm 0.7$ .

We now combine the two cases illustrated in figures 5.6 and 5.7, having recombination only and then detector resolution only. The combined variance projected in  $n_\gamma$  and  $n_e$  can be determined, given a cut in energy. The contribution to variance from the two can be added as they are independent processes.

$$\chi_{n_\gamma}^2 = \sigma_R^2 + \chi_{n_{\gamma_{\text{Det}}}}^2 \quad (5.42)$$

$$\chi_{n_e}^2 = \sigma_R^2 + \chi_{n_{e_{\text{Det}}}}^2 \quad (5.43)$$

$$(5.44)$$

where  $\sigma_R^2$  are the recombination fluctuations, and the values  $\chi_{n_{\gamma_{\text{Det}}}}^2$  and  $\chi_{n_{e_{\text{Det}}}}^2$  are given in equation 5.41. The recombination fluctuation can be measured by rearranging equation 5.42 and 5.43

$$\sigma_{R_\gamma}^2 = \chi_{n_\gamma}^2 - \chi_{n_{\gamma_{\text{Det}}}}^2 \quad (5.45)$$

$$\sigma_{R_e}^2 = \chi_{n_e}^2 - \chi_{n_{e_{\text{Det}}}}^2 \quad (5.46)$$

Using equations 5.45 and 5.46 we can extract recombination fluctuations directly from the  $n_\gamma$  (S1) and  $n_e$  (S2) signals. The quantities  $\chi_{n_\gamma}^2$  and  $\chi_{n_e}^2$  are the observables and  $\chi_{\text{Det}}^2$  is determined from calibrations.

### 5.4.1 Application to $^{83}\text{Kr}$

We now have a method to extract recombination fluctuations from data binned in energy in equation 5.45 and 5.46. Before applying the method to the tritium beta

spectrum we test the method using a  $^{83m}\text{Kr}$  calibration data set. The result is shown in figure 5.7 for a bin width of 1 keV, and listed for several bin width in table 5.5.

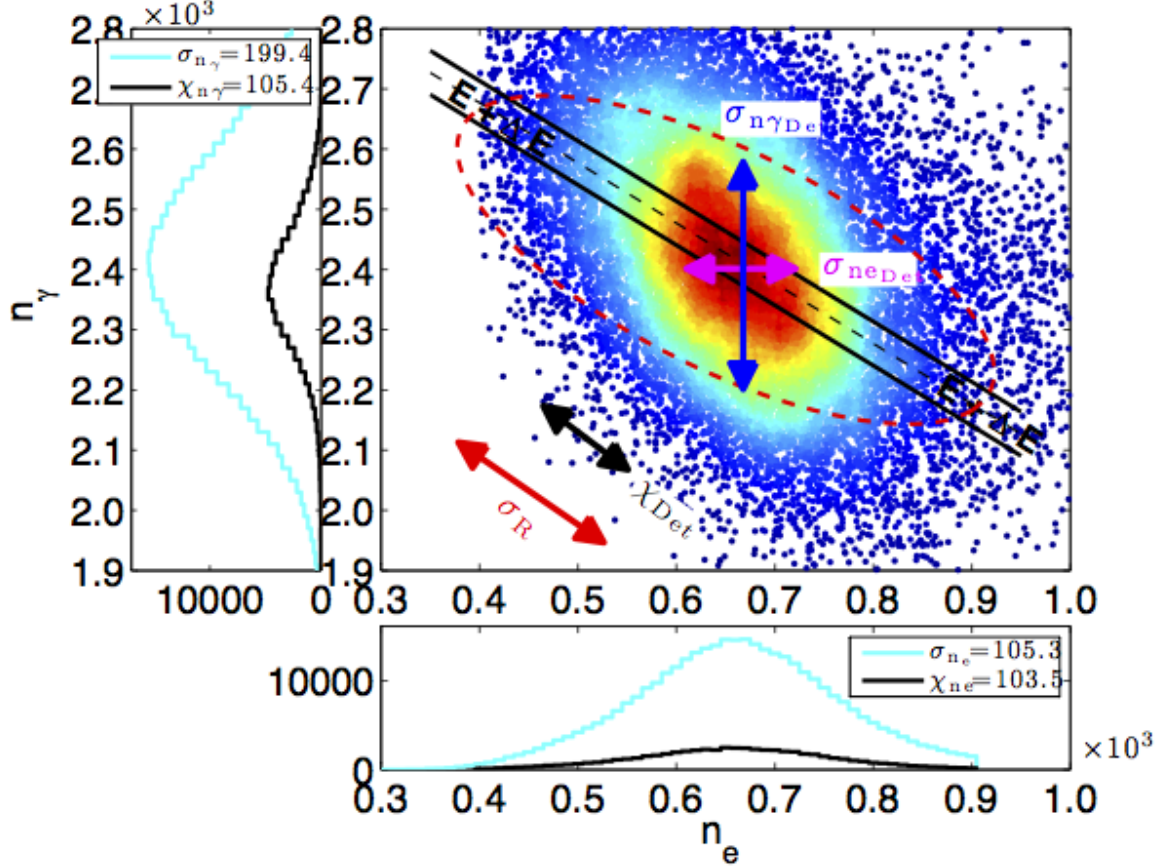


Figure 5.9: Data from a  $^{83m}\text{Kr}$  data set, plotting the number of photons against the number of electrons. The red-dashed oval represents where the population would lie if recombination fluctuations were the dominant fluctuation. The solid black line represents constant energy about the center, and the region between the black dashed lines represents the cut in energy with bin width  $\Delta_E = 1$ . The events that fall between the black dashed lines are projected onto the  $n_\gamma$  and  $n_e$  axes. The observed standard deviation in  $n_\gamma$  and  $n_e$  is shown on the plot labels as  $\chi$  and  $\sigma$ .

The  $^{83m}\text{Kr}$  data set contained 400,000 events in the fiducial volume of the detector. Using equations 5.45 and 5.46 we calculate recombination fluctuations, finding good agreement with the method described for in equation 5.29. The agreement between the two methods is within 5% and implies that the detector resolution has

$\sigma_R$ 5.30 (Quanta)	$\Delta_E$ (keV)	Count	$\sigma_{R_\gamma} = \sqrt{\chi_{n_\gamma}^2 - \chi_{n_{\gamma_{\text{Det}}}^2}$ (Quanta)	$\sigma_{R_e} = \sqrt{\chi_{n_e}^2 - \chi_{n_{e_{\text{Det}}}^2}$ (Quanta)
89.1 $\pm$ 0.6	0.025	1518	87.2 $\pm$ 2.9	87.1 $\pm$ 2.9
	0.05	3124	85.0 $\pm$ 2.0	84.9 $\pm$ 2.0
	0.1	6269	87.8 $\pm$ 1.3	87.6 $\pm$ 1.3
	0.2	12508	90.0 $\pm$ 1.0	89.7 $\pm$ 1.0
	0.25	15557	88.5 $\pm$ 0.8	88.3 $\pm$ 0.8
	0.5	30826	92.5 $\pm$ 0.6	91.2 $\pm$ 0.6

Table 5.5: The extraction of recombination fluctuations from a  $^{83m}\text{Kr}$  data set using various bin widths  $\Delta E$  about the central value of energy. The standard deviation of recombination fluctuations  $\sigma_R$  are calculated from the fluctuations observed in  $n_\gamma$  and  $n_e$  using equations 5.45 and 5.46. The value of  $\chi_{\text{Det}}$  is 49 quanta.

been modeled well. Having demonstrated the method for a line source calibration source the next step is to apply the method outlined in this section to simulated tritium data and see how well the method can extract test values of recombination fluctuations.

### 5.4.2 Application to Simulated Tritium Data

In this section the method outlined in section 5.4 for line sources will be applied to the tritium beta spectrum. To first order, the treatment of a continuous spectrum is identical to the method outlined for  $^{83m}\text{Kr}$  if we consider that the tritium beta spectrum is comprised of multiple line sources. It will be shown that the formalism developed can be applied to continuous spectra by testing the concepts using simulations.

As was done for the  $^{83m}\text{Kr}$  source, we start by simulating a tritium beta spectrum with only recombination fluctuations. Figure 5.10 on the top, shows a tritium beta spectrum propagated at every 1 keV energy bin and on the right from every 0.1 keV.

As expected, we find that the recombination fluctuations events along the lines of constant energy. Figure 5.10 is analogous to the illustration shown for the case of  $^{83m}\text{Kr}$  in figure 5.6. We now add in detector resolution (S1 and S2 fluctuations) and propagate events from every 0.1 keV bin along the tritium spectrum. The detector resolution included is that modeled for the LUX detector. The resulting spectrum is shown in figure 5.11.

The recombination fluctuations can now be extracted by plotting the photon and electron populations as a function of energy. The results from the simulation are shown in figure 5.12. By plotting the photon and electron spectra as a function of energy we immediately see the effect to recombination fluctuations and detector resolution  $\chi_{\text{Det}}$ , as these cause the fluctuations up and down in constant energy.

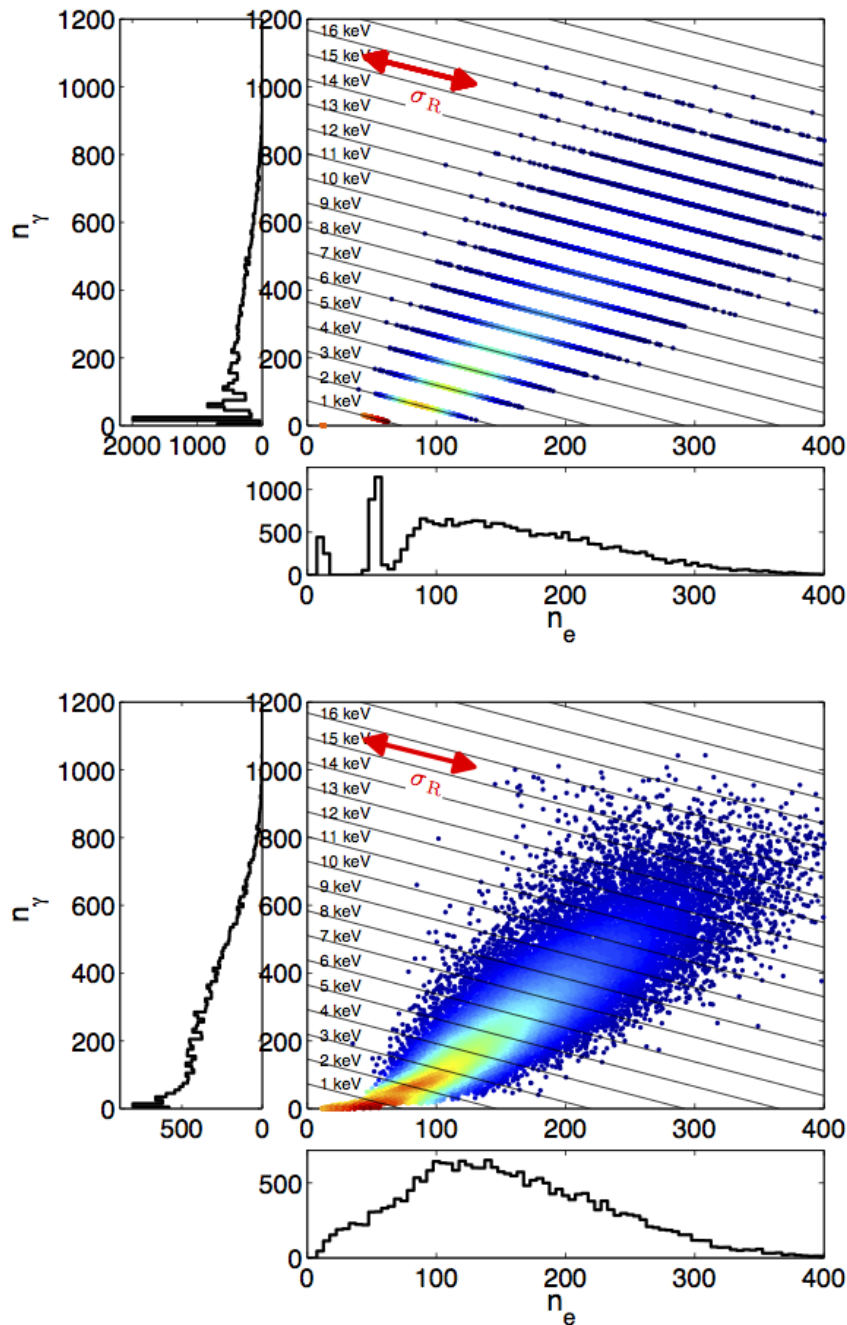


Figure 5.10: Number of photons plotted against the number of electrons from a simulated tritium data set having only recombination fluctuations. Top: Tritium events propagated from 1 keV bins from 1-18 keV. Bottom, the tritium events propagated from 0.1 keV bins from 1-18 keV. The recombination fluctuations move events along the lines of constant energy.

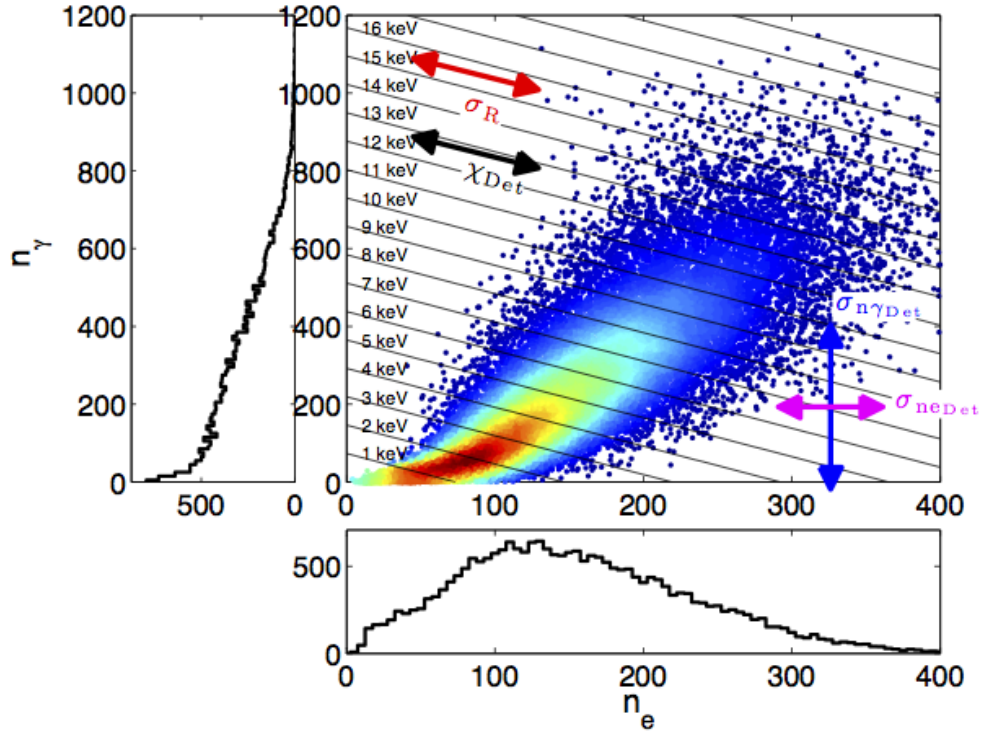


Figure 5.11: The number of photons plotted against the number of electrons from a simulated tritium data set having recombination fluctuations and detector resolution. The tritium events propagated from 0.1 keV bins from 1-18.6 keV. Events move along the lines of constant energy due to recombination fluctuations and  $\chi_{\text{Det}}$ .

Before extracting the recombination fluctuation from the simulated data shown in figure 5.12 we must consider the slopes of the population  $M$ . The slope of the  $n_\gamma$  was defined earlier in equation 5.36 purely as a function of the detector resolution. However, the slope of a continuous spectrum is effected by the functional form of light yield and charge yield as a function of energy. This issue is easily solved by fitting a line to the population. For this analysis we fit a quadratic to  $n_\gamma$  as a function of energy, the slope of the fit is by definition the value of  $M$ . Note, for the case of LUX the value of  $M$  is dominated by statistical fluctuations and using 5.12 is a good approximation.

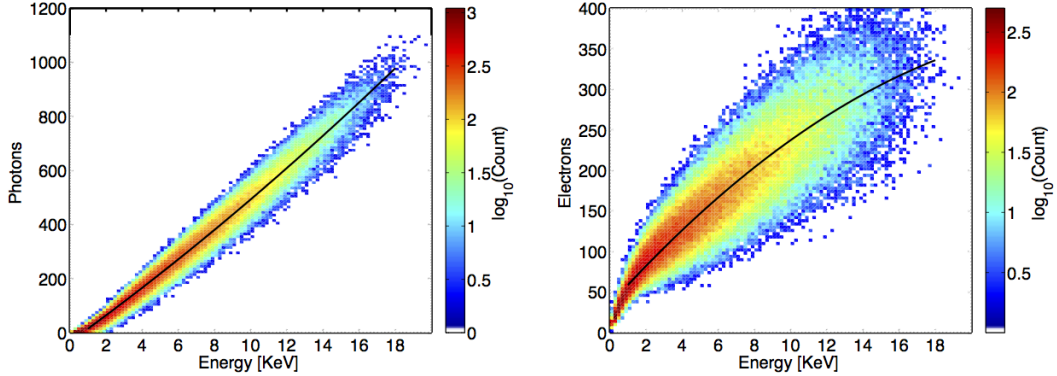


Figure 5.12: Light yield (left) and Charge yield (right) of a simulated tritium spectrum, with the fit to the centroid show in black. The variance in number of photon and electrons per energy bin is used to extract recombination fluctuations. Recombination fluctuations and detector resolution  $\chi_{\text{Det}}$  move events up and down along lines of constant energy.

The quadratic fit to both  $n_\gamma$  and  $n_e$  as a function of energy is used to subtract the centroid of the population calculating the variance in each energy bin. Making the centroid subtraction removes the additional term due to slope and bin width given in 5.41, allowing us to only dealing with  $\chi_{\text{Det}}$  without having to keep track of the energy bin size. Recombination fluctuations are calculated by binning the data in energy, extracting the raw variance in  $n_\gamma$  and  $n_e$  in each bin (identical to fitting a Gaussian) and subtracting off  $\chi_{\text{Det}}^2$ , following equation 5.46. The value of  $\chi_{\text{Det}}^2$  is explicitly,

$$\chi_{\text{Det}}^2 = M^2 \left( (1.04 \pm 0.26 \sqrt{n_e})^2 + \left( \frac{6.6 \pm 0.9}{100} n_e \right)^2 \right) + (M - 1)^2 \left( (3.45 \pm 0.17 \sqrt{n_\gamma})^2 + \left( \frac{6.4 \pm 1.7}{100} n_\gamma \right)^2 \right) \quad (5.47)$$

where the values of  $\sigma_{n_{\gamma_{\text{Det}}}}$  and  $\sigma_{n_{e_{\text{Det}}}}$  are taken from equation 5.17 and have been input to equation 5.36. Note, the value of M for the case of a continuous source should be taken from a fit to the slope of  $n_{\gamma}$  as a function of quanta (E/W). With equation 5.47 the value of  $\chi_{\text{Det}}$  in every energy bin is known, since we measure the mean value of  $n_{\gamma}$  and  $n_e$  for each. The result of extracting recombination fluctuations is shown in figure 5.13 for various energy bin widths.

We find good agreement between the recombination fluctuations extracted from the simulation to the true value. Importantly, we have demonstrated that the concept of  $\chi_{\text{Det}}$  that was introduced to deal with fluctuations in energy bins is in fact applicable to a continuous spectrum. We see in figure 5.13 that  $\chi_{\text{Det}}$  reduces to the detector resolution of the best quanta collection channel (S2 for LUX). This is exactly what we found from the examples with the  $^{83m}\text{Kr}$  line source and it is non-trivial that the result would hold for a continuous spectrum. Thus, as long as the recombination fluctuation are greater than  $\chi_{\text{Det}}$  the value of recombination can be determined to good precision even with a considerable error on  $\chi_{\text{Det}}$ , as the two fluctuations add in quadrature. The analytic solution for extracting recombination outlined in this section is sufficient to first order. We are now ready to apply this method to the tritium calibration data.

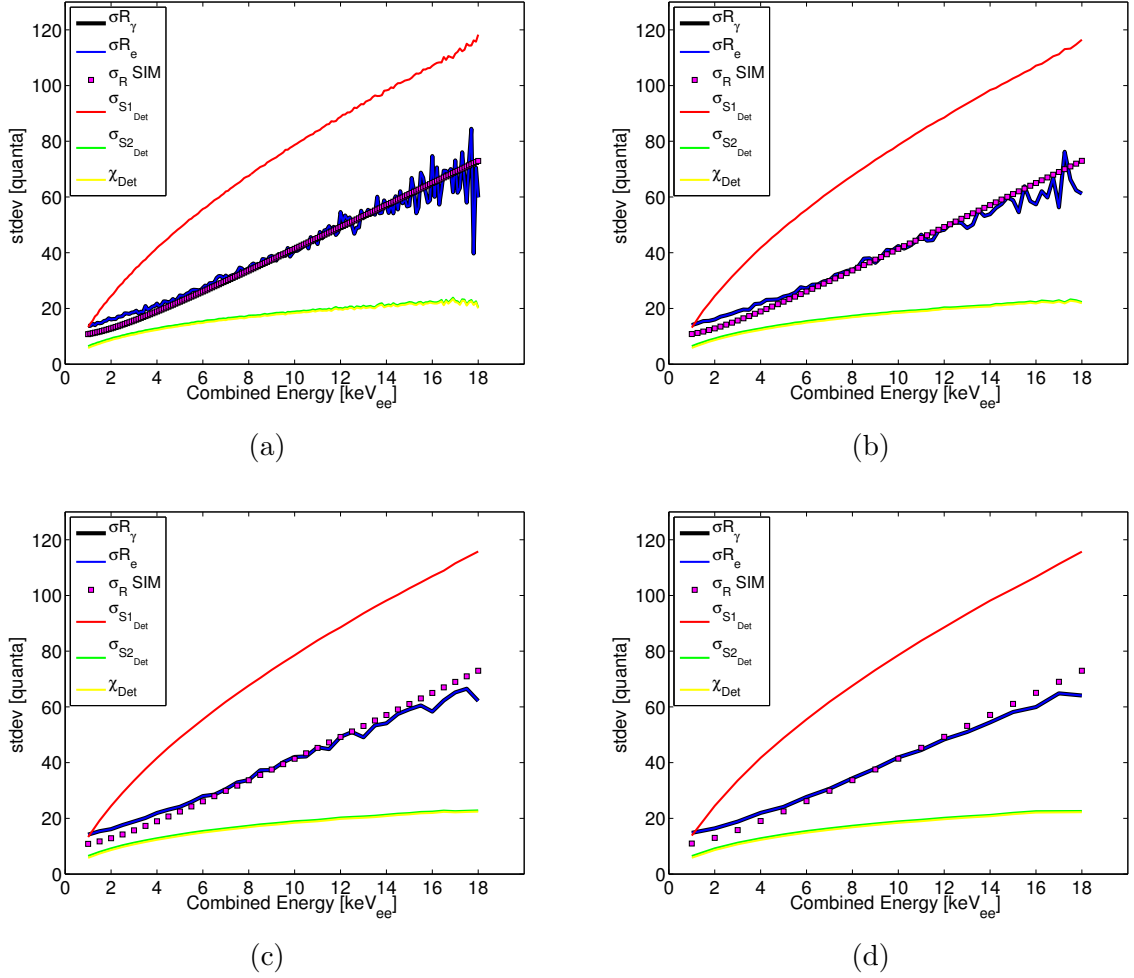


Figure 5.13: Simulated tritium spectrum with the detector resolution of the LUX detector and an initial guess of recombination fluctuations. The detector resolution, labeled as  $\sigma_{S1_{\text{Det}}}$  and  $\sigma_{S2_{\text{Det}}}$  is shown in red and green, respectively. The value of recombination fluctuation  $\sigma_R$  input into the simulation is shown in magenta. The methodology described in this previous section is applied to extract  $\sigma_R$  from the electron and photon spectrum, black and blue respectively. The statistical component of the standard deviation in each bin is  $\chi_{\text{Det}}$  is shown in green, equation 5.47. The plots show cases for various bin widths in keV: a)  $\Delta E = 0.1$  b)  $\Delta E = 0.25$  c)  $\Delta E = 0.5$  d)  $\Delta E = 1$ .

## 5.5 Extracting Recombination Fluctuations from Tritium Calibration Data

In this section we apply the methods outlined in this chapter and use them to extract the recombination fluctuations from the tritium data. The first step in this process was calibrate the energy scale solving for  $g_1$  and  $g_2$  as outlined in 4. Second, the S1 and S2 signals of the tritium calibration data have been corrected for spectral shape, as will be discussed in chapter 6.1. Finally, having modeled and measured the statistical and instrumented variances for light collection of the LUX detector 5.17, 5.15, 5.16 the amount of fluctuations from detector resolution on each energy contour is known, equation 5.47.

The events from the tritium calibration data are binned in energy and the mean value of S1 and S2<sub>b</sub> is calculated for each. The S1 and S2 signal is converted into mean number of photons and electrons using  $g_1$  and  $g_2$ . Using the mean number of photons and electrons in each bin the value of  $\chi_{\text{Det}}^2$  is calculated using 5.47. Next the total variance in the number of photons and electrons in each energy bin is calculated, defined as  $\chi_{n_\gamma}^2$  and  $\chi_{n_e}^2$  respectively. We then solve for  $\sigma_{R_\gamma}^2$  and  $\sigma_{R_e}^2$  given in equation 5.48,

$$\sigma_R^2 = \sigma_{R_\gamma}^2 = \sigma_{R_e}^2 = \chi^2 - \chi_{\text{Det}}^2 \quad (5.48)$$

where the subscripts  $\gamma$  and  $e$  denote counting photon and electron respectively. The density plot of  $n_\gamma$  and  $n_e$  is shown in figure 5.14 and the value of recombination

fluctuation is shown in 5.15, for both the 170 V/cm and 100 V/cm data. The 170 V/cm data contained 140,000 tritium beta decays in the fiducial volume and the 100 V/cm data contains 4,500 events.

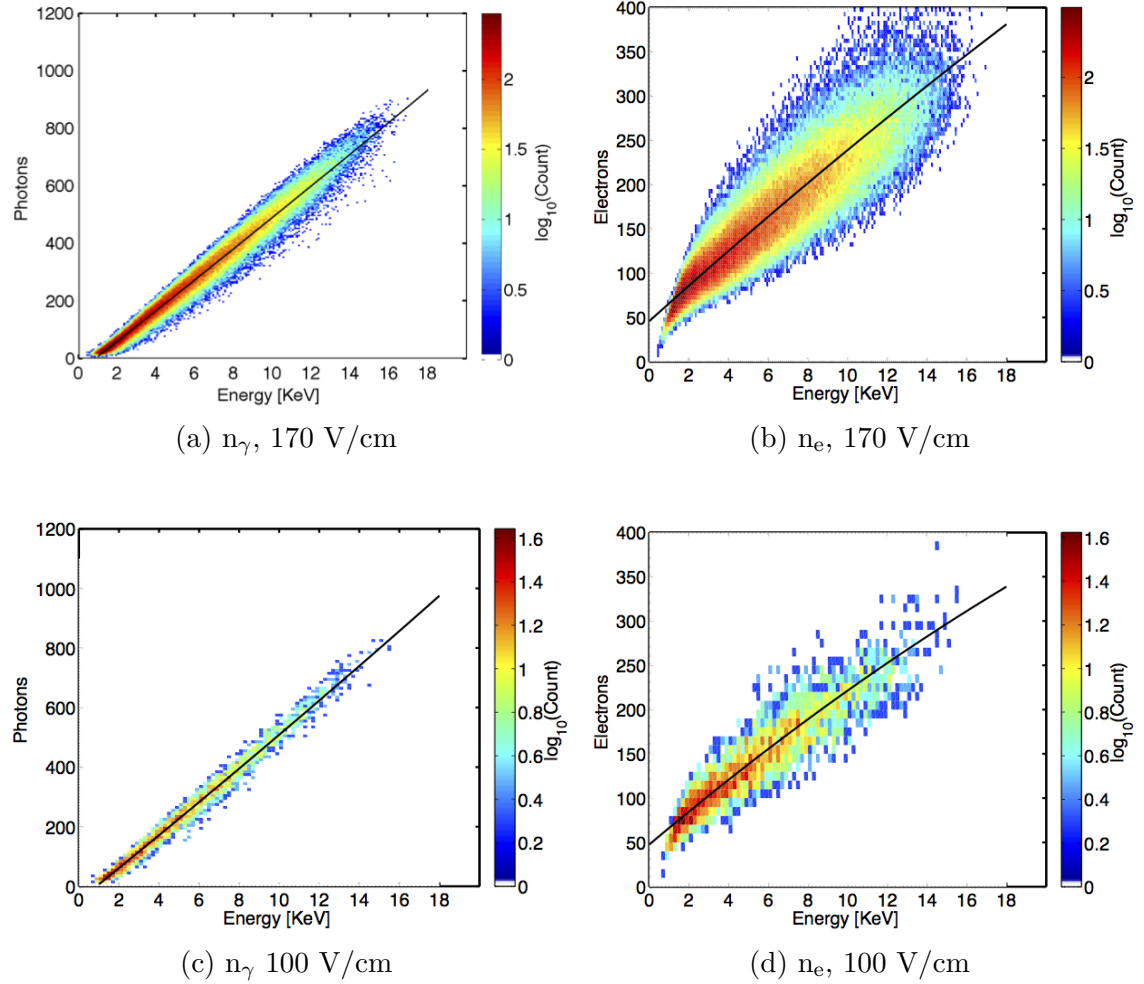


Figure 5.14: a: Density plot of number of photons vs. energy in keV using the tritium calibration data at 170 V/cm. b: Number of electrons vs. energy in keV using the tritium calibration data at 170 V/cm. c: Number of photons vs. energy in keV using the tritium calibration data at 100 V/cm. d: Number of electrons vs. energy in keV using the tritium calibration data at 100 V/cm. The data has been corrected for spectral shape. The black line indicates the quadratic fit to the centroid of the population.

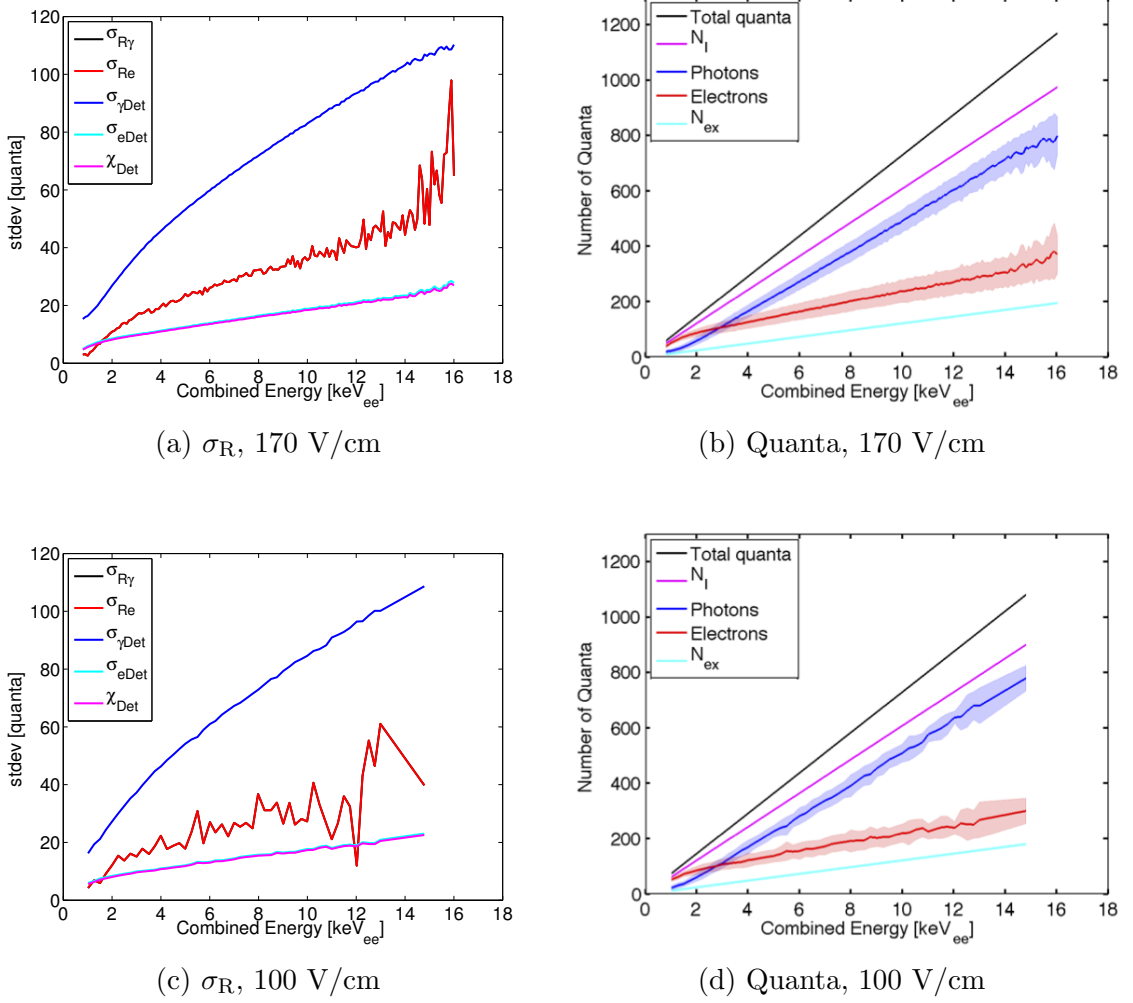


Figure 5.15: The figures on the left in 5.15 (a: 170 V/cm, c: 100 V/cm) show the extracted recombination fluctuation  $\sigma_R$  from the light (black) and charge (red) channel denoted with subscript  $\gamma$  and  $e$  respectively, note they are identical. Also shown are the fluctuations in light collection  $\sigma_{\gamma\text{Det}}$  (blue), charge collection  $\sigma_{e\text{Det}}$  (cyan), and their manifestation in a combined energy bin,  $\chi_{\text{Det}}$  (magenta). The figures on the right in 5.15 (b: 170 V/cm, d: 100 V/cm) show the mean and one sigma standard deviation of the measured number of photons (blue) and electrons (red). Also shown is the total quanta (in black) which is the sum of photons and electrons and the expected number of ions (magenta) and excitons (cyan) using  $\alpha = 0.20$ .

The figures on the left in 5.15 (a: 170 V/cm, c: 100 V/cm) show the extracted recombination fluctuation  $\sigma_R$  from the light (black) and charge (red) channel denoted with subscript  $\gamma$  and  $e$  respectively, note they are identical. Also shown is the

detector resolution of light collection  $\chi_{\sigma_{\text{Det}}}$  (blue), charge collection  $\sigma_{e_{\text{Det}}}$  (cyan), and their manifestation in an energy bin  $\chi_{\text{Det}}$  (magenta). In regions where the measured recombination fluctuations are larger than the fluctuations from  $\chi_{\text{Det}}$  any error from the constraint on  $g_1$  and  $g_2$  is negligible. At the higher energy bins the uncertainty grows as the measurements become statistics limited. The size of the bin to bin fluctuations represent the statistical errors. The figures on the right in 5.15 (b: 170 V/cm, d: 100 V/cm) show the total quanta (black) which is the sum of the photons (blue) and electrons (red) and the expected number of ions (magenta) and excitons (cyan), using the exciton-to-ion ratio  $\alpha = 0.20$ . Since  $\chi_{\text{Det}}$  is solved for in terms of photons and electrons the means of the of number of photons and electrons in each energy bin must be measured first.

### 5.5.1 Extracting Recombination fraction From Tritium Data

Having measured the mean number of photons and electrons in each bin, the recombination probability  $r_p$  can be determined by taking the average value of recombination, given in 5.23. Figure 5.16 shows the measurement of the recombination fraction  $r$  for the 170 V/cm and 100 V/cm tritium calibration data. The value  $r_p$ , or  $\langle r \rangle$ , defines the mean location of the ER band and is fundamental to the liquid xenon, at a given energy and electric field. The shaded region represents the one sigma of the recombination fraction, which can be thought of in terms of the recombination fluctuation  $\sigma_r = \sigma_R/n_{\text{ions}}$ . We find that the bands at 100 V/cm and 170 V/cm converge below 4 keV<sub>ee</sub> meaning that the light yields and charge yields also converge (discussed in chapter 6). Having extracted the apparent recombination probability  $r_p$  we can begin to think about recombination fluctuations in terms of a binomial process where an electron ion pair will either recombine or not with probability  $r_p$ .

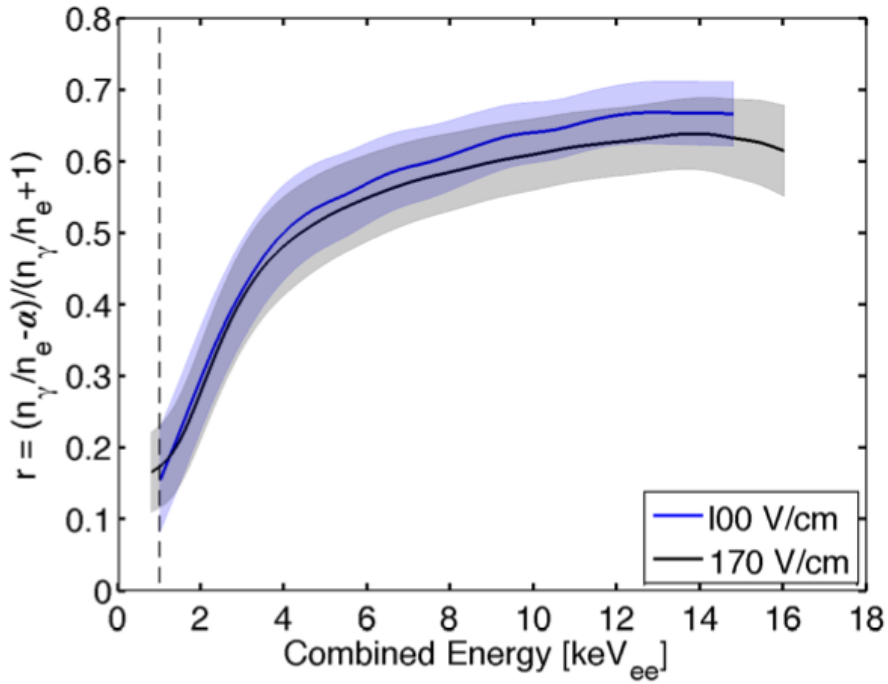


Figure 5.16: Recombination Fraction at 170 V/cm (black) and 100 V/cm (blue). The shaded regions represent the one sigma of the observed fluctuations in recombination fractions  $\sigma_r$ . The dashed line at 1.0 keV<sub>ee</sub> represents the 50% detection threshold.

### 5.5.2 Modeling the ER Band

The ultimate goal of this chapter, and the tritium calibrations, is to be able to make predictions about WIMP sensitivity at various electric fields in the WIMP search energies of interest, 1-5 keV<sub>ee</sub>. Having extracted  $r_p$  and the recombination fluctuations, we have the ability to reconstruct the electronic recoil band for liquid xenon as it would appear with infinite detector resolution. Starting with the recombination fluctuations, which are fundamental to the xenon, the base ER band can be modeled by adding the resolution of any detector. Using the mean and width of the

ER band along with the mean of the NR band we can make predictions for WIMP background rejection.

The mean of the ER band in the commonly used discrimination variable  $\log_{10}(S2_b/S1)$  can be written as a function of number of ions,

$$\log_{10}(S2_b/S1) = \log_{10} \left( \frac{(1-r)N_i}{(r+\alpha)N_i} \right) + \log_{10} \left( \frac{g_2}{g_1} \right) \quad (5.49)$$

where the observed charge and light signals  $S2_b$  and  $S1$  have been converted to recombination probability  $r$ , number of ions  $N_i$  and the exciton to ion ratio  $\alpha$  using equations 5.2, 5.3 and 5.19. The variance of the band can be written as,

$$\text{Var}_{\log_{10}(S2_b/S1)} = \frac{1}{(\log(10))^2} \times \sigma_R^2 \left( \frac{-(\alpha+1)}{(1-r)(r+\alpha)N_i} \right)^2 \quad (5.50)$$

Which has been written in terms of the number of ions  $N_i$ , the recombination fraction  $r$ , and the measured recombination fluctuation  $\sigma_R$ , defined to be  $\sigma_r \times N_i$ . The result of the ER band's mean population and its corresponding 1 sigma fluctuation are shown in figure 5.17 for the case of 100 V/cm (blue) and 170 V/cm (black). This result shows the ER band with recombination fluctuations only. One can add light and charge collection fluctuations in quadrature to complete the modeling specific to any detector.

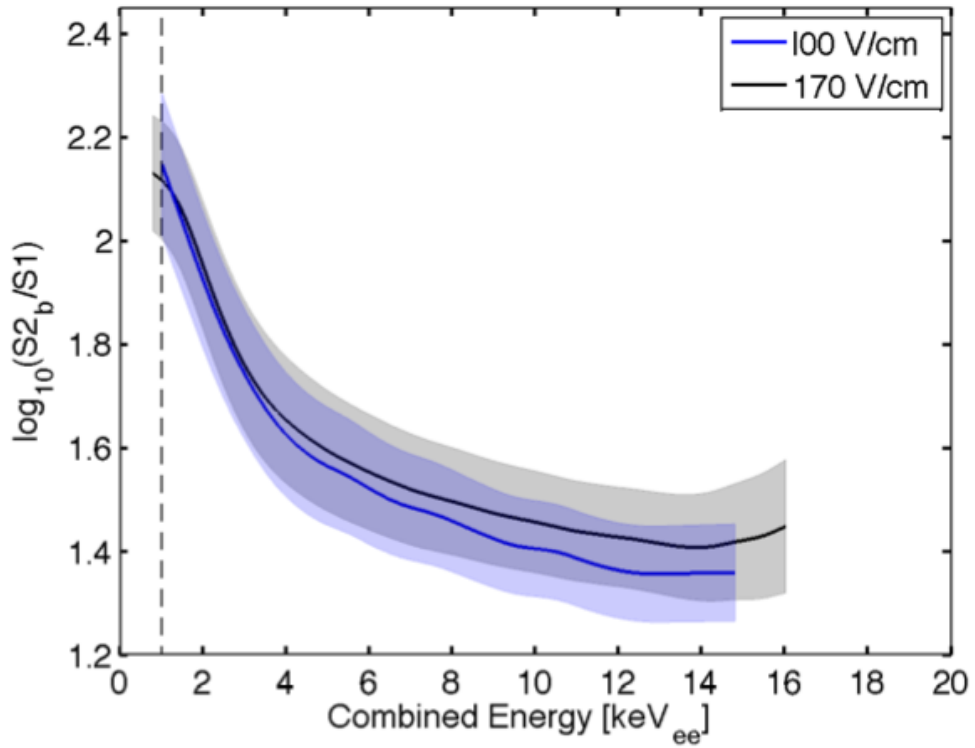


Figure 5.17: The result of the ER band's mean population and its corresponding 1 sigma fluctuation for the case of 100 V/cm (blue) and 170 V/cm (black). We find an overlap below 4 keV<sub>ee</sub> where the additional strength of the drift field is higher improving threshold of discrimination. Above 4 keV<sub>ee</sub> the band separate as the higher drift field increased the charge extraction leading to better discrimination.

## 5.6 Measuring Alpha From the Tritium Data

Having measured  $r_p$  and  $\sigma_r$  from the tritium calibration data the exciton to ion ratio  $\alpha$  determined by requiring that as the number of ions tends to one the recombination fluctuations tend to that of a binomial process. This is justified, as at low energies the handful of ion-electron pairs will either recombine or not with recombination

probability  $r_p$ . Such a process has a binomial variance written as,

$$\text{Var}_{\text{Bino}} = (1 - r_p)r_p N_i \quad (5.51)$$

where  $r_p$  is the recombination probability and  $N_i$  is the number of ions which can be thought of as the number of trials for the binomial process.

The value of alpha can be extracted by requiring that the recombination fluctuations  $\sigma_R^2$  tend to that of equation 5.51 for a small number of ions. In figure 5.18 the y axis shows the ratio of the measured recombination standard deviation( $\sigma_R$ ) to the standard deviation of a purely binomial process. The plot on the left shows the expected binomial standard deviation on the x axis. The best alpha is one in which the observed standard deviation converges with that of a binomial process as the binomial variance tends to 1. The figure on the right has the number of ions available for recombination on the x axis. As the number of ions approaches one the standard deviation of recombination should become that of a binomial process. A single ion will either recombine or not with probability  $r$ . The extrapolation is made by fitting the lowest energy bins above 90% threshold 1.3 to 3 keV. Going below the value of one on the y axis implies that recombining electron-ion pairs have a variance better than binomial, which is nonphysical if it is a random process. The best intercept converging to a purely binomial process is with  $\alpha = 0.18 \pm 0.02$ , consistent with the measurement in [49] and not 0.06 as used in [11]. Note, for this analysis we continue to use  $\alpha = 0.20$  as measured by [49].

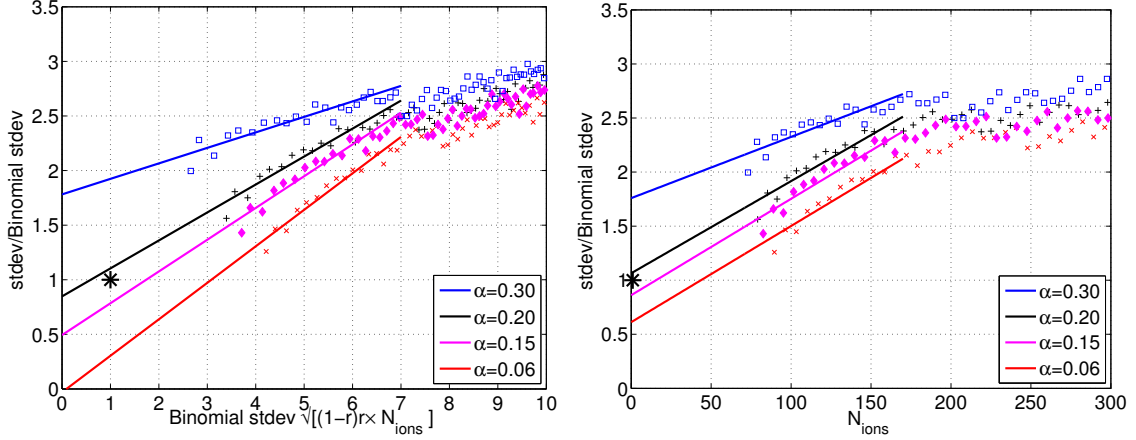


Figure 5.18: Determining the best  $\alpha$  using the tritium calibration data, with  $\alpha = 0.3$ (blue), 0.2(black), 0.15(magenta) and 0.06(red). Left: The y axis is the ratio of the measured standard deviation of recombination to that of a binomial processes and is plotted vs. the expected binomial standard deviation on the x axis. The best  $\alpha$  is one for which the observed standard deviation converges with that of a binomial process as the binomial variance tends to 1. Right, the same y axis as on the left but plotted vs. the number of ions available for recombination. As the number of ions approaches one the standard deviation of recombination should become that of a binomial process. A single ion will either recombine or not with probability  $r$ . The best intercept converging to a purely binomial process (black star) is with  $\alpha = 0.20$ . Falling below the value of one on the y axis implies that recombining electron-ion pairs have a variance better than binomial, which is nonphysical if it is a random process. Note, the fits use only data above 90% threshold at 1.3 keV, starting from the third data point from the left. The higher end cut off at 3 keV corresponds to the end of the fitted lines.

## 5.7 Extracting Recombination Fluctuations from $^{137}\text{Cs}$ Calibration

To expand the picture of recombination fluctuation to higher energies the same method used for the tritium calibration was applied to Compton scatters from an external  $^{137}\text{Cs}$  calibration source. The  $^{137}\text{Cs}$  source provides ER calibration data from the back-scatter peak around 150 keV to the photo peak at 662 keV. Figure 5.19 on the left shows the measured mean number of photons, electron in each energy bin along with their one sigma fluctuation (shaded). The number of excitons and

ions are also shown assuming an  $\alpha = 0.20$ . Once the mean number of photons and electrons are measured the recombination probability is determined and plotted on the right in figure 5.19. The inflection around 662 keV is due to the sharp rise and fall of the photo peak skewing the measurement of number of photons and electrons.

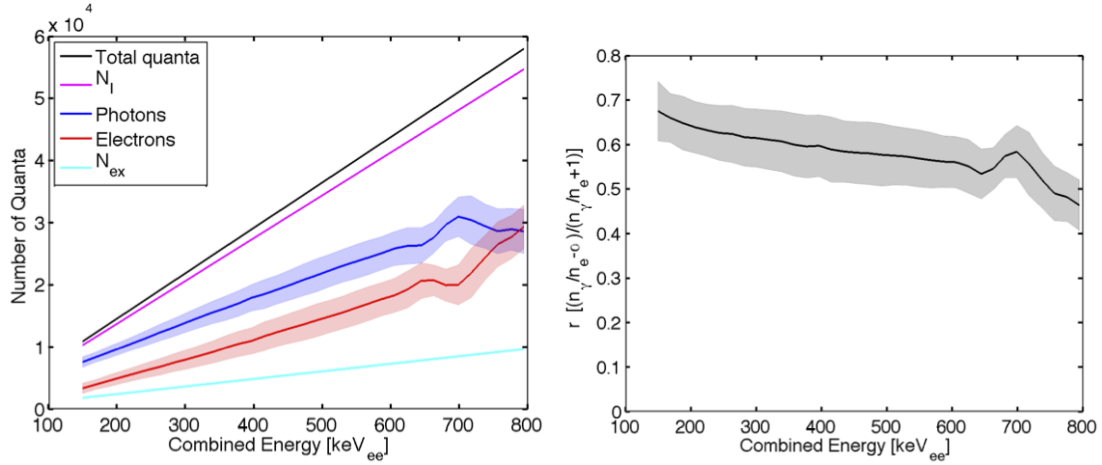


Figure 5.19: Left: The mean and one sigma standard deviation of the measured number of photons (blue) and electrons (red). Also shown is the total quanta (in black) which is the sum of photons and electrons and the expected number of ions (magenta) and excitons (cyan) using  $\alpha = 0.20$ . Right: The recombination probability  $r$  (solid black) and the one sigma fluctuation  $\sigma_r$  (shaded).

## 5.8 Recombination Fluctuations, The Bigger Picture

We have now measured the recombination probability and fluctuation over a wide range of energies and at two fields for tritium (100 and 170 V/cm). The calibrations range from the 1.0 keV with tritium to about 700 keV with  $^{137}\text{Cs}$ , and include the line sources used for the energy scale calibration in chapter 4 given in table 4.1. We also use data from a  $^{57}\text{Co}$  calibration at a variety of electric fields ranging from 60 to 5000 V/cm from a test detector[11].

The picture of the recombination process in liquid xenon is that it is binomial, essentially each electron-ion pair in an independent trial. The observed recombination fraction is thought to be the result of each electron-ion pair either recombining or not with some probability  $r_p$  , [62], [73], [74]. Though the modeling has been able to reproduce the recombination fraction, it has failed by orders of magnitude to reproduce the variance, as shown in figure 5.20. For a binomial system, given a recombination probability  $r_p$  the variance is

$$\text{Var}_{\text{Bino}} = (1 - r_p)r_p N_i \quad (5.52)$$

where  $\text{Var}_{\text{Bino}}$  represents the binomial variance,  $r_p$  is the recombination probability, and  $N_i$  is the number of ions and also the number of trials.

Figure 5.20 shows  $\sigma_R$  plotted against the number of ions available for recombination  $N_i$ . The x-axis is chosen to be number of ions as recombination fluctuations only act on ions and not excitons. The conversion to energy on the x axis is  $E = W \times n_i(1 + \alpha)$ . The black dashed line in the figure on the right shows the expected

standard deviation for a binomial process.

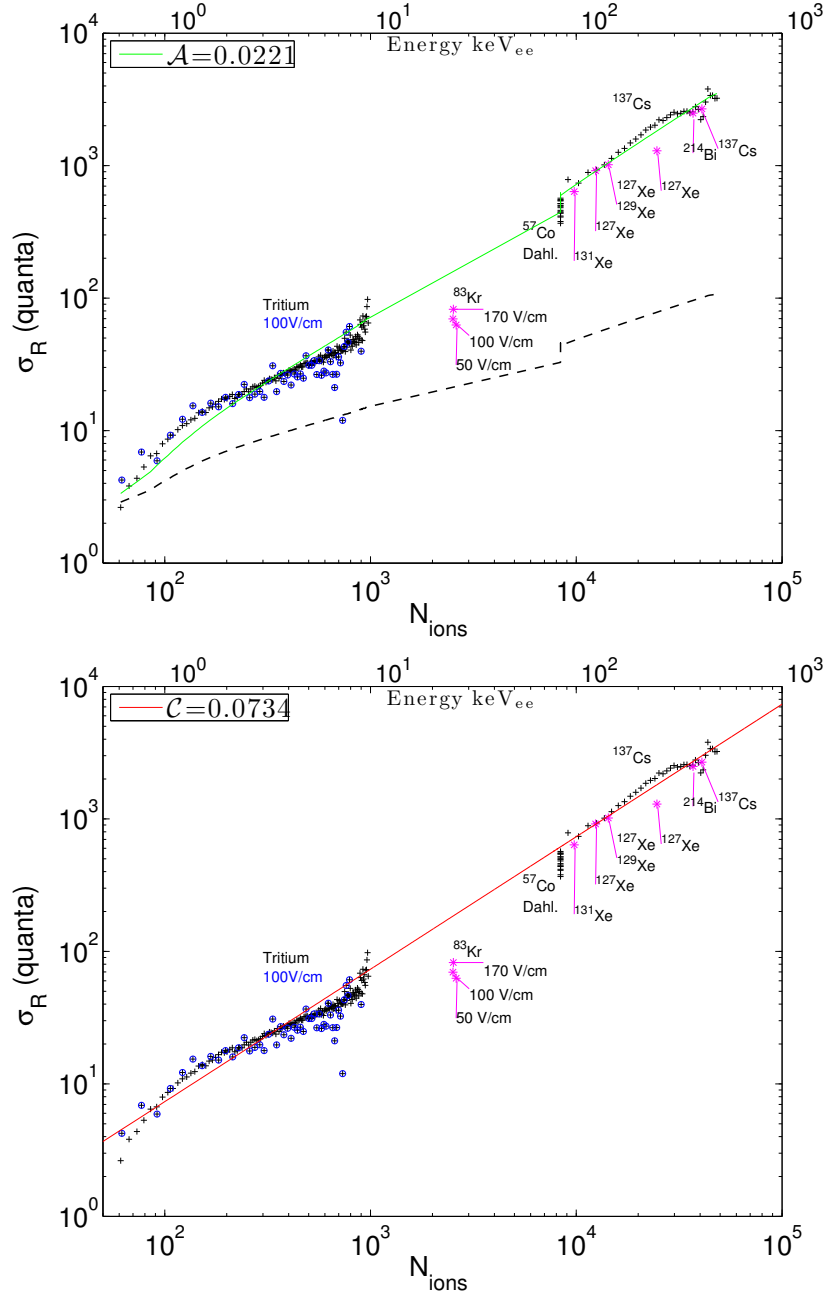


Figure 5.20: Recombination fluctuations (in quanta) vs. number of ions. The measurements include data from tritium at 170 V/cm, tritium at 100 V/cm,  $^{137}\text{Cs}$  calibration, the line sources used for the energy scale calibration listed in table 4.1 and a  $^{57}\text{Co}$  calibration at several electric fields ranging from 60 to 5000 V/cm from [11]. Top: Black dashed lines represent the values expected from a binomial process and the green line is a fit to the data with a constant amplification given in equation 5.53. Bottom: a linear fit to the data from equation 5.54. Note,  $^{83m}\text{Kr}$  is shown here is the combination of two decays and is expected to fall below the curve by 40%.

The data suggests that the size of the standard deviation  $\sigma_R$  grows linearly with respect to the number of ions. We fit to two cases, first assuming a “Binomial Amplification”,  $\mathcal{A}$ , described by

$$\sigma_R^2 = \text{Var}_{\text{Bino}} \times \mathcal{A} N_i \quad (5.53)$$

where  $\sigma_R^2$  is the measured recombination fluctuation in quanta<sup>2</sup>,  $N_i$  is the number of ions,  $\mathcal{A}$  is a constant and  $\text{Var}_{\text{Bino}}$  is from equation 5.52. We find from figure 5.20 that the data is fit to within 30% over the entire energy range with with a constant value of  $\mathcal{A} = 0.022$ .

There is no physical justification for the fit in figure 5.20 to the apparent binomial variance amplification,  $\mathcal{A}$ . Instead we fit a line to the standard deviation as a function of number of ions, described by

$$\sigma_R^2 = (\mathcal{C} N_i)^2 \quad (5.54)$$

where  $\mathcal{C}$  is the constant ratio of observed standard deviation,  $\sigma_R$ , to the number of ions,  $N_i$ . The value of  $\mathcal{C}$  is found to be 0.073. So the recombination fluctuations (the variance) appears to be growing like  $\frac{1}{185} \times N_i^2$ .

The  $N_i^2$  growth suggested by the data means there is a flaw in our recombination picture. The observed variance deviated from binomial by a factor of  $N_{\text{ions}}$ . There is another issue with the picture of electron-ion self recombination. The decline of recombination probability as the energy (or  $N_i$ ) tends to zero is nonphysical, yet is observed in the data, shown in figure 5.16. The probability of the electron

ion-pair to recombine should be insensitive to the number of electron-ion pairs created by the energy deposit. It is found that both ER and NR fluctuations can be well described by equation 5.54 [62]. Curiously, the exciton to ion ratio  $\alpha$  and the initial energy lost to heat for an NR is vastly different than for an ER event. This suggests something fundamental occurring during the recombination process that depends on the number of ions produced.

The the additional  $N_i$  term in the variance may be arising from an additional term in the recombination probability that allows for electrons to recombine with ions other than their own. Even a small term for an “encounter probability” could give rise to the correct variance [75]. The idea seems justified by observations from the  $^{83m}\text{Kr}$  source. The decay of the calibration source  $^{83m}\text{Kr}$  has been observed to receive an enhancement of several percent in the light yield of the second 9.4 keV following the first decay of 32.1 keV [70]. This can be attributed to the second decay occurring surrounded by a cluster of charge from the first decay, resulting in an enhanced encounter recombination probability and increased light yield. The shorter the timing separation between the two decays the greater the light yield enhancement, with light yield enhancement observed past 1000 ns [12], [13]. LUX data shows enhancement out to 2000 ns, as shown in figure 6.12. This lends evidence that freed electrons can be attracted to ions while diffusing from the interaction site on the time scales of hundreds of nano seconds. However, even with a small encounter probability one finds that for large values of  $N_i$  all the electron-ion pairs would annihilate, which is inconsistent with the observed recombination fraction. Perhaps a careful consideration of clustering could resolve this.

Another potential source of the fluctuation is the event to event variation of the exciton-to-ion ratio  $\alpha$ , which we have taken to be 0.20. If we allow for variations in the number of excitons of each track produced to fluctuate as  $\alpha = 0.2 \pm 0.09$  we would reproduce the correct variance. However, having the sigma of the number of excitons produced fixed to the mean values also seems nonphysical.

The growth of the variance as  $\frac{1}{185} N_i^2$  suggest that events may be being drawn from a narrow uniform distribution. We would like to improve upon the current NEST model [62] to be able reproduce both mean recombination fraction and also the correct variance from first principles. In future calibration, tritium calibration data taken at a wide range of fields may aid in producing better modeling.

## 5.9 Conclusion

There have been numerous steps in this chapter culminating in expanding our knowledge by extracting as much information as possible from the calibration sources. We have described statistical fluctuations in the S1 and S2 signal which result from detector resolution. Next, line sources were used to extract recombination fluctuations and the instrumental component of signal fluctuations. Finally, we discuss the methodology to extract recombination from continual sources and use it for the tritium and  $^{137}\text{Cs}$  data.

The best fit to the exciton-to-ion ratio was found to be  $\alpha$  of  $0.18 \pm 2$ , consistent with the measurement from [49]. The value of alpha was constrained by extrapolating the recombination fluctuations from the tritium data from 3 to 1.2 keV and

requiring that for a single ion-electron pair the fluctuation be purely binomial, shown in figure 5.18.

The recombination data measured in this section can be used to predict the ER band for any xenon detector (at 170 V/cm), as shown in figure 5.17. It is surprising to find that changing the drift field from 100 V/cm to 170 V/cm had only a small impact on the mean of ER band below 4 keV<sub>ee</sub>, figure 5.17. Further, there was no impact on the energy threshold since the light and charge yields merge at the threshold of 1 keV. A more dramatic field dependence was expected from [11] and [62]. To expand upon the modeling of the recombination process in xenon, at low energies, it will be useful for the next science run using the LUX detector to take tritium calibration data at a variety of fields.

## Chapter 6: Ionization and Scintillation Yields of Liquid Xenon at Low Energy

In this section we measure the scintillation yield and ionization yield from the tritium calibration data. Using the measurement of gains  $g_1$  and  $g_2$  in chapter 4, the average number of photons, electrons and the corresponding combined energy can be determined. With that information the light yield ( $n_\gamma/\text{keV}$ ) and charge yield ( $n_e/\text{keV}$ ) are extracted from tritium data down to 1 keV<sub>ee</sub>. Before the yields can be measured, the effect of finite detector resolution convolved with the tritium spectral shape must be accounted for. Detector resolution was characterized in chapter 5 and will be used to model the smeared tritium spectra as observed by the LUX detector. Once the spectral shape has been corrected we report the values of light yield and charge yield measured at 170 and 100 V/cm. The results are compared to two recent measurements for light yield in the keV range using Compton scatters. This provides a crucial cross check that the ER band calibration using the tritium beta source is valid for use with the more generic backgrounds found in WIMP search data consisting of Compton scatter from high energy gammas. At low energies the light yields and charge yields from betas and gammas are expected to be identical [61] [62].

## 6.1 Correcting for the Spectral Shape for Finite Resolution

The distribution of tritium events convolved with the detector's finite resolution for S1 (scintillation) and S2 (ionization) causes the observed mean of the spectra to shift from the actual mean. The shift is non-trivial and depends on the spectral shape and the functional form of the resolution over a range of energies. A large negative derivative of the spectral shape will tend to pull the observed mean to lower values, and a large positive slope will pull the observed mean to higher values. Figure 6.1 and equations 6.2 and 6.4 demonstrate a simple model to solve for the relation between observed mean and actual mean. Consider, for example, a linearly declining distribution. Starting with infinite detector resolution we set up bins of width  $\Delta x$ . To account for finite energy resolution we distribute the counts in each rectangular bin into Gaussians centered at  $\mu_i$ , with a spread of  $\sigma_i$ , and normalized to the area of the bin  $N_i \times \Delta x$  with amplitude  $c_i$ . Each rectangular bin( $i$ ) can be written as a Gaussian  $G(i)$ :

$$c_i = \frac{N_i \times \Delta x}{\sigma_i \sqrt{2\pi}}$$

$$G_i(x) = c_i \times \exp\left(\frac{-(x - \mu_i)^2}{2\sigma_i^2}\right)$$
(6.1)

where  $N_i$  is the count in the  $i^{\text{th}}$  bin,  $\Delta x$  is the bin width,  $\mu_i$  is the bin center and  $\sigma_i$  is the resolution at the  $i^{\text{th}}$  bin. Figure 6.1 show the application of equation 6.1 to a

linear energy distribution with a  $\sqrt{E}$  dependent  $\sigma$ . The observed distribution is the sum of the Gaussians, shown in red.

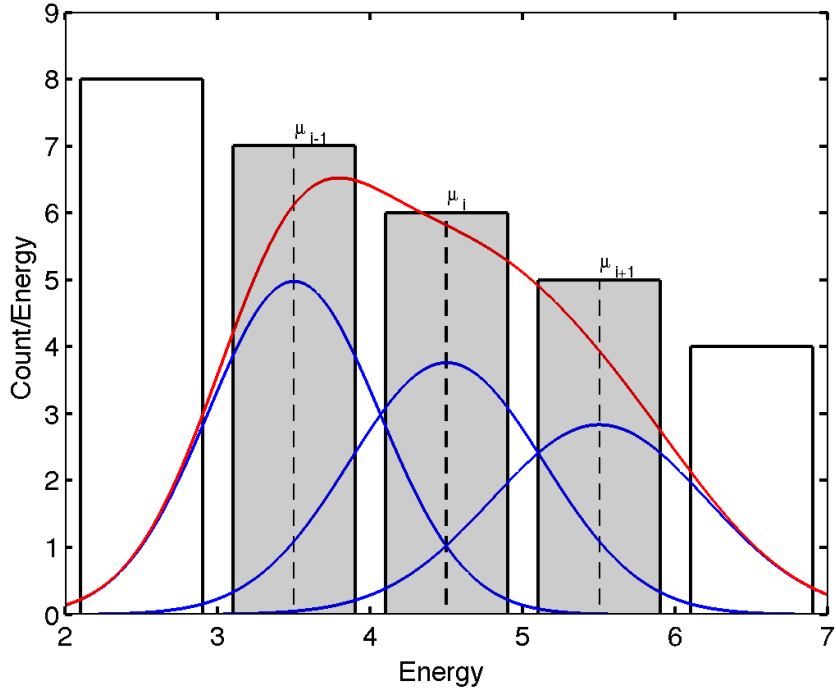


Figure 6.1: Smearing of a linear spectrum using equation 6.1 for an arbitrary energy scale  $E$ . The counts in each shaded bin are redistributed into normalized Gaussians (blue) with the resolution  $\sigma_E$  growing like  $\sqrt{E}$ . The spectrum smeared with detector resolution is the sum of Gaussians shown in red.

### 6.1.1 Calculating the Observed Energy

After modeling the finite resolution with Gaussians the mean observed at each bin can be calculated from the overlap of all bins weighted by the corresponding means. We can write the observed mean in the  $i^{\text{th}}$  bin,  $\nu_i$ , in terms of the bin centers  $\mu$  and

overlapping areas of all bins using the normalizations  $c_i$  from equation 6.1:

$$\nu_i = \frac{\sum_{j=1}^n \mu_j \int_{\mu_i - \frac{\Delta x}{2}}^{\mu_i + \frac{\Delta x}{2}} G_j(x) dx}{\sum_{j=1}^n \int_{\mu_i - \frac{\Delta x}{2}}^{\mu_i + \frac{\Delta x}{2}} G_j(x) dx} \quad (6.2)$$

Equation 6.2 can be solved in terms of error function and complimentary error function. First we will generalize a formula to solve for the overlapping area from the  $j^{\text{th}}$  bin into the  $i^{\text{th}}$  bin.

$$A_{i,j} = \int_{\mu_i - \frac{\Delta x}{2}}^{\mu_i + \frac{\Delta x}{2}} G_j(x) dx = \begin{cases} c_i \operatorname{erf}\left(\frac{\Delta x}{\sigma_i \sqrt{2}}\right), & j = i \\ \frac{c_j}{2} \operatorname{erfc}\left(\frac{|\mu_j - \mu_i| - \frac{\Delta x}{2}}{\sigma_j \sqrt{2}}\right) - \frac{c_i}{2} \operatorname{erfc}\left(\frac{|\mu_j - \mu_i| + \frac{\Delta x}{2}}{\sigma_j \sqrt{2}}\right), & j \neq i \end{cases} \quad (6.3)$$

The error function and complementary error function are defined in equation 6.4 and the coefficient  $c_i$  is defined in equation 6.1.

$$\begin{aligned} \operatorname{erf}(x) &= \frac{2}{\sqrt{\pi}} \times \int_0^x \exp(-t^2) \\ \operatorname{erfc}(x) &= \frac{2}{\sqrt{\pi}} \times \int_x^\infty \exp(-t^2) = 1 - \operatorname{erf}(x) \end{aligned} \quad (6.4)$$

As  $\mu$  approaches zero the Gaussian distribution of equation 6.1 begins to spill over into negative values, which in some cases may be nonphysical. For instance, the Gaussian assumption leads to negative photons. We can chose to ignore this area or make the distribution more Poisson-like by bouncing the Gaussian back at  $\mu = 0$ .

The formula for accounting for the area of the reflected Gaussian is described in 6.5. Ultimately this assumption has little impact on the S1 and S2 analysis because the threshold cut off well before the zero interface is reached, but it does make the distributions more Poisson like near the zeroth bins. Equation 6.5 is the same as 6.3 with the bin center  $\mu_i$  mapped to  $-\mu_i$ .

$$B_{i,j} = \frac{c_j}{2} \operatorname{erfc} \left( \frac{|\mu_j + \mu_i| - \frac{\Delta x}{2}}{\sigma_j \sqrt{2}} \right) - \frac{c_j}{2} \operatorname{erfc} \left( \frac{|\mu_j + \mu_i| + \frac{\Delta x}{2}}{\sigma_j \sqrt{2}} \right) \quad (6.5)$$

Finally, we solve for the observed mean in the  $i^{\text{th}}$  bin by summing all the Gaussian overlaps  $A_{i,j} + B_{i,j}$  (equations 6.3,6.5), weighting the overlapping area from each bin by the corresponding bin center  $\mu_j$ . The result is shown in equation 6.6 and is equivalent to equation 6.2 when the area from the reflected Gaussian is not considered,  $B_{i,j}=0$ .

$$\nu_i = \frac{\sum_{j=1}^n \mu_j \cdot (A_{i,j} + B_{i,j})}{\sum_{j=1}^n (A_{i,j} + B_{i,j})} \quad (6.6)$$

### 6.1.2 Smearing a Toy Spectrum

To demonstrate the application of equation 6.6 we use it to smear a toy linearly decaying spectrum. By modifying the dependence of  $\sigma_i$  on  $\mu_i$  we can better understand the effects of the spectral shape and the functional form of the resolution.

Figure 6.2 shows the effect of the finite resolution on a linearly decaying spectral shape. Using a constant resolution  $\sigma$  the observed mean, when accounting for finite resolution, shifts down due to the spectral shape. In the case with  $\sigma_i \sim \sqrt{\mu_i}$

the observed mean at first shifts higher as the increasing width at higher value bin centers, even with lower counts, out weighs the lower bin centers with higher counts and narrower widths. In both cases as the bin centers approach zero the observed mean shifts higher due to an imposed threshold at zero, where Poisson statistics take over and the Gaussian characterization leads to a loss of events below zero. Thus, for the sake of the toy model in figure 6.2 we only characterize the relation between the real mean and the observed mean from the second bin center. It is also worth mentioning that for the case of having a varying resolution in figure 6.2 the shift in spectral shape seems minor, yet there is a significant 20% deviation in the observed mean of the last bin.

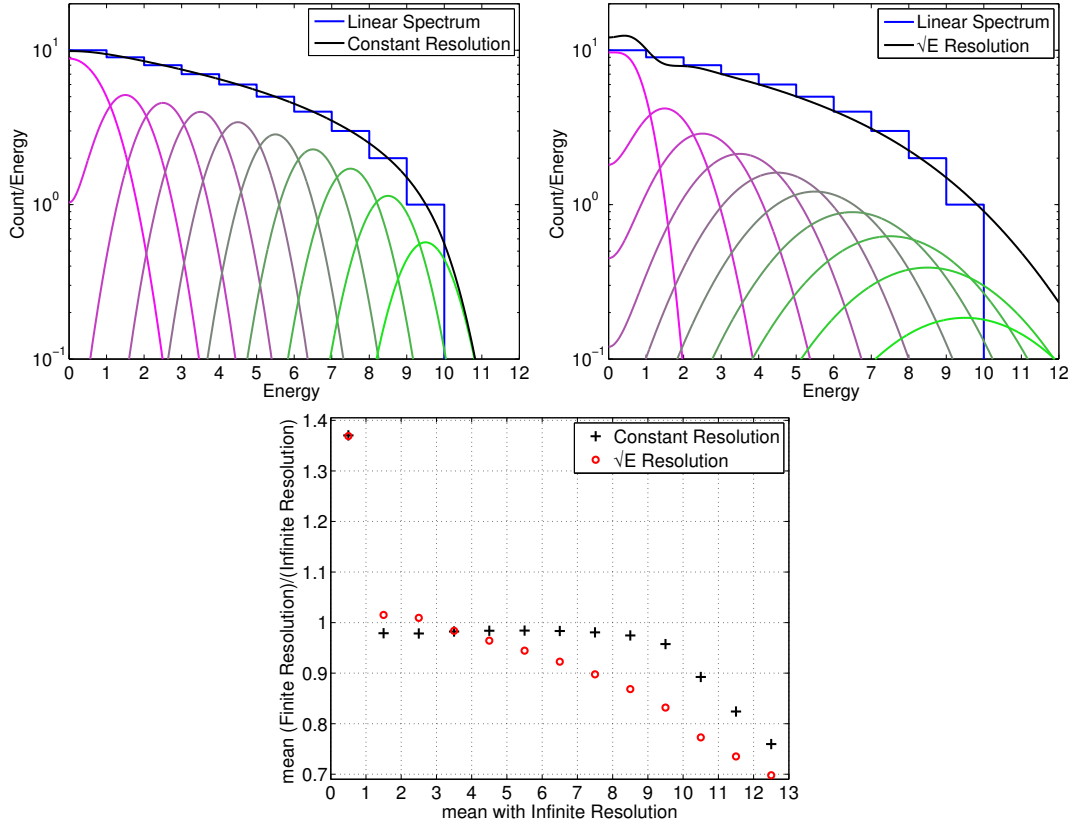


Figure 6.2: Top Left: A linearly decaying spectrum, in blue. The black curve represents the sum of the Gaussians assuming a constant resolution. Top Right: A linearly decaying spectrum, in blue. The black curve represents the sum of the Gaussians with a  $\sigma = \sqrt{E}$  dependent resolution. Bottom: The observed mean, with finite resolution, compared to the real mean with infinite resolution. The black points are for the case with linear resolution and the red points represent the case with  $\sigma = \sqrt{E}$  dependent resolution.

## 6.2 Light Yield, Charge Yield and Comparison to NEST Modeling

The first attempt to remove the effect of the tritium spectral shape and finite detector resolution is to use the NEST model from [62]. NEST stands for Nobel Element

Simulation Technique. NEST fits data from previous xenon and argon detectors to recombination models, producing predictions for light yield  $n_\gamma/\text{keV}$  and charge yield ( $n_e/\text{keV}$ ) at a verity of electric fields, energy deposits, and particle types. We take the light yield (LY) and charge yields (QY) from NEST and convolve it with the known tritium energy spectrum to produce the S1 and S2 spectra. The S1 and S2 spectra are then smeared with detector resolution and recombination fluctuations, determined in chapter 5. It is found that the S1 and S2 spectra from the data deviate from the NEST model making it difficult to reverse-engineer the effect of smearing. However, taking the NEST model to be correct within 20%, the spectral shape correction is calculated and found to be small. We proceed to extract LY, QY and recombination fluctuation ( $\sigma_R$ ) from the tritium data without any correction producing a model that is more accurate than NEST. It should be noted that the NEST model which has not been confirmed at our electric field and energy.

### 6.2.1 Tritium S1 and S2 vs. NEST

The spectral shape correction for the mean of the observed S1 and S2 signal from tritium beta decay can be found using equation 6.6. We start with NEST to get the expected S1 and S2 tritium spectrum. The variance of S1 and S2 arise from recombination fluctuations and detector resolution (statistical and instrumental fluctuations), given in equation 5.15 and 5.16. We use equations 6.7 and 6.8 to smear the photon and electron yields, essentially putting in detector resolution by hand. Then, by applying equations 6.1-6.6 the S1 and S2 bin centers after smearing can

be mapped back to the true bin centers before smearing.

$$\begin{aligned}\sigma_{S1_R}^2 &= g_1^2(\sigma_R^2) \\ \sigma_{S1_{\text{Det}}}^2 &= g_1^2(\sigma_{n_{\gamma_{\text{stat}}}}^2 + \sigma_{n_{\gamma_{\text{inst}}}}^2) \\ \sigma_{S1}^2 &= \sigma_{S1_R}^2 + \sigma_{S1_{\text{Det}}}^2\end{aligned}\tag{6.7}$$

$$\begin{aligned}\sigma_{S2_R}^2 &= g_2^2(\sigma_R^2) \\ \sigma_{S2_{\text{Det}}}^2 &= g_2^2(\sigma_{n_{e_{\text{stat}}}}^2 + \sigma_{n_{e_{\text{inst}}}}^2) \\ \sigma_{S2}^2 &= \sigma_{S2_R}^2 + \sigma_{S2_{\text{Det}}}^2\end{aligned}\tag{6.8}$$

where  $g1$  and  $g2$  are the gains to convert S1 and S2 to number of photons and electrons, respectively. The values  $\sigma_{S1_R}^2$  and  $\sigma_{S2_R}^2$  are the variances in S1 and S2 given only recombination fluctuations, this is what a detector with infinite resolution would observe. Detector resolution is comprised of the statistical and instrumental fluctuations in light and charge collection written as  $\sigma_{S1_{\text{Det}}}^2$  and  $\sigma_{S2_{\text{Det}}}^2$ , this would be the resolution given no recombination fluctuations. The total variance in S1 and S2 observed by a detector with finite resolution is the sum of recombination fluctuations and detector resolution  $\sigma^2 = \sigma_R^2 + \sigma_{\text{Det}}^2$  (where the subscripts S1 and S2 have been removed). The use of Gaussian sigma down to low S1 is an acceptable approximation since the underlying distribution actually consists of the number of photons,  $n_\gamma = \frac{S1}{g1}$ . With  $g1=0.097$  there are still 30 photons near the S1 threshold of 3 PE. The S2 threshold for golden events is around 400 PE,  $n_e = \frac{S2}{g2}$ . With  $g2=5.75$  there are still 70 electrons near the lower end of the tritium spectrum.

Figure 6.3 (a,c) shows the application of smearing from equation 6.7 and 6.8

to the expected S1 and S2 tritium spectrum, respectively, overlaid with the data. The mapping of the observed S1 and S2 mean values to the real S1 and S2 mean values is shown in 6.3 (b,d). The mapping from observed mean to real mean is the result of starting with infinite resolution containing recombination fluctuations only ( $\sigma_R$ ) and applying the model as outlined in 6.1 with detector resolution ( $\sigma_{\text{Det}}$  of equations 6.7 and 6.8).

We find that that peak location of the S2 spectra from NEST deviates from the data by up to 20%. These discrepancies maybe arising from the error in  $g_1$  and  $g_2$  which could systematically shift light yield and charge yield by the appropriate amount. However, modifying  $g_1$  and  $g_2$  only induces a horizontal shift left or right, and the data indicates the need to modify the derivative of LY and QY from NEST.

Since the means of the model do not line up with the data the calculated corrections in figure 6.3 can't be applied. In order to account for detector resolution as outlined in section 6.1 we must have a reasonably accurate initial guess of the spectrum with infinite resolution. In this case we do not. However, even though the means from NEST light and charge yields are off we find that the effect of recombination fluctuations and detector resolution is relatively small. The correction for the S1 ranges from +30% to -20% and the S2 correction from +2% to -10%. We takes these as small enough to proceed with extracting light yield, charge yield and recombination without any correction in order to construct a more accurate model than our initial NEST prediction. Having outlined a method for mapping the observed S1 and S2 means to their real values we will now gauge the effect of finite resolution on the observed total energy.

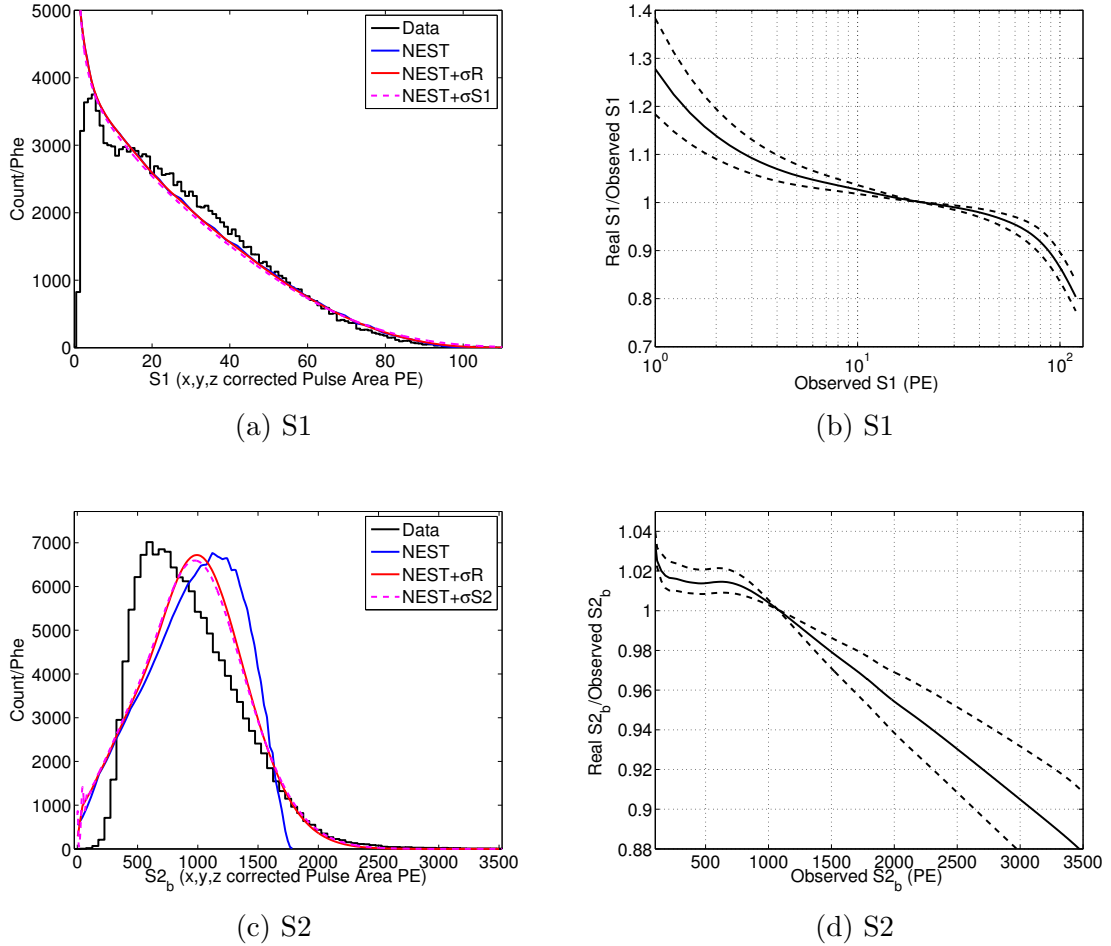


Figure 6.3: a): In Black S1 tritium S1 spectrum extracted from the data. In blue, The NEST light yield curve. In red, the NEST light yield curve with recombination fluctuations. Dashed magenta is NEST light yield with smearing from equations 6.7. b): The ratio of the real S1 mean to the S1 observed mean vs. the observed mean after smearing. Note, the S1 threshold at about 3 PE in S1. c): In Black S2 tritium spectrum extracted from the data. In blue, The NEST light yield curve. In red, the NEST light yield curve with recombination fluctuations. Dashed magenta is NEST light yield with smearing from equations 6.8. d): The ratio of the real S2 mean to the S2 observed mean vs. the observed mean after smearing.

## 6.2.2 Tritium Energy Spectrum

Unlike the S1 and S2 spectra which are dependent on light and charge yield, the tritium energy spectrum is well known [17]. The tritium spectrum is perhaps the most studied beta spectra, so there is no need to rely on modeling. Also, recombination

fluctuations cancel out in combined energy space leaving only detector resolution to be applied for smearing, given equation 6.11. The accuracy of the smearing model described in equations 6.1-6.6 can be tested by comparing it against the energy observed after a full simulation, which accounts for detector geometry and having been processed by the full offline framework. Using equation ??, ?? and 6.9 we solve for the the variance of E ( $\sigma_E^2$ ),

$$E = W(n_\gamma + n_{e^-}) \quad (6.9)$$

$$\sigma_E^2 = W^2(\sigma_{n_\gamma}^2 + \sigma_{n_{e^-}}^2) \quad (6.10)$$

$$\sigma_E^2 = W^2(a_\gamma^2 n_\gamma + a_e^2 n_{e^-}) \quad (6.11)$$

W is the work function  $0.0137 \pm 0.002 \frac{\text{keV}}{\text{N}_{\text{quanta}}}$ ,  $n_\gamma$  and  $n_e$  and number of photons and electrons respectively. The constants  $a_\gamma$  and  $a_e$  represent the coefficients of the  $\sqrt{n}$  term for the statistical uncertainty given in equation 5.15. There is also an instrumental component which is proportional to  $n_\gamma$  and  $n_e$ . However, the instrumental term is sub-dominant at the low tritium energies with coefficients given in equation 5.16.

Starting with the tritium energy spectrum with infinite resolution we apply the empirically determined resolution in equation 6.11. Figure 6.4 shows the comparisons of the true tritium spectrum, the spectrum with smearing from equation 6.11, the expectation from LUXSIM and the data. The smearing from the model described in equations 6.1-6.6 is found to be almost identical to the output of LUXSIM.

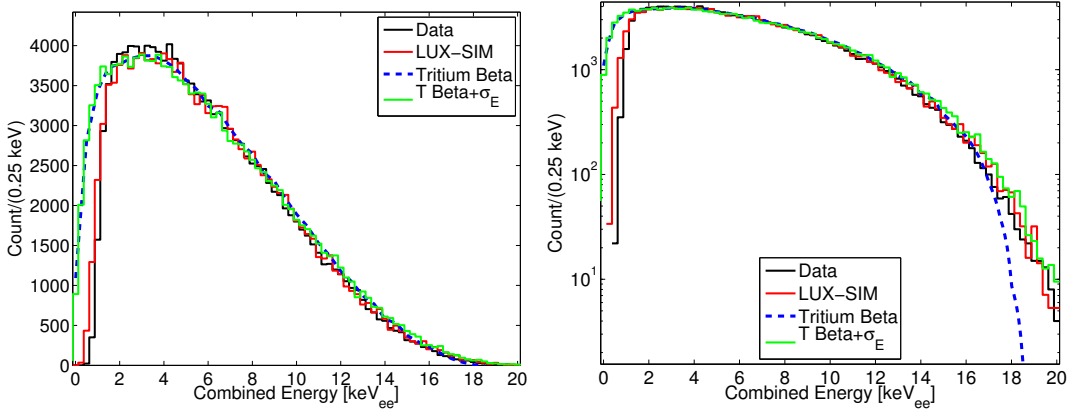


Figure 6.4: The tritium energy spectrum reconstructed from the data (black). Along with LUX SIM (red), the true tritium beta spectrum (dashed blue) and a tritium spectrum smeared with detector resolution of equation 6.11 (green).

Comparing the true tritium spectrum, the data, LUXSIM and the spectrum with 6.11, we find that for the cases with finite resolution the endpoint flare out above 16 keV. With the endpoint reaching out past 20 keV instead of terminating at 18.6 keV. This effect is precisely what the modeling in section 6.1 attempts to undo. Clearly events observed at 20 keV must have fluctuated up from bins below the tritium endpoint at 18.6 keV [71]. Most importantly, besides the additional fluctuation around the endpoint the difference in spectral shape after accounting for finite resolution is hardly noticeable.

The mapping for observed energy to true energy is calculated for both LUXSIM and the simpler smearing model of equation 6.11. From the LUXSIM data the initial Monte Carlo values of each event are compared to the final reconstructed energies. Each energy deposit is simulated with photon and electron propagation along with light collection in the LUX detector. Figure 6.5 shows the results for mapping

observed energy to real energy using both smearing methods.

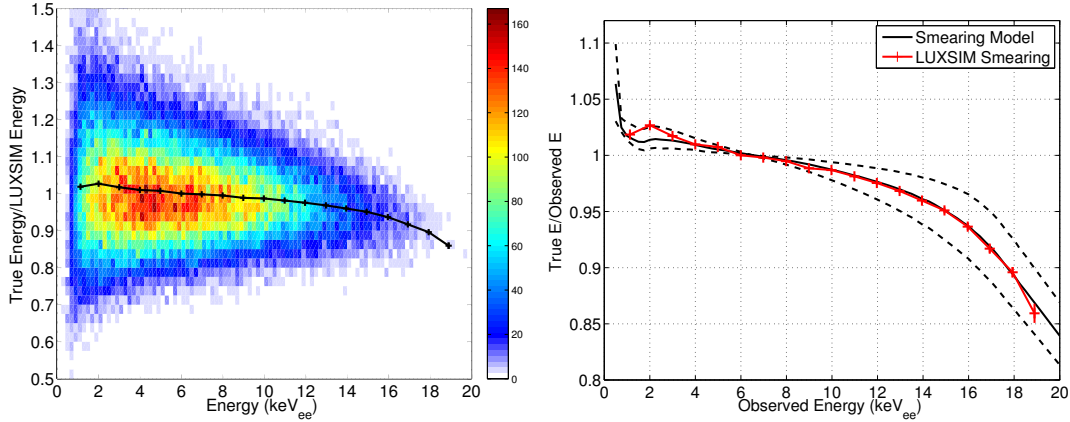


Figure 6.5: Left, mapping from real Monte Carlo energy to observed energy plotted vs the observed energy after applying a finite resolution using LUXSIM. Right, comparing the correction determined from the Monte Carlo (Red) to the detector smearing model (black) given in equation 6.11. The dashed lines represent the uncertainty in the measured values. The agreement is within errors from 1 to 18 keV<sub>ee</sub>. The Energy threshold is 50% at 1.0 keV<sub>ee</sub>.

The shift in the observed mean from the true mean for both LUXSIM and the model of equation 6.11 are in good agreement down to the threshold of 1.5 keV, the agreement with simulation is always within 1%. Below 2 keV the model predicts the ratio of true energy to observed energy to rise as there are greater number of events at higher energy spilling over to lower energy. The simulation however does not show this behavior leading to a 5% discrepancy in the 1 keV bin. Comparing the modeled detector resolution to the more complex LUXSIM simulations provides a proof of principle of the model.

The effect of detector resolution on skewing the true energy to observed energy

is found to be minor, blowing up only at the tail end of the tritium spectrum. Over 95% of the tritium event occur between 1 and 15 keV were the correction is less than 5%. With this information we proceed with extracting light and charge yields without concern about incorrectly assigning the energy bin.

### 6.2.3 Results for Light Yield, Charge Yield and Recombination

As shown in figure 6.3 the S1 and S2 spectral shape is not a good match with the light yield model from NEST, thus applying a correction to the observed means using NEST is not prudent. Fortunately, both for the S1 and S2 the spectral shape correction is less than 10% in the region where the vast majority of the tritium events are populated. Further, the reconstructed energy is also valid to within 5%. Knowing this we can move forward with extracting a more accurate light yield and recombination fluctuations.

By the same method outlined in section 5.5, the number of photons, electrons and recombination fluctuation is extracted from the tritium data. This is the result of the raw data uncorrected for the spectral shape. The result is shown in figure 6.6.

Having measured number of photons, electrons in each energy bin we compare the tritium data to NEST yields, shown in figure 6.7. The disagreement between the data and the NEST yields was expected since before the S1 and S2 tritium spectrum did not line up, shown in figure 6.3 . Though the means do not match the measured light yield is within 1 sigma considering the large systematic uncertainty in gains

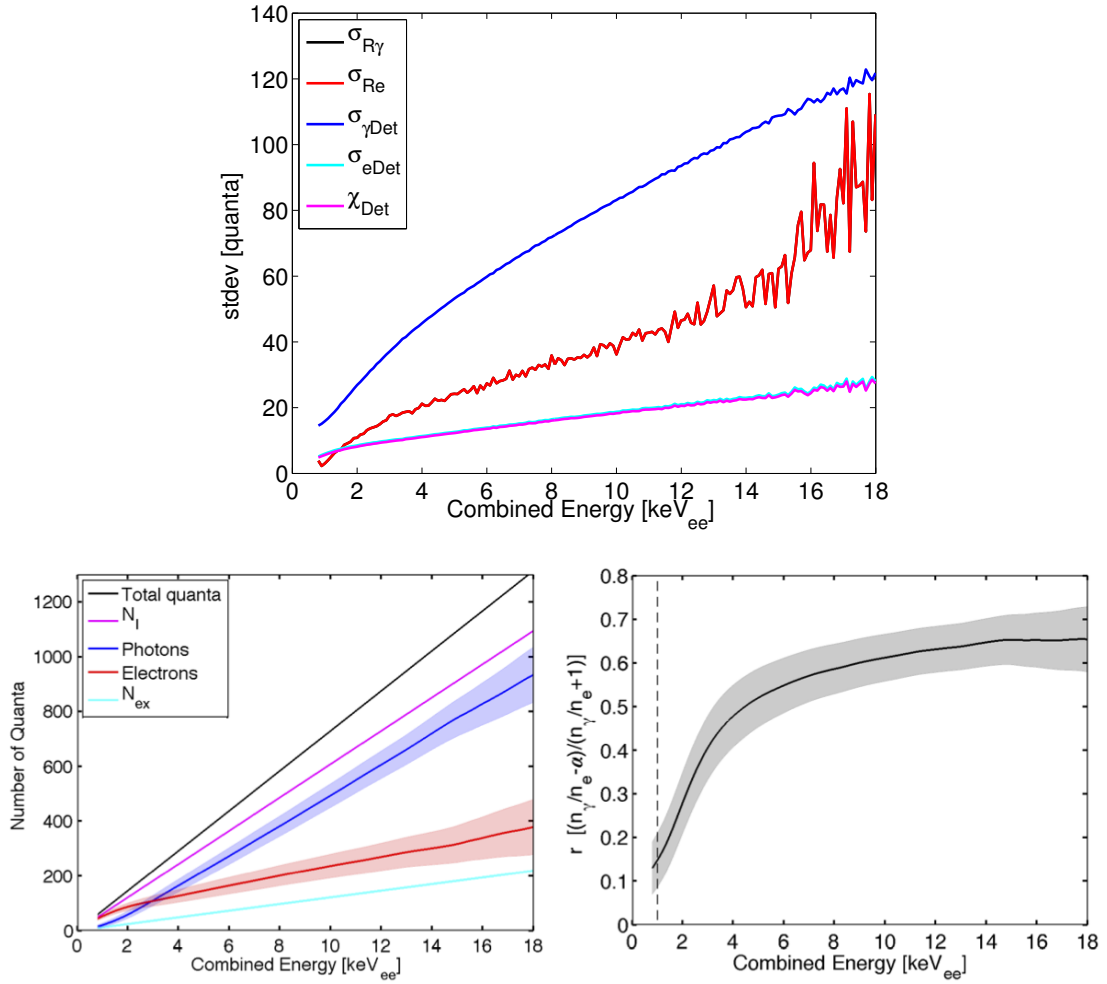


Figure 6.6: Top: Extracted recombination fluctuation from the tritium data from fluctuations in photons and electrons (Black and Red respectively). Bottom right: mean number of quanta in photons, electrons, ions, excitons vs. energy keV for the tritium calibrations. Bottom left: Recombination fraction and the one sigma (shaded) vs. energy keV.

g1 and g2. The figure also shows the one sigma prediction of the yields from NEST [62] shaded in blue where the model is interpolated and magenta where the model is extrapolated.

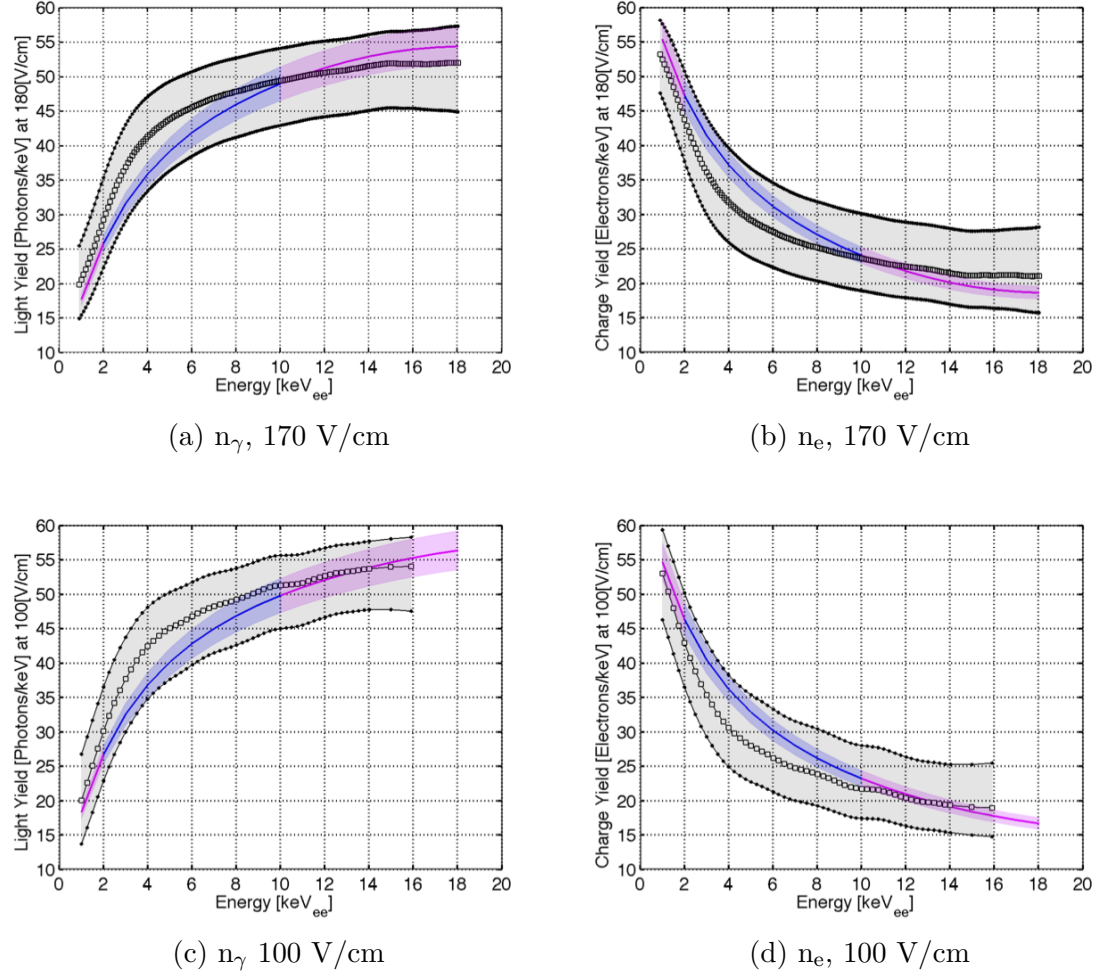


Figure 6.7: Light yield and charge yield from tritium data without spectral shape correction at 170 V/cm in black. The shaded region represents the one sigma systematic uncertainty on g1 and g2. The NEST yield prediction and its corresponding 1 sigma is shaded in blue. NEST interpolation is shown in magenta to energies where the model is not vetted. Note that the statistical errors are about the size of the data points and the dominant uncertainty illustrated by the shaded region is 100% correlated bin-to-bin. A one sigma shift up in light yield corresponds to a one sigma shift down in charge yield and visa versa.

The yields and recombination fluctuations measured from the tritium data

can be used to construct an improved model over the initial NEST prediction. As mentioned previously, the effect of detector resolution can be ignored in the region where the vast majority of the tritium events occur. Having built a new model for yields we now proceed to patch up the 20-30% shifts which occur at the edges of the S1 and S2 tritium spectra.

### 6.3 Measuring Light Yield, Charge Yield and Recombination, Corrected for Spectral Shape

Using the light yield and charge yield measurements extracted from the uncorrected tritium data we improve the light yield and charge yield model over the initial NEST-based model. In this section we will take the information gathered in the previous section to calculate the spectral shape correction for the tritium S1 and S2. With the improved model for LY and QY we can determine the efficiency for detecting S1s, S2s and the energy threshold. Finally, after applying the correction we can extract the true light yield and charge yield information from the tritium data.

#### 6.3.1 Tritium S1 and S2 Correction

We now proceed to calculate the spectral shape correction using the method outlined in section 6.2.1 with NEST yields replaced by those measured from the uncorrected tritium data. Figure 6.8 (a,c) shows the application of smearing from equation 6.7 and 6.8 applied to the light and charge yield extracted from the uncorrected tritium

data. The mapping of the observed S1 and S2 to the real S1 and S2 is also shown in the figure 6.8 (b,d). The correction is determined by using the extracted yields, applying the gains  $g_1$  and  $g_2$ , and convolving it with a true tritium beta spectrum along with the measured recombination fluctuations, equation 6.7 and 6.8. Given infinite detector resolution this is the spectrum the LUX detector would observe for S1 and S2, labeled on the figure as  $LY-T + \sigma_R$  and  $QY-T + \sigma_R$  respectively. After applying detector resolution from equation 5.17 to the plotted  $LY-T + \sigma_R$  and  $QY-T + \sigma_R$  spectrum we calculate the mapping from the real S1 and S2 means to the observed means using the model outlined in 6.1. The final spectrum with recombination fluctuations and detector resolution is labeled as  $LY-T + \sigma_R + \sigma_{S1}$  and  $QY-T + \sigma_R + \sigma_{S2}$ .

As expected, we find good agreement between the smeared tritium S1 and S2 spectra with the data. The spectral shape correction found for both S1 and S2 is consistent with those found by using NEST previously, shown in figure 6.8. This gives us confidence that we can apply the mapping of true mean to observed to the data.

The meaning of the spectral shape corrections for S1 and S2 shown in figure 6.8 (b) and (d) can be understood as a mixture of spectral shape and varying resolution. As the measured value of S1 drops to 1 PE (20% detection efficiency) we find the correction factor rises to a factor of 1.3. Even though the count rate is growing in lower S1 bins the narrowing S1 resolution cancels out the spill over from lower S1s as compared to the overlap from larger S1s with a lower count. This effect causes an observed S1 mean of 1 PE to actually be comprised of events with a mean of 1.3

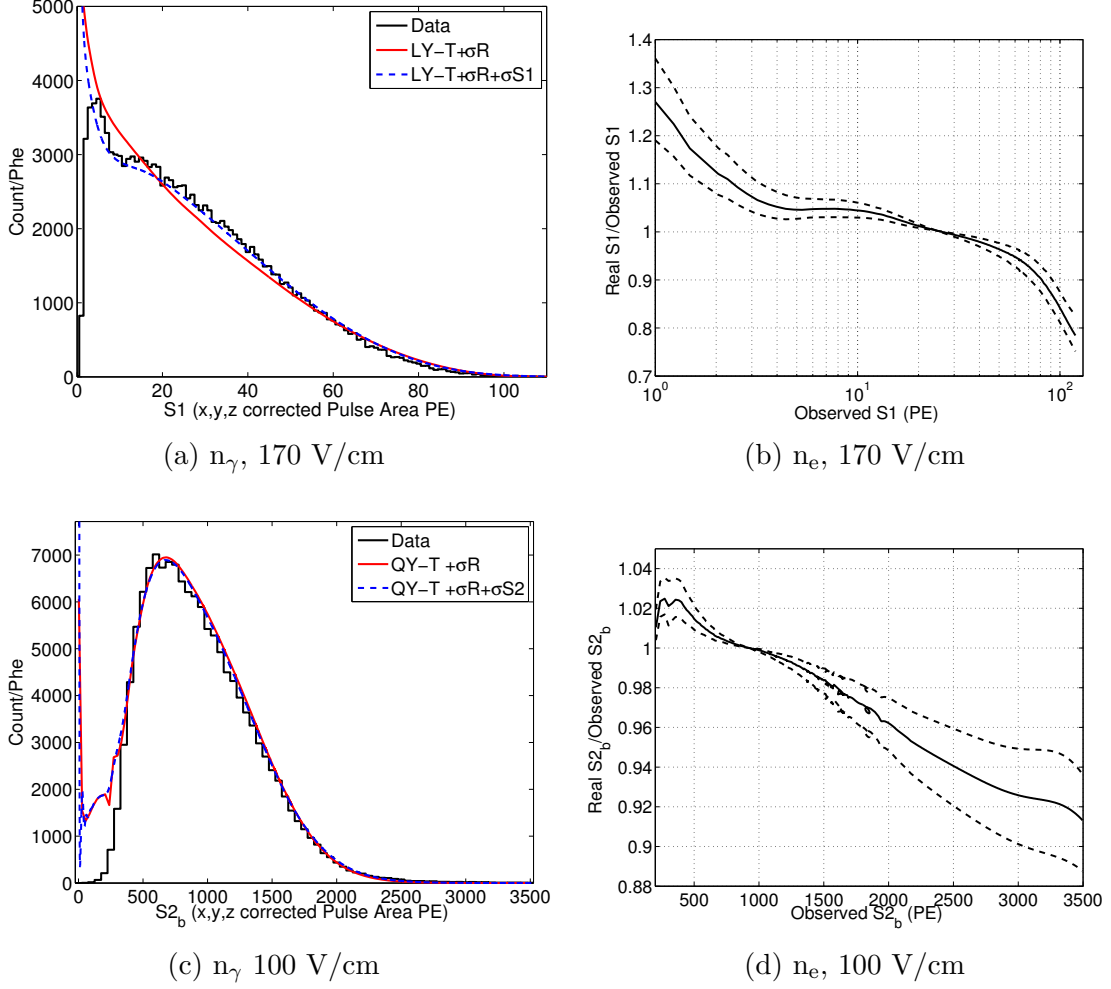


Figure 6.8: a): In Black S1 tritium S1 spectrum extracted from the data. In red, the S1 spectrum based upon the LY and QY measured from the tritium data after applying recombination fluctuations. In dashed blue, the expected S1 spectrum after applying finite detector resolutions of equation 6.7. b): The ratio of the real mean to the observed mean vs. the observed mean after smearing the tritium photon spectrum with detector resolution. Note the S1 threshold at about 3 PE in S1. c): In black, tritium S2 spectrum from the data. In red, the S2 spectrum based upon the LY and QY measured from the tritium data after applying recombination fluctuations. In dashed blue, the expected S2 spectrum after applying finite detector resolutions of equation 6.8. d): The ratio of the real mean to the observed mean vs. the observed mean after smearing the tritium electron spectrum from NEST with detector resolution. Note the S2 threshold at about 400 PE in S2.

PE. On the other end the correction is straight forward. As the beta spectrum is dropping sharply to reach 0 at the Q value of 18.6 keV [71] events from the more populated lower energy bins spill over into higher energy regions. This effect causes

the observed mean at the endpoint of 18.6 keV to actually be comprised of events with an average energy of 15 keV. Note, that the energy spectrum with detector resolution extends to 21-22 keV due to upward statistical fluctuations in S1 and S2. The S2 spectrum exhibits the same behavior at the high end above the peak of the spectrum around 1000 PE. As the S2 approaches threshold of 400 PE there is a < 3% correction to the mean to account for the spill over of the more populated regions to the right. This is different than case of S1 at low PE as the S2 resolution is about a factor of three better at the threshold.

## 6.4 Ionization and Scintillation Yield After Correction

The light and charge yield which can now be extracted from the tritium data are unique properties of liquid xenon given for ER interaction at low energies. Figure 6.9 shows the data used to calculate the means after having corrected for the S1 and S2 spectral shape. Two tritium calibration data sets are shown, one with high statistics at 170 V/cm containing 140,000 events and the second at 100 V/cm with a modest 2,500 events. (Both numbers correspond to events in the fiducial volume).

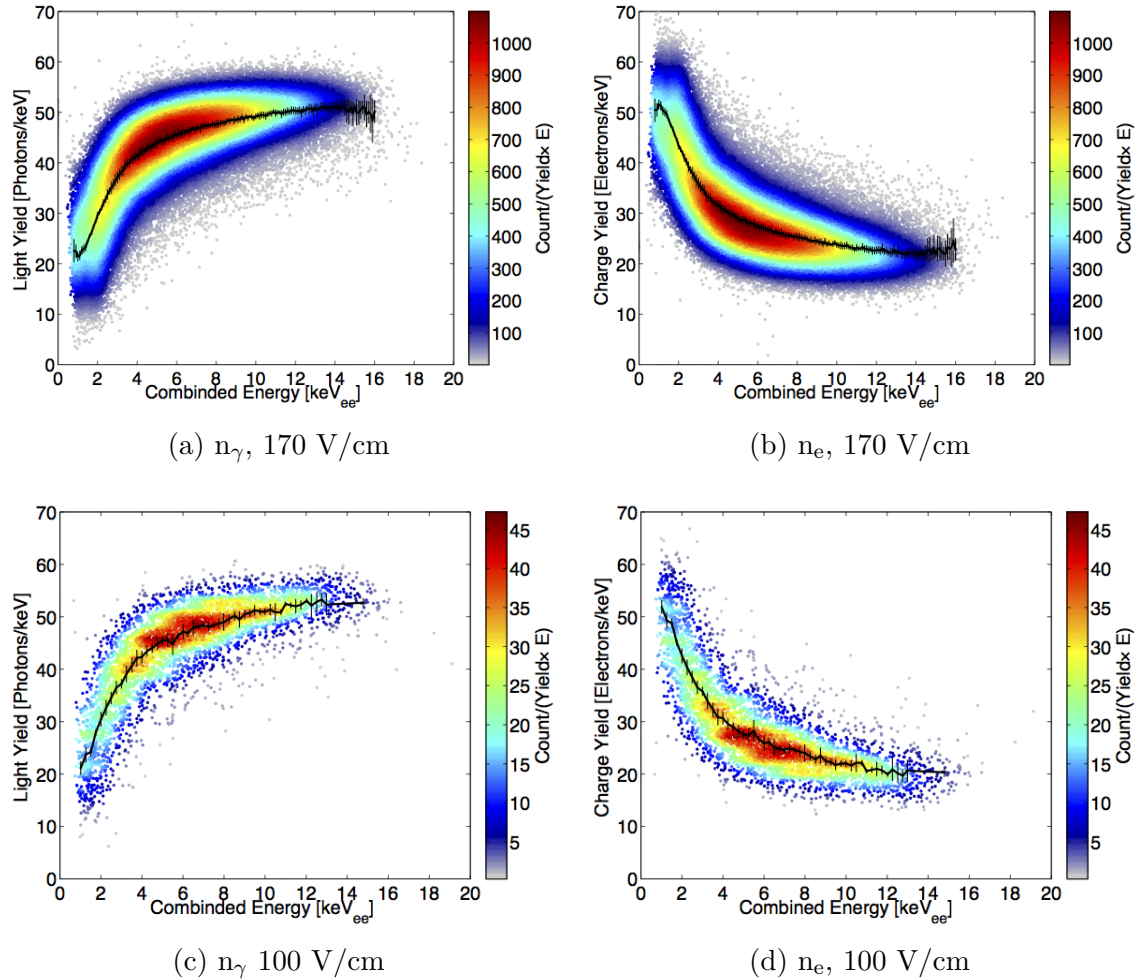
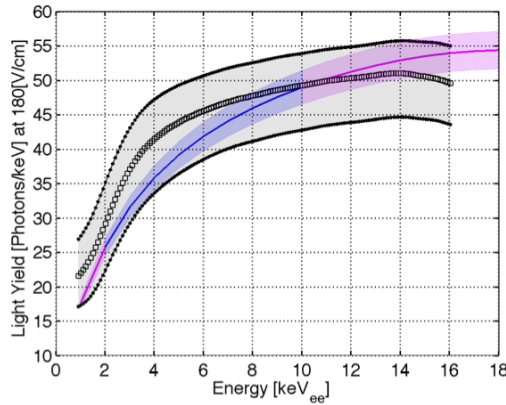


Figure 6.9: Means of the light yield and charge yield from tritium data corrected for spectral shape along with the 1 sigma statistical errors.

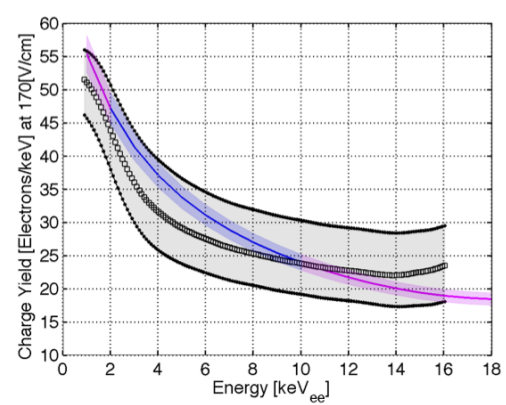
The means used for LY and QY are the population means in each slice of energy for our best value of g1 and g2. The errors shown are the statistical errors along with a small systematic component from the difference of the population mean from the Gaussian mean. The systematic offset from the constraint of g1 and g2 are treated in figure 6.10. With the potential for tighter constraints on the value of gains g1 and g2, the remaining uncertainty in the measurement of LY and QY would be less than 3% below 10 keV. The tritium calibration source has the potential to be used to determine the light and charge yield in liquid xenon to less than 3% including at the detector threshold. This calibration source hold great promise considering that few yield measurements exist below 5 keV.

Figure 6.10 shows the mean yields with the one sigma bands from the uncertainty in gains g1 and g2. The errors are anti-correlated, thus a shift up in light yields corresponds to a shift down in charge yield preserving the energy. The figure also shows the one sigma prediction of the yields from NEST [62] shaded in blue where the model is interpolated and magenta where the model is extrapolated.

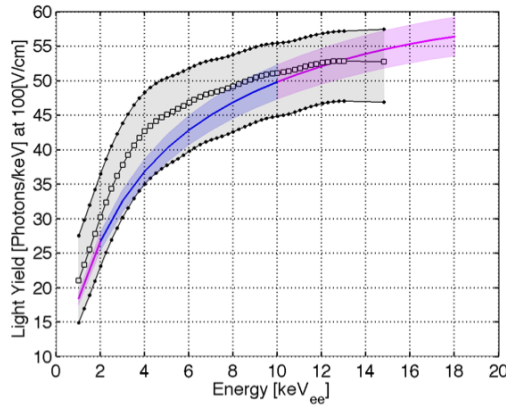
The overlap between the data and the NEST model is within one sigma considering errors in g1 and g2. However, as the errors in g1 and g2 are systematic and 100% correlated bin-to-bin they can only shift the curves up or down. Even under such a shift, the shape of the tritium data would not agree perfectly with the NEST prediction. As the statistical uncertainty alone constrains the means to better than 3% below 10 keV for the 170 V/cm data set.



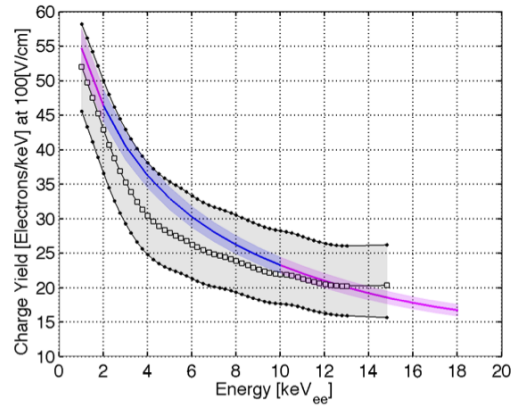
(a)  $n_\gamma$ , 170 V/cm



(b)  $n_e$ , 170 V/cm



(c)  $n_\gamma$  100 V/cm



(d)  $n_e$ , 100 V/cm

Figure 6.10: Light yield and charge yield from tritium data corrected for spectral shape along with the 1 sigma systematic constraint on  $g1$  and  $g2$ . The blue and magenta curve are NEST extrapolation and interpolation, respectively.

The comparison of measured light and charge yield before and after the tritium spectral shape correction is shown in figure 6.11 . The band in red is the result from using the raw data and combined energy, the band shown in blue is after the correction. The yields before and after the correction overlap with the exception of the last 15-18 keV bins which are pulled back as the events reconstructed at those energies on average were the result of events with 20% less energy, having upward fluctuated. In the middle regions however the spectral shape correction of the energy, the photon (S1) and electron (S2) spectrum are canceled. Recalling that yield is defined as  $n_\gamma/E$ , and  $n_e/E$ , with  $E = W(n_\gamma + n_e)$ . Thus, on average the upward or downward fluctuations in collected photons and electron are canceled by the corresponding fluctuations in reconstructed energy E.

One question remaining to be answered is if the yields and ER band defined by tritium beta decays are consistent with the more generic Compton Scatter backgrounds, which are expected to be found in the WIMP search data. It is expected that betas and gammas are indistinguishable below 10 keV [61] [62]. In the following section we will compare the light yield results from the tritium data with recent Compton scattering measurements that have probed light yield in xenon down to 1.5 keV.

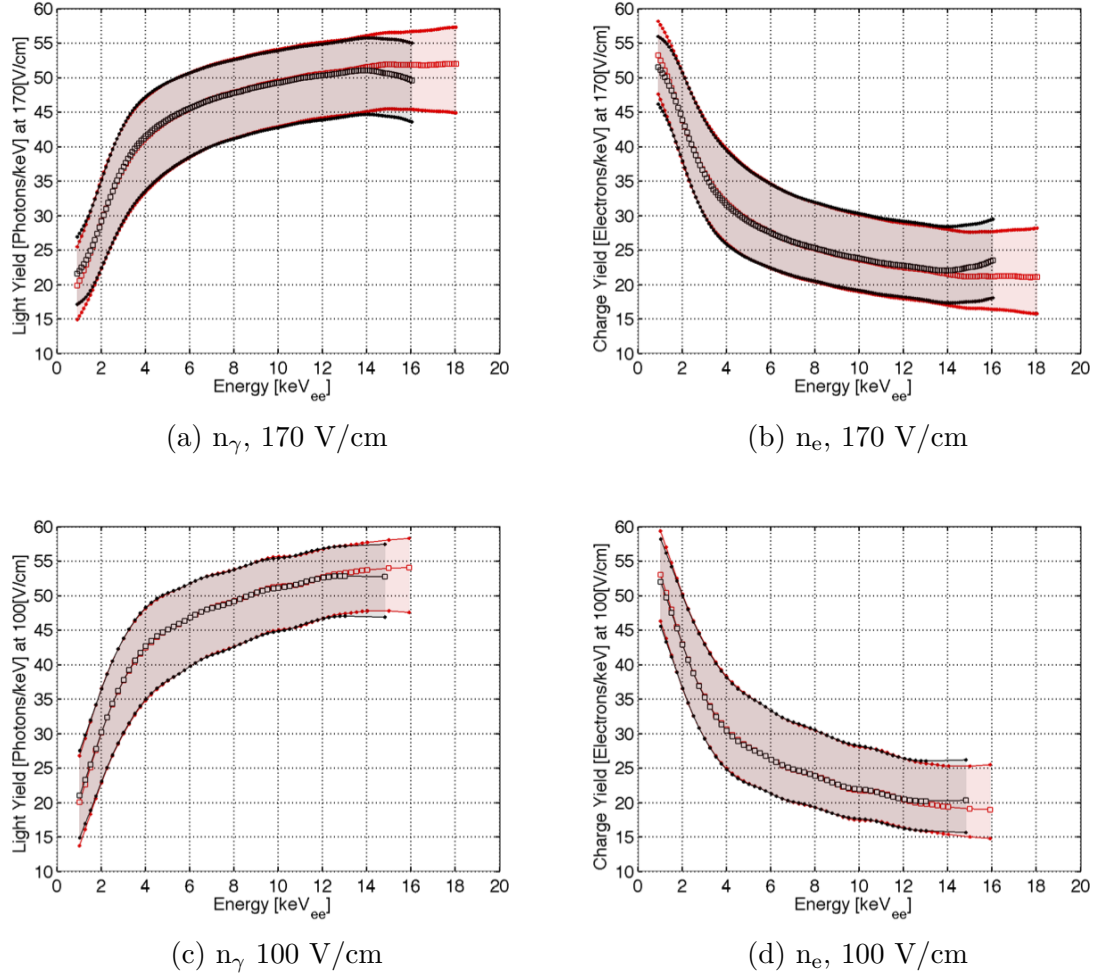


Figure 6.11: In black, the light yield and charge yield from tritium data corrected for spectral shape. In red, the light yield and charge yield from tritium data uncorrected for spectral. The shaded region represent the one sigma systematic error from the constraint on  $g_1$  and  $g_2$  shaded.

## 6.5 Comparison of Light Yield Measured With Tritium to Other Measurements With Compton Scatters

In this section we compare the LY measured with tritium in LUX to that measured with Compton scatters by other researchers. When comparing measurements from different xenon detectors it is prudent to report the result relative to that of a standard calibration source. The light yields reported for low energy Compton scatter measurements from [13] [16] are normalized to the first 32.1 keV decay of  $^{83m}\text{Kr}$ . Before comparing the light yields results from the tritium calibration we first need to measure the light yield in LUX at zero field from  $^{83m}\text{Kr}$ .

### 6.5.1 The Standard Candle: Light Yield from $^{83m}\text{Kr}$

The  $^{83m}\text{Kr}$  source was discussed in greater in chapter 3. The decay of  $^{83m}\text{Kr}$  consists primarily of the emission of two internal conversion electrons at 32.1 keV and 9.4 keV, with a half life of 154 ns between the two [12] [14] [15]. The combined signal (41.6 keV) is found by the LUX pulse finder in the majority of cases. However, the combined signal is not useful as a standard calibration. The second 9.4 keV decay receives an enhancement in light yield due to increased recombination probability from the presence of ions and electrons from the initial 32.1 keV decay. It has been observed that the light yield enhancement depends upon the decay time separation, out to 1000 ns [12] and [13]. In the LUX detector we have also observe the enhancement of the light yield of the second 9.4 keV out to 2000 ns shown in

figure 6.12. Our ability to split pulses with 100% efficiency starts at 1200 ns.

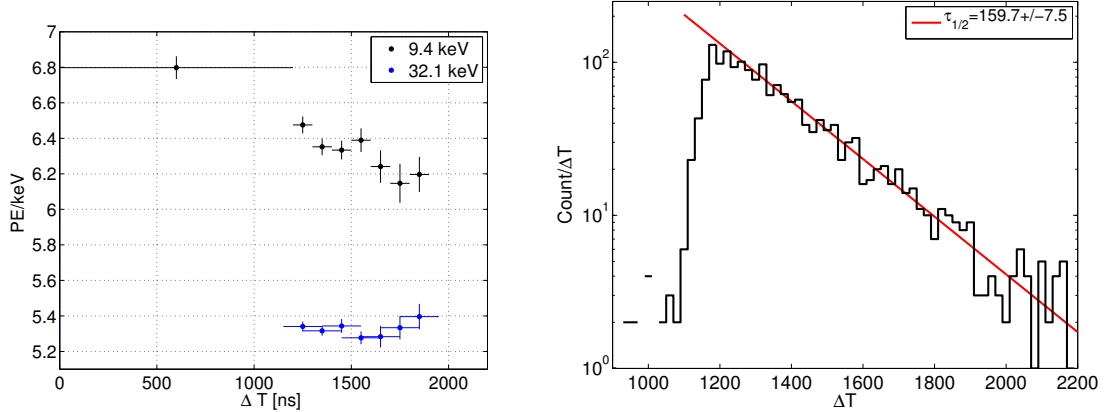


Figure 6.12: Left: The light yields of the 9.4 and 32.1 keV decay of  $^{83\text{m}}\text{Kr}$  plotted vs. timing separation, for events separated by more than 1200 ns. The point at 600 ns is calculated assuming the 32.1 keV yield remains flat to 200 ns as observed in [12] and [13]. Right: the histogram of  $^{83\text{m}}\text{Kr}$  events vs timing separation finding a best fit to the half life of  $159.7 \pm 7.5$  consistent with the measured value of 154 ns [14] [15].

Fortunately, the first 32.1 keV appears to have no time dependence as it decays under normal circumstances in the xenon, without the presence of additional free ions or electron [13], [16]. Using a  $^{83\text{m}}\text{Kr}$  data set at zero field the yield of the 32.1 keV decay was determined. Since the S2 (charge) signal is unavailable at zero drift field we rely on the top-bottom asymmetry of the PMTs to define the Z coordinate of the event,  $\frac{\text{top-bottom}}{\text{top+bottom}}$ . We must know at least the Z coordinate in order to apply the position dependent corrections outlined in chapter 3. The XY correction is subdominant to the Z-dependent correction for the S1 signal and can be ignored. Each event, given a top-bottom asymmetry, is mapped to a detector depth

$Z$  allowing for the  $Z$ -dependent correction to be applied. The correction normalizes the pulse area PE to the detector center (241.6 mm below the gate grid). The result for the zero field data set is shown in figure 6.13 and is reported in table 6.1.

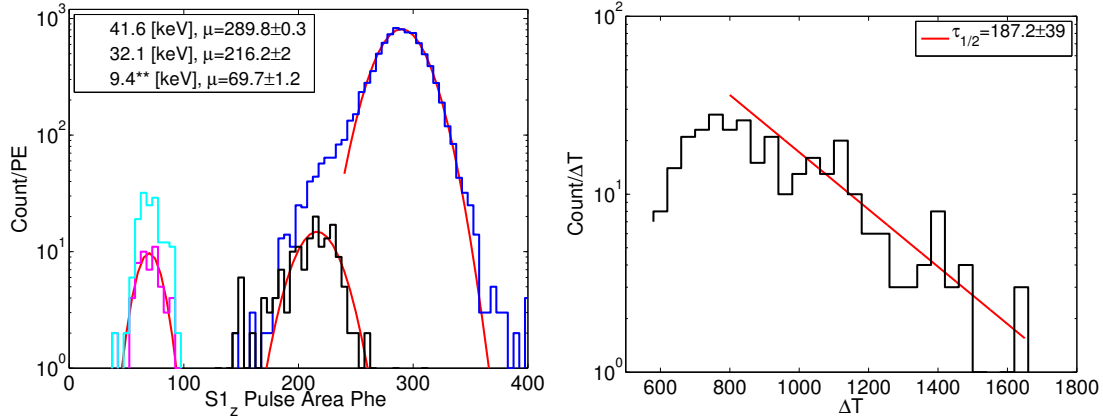


Figure 6.13: Left: S1 <sup>83m</sup>Kr peaks at zero field. Right: shows the histogram of the separated 32.1 and 9.4 keV decays plotted above vs. time. The half life fit to the population is in good agreement with the measured half-life of 154 ns [14] [15].

Table 6.1 shows the measured scintillation of the 32.1 keV internal conversion electron from <sup>83m</sup>Kr using the LUX detector at various fields. The table also includes the NEST predictions [62]. Electron mobility and charge separation at the interaction site increases with drift field leading to less recombination, causing scintillation yield to be quenched. The field effect is more dramatic at higher energies than in the low energy regions probed by the tritium data.

## 6.5.2 Comparing Tritium Scintillation Yield with Compton Scatters

We report the measured light yield of tritium relative to the 32.1 keV decay of <sup>83m</sup>Kr at zero field, defined as  $\mathcal{R}_e$ . The comparison is done as a proof of principle

Field V/cm	S1 PE	Photons $\langle n_\gamma \rangle$	Yield $\langle n_\gamma \rangle / \text{keV}$	NEST $\langle n_\gamma \rangle / \text{keV}$
0	$216.2 \pm 5.0$	$2228.9 \pm 50.5$	$69.4 \pm 1.6$	$64.2 \pm 3.2$
50	$195.0 \pm 0.7$	$2010.3 \pm 7.2$	$62.6 \pm 0.2$	$59.8 \pm 3.0$
100	$178.4 \pm 0.7$	$1839.2 \pm 7.2$	$57.3 \pm 0.2$	$55.8 \pm 2.8$
170	$171.4 \pm 0.9$	$1767.0 \pm 9.2$	$55.0 \pm 0.3$	$51.9 \pm 2.6$

Table 6.1: Field dependence of the light yield form the 32.1 keV decay of  $^{83\text{m}}\text{Kr}$  along with the NEST [62] predictions.

that the light yield from betas and gammas overlap at low energies, at least within the rather large systematic uncertainties. Further, this is a cross check that the residual  $< 10 \times 10^{-12} \text{ g/g}$  concentration of methane injected for the tritiated-methane calibration had negligible impact on the light yield, as expected from previous measurements with methane[76]. The result for  $\mathcal{R}_e$  is shown in figure 6.14, with the one sigma regions plotted as bands for the tritium data.

We find good agreement between the centroids of the tritium data at 100 and 170 V/cm with the zero field and 450 V/cm Compton scattering measurements from [16] and [13]. The finding are consistent with the expectation that tritium light yield data at 100 and 170 V/cm lie between the zero field light yield measurements the light yield at 450 V/cm. The error bars from the Compton scattering measurement are rather large due to the uncertainty in scattering angle and the need for Monte Carlo to reconstruct the energy deposit in the liquid xenon. In those measurements, the combined energy of the deposit in the liquid xenon is uncertain as both experiments were done in light-only collection mode [16] [13] (even for the 450 V/cm measurement). The errors on the tritium results are systematic and dominated by the constraint of g1 and g2 and are comparable with the errors on the Compton

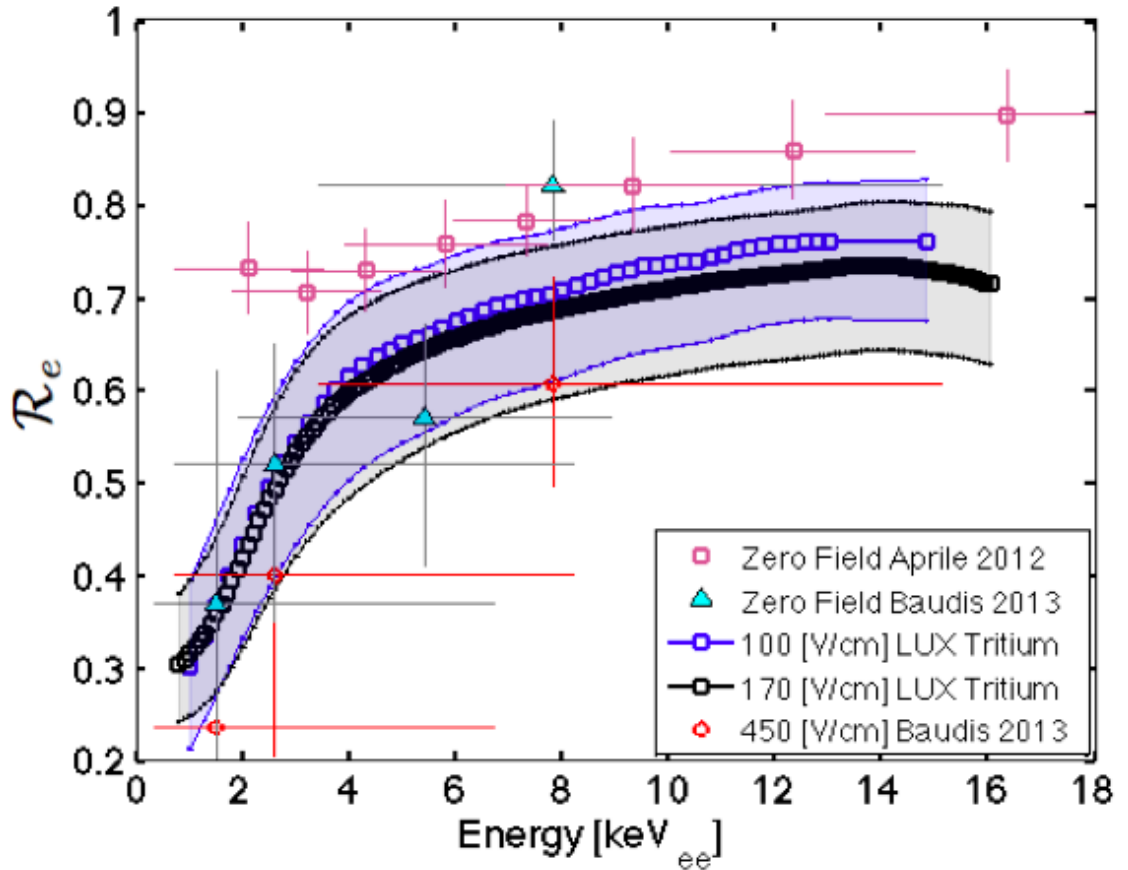


Figure 6.14: LY relative to the light yield of the 32.1 keV decay of  $^{83\text{m}}\text{Kr}$  at zero field.

The black and blue bands represent the results from tritium at 170 and 100 V/cm respectively. The shaded region represents the systematic error due to the one sigma constraints on  $g_1$  and  $g_2$ . Magenta points are Compton scattering measurements from [16]. The gray and red represent zero field and 450 V/cm Compton Scattering measurements from [13].

scattering measurements.

If the constraint on  $g_1$  and  $g_2$  in LUX is improved by future calibrations, then the errors on the tritium data will shrink significantly to below 3% making the tritium calibration a powerful tool for calibrating both light yields and charge

yields all the way to the energy threshold. The tritium light and charge yields reported here extend down to 1 keVee corresponding to the 50% threshold of LUX. The measurements also confirm, within systematic errors, that the ER band as calibrated by the tritium data is applicable to the more generic Compton scatter backgrounds in the WIMP search region of 1 to 5 keV<sub>ee</sub>. Compton scatters comprises about 2/3 of the expected background in LUX with the remaining 1/3 being from the beta decay of <sup>85</sup>Kr [6].

## 6.6 Summery

In this section we have extracted the light and charge yields using the tritium calibration source in energies ranging from 1 to 16 keV<sub>ee</sub>, shown in figures 6.9 and 6.10. The light and charge yields measured are a fundamental property electronic recoils in liquid xenon, in this work the liquid density was 2.888 g/cm<sup>3</sup>. We find agreement, within the systematic errors, between the light yields measured with the tritiated-methane source with Compton scattering measurements down to 1.5 keV<sub>ee</sub>, figure 6.14. The result supports the model that low energy betas leave identical tracks to low energy Compton scatters in liquid xenon [61] [62]. Having measured the yields, the S1 and S2 signals can be modeled for any background source only requiring the energy spectrum as an input. The ratio of charge (S2) to light (S1) characterizes a xenon detector's ability to reject background events from WIMP candidates at a particular energy. We have also found that the light and charge yields measured at 170 and 100 V/cm merge below 5 keV<sub>ee</sub>, indicating that below this energy recom-

bination is insensitive to field. The results for ER and NR discrimination using the tritium calibration source will be discussed in the chapter 7.

## Chapter 7: The Electron Recoil Band of LUX

In this chapter we overview the development, implementation and the main results of the tritiated-methane calibration source. The source was developed to be a method of calibrating the electronic recoil (ER) band in current and future large scale xenon detectors (+100 kg). As opposed to external ER calibration sources, the tritiated-methane is internal and mixes with the bulk xenon. Internal sources have a great advantage over external sources as they trivially overcome the formidable stopping power of liquid xenon, illuminating the fiducial volume of the detector. The tritiated-methane calibration source was ultimately used to characterize background ER events in LUX. Once the ER band is defined the background rejection of WIMP candidates at a particular energy is treated with a profile likelihood analysis, described in [7].

### 7.1 The need for an Internal Calibration Source

Over the past two decades liquid noble TPCs used for dark-matter experiments have grown to net more kg-days of exposure. With the additional mass, noble detectors benefit from the self shielding properties of the dense liquid inside the inner fiducial volume of the detector, as the outer volume is used as an active veto [44]. With

current generation liquid xenon detectors containing more than 100 kg, the detectors are virtually insensitive to external gamma radiation in the WIMP search region of interest of 1-10 keV<sub>ee</sub> [6] [35] [36] [37]. Being insensitive to external radioactivity improves the signal to background ratio for WIMP searches. Unfortunately, it is also shields against external calibration sources. With plans for even larger xenon detectors already moving forward [77] [78], we must develop a new method for introducing controlled radioactivity for calibration purposes.

The fiducial volume of the LUX detector is surrounded by more than 6 cm of liquid xenon providing excellent shielding from both external backgrounds and calibration sources [6]. For example, a 100 keV gamma has a mean free path of about 2 mm in liquid xenon and would require thirty mean free paths to penetrate into the fiducial volume. A higher energy source such as <sup>137</sup>Cs (662 keV) has a longer mean free path of 4 cm however, the probability of a low energy deposit from forward scattering in the fiducial followed by an escape is greatly suppressed. We would expect less than one ER event per day between 1-10 keV<sub>ee</sub> in the fiducial region if calibrating with an external <sup>137</sup>Cs or Th source, [6]. Furthermore, calibrating with high energy sources or high rate sources introduces systematic uncertainties from high energy deposits near the detector edge, the high rates would also overwhelm the DAQ.

## 7.2 Tritiated-Methane as a Calibration Source

To overcome the issues with external calibrations, the source used to calibrate the ER band must satisfy three requirements. First, it should illuminate the WIMP search band with single scatter events (1-10 keV<sub>ee</sub>). Second, it must be able to mix with the xenon and be delivered as an internal source. Third, it should either have a short half-life or be easily separated from xenon by commercially available gettering technology. <sup>83m</sup>Kr has been developed and used as an internal source with liquid xenon detectors [12] [13]. However, in LUX <sup>83m</sup>Kr only produces a mono-energetic peak at 42.1 keV<sub>ee</sub>, which is too high in energy to calibrate the WIMP search region. In order to populate the ER band with single scatter events between 1- 10 keV a beta emitter should be injected. Tritium is an ideal candidate, satisfying all but the removal requirement. Tritium has a Q value of 18.6 keV [71], a mean beta energy of 5.6 keV [72] and a mode of 3 keV [17], (see figure 7.1).

Tritium has a half life of 12.3 years [79]. Thus, it is not practical to wait for the tritium activity to decay away. The tritium must be removed after the calibration is complete in order to continue a low background WIMP search run. Hydrogen, being chemically identical to tritium, can be removed from the bulk xenon by standard gettering technology [80]. However, the removal is complicated by tritium's high diffusion rate into plastics and other detector materials [81]. Failure to remove the tritium would mark the end of a dark matter search.

To mitigate the effect of tritium diffusion into plastics we use a tritiated-methane source instead of bare tritium. Tritiated-methane consists of a tritium

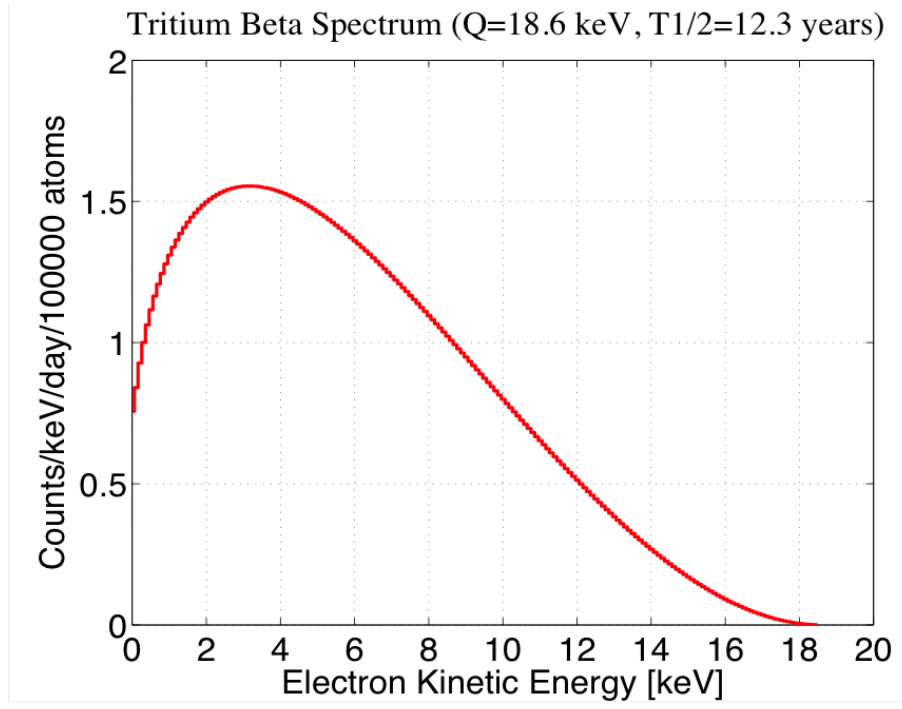


Figure 7.1: True tritium beta spectrum from [17].

atom and three hydrogen atoms bound to a carbon molecule, and is chemically identical to methane. Using tritiated-methane reduces the diffusion of tritium into detector internals by an order of magnitude [81]. The weak molecular bond,  $< 1$  eV, to the methane molecule does not impact the nuclear physics of the tritium beta decay. Also, methane is known to be soluble in liquid xenon and is sometimes used to quench scintillation light when injected in relatively large amounts [82], [76], [83]. Finally, we have studied the removal of methane by the SAES heated zirconium getter (used in LUX) and found that significant amounts of methane can be removed from xenon at our flow rates [84],[85].

### 7.3 Removal of CH<sub>4</sub> from LUX

The injection and removal of tritiated-methane into a liquid xenon vessel containing plastics was first conducted in an experimental setup at UMD. Even with conservative estimates for diffusion rates into plastics, we could not be certain about the behavior of tritiated-methane in the much larger LUX detector. Prior to injecting the tritiated-methane into LUX a much larger natural methane (non-tritiated) injection was performed in order to characterize diffusion, being chemically identical tritiated-methane. A xenon gas analysis system, developed at the University of Maryland, allowed for on site purity analysis from several ports plumbed directly into the LUX xenon circulation loop. The analysis system has ppt (part-per-trillion) sensitivity to CH<sub>4</sub> and better than ppt sensitivity to Kr. The compact system allows for hourly sampling and is used for detection of several key impurities (N<sub>2</sub>, O<sub>2</sub>, He, Ar, Kr, CH<sub>4</sub>, H<sub>2</sub>). The system is significantly less expensive than the more complex techniques used by [86] and [87]. The purity analysis technique is described in [85], [84], [88], [45], and will be described specifically for the LUX system in a future publication.

Figure 7.2 shows the results from the xenon gas analysis system for a 50 ppb (g/g) methane injection into the bulk xenon. The xenon of the LUX detector is continually cycled at 27 SLPM, with the xenon gas being passed through a heated zirconium getter which removes impurities, including methane. After the first hour, the 50 ppb of methane mixes into the liquid and appears as 300 ppb in the gas returning from the bulk liquid. The enhancement in the gas phase is due to the

solubility of methane dissolved in liquid xenon and is characterized by the Henry's constant .

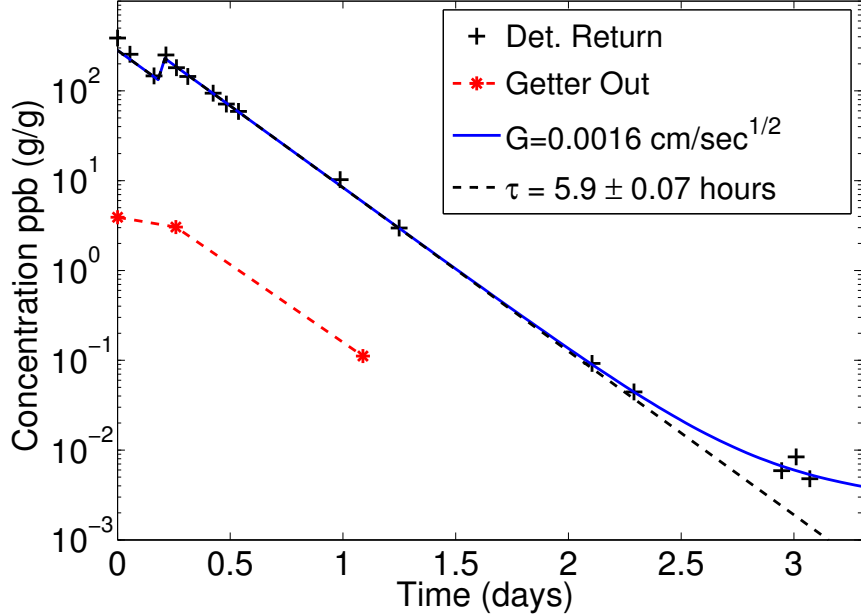


Figure 7.2: Removal of natural methane observed by the integrated xenon sampling system prior to the tritiated-methane injections. The red points indicate measurements at the getter outlet. We find a 97% one-pass removal efficiency at a flow rate of 27 SLPM. The blue curve shows the improved upper limit on the effect of outgassing from the plastics. The black dashed lines shows the exponential fit to the natural methane removal from the xenon with a time constant of  $5.9 \pm 0.07$  hours.  $5 \times 10^{-3}$  ppb (g/g) is the limit of detection for methane.

The measurements provided crucial diagnostics for methane removal and diffusion into plastic components in the LUX detector. We measured the one-pass purification efficiency for methane to be 97% by the SAES PS4-MT15-R-1 Mono-Torr getter ([80]) at a xenon gas flow rate of 27 SLPM. The getter's health for hydrocarbon removal is important to check prior to a tritiated methane injection, as an aged zirconium getter will lose its ability to remove CH<sub>4</sub> before failing for N<sub>2</sub> and O<sub>2</sub> [84]. We confirmed that natural methane could be removed by more than

five orders of magnitude without residual back diffusion. (The plateau seen in the end of figure 7.2 is caused by the 5 ppt limit for methane detection rather than diffusion from plastic components which absorb the impurity when it is initially injected).

The results from the natural methane injection gave us the confidence to proceed with injecting tritiated methane, knowing that the goal of reducing the tritium rate to less than 5% of background could be met in the LUX detector. The purification time constant for natural methane removal was measured to be  $5.9 \pm 0.07$  hours as seen in figure 7.2. The removal time constant is 1/6 of that expected based on xenon circulation rates alone, and is exactly the ratio of methane concentration in the gas to the methane concentration in the liquid. The enhanced purification time constant is reasonable as the methane is purified from the gas phase where it is more abundant, with the equilibrium concentration in the gas above the liquid set by the solubility.

## 7.4 Light Yield Quenching from CH<sub>4</sub> in LUX

It is well known that at high concentrations (several percent) methane will quench scintillation in liquid xenon [82], [76], [83] [89]. The quenching of scintillation in liquid argon has been observed with methane concentrations as low as 10 ppb (part-per-billion) [90]. When performing a tritiated-methane calibration for the LUX detector, containing 350 kg of xenon, the amount of natural methane injected is <10 ppt (parts-per-trillion). This is far too low to cause any shift in the ob-

served light yield and impact the ER band measurement. To prove this, a natural methane injection of 1 ppm (parts per million) was performed along with periodic  $^{83m}\text{Kr}$  calibrations that were used to track the light yield of the line source normalized at the center of the detector. Figure 7.3 shows the result of  $^{83m}\text{Kr}$  calibration along with the methane concentration in the gas measured by the analysis system.

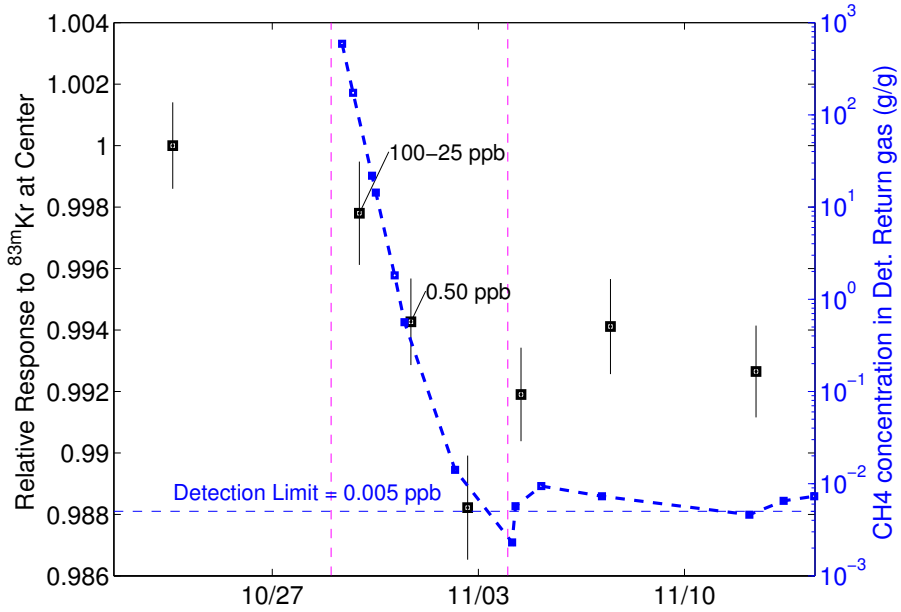


Figure 7.3: In black, the response to scintillation from  $^{83m}\text{Kr}$  at the center of the detector normalized to the first data point before the natural methane ( $\text{CH}_4$ ) injection. The dashed magenta lines represent the time window from the beginning of the natural methane injection to the time the background of 5 ppt is reached. The blue points represent that methane concentration in the gas returning from the bulk liquid of the detector. The concentration in the liquid xenon is roughly 1/6 of the concentration measured in the gas phase due to solubility.

In figure 7.3, there are two  $^{83m}\text{Kr}$  data sets that had methane concentrations above background levels. The first measurement is made with greater than 25 ppb in the gas corresponding to greater than 4 ppb in the liquid. The second contained greater than 500 ppt in the gas corresponding to greater than 83 ppt in the liquid. The shifts in yield are purely systematic, as the two light yield measurements

containing methane fall between the measured yields of the first (prior to injection) and last (well below 5ppt) data points. We constrain light yield quenching induced by 4 ppb (g/g) of methane in liquid xenon to  $< 1\%$ . Note, that a typical tritiated-methane calibration contains roughly three orders of magnitude less methane than 4 ppb (g/g).

#### 7.4.1 Tritiated Methane injection into the LUX detector

Following the natural methane test, the tritiated-methane injection was conducted at the end of the first underground science run, on Aug 8th 2013. An absolute activity of 20 mBq of tritiated-methane was injected at the purifier's outlet while circulating the xenon at 27 SLPM. A removal time constant of  $6.0 \pm 0.5$  hours was measured in the liquid volume (figure 7.4) and is consistent with the natural methane removal measured in the gas by the sampling system (figure 7.2).

After a day of circulating through the getter the tritium decay rate had fallen below detectable levels confirming the effective removal of the tritiated-methane with the getter. A second, larger injection of 800 mBq was performed a week later yielding a similar removal time constant of  $6.4 \pm 0.1$ . The second injection produced 20,000 beta decays in the LUX detector, 7000 of which were in the fiducial volume and could be used to calibrate the ER band in the WIMP search region of 1-50 PE (about 1-8 keVee). Prior to LUX detector upgrades in December 2013, a total of 10 Bq of tritiated-methane was injected into the LUX detector and successfully removed providing over 140,000 beta decays within the fiducial volume.

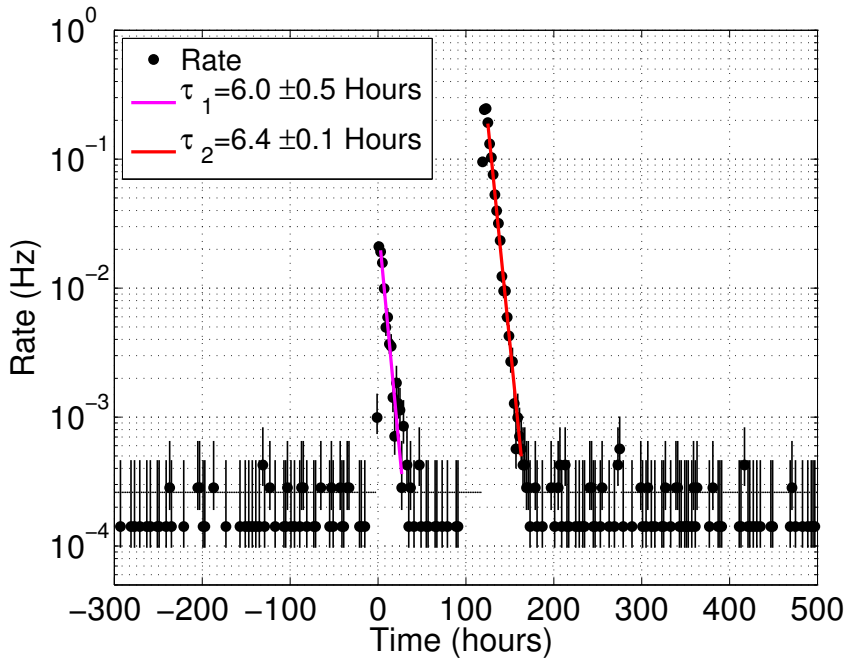


Figure 7.4: The rate of single scatter events with S1 below 100 PE in the fiducial volume. (100 PE in S1 is about 18.6 keV<sub>ee</sub>, the endpoint to the tritium beta spectrum). The magenta and red curves are fits to the first and second tritium injection's removal rate. The removal rate of tritiated-methane from the liquid is consistent with the natural methane removal rate observed in the gas by the gas analysis system (figure 7.2).

#### 7.4.2 Mixing of Tritiated Methane in Liquid Xenon

Tritium events appear uniformly distributed in the liquid xenon volume several minutes after injecting the tritiated-methane into with the xenon gas circulation path. Figure 7.5 shows the R<sup>2</sup> vs. Z distribution of tritium events thirty minutes after an injection. The events shown cover the region from the gate to the cathode and radially outward to the edge of the detector.

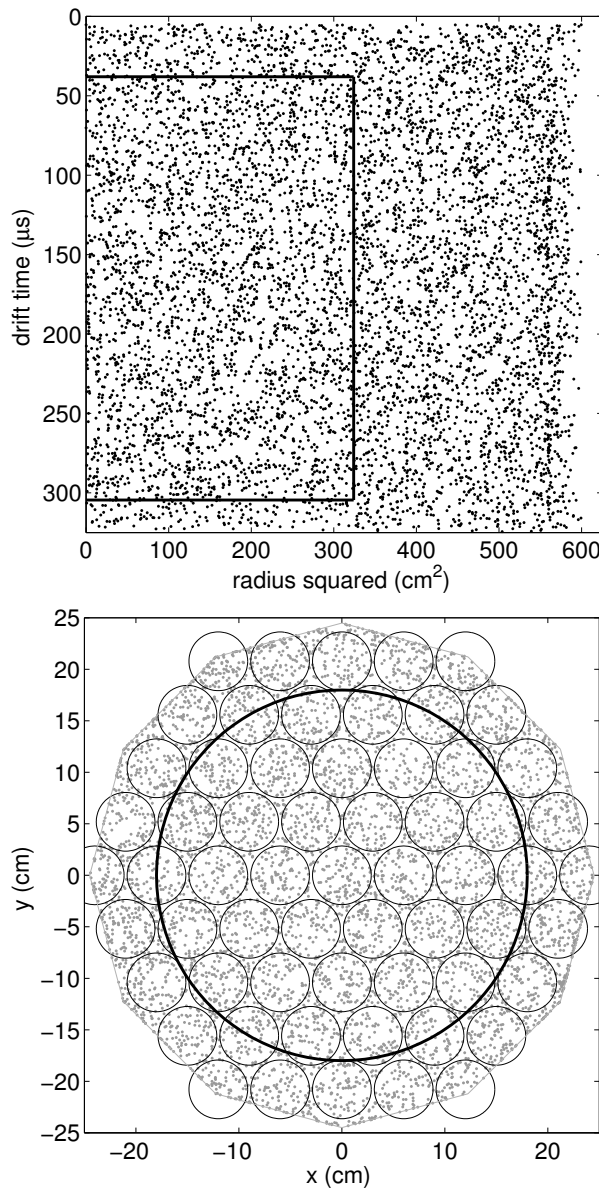


Figure 7.5: The distribution of tritium events vs. detector radius squared. The solid black line represents the fiducial volume. Right: The distribution of tritium events vs. XY in the region between the gate and the cathode. The solid black line represents the fiducial volume and the black circles represent the locations of PMTs (photo multiplier tubes).

### 7.4.3 Definition of the Electronic Recoil Band and the ER Discrimination Factor

The electronic recoil band in the fiducial volume of the LUX detector was calibrated to unprecedented accuracy using the tritium source. The calibration data was acquired in a 40 hour time window in which less than four out of the 140,000 events in the fiducial are expected to be non-tritium [6]. Nearly every data point (99.997%) that will be presented in the subsequent figures is the result of a tritium beta decay in the fiducial volume of the LUX detector.

Figure 7.6 shows the tritium calibration data with fits to the mean of the ER band along with the 10-90% confidence bounds ( $\pm 1.28\sigma$ ), at a drift field of 170 V/cm. Also shown in red is the nuclear recoil (NR) mean measured using a mono-energetic DD neutron generator calibration, described in a future LUX publication.

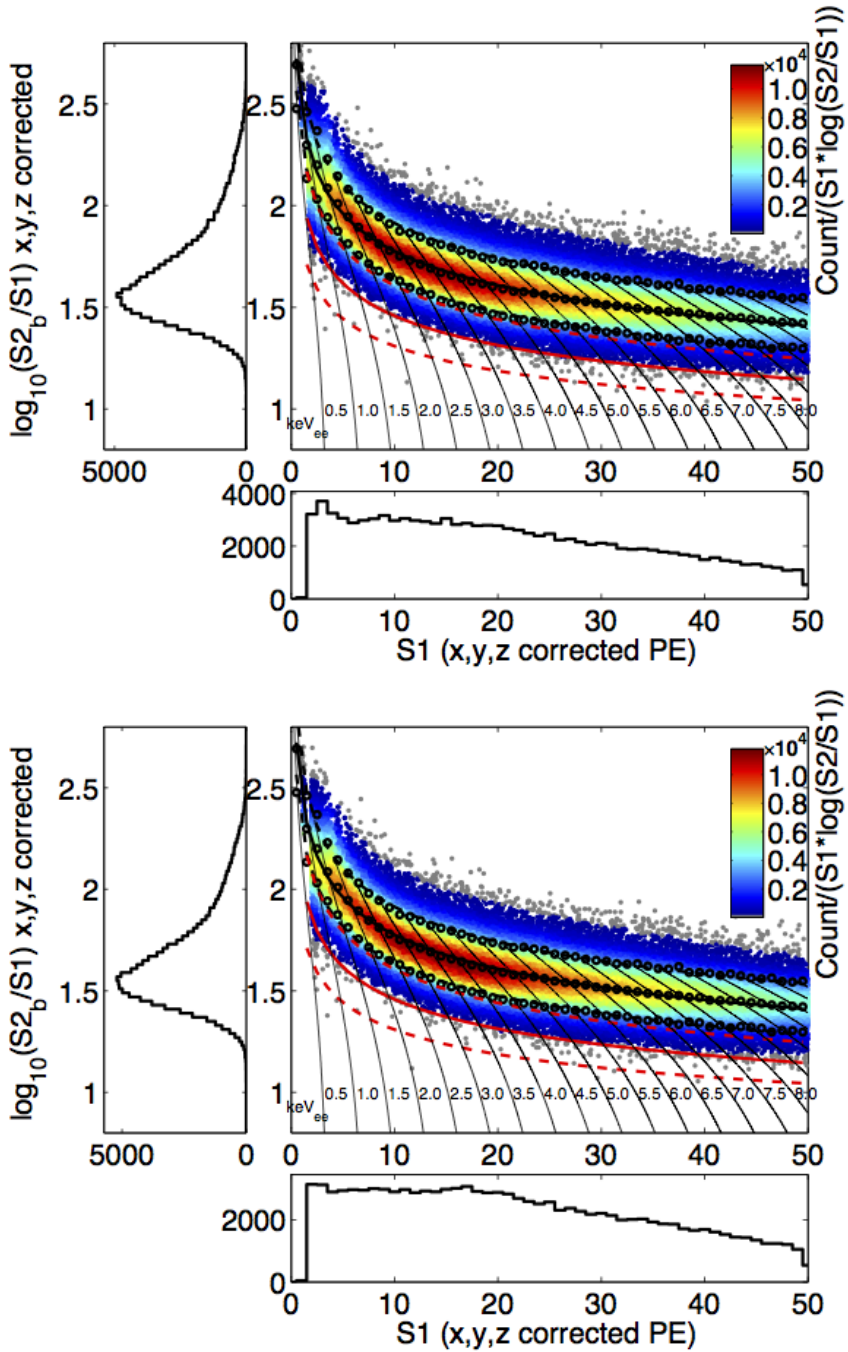


Figure 7.6: Charge-to-light ratio ( $\log_{10}(S2_b/S1)$ ) plotted vs.  $S1$ . The energy contours are also shown labeled in  $\text{keV}_{ee}$ . Top, the tritium data uncorrected for spectral shape. Bottom, with the spectral shape correction discussed in section 6.1. The calibration consists of over 112,000 tritium beta decays between 1 and 50 PE in  $S1$  (1 – 10  $\text{keV}_{ee}$ ), in the fiducial volume of the detector. The black circles represent the ER band mean and 10% to 90% bounds,  $\pm 1.28\sigma$ . The red solid line is the NR band mean determined using a DD neutron generator calibration. The dashed red lines indicate the 10% to 90% bounds of the NR band.

The ER band defined by the tritium data shown in figure 7.6 has been corrected for spectral shape discussed in section 6.1. The spectral shape correction recovers the true ER band for a flat energy spectrum. Left uncorrected, the ER band would rise slightly faster in the lowest S1 bins, below 5 PE.

The ER discrimination factor is defined as the fraction of ER events that do not fall below the mean of the NR band. The ER discrimination can also be thought of as the fraction of ER events that leak below the NR mean, or the leakage fraction. We measure the ER discrimination factor, using the tritium calibration, by counting the number of events that leak below the NR mean. Values of leakage fraction at 50% NR acceptance per 1 PE bins in S1 are shown in 7.7. Discrimination and leakage fraction is listed listed at several acceptance fractions in table 7.1. Note, Below 15 PE in S1 the NR acceptance actually becomes greater than 50% due to the asymmetric shape of the NR band at low energies, which works in our favor [61] [62].

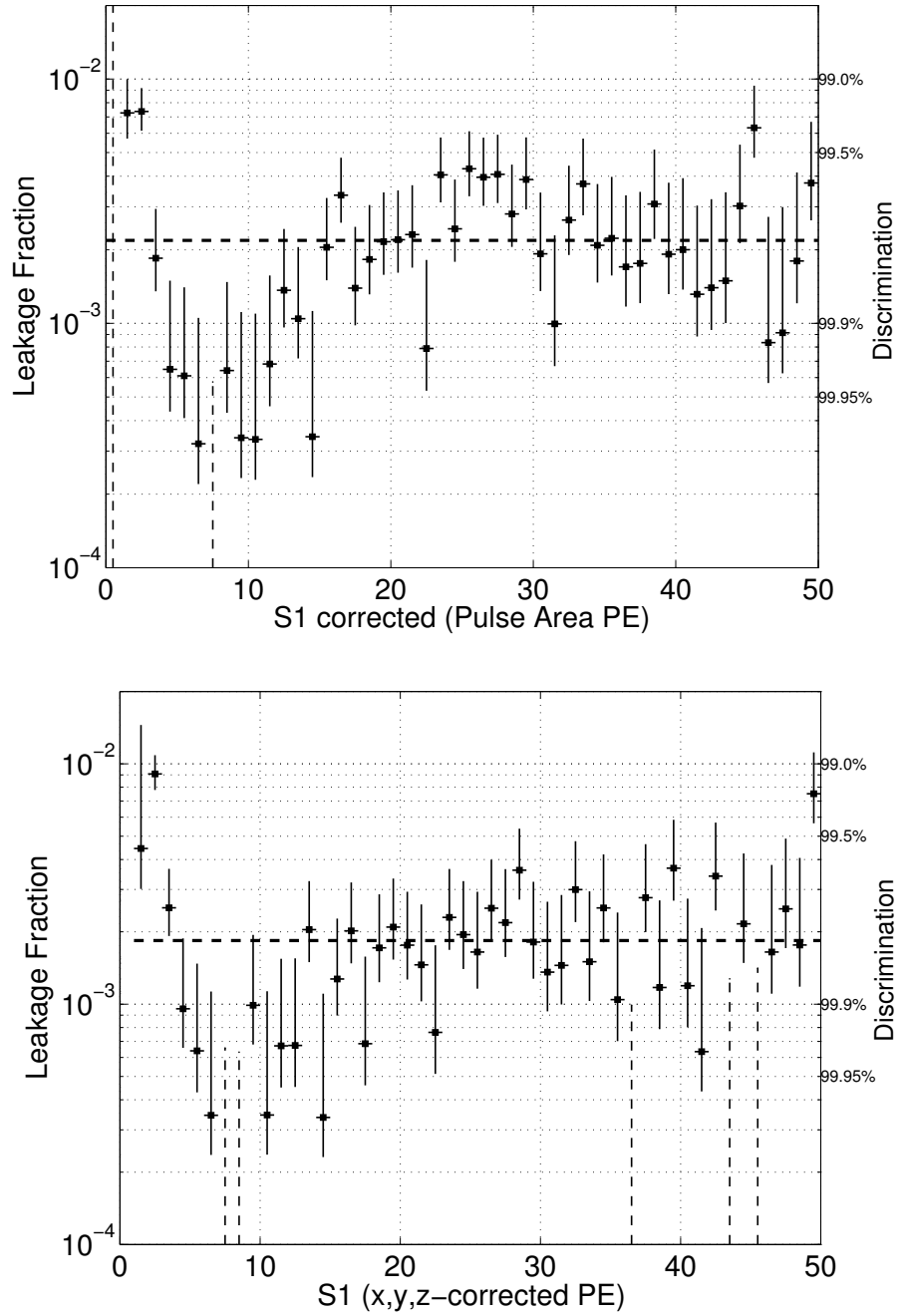


Figure 7.7: ER discrimination factor and leakage vs. S1 using over 112,000 tritium beta decays between 1 and 50 PE in S1 ( $1-10 \text{ keV}_{ee}$ ), at 170 V/cm. Top, the tritium data uncorrected for spectral shape. Bottom, with the spectral shape correction discussed in chapter 6.1. The dashed horizontal lines indicate the mean leakage fraction from 1 to 50 PE.

NR %	Leakage Fraction $\times 10^{-3}$	Discrimination %	Leakage Fraction* $\times 10^{-3}$	Discrimination* %
90	$52 \pm 0.70$	$94.8 \pm 0.07$	$49 \pm 0.60$	$95.1 \pm 0.06$
80	$18.8 \pm 0.40$	$98.1 \pm 0.04$	$17.4 \pm 0.40$	$98.3 \pm 0.04$
70	$8.6 \pm 0.30$	$99.1 \pm 0.03$	$7.6 \pm 0.30$	$99.2 \pm 0.03$
60	$4.2 \pm 0.20$	$99.58 \pm 0.02$	$3.7 \pm 0.20$	$99.63 \pm 0.02$
50	$2.1 \pm 0.14$	$99.79 \pm 0.014$	$1.8 \pm 0.13$	$99.82 \pm 0.013$
40	$0.97 \pm 0.09$	$99.90 \pm 0.009$	$0.87 \pm 0.09$	$99.91 \pm 0.009$
30	$0.49 \pm 0.07$	$99.95 \pm 0.007$	$0.44 \pm 0.06$	$99.96 \pm 0.006$
20	$0.23 \pm 0.05$	$99.977 \pm 0.005$	$0.22 \pm 0.04$	$99.978 \pm 0.004$
10	$0.08 \pm 0.03$	$99.992 \pm 0.003$	$0.08 \pm 0.03$	$99.992 \pm 0.003$

Table 7.1: Leakage fraction at various NR acceptance % over the range of 1-50 PE in S1, using tritium data at 170 V/cm. For the case without spectral shape correction, and with spectral shape correction (columns marked with \*). These are conservative estimates assuming Gaussian behavior for NR events about the mean. Below 15 PE in S1 the NR band actually becomes bottom heavy, which works in our favor by increasing NR acceptance [61] [62].

## 7.5 ER Band Gaussianity

With the high-statistics tritium data set we can test the Gaussianity of the ER band in the WIMP search region. The charge-to-light ratio used to discriminate ER and NR events (plotted as  $\log(S_2/S_1)$  in figure 7.6) has been assumed to be Gaussian in past experiments. The largest tritium calibration yielded 112,000 tritium beta decays with only four expected to be non-tritium events [6] in the LUX fiducial region. Figure 7.8 shows the same ER band of figure 7.6 but with the centroid subtracted, and is plotted with and without the spectral shape correction. We find that below 3 sigma of the ER mean the fluctuations begin to deviate from Gaussian, potentially due to instrumental effects. For example, the probability of finding an ER event 4 sigma below the ER mean is nearly 10 times higher than the probability

that would be naively assumed for a purely Gaussian PDF. If not treated properly by data-driven calibrations, such an event could be falsely interpreted as a WIMP event by a profile likelihood analysis.

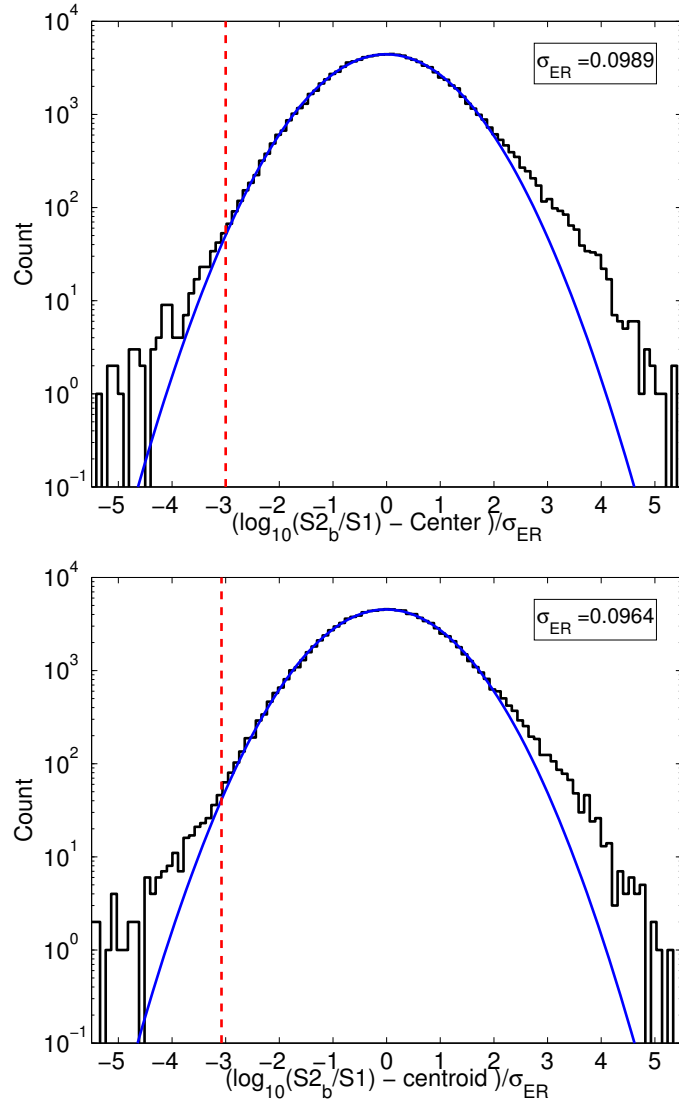


Figure 7.8: ER band Gaussianity from 0-50 PE with the centroid of the ER band subtracted off, using tritium data at 170 V/cm. Top, the tritium data uncorrected for spectral shape. Bottom, with the spectral shape correction discussed in section 6.1. The dashed vertical red line indicates the mean of the NR band from 1 to 50 PE.

## 7.6 S1 Threshold For Golden Events, Using Tritium

The tritiated-methane calibration source provides beta decays with energies well below the energy threshold of the detector ( $1.5\text{keV}_{\text{ee}}$ ). The energy threshold was measured by comparing to the combined energy to the true tritium spectrum in section 4.7. The S1 detection threshold for detecting golden events, can be determined in the same manner by taking the ratio of the S1 spectrum observed to expected S1 spectrum. The observed S1 spectrum overlaid with the expected S1 spectrum is shown in figure 6.8 a). The result for detection efficiency of S1 measured using tritium data at 170 and 100 V/cm is shown in figure 7.9, along with the efficiency measured using LED calibrations. The efficiency for detecting S1 signals at 2 PE is found to be 75%, rising to  $>95\%$  at 3 PE. The LUX trigger threshold is set by the efficiency for detecting S1 signals.

## 7.7 Conclusion

In this chapter we have described the implementation of a tritiated-methane calibration source for the LUX experiment. The primary application of the source is to characterize the ER band in the WIMP search region, of 1-50 PE ( $1\text{-}10\text{ keV}_{\text{ee}}$ ). This is of great importance, as it gauges the detector's ability to reject background (ER) events from potential WIMP signals (NR). The future LUX WIMP search will not have to rely on the assumption that the ER band can be characterized by a Gaussian PDF. All previous liquid xenon dark-matter searches have relied upon

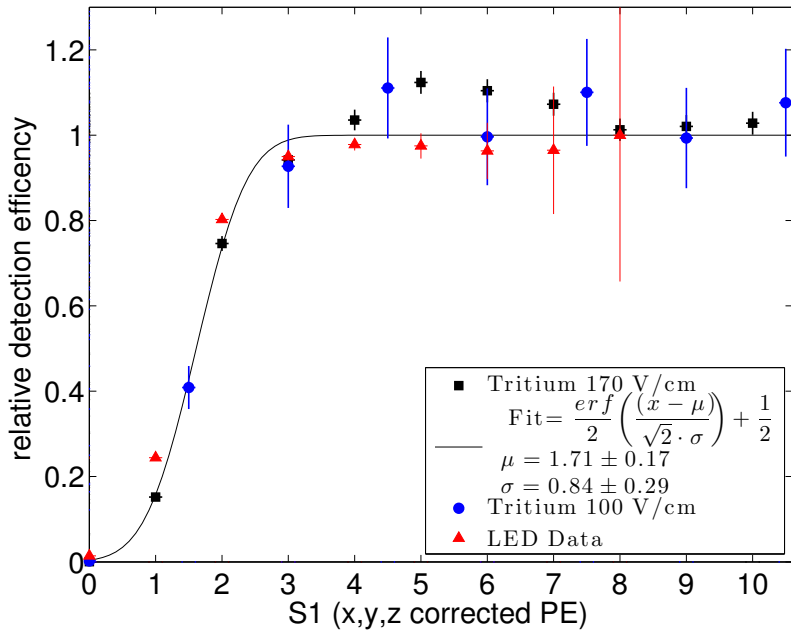


Figure 7.9: The S1 detection efficiency measured from tritium data at 170 V/cm (black square) and 100 V/cm (blue circle) is plotted along with the best fit to an error function to the higher statistics 170 V/cm data. The red triangles are detection efficiency determined from LED pulsing.

Compton scatter events to calibrate the ER band and due to lack of statistics have assumed ER band Gaussianity in the WIMP search region. We find that the use of a Guassian PDF, for the LUX detector, fails below 3 sigma of the ER mean as shown in figure 7.8. The deviation may be arising from instrumental fluctuations or is perhaps a fundamental property of electronic recoils.

Using the tritium calibration data, a data-driven PDF can be constructed to characterize the distribution of ER events in each S1 bin, greatly improving the systematics of the next WIMP search. Fundamental xenon physics could also be probed with the tritium calibration source as discussed in chapters 4, 5 and 6. The tritium calibration was used to test the energy scale calibration over the range from 1 to 18 KeV<sub>ee</sub>, and to measure the light yield, charge yield and recombination

fluctuations, and the detection thresholds down to 1 keV<sub>ee</sub>. The data taken with the LUX detector will allow for improvements to the NEST modeling at low energies.

## Chapter 8: LUX and Beyond

### 8.1 LUX 2013 Science Run Reanalysis

The LUX collaboration is currently working on an updated analysis of the 2013 science run, initially published in [7]. The reanalysis will include an improved characterization of the ER band, using the tritium data. The measurement of the NR mean has also been improved with calibration using a DD neutron generator. The new ER discrimination factor, from the improved calibration, are described in section 7.4.3. The tritium calibration set contains twenty times the statistics of the calibration used for the initial LUX WIMP result [7]. With the high statistics, the ER discrimination used in the profile likelihood analysis will be purely data-driven. Past experiments have assumed Gaussian behavior about the ER mean, however the tritium calibration has unveiled non-Gaussian tails of the ER band past three sigma of the mean (for energies between 1 to 10 keV<sub>ee</sub>).

In addition to ER discrimination, described in chapter 7, the updated WIMP analysis will benefit from improved background modeling using the data presented in chapters 4, 5, 6. The scintillation and ionization yields measured from the tritium calibration is also being used to improve upon the NEST package. With the improvements the low energy depositions of  $\gamma$  and  $\beta$  backgrounds can be precisely

converted into of the observables ( $S_1$  and  $S_2$ ).

## 8.2 Fundamental Properties of Liquid Xenon

In chapter 5 event-to-event fluctuations are discussed. The fluctuations are caused by electron-ion recombination in the liquid xenon and detector resolution. It is found that the recombination fluctuations grow like the number of ions squared, discrediting modeling based on a binomial recombination process. Future experiments, with lower photon detection thresholds, will be able to shed more light on recombination using the tritium calibration source. At low energies, as the number of ion-electron pairs goes to one, it may be found that recombination fluctuation do indeed tend to that of a binomial process.

In chapter 6 the scintillation and ionization yield of xenon was constrained and found consistent with other measurement, having rather large systematic errors. The errors on the yield measurement were dominated by the constant on gains  $g_1$  and  $g_2$ . In future calibration we plan to tighten the constraints on the gains in order to measure the light yield and charge yield to within 5%.

## 8.3 Internal Calibration Sources

The tritiated methane source developed by LUX solves the problem of ER calibration, for any detector in the foreseeable future. No matter how big a detector gets, the self-shielding is overcome by mixing the source with the xenon and then removing it. The implementation of the tritiated-methane source is also an important

proof of principle that even a long lived radio active isotope can be injected into a xenon detector for calibration purposes. As a complement to the tritiated-methane calibration source, we have developed a method track trace impurities in the xenon gas to the parts-per-trillion ( $10^{-12}$ ) level, with a specific focus on methane and krypton detection [85], [84], [45]. Having such a system is what ultimately allowed for the use of the source with the LUX detector. We could characterize both the removal and diffusion of natural-methane specifically for the LUX detector, with no reliance of diffusion modeling into plastic components.

The methodology used for the tritium source can be transferred over for use with other sources. Any new radioactive isotope can be introduced into the xenon as long as its removal (either chemically or through distillation) can be tracked by the gas analysis system. Having characterized methane removal from liquid xenon, methane molecule with  $^{14}\text{C}$  could also be used as a calibration source. There may be a variety of molecules that could be radio-tagged . As long as the molecule can be observed by the gas analysis system the purification efficiency and diffusion rate can be measured and thus carefully used as a calibration source for a xenon detector.

## Bibliography

- [1] M. Weber and W. de Boer. Determination of the local dark matter density in our Galaxy. *AAP*, 509:A25, jan 2010. doi:10.1051/0004-6361/200913381.
- [2] Anse Slosar, et al. Measurement of Baryon Acoustic Oscillations in the Lyman-alpha Forest Fluctuations in BOSS Data Release 9. *JCAP*, 1304:026, 2013. doi:10.1088/1475-7516/2013/04/026.
- [3] J.D. Lewin and P.F. Smith. Review of mathematics, numerical factors, and corrections for dark matter experiments based on elastic nuclear recoil. *Astropart.Phys.*, 6:87–112, 1996. doi:10.1016/S0927-6505(96)00047-3.
- [4] V. Chepel and H. Araújo. Liquid noble gas detectors for low energy particle physics. *Journal of Instrumentation*, 8:R04001, April 2013. doi:10.1088/1748-0221/8/04/R04001.
- [5] Richard H. Helm. Inelastic and elastic scattering of 187-mev electrons from selected even-even nuclei. *Phys. Rev.*, 104:1466–1475, Dec 1956. doi:10.1103/PhysRev.104.1466.
- [6] D. S. Akerib, et al. Radiogenic and muon-induced backgrounds in the LUX dark matter detector. *Astroparticle Physics*, 62:33–46, March 2015. doi:10.1016/j.astropartphys.2014.07.009.
- [7] S. Akerib, D. et al. First results from the lux dark matter experiment at the sanford underground research facility. *Phys. Rev. Lett.*, 112:091303, Mar 2014. doi:10.1103/PhysRevLett.112.091303.
- [8] Scott Hertel. private communication, 2014.
- [9] Tom Shutt. private communication, 2014.
- [10] M. Arenz and R. Vianden. 83mkr, a potentially powerful pac probe. *Hyperfine Interactions*, 222(1-3):73–76, 2013. ISSN 0304-3843. doi:10.1007/s10751-012-0723-3.

- [11] C. E. Dahl. *Ph.D. Thesis*. Ph.D. thesis, Princeton University, 2009.
- [12] L.W. Kastens, S. Bedikian, S.B. Cahn, A. Manzur, and D.N. McKinsey. A 83Krm Source for Use in Low-background Liquid Xenon Time Projection Chambers. *JINST*, 5:P05006, 2010. doi:10.1088/1748-0221/5/05/P05006.
- [13] L. Baudis, et al. Response of liquid xenon to compton electrons down to 1.5 kev. *Phys. Rev. D*, 87:115015, Jun 2013. doi:10.1103/PhysRevD.87.115015.
- [14] I. Ahmad, et al. Half-lives of isomeric states in fe57 and kr83. *Phys. Rev. C*, 52:2240–2241, Oct 1995. doi:10.1103/PhysRevC.52.2240.
- [15] S. L. Ruby, Y. Hazoni, and M. Pasternak. Lifetimes of the low-energy m1 transitions in la137 and kr83. *Phys. Rev.*, 129:826–828, Jan 1963. doi:10.1103/PhysRev.129.826.
- [16] E. Aprile, et al. Measurement of the scintillation yield of low-energy electrons in liquid xenon. *Phys. Rev. D*, 86:112004, Dec 2012. doi:10.1103/PhysRevD.86.112004.
- [17] P Venkataramaiah, K Gopala, A Basavaraju, S S Suryanarayana, and H Sanjeeviah. A simple relation for the fermi function. *Journal of Physics G: Nuclear Physics*, 11(3):359, 1985.
- [18] J. H. Oort. The force exerted by the stellar system in the direction perpendicular to the galactic plane and some related problems. *BAIN*, 6:249, August 1932.
- [19] F. Zwicky. On the Masses of Nebulae and of Clusters of Nebulae. *API*, 86:217, October 1937. doi:10.1086/143864.
- [20] K. G. Begeman, A. H. Broeils, and R. H. Sanders. Extended rotation curves of spiral galaxies: dark haloes and modified dynamics. *Monthly Notices of the Royal Astronomical Society*, 249(3):523–537, 1991. doi:10.1093/mnras/249.3.523.
- [21] Robert H. Brandenberger. Formation of structure in the universe. 1995.
- [22] Ryan Cooke, Max Pettini, Regina A. Jorgenson, Michael T. Murphy, and Charles C. Steidel. Precision measures of the primordial abundance of deuterium. 2013.
- [23] P.A.R. Ade et al. Planck 2013 results. XVI. Cosmological parameters. *Astron. Astrophys.*, 2014. doi:10.1051/0004-6361/201321591.
- [24] D. J. Fixsen. The Temperature of the Cosmic Microwave Background. *APJ*, 707:916–920, December 2009. doi:10.1088/0004-637X/707/2/916.
- [25] P.A.R. Ade et al. Planck 2013 results. I. Overview of products and scientific results. 2013. doi:10.1051/0004-6361/201321529.

- [26] Daniel J. Eisenstein, Hee-jong Seo, and 1 White, Martin J. On the Robustness of the Acoustic Scale in the Low-Redshift Clustering of Matter. *Astrophys.J.*, 664:660–674, 2007. doi:10.1086/518755.
- [27] W. J. Percival, et al. Baryon acoustic oscillations in the Sloan Digital Sky Survey Data Release 7 galaxy sample. *mnras*, 401:2148–2168, February 2010. doi:10.1111/j.1365-2966.2009.15812.x.
- [28] Maxim Markevitch. Chandra observation of the most interesting cluster in the universe. 2005.
- [29] Douglas Clowe, et al. A direct empirical proof of the existence of dark matter. *Astrophys.J.*, 648:L109–L113, 2006. doi:10.1086/508162.
- [30] Peter J. Kernan and Lawrence M. Krauss. Refined big bang nucleosynthesis constraints on Omega (baryon) and N (neutrino). *Phys.Rev.Lett.*, 72:3309–3312, 1994. doi:10.1103/PhysRevLett.72.3309.
- [31] Q.R. Ahmad et al. Direct evidence for neutrino flavor transformation from neutral current interactions in the Sudbury Neutrino Observatory. *Phys.Rev.Lett.*, 89:011301, 2002. doi:10.1103/PhysRevLett.89.011301.
- [32] George R. Blumenthal, S.M. Faber, Joel R. Primack, and Martin J. Rees. Formation of Galaxies and Large Scale Structure with Cold Dark Matter. *Nature*, 311:517–525, 1984. doi:10.1038/311517a0.
- [33] Gerard Jungman, Marc Kamionkowski, and Kim Griest. Supersymmetric dark matter. *Phys.Rept.*, 267:195–373, 1996. doi:10.1016/0370-1573(95)00058-5.
- [34] Andriy Kurylov and Marc Kamionkowski. Generalized analysis of weakly interacting massive particle searches. *Phys.Rev.*, D69:063503, 2004. doi:10.1103/PhysRevD.69.063503.
- [35] E. Aprile, et al. Dark Matter Results from 225 Live Days of XENON100 Data. *Physical Review Letters*, 109(18):181301, November 2012. doi:10.1103/PhysRevLett.109.181301.
- [36] Mengjiao Xiao et al. First dark matter search results from the PandaX-I experiment. 2014.
- [37] K. Abe, et al. Light WIMP search in XMASS. *Physics Letters B*, 719:78–82, February 2013. doi:10.1016/j.physletb.2013.01.001.
- [38] A. Wright. The DarkSide Program at LNGS. In S. Giani and et al., editors, *Astroparticle, Particle, Space Physics and Detectors For Physics Applications - Proceedings of the 13th ICATPP Conference. Edited by Giani Simone et al. Published by World Scientific Publishing Co. Pte. Ltd., 2012. ISBN #9789814405072, pp. 414-420, pages 414–420*. August 2012. doi:10.1142/9789814405072\_0061.

- [39] A. Hime. The MiniCLEAN Dark Matter Experiment. *ArXiv e-prints*, October 2011.
- [40] CDMS II Collaboration, et al. Dark Matter Search Results from the CDMS II Experiment. *Science*, 327:1619–, March 2010. doi:10.1126/science.1186112.
- [41] C. E. Aalseth, et al. CoGeNT: A search for low-mass dark matter using p-type point contact germanium detectors. *prd*, 88(1):012002, July 2013. doi:10.1103/PhysRevD.88.012002.
- [42] S. Archambault et al. Constraints on Low-Mass WIMP Interactions on  $^{19}F$  from PICASSO. *Phys.Lett.*, B711:153–161, 2012. doi:10.1016/j.physletb.2012.03.078.
- [43] E. Behnke, et al. First dark matter search results from a 4-kg  $\text{CF}_3\text{I}$  bubble chamber operated in a deep underground site. *prd*, 86(5):052001, September 2012. doi:10.1103/PhysRevD.86.052001.
- [44] E. Aprile and T. Doke. Liquid xenon detectors for particle physics and astrophysics. *Rev. Mod. Phys.*, 82:2053–2097, Jul 2010. doi:10.1103/RevModPhys.82.2053.
- [45] Attila Dobi, et al. Detection of krypton in xenon for dark matter applications. *Nucl.Instrum.Meth.*, A665:1–6, 2011. doi:10.1016/j.nima.2011.11.043.
- [46] A.I. Bolozdynya, P.P. Brusov, T. Shutt, C.E. Dahl, and J. Kwong. A chromatographic system for removal of radioactive  $^{85}\text{Kr}$  from xenon. *Nuclear Instruments and Methods in Physics Research Section A: Accelerators, Spectrometers, Detectors and Associated Equipment*, 579(1):50 – 53, 2007. ISSN 0168-9002. doi: DOI:10.1016/j.nima.2007.04.011. Proceedings of the 11th Symposium on Radiation Measurements and Applications.
- [47] K. Abe, et al. Distillation of liquid xenon to remove krypton. *Astroparticle Physics*, 31(4):290 – 296, 2009. ISSN 0927-6505. doi:DOI:10.1016/j.astropartphys.2009.02.006.
- [48] John R de Laeter, et al. Atomic weights of the elements. review 2000 (iupac technical report). *Pure and Applied Chemistry*, 75(6):683–800, 2003.
- [49] Tadayoshi Doke, et al. Absolute scintillation yields in liquid argon and xenon for various particles. *Japanese Journal of Applied Physics*, 41(3R):1538, 2002.
- [50] M. Miyajima, et al. Average energy expended per ion pair in liquid argon. *Phys. Rev. A*, 9:1438–1443, Mar 1974. doi:10.1103/PhysRevA.9.1438.
- [51] R. L. Platzman. *Int.J.Appl.Radiat.Isotopes*, page 116, 1961.
- [52] T. Doke and K. Masuda. Present status of liquid rare gas scintillation detectors and their new application to gamma-ray calorimeters. *Nucl.Instrum.Meth.*, A420:62–80, 1999. doi:10.1016/S0168-9002(98)00933-4.

- [53] S Kubota, M Hishida, and J Raun. Evidence for a triplet state of the self-trapped exciton states in liquid argon, krypton and xenon. *Journal of Physics C: Solid State Physics*, 11(12):2645, 1978.
- [54] Akira Hitachi, et al. Effect of ionization density on the time dependence of luminescence from liquid argon and xenon. *Phys.Rev.*, B27:5279–5285, 1983. doi:10.1103/PhysRevB.27.5279.
- [55] Jeremy Mock, et al. Modeling Pulse Characteristics in Xenon with NEST. *JINST*, 9:T04002, 2014. doi:10.1088/1748-0221/9/04/T04002.
- [56] J. V. Dawson, et al. A study of the scintillation induced by alpha particles and gamma rays in liquid xenon in an electric field. *Nuclear Instruments and Methods in Physics Research A*, 545:690–698, June 2005. doi:10.1016/j.nima.2005.01.343.
- [57] David P. Lide, editor. *CRC Handbook of Chemistry and Physics*. CRC PRESS, 81 edition, 2000.
- [58] T. Doke, A. Hitachi, S. Kubota, A. Nakamoto, and T. Takahashi. Estimation of Fano factors in liquid argon, krypton, xenon and xenon-doped liquid argon. *Nucl.Instrum.Meth.*, 134:353–357, 1976. doi:10.1016/0029-554X(76)90292-5.
- [59] T. Takahashi, et al. Average energy expended per ion pair in liquid xenon. *Phys. Rev. A*, 12:1771–1775, Nov 1975. doi:10.1103/PhysRevA.12.1771.
- [60] Jens Lindhard, V Nielsen, M Scharff, and PV Thomsen. *Integral equations governing radiation effects*. Munksgaard i komm., 1963.
- [61] M. Szydagis, et al. NEST: A Comprehensive Model for Scintillation Yield in Liquid Xenon. *ArXiv e-prints*, June 2011.
- [62] Matthew Szydagis, Adalyn Fyhrie, Daniel Thorngren, and Mani Tripathi. Enhancement of NEST Capabilities for Simulating Low-Energy Recoils in Liquid Xenon. *JINST*, 8:C10003, 2013. doi:10.1088/1748-0221/8/10/C10003.
- [63] W. . Chen, et al. Measurement of the transverse diffusion coefficient of charge in liquid xenon. *ArXiv e-prints*, September 2011.
- [64] R. Agnese et al. Search for Low-Mass Weakly Interacting Massive Particles Using Voltage-Assisted Calorimetric Ionization Detection in the SuperCDMS Experiment. *Phys.Rev.Lett.*, 112(4):041302, 2014. doi:10.1103/PhysRevLett.112.041302.
- [65] G. Angloher, et al. Results from 730 kgdays of the cresst-ii dark matter search. *The European Physical Journal C*, 72(4):1971, 2012. ISSN 1434-6044. doi:10.1140/epjc/s10052-012-1971-8.

- [66] R. Bernabei, et al. Final model independent result of DAMA/LIBRA-phase1. *European Physical Journal C*, 73:2648, December 2013. doi:10.1140/epjc/s10052-013-2648-7.
- [67] A. Dobi, et al. A xenon gas purity monitor for EXO. *Nuclear Instruments and Methods in Physics Research A*, 659:215–228, December 2011. doi:10.1016/j.nima.2011.09.017.
- [68] C. Silva, et al. A model of the reflection distribution in the vacuum ultra violet region. *Nuclear Instruments and Methods in Physics Research A*, 619:59–62, July 2010. doi:10.1016/j.nima.2009.10.086.
- [69] C. Silva, et al. Reflectance of polytetrafluoroethylene for xenon scintillation light. *Journal of Applied Physics*, 107(6):064902, March 2010. doi:10.1063/1.3318681.
- [70] V. Eckardt, et al. Calibration of the STAR forward time projection chamber with krypton-83m. 2001.
- [71] Sz. Nagy, T. Fritioff, M. Bjorkhage, I. Bergström, and R. Schuch. On the q -value of the tritium  $\beta$ -decay. *EPL (Europhysics Letters)*, 74(3):404, 2006.
- [72] D. P. Gregory and D. A. Landsman. Average decay energy of tritium. *Phys. Rev.*, 109:2091–2091, Mar 1958. doi:10.1103/PhysRev.109.2091.
- [73] J. Thomas and D. A. Imel. Recombination of electron-ion pairs in liquid argon and liquid xenon. *Phys. Rev. A*, 36:614–616, Jul 1987. doi:10.1103/PhysRevA.36.614.
- [74] J. B. Birks. *Proc. Phys. Soc.*, A64:874, 1951.
- [75] A. Mozumder. Free-ion yield and electron-ion recombination rate in liquid xenon. *Chemical Physics Letters*, 245(45):359 – 363, 1995. ISSN 0009-2614. doi:[http://dx.doi.org/10.1016/0009-2614\(95\)01024-4](http://dx.doi.org/10.1016/0009-2614(95)01024-4).
- [76] K. N. Pushkin, et al. Scintillation light, ionization yield and scintillation decay times in high pressure xenon and xenon methane. *Nuclear Science, IEEE Transactions on*, 54(3):744–750, June 2007. ISSN 0018-9499. doi:10.1109/TNS.2007.894815.
- [77] D. C. Malling, et al. After LUX: The LZ Program. *ArXiv e-prints*, October 2011.
- [78] E. Aprile and XENON1T collaboration. The XENON1T Dark Matter Search Experiment. *ArXiv e-prints*, June 2012.
- [79] L. L. Lucas and M. P. Unterweger. Comprehensive review and critical evaluation of the half-life of tritium. *Journal of Research of NIST*, 105(4):541 – 551, 2000. ISSN 0883-2889. doi:<http://dx.doi.org/10.6028/jres.105.043>.

- [80] *PS4-MT3/15-R/N SPECIFICATIONS.*
- [81] Hitoshi Miyake, Masao Matsuyama, Kan Ashida, and Kuniaki Watanabe. Permeation, diffusion, and solution of hydrogen isotopes, methane, and inert gases in/through tetrafluoroethylene and polyethylene. *Journal of Vacuum Science Technology A: Vacuum, Surfaces, and Films*, 1(3):1447–1451, Jul 1983. ISSN 0734-2101. doi:10.1116/1.572038.
- [82] A Bondar, et al. Two-phase argon and xenon avalanche detectors based on gas electron multipliers. *Nuclear Instruments and Methods in Physics Research Section A: Accelerators, Spectrometers, Detectors and Associated Equipment*, 556(1):273–280, 2006.
- [83] Eido Shibamura, et al. Drift velocities of electrons, saturation characteristics of ionization and w-values for conversion electrons in liquid argon, liquid argon-gas mixtures and liquid xenon. *Nuclear Instruments and Methods*, 131(2):249 – 258, 1975. ISSN 0029-554X. doi:[http://dx.doi.org/10.1016/0029-554X\(75\)90327-4](http://dx.doi.org/10.1016/0029-554X(75)90327-4).
- [84] A. Dobi, et al. Study of a zirconium getter for purification of xenon gas. *Nuclear Instruments and Methods in Physics Research Section A: Accelerators, Spectrometers, Detectors and Associated Equipment*, 620(23):594 – 598, 2010. ISSN 0168-9002. doi:<http://dx.doi.org/10.1016/j.nima.2010.03.151>.
- [85] D.S. Leonard, et al. A simple high-sensitivity technique for purity analysis of xenon gas. *Nuclear Instruments and Methods in Physics Research Section A: Accelerators, Spectrometers, Detectors and Associated Equipment*, 621(1-3):678 – 684, 2010. ISSN 0168-9002. doi:DOI:10.1016/j.nima.2010.04.152.
- [86] E. Aprile, T. Yoon, A. Loose, L. W. Goetzke, and T. Zelevinsky. An atom trap trace analysis system for measuring krypton contamination in xenon dark matter detectors. *Review of Scientific Instruments*, 84(9):093105, September 2013. doi:10.1063/1.4821879.
- [87] Sebastian Lindemann and Hardy Simgen. Krypton assay in xenon at the ppq level using a gas chromatographic system and mass spectrometer. *Eur.Phys.J.*, C74:2746, 2014. doi:10.1140/epjc/s10052-014-2746-1.
- [88] A. Dobi, et al. Xenon purity analysis for EXO-200 via mass spectrometry. *Nucl.Instrum.Meth.*, A675:40–46, 2012. doi:10.1016/j.nima.2012.01.066.
- [89] J. Escada, et al. A Monte Carlo study of the fluctuations in Xe electroluminescence yield: pure Xe vs Xe doped with CH<sub>4</sub> or CF<sub>4</sub> and planar vs cylindrical geometries. *Journal of Instrumentation*, 6:8006, August 2011. doi:10.1088/1748-0221/6/08/P08006.
- [90] B.J.P. Jones, et al. The Effects of Dissolved Methane upon Liquid Argon Scintillation Light. *JINST*, 8:P12015, 2013. doi:10.1088/1748-0221/8/12/P12015.